University of Alberta

Carbonyl sulfide-doped and cyanoacetylene-doped hydrogen clusters studied with rotational spectroscopy

by

Julie Michelle Michaud ©

A thesis submitted to the Faculty of Graduate Studies and Research
in partial fulfillment of the requirements for the degree of

Doctor of Philosophy

Department of Chemistry

Edmonton, Alberta
Spring 2008

Library and
Archives Canada

Published Heritage
Branch

395 Wellington Street
Ottawa ON K1A 0N4
Canada

Bibliothèque et
Archives Canada

Direction du
Patrimoine de l'édition

395, rue Wellington
Ottawa ON K1A 0N4
Canada

Your file Votre référence
ISBN: 978-0-494-45568-5
Our file Notre référence
ISBN: 978-0-494-45568-5

NOTICE:
The author has granted a non-exclusive license allowing Library and Archives Canada to reproduce, publish, archive, preserve, conserve, communicate to the public by telecommunication or on the Internet, loan, distribute and sell theses worldwide, for commercial or non-commercial purposes, in microform, paper, electronic and/or any other formats.

The author retains copyright ownership and moral rights in this thesis. Neither the thesis nor substantial extracts from it may be printed or otherwise reproduced without the author's permission.

AVIS:
L'auteur a accordé une licence non exclusive permettant à la Bibliothèque et Archives Canada de reproduire, publier, archiver, sauvegarder, conserver, transmettre au public par télécommunication ou par l'Internet, prêter, distribuer et vendre des thèses partout dans le monde, à des fins commerciales ou autres, sur support microforme, papier, électronique et/ou autres formats.

L'auteur conserve la propriété du droit d'auteur et des droits moraux qui protège cette thèse. Ni la thèse ni des extraits substantiels de celle-ci ne doivent être imprimés ou autrement reproduits sans son autorisation.

In compliance with the Canadian Privacy Act some supporting forms may have been removed from this thesis.

While these forms may be included in the document page count, their removal does not represent any loss of content from the thesis.

Conformément à la loi canadienne sur la protection de la vie privée, quelques formulaires secondaires ont été enlevés de cette thèse.

Bien que ces formulaires aient inclus dans la pagination, il n'y aura aucun contenu manquant.

Canada

Abstract

The weakly bound $(H_2)_N - OCS$ ($N = 1 - 7$) and $(H_2)_N - HCCCN$ ($N = 1 - 6$) clusters were measured using a Fourier transform microwave spectrometer. Complexes and clusters containing both spin isomers of hydrogen (*para*-hydrogen and *ortho*-hydrogen) were observed. The nuclear quadrupole hyperfine patterns were observed for clusters containing ^{14}N ($I = 1$), D ($I = 1$) and ^{33}S ($I = 3/2$) nuclei. The spin-spin hyperfine patterns due to *ortho*-hydrogen molecules were measured and assigned.

For the *ortho*H_2 – OCS and *ortho*H_2 – HCCCN complexes, both *a*- and *b*-type transitions were observed and assigned to a distortable rotor model. For the *para*H_2 – OCS and *para*H_2 – HCCCN complexes, only *a*-type transitions were observed. Both dimers are floppy and near T-shaped. An *ab initio* intermolecular potential energy surface was calculated using the coupled cluster method for the H_2 – HCCCN system and three extreme orientations of the hydrogen molecule were considered. Bound-state rotational energy levels supported by the potential were obtained for the parallel orientations (*ortho*H_2 – HCCCN) as well as for the averaged potential (*para*H_2 – HCCCN). Both potentials were scaled and the agreement with the experimental transition frequencies improved.

For most larger clusters (N = 2-7), only one rotational transition was observed. The spectra clusters with $N > 2$ were fit to a near prolate symmetric top model. Larger clusters can be pure *para*H_2 clusters, pure *ortho*H_2 clusters, or mixed clusters with a combination of both spin isomers. Mixed clusters were observed and assigned based partly on the evolving hyperfine pattern due to the spin-spin coupling of the *ortho*H_2 molecules. Additionally, structural isomers of some mixed clusters were observed and assigned. The rotational constant of the clusters decreases as the size of the cluster increases. These studies provide a stepping stone for the study of larger doped hydrogen clusters and for the observation of possible onset of superfluidity.

Acknowledgements

First and foremost, I thank my supervisor, Wolfgang Jäger, for being there to answer my many questions and to give constructive criticism. I have learned more than I thought I would ever need to know. I am appreciative for the many travel opportunities that my graduate studies have afforded me. I have enjoyed all the networking and presenting that comes along with conferences.

To all those in the immediate Jäger group and the almost immediate Xu group, I am grateful for all the guidance and discussions. Specifically, I am forever grateful to Wendy Topic for being a ray of sunshine even on the cloudiness of days. To Rudolf Lehnig and Nicole Borho thank you for always asking questions and giving great advice. I owe much gratitude to Qing Wen and Zheng Su for many discussions about science and for many others about life. To Laura Downie, even though your time in the group was short, I thank you for making the summer a great one. I owe a few good nights' out to Paul Raston, you crazy Aussies. I am grateful to Martin Losada and Qadir Timerghazin for the help with technical issues with our cluster.

To all the sports teams, thank you for giving me a way to get through the tough days. I am deeply grateful for the support from my dearest friends, Lesley, Berenice, Mel, and Magda, you all help to keep me sane. I am grateful for the encouragement and support from my family. Last but not least, to Stuart Chambers, you're even better than the degree that I came here for.

Table of Contents

Chapter Page

1 Introduction **1**

1.1 References 13

2 Basic theory and experimental techniques of rotational spectroscopy **19**

2.1 Molecular rotational spectroscopy 20
2.2 Rigid Rotor 21
2.3 Selection rules for asymmetric top molecules 22
2.4 Centrifugal distortion: The distortable rotor 24
2.5 Nuclear hyperfine interactions 25
    2.5.1 Nuclear electric quadrupole interaction 27
    2.5.2 Nuclear magnetic spin-spin interaction 29
    2.5.3 Nuclear magnetic spin-rotation interaction 31
2.6 Molecular structure 32
2.7 Theoretical description of microwave spectroscopy 34
2.8 General description of the Fourier transform microwave spectrometer 39
2.9 Microwave-microwave decoherence double resonance experiments 42
2.10 Construction of the *para*-hydrogen converter 43
2.11 Figures 44
2.12 References 48

3 Study of H_2 – OCS dimer: Minor Isotopologues of OCS **51**

3.1 Experimental details 51
3.2 Experimental results and spectroscopic analyses 53
3.3 Discussion 56
3.4 Conclusions 60
3.5 Figures 62
3.6 Tables 66
3.7 References 70

4 Spectroscopic and theoretical study of the weakly bound H_2 – HCCCN dimer **72**

4.1 Experimental details 73
    4.1.1 Synthesis of cyanoacetylene 73
    4.1.2 *Para*H_2 enrichment 75
4.2 Experimental results and analyses 77
4.3 Discussion of experimental results 82
4.4 Construction of potential energy surfaces 89
4.5 Properties and accuracy of the H_2 – HCCCN potential energy surfaces 93

4.6 Conclusions 97
4.7 Figures 99
4.8 Tables 105
4.9 References 117

5 Spectroscopic investigations of $(H_2)_N$ – OCS clusters ($N = 2$-7) 120

5.1 Experimental details 121
5.2 Results and analyses 123
  5.2.1 $N = 2$ 124
  5.2.2 $N = 3,4,5$ 125
    5.2.2.1 $(\textit{para}H_2)_{3,4,5}$ – OCS clusters 125
    5.2.2.2 $(\textit{ortho}H_2)_{3,4,5}$ – clusters 126
    5.2.2.3 $(\textit{para}H_2)_x(\textit{ortho}H_2)_{N-x}$ – OCS mixed clusters ($N = 3,4,5$) 127
  5.2.3 $N = 6,7$ 127
    5.2.3.1 $(\textit{para}H_2)_{6,7}$ – OCS clusters 127
    5.2.3.2 $(\textit{ortho}H_2)_{6,7}$ – OCS clusters 128
    5.2.3.3 $(\textit{para}H_2)_x(\textit{ortho}H_2)_{N-x}$ – OCS mixed clusters ($N = 6,7$) 128
5.3 Discussion 130
  5.3.1 Cluster size assignment 130
  5.3.2 Spin-spin hyperfine patterns from *ortho*H_2 molecules 130
  5.3.3 ^{33}S nuclear quadrupole hyperfine pattern 134
  5.3.4 Trend in rotational constant with increasing cluster size 134
5.4 Summary 136
5.5 Figures 138
5.6 Tables 146
5.7 References 152

6 Spectroscopic investigations of $(H_2)_N$ – HCCCN clusters 154

6.1 Experimental details 154
6.2 Results and analyses 155
  6.2.1 $N = 2$ 156
  6.2.2 $N = 3$ 157
  6.2.3 $N > 3$ 158
6.3 Discussion of experimental results 160
6.4 Assignment of N, the number of solvating hydrogen molecules 164
6.5 Summary 165
6.6 Figures 167
6.7 Tables 173
6.8 References 184

7 Conclusions 185

7.1 References 188

Appendices **189**

A. *Ab initio* single point energies for four H_2 – HCCCN orientations of intermolecular potential energy surfaces 189

B. Determined theoretical rotational energy levels, up to $J = 3$ for unscaled and scaled H_2 – cyanoacetylene potential energy surfaces. 201

List of Tables

Table Page

2.1 Character table for the D_2 point group 24

2.2 Selection rules for rotational transitions 24

3.1 Measured transition frequencies (in MHz) and quantum number assignments of isotopologues of the *ortho*H_2 – OCS dimer. 66

3.2 Measured transition frequencies (in MHz) with quantum number assignments and spectroscopic constants (in MHz) for *ortho*H_2 – $OC^{33}S$ and *ortho*H_2 – $O^{13}C^{33}S$ dimers. 67

3.3 Measured transition frequencies (in MHz) of isotopologues of the *para*H_2 – OCS dimer. 67

3.4 Measured transition frequencies (in MHz) and spectroscopic constants (in MHz) for *para*H_2 – $OC^{33}S$ and *para*H_2 – $O^{13}C^{33}S$ dimers. 68

3.5 Spectroscopic constants (in MHz) of isotopologues of the *ortho*H_2 – OCS dimer. 68

3.6 Spectroscopic constants (in MHz) of isotopologues of the *para*H_2 – OCS dimer. 69

3.7 Experimental structural parameters for *ortho*H_2 – OCS, *para*H_2 – OCS, and He – OCS van der Waals complexes. 69

4.1 Measured rotational transition frequencies (in MHz) and quantum number assignments for the *ortho*H_2 – HCCCN dimer. 105

4.2 Measured rotational transition frequencies (in MHz) and quantum number assignments for the *ortho*H_2 – $HCCC^{15}N$. 107

4.3 Measured rotational transition frequencies (in MHz), quantum number assignments, and determined spectroscopic constants (in MHz) for various ^{13}C dimers of *ortho*H_2 – HCCCN. 107

4.4 Measured rotational transition frequencies (in MHz) and quantum number assignments for the *ortho*H_2 – DCCCN dimer. 108

4.5 Measured rotational transition frequencies (in MHz) and quantum number assignments for the *para*H_2 – HCCCN dimer and *para*H_2 – $HCCC^{15}N$. 109

4.6 Measured rotational transition frequencies (in MHz), quantum number assignments, and determined spectroscopic constants (in MHz) for various ^{13}C dimers of *para*H_2 – HCCCN. 110

4.7 Measured rotational transition frequencies (in MHz) and quantum number assignments for the *para*H_2 – DCCCN dimer. 110

4.8 Determined spectroscopic parameters for the *ortho*H_2 – HCCCN, *ortho*H_2 – $HCCC^{15}N$, and *ortho*H_2 – DCCCN dimers. 111

4.9 Experimental structural parameters for *ortho*H_2 – HCCCN, *para*H_2 – HCCCN, and He – HCCCN van der Waals complexes. 112

4.10 Determined spectroscopic parameters for the *para*H_2 – HCCCN, *para*H_2 – $HCCC^{15}N$, and *para*H_2 – DCCCN dimers. 112

4.11 Topographical features of various H_2 – HCCCN potential energy surfaces. 112

4.12 Hypothetical unsplit centre line frequencies and spectroscopic parameters of the *ortho*H_2 – HCCCN complex from potential energy surfaces compared with experimental values. 113

4.13 Hypothetical unsplit centre line frequencies and spectroscopic parameters of the *para*H_2 – HCCCN complex from potential energy surfaces compared with experimental values. 114

4.14 Hypothetical unsplit centre line frequencies and spectroscopic parameters of the *ortho*H_2 – DCCCN and *ortho*H_2 – $HCCC^{15}N$ complexes from potential energy surfaces compared with experimental values. 115

4.15 Hypothetical unsplit centre line frequencies and spectroscopic parameters of the *para*H_2 – DCCCN and *para*H_2 – $HCCC^{15}N$ complexes from potential energy surfaces compared with experimental values. 116

5.1 Measured frequencies (MHz) of the $J = 1\text{-}0$ rotational transitions of $(pH_2)_N$ – OCS clusters. 146

5.2 Rotational transition frequencies (in MHz) of $(orthoH_2)_N$ – OCS clusters. 147

5.3 Rotational transition frequencies and *ortho*H_2 spin-spin coupling constants (in MHz) of the mixed $(paraH_2)_x(orthoH_2)_{N-x}$ – OCS clusters. 148

5.4 Rotational transition frequencies of the nuclear quadrupole hyperfine components (MHz) of the $J = 1\text{-}0$ transitions and nuclear quadrupole coupling constants (in MHz) of the $(orthoH_2)_N$ – $OC^{33}S$ clusters. 151

6.1 Measured rotational transition frequencies (in MHz), quantum number assignments, and determined spectroscopic constants (in MHz) for $(H_2)_2$ – HCCCN clusters. 173

6.2 Measured rotational transition frequencies (in MHz), quantum number assignments, and determined spectroscopic constants (in MHz) for $(H_2)_2$ – DCCCN and $(H_2)_2$ – $HCCC^{15}N$ clusters. 174

6.3 Measured rotational transition frequencies (in MHz), quantum number assignments and determined spectroscopic constants (in MHz) for $(H_2)_3$ – HCCCN clusters. 175

6.4 Measured rotational transition frequencies (in MHz), quantum number assignments, and determined spectroscopic constants (in MHz) for $(H_2)_3$ – DCCCN and $(H_2)_3$ – $HCCC^{15}N$ clusters. 177

6.5 Measured rotational transition frequencies (in MHz), quantum number assignments, and determined spectroscopic constants (in MHz) for $(H_2)_4$ – HCCCN clusters. 178

6.6 Measured rotational transition frequencies (in MHz), quantum number assignments, and determined spectroscopic constants (in MHz) for $(H_2)_5$– HCCCN clusters. 179

6.7 Measured rotational transition frequencies (in MHz), quantum number assignments, and determined spectroscopic constants (in MHz) for $(H_2)_6$ – HCCCN clusters. 181

6.8 Measured rotational transition frequencies (in MHz), quantum number assignments, and determined spectroscopic constants for $(H_2)_N$ – $HCCC^{15}N$ clusters with $N = 4$-6. 182

6.9 Measured rotational transition frequencies (in MHz), quantum number assignments, and determined spectroscopic constants for $(H_2)_N$ – DCCCN clusters with $N = 4$-6. 183

6.10 Measured $J = 1$ -0 transition frequencies (in MHz) for unassigned $(H_2)_N$ – HCCCN clusters. 183

A.1 *Ab initio* single point energies of the parallel orientation of H_2 – HCCCN potential energy surface. 189

A.2 *Ab initio* single point energies of the perpendicular orientation of H_2 – HCCCN potential energy surface. 192

A.3 *Ab initio* single point energies of the out-of-plane orientation of H_2 – HCCCN potential energy surface. 195

A.4 *Ab initio* single point energies of the averaged H_2 – HCCCN potential energy surface (equal weighting of the three orientations). 198

B.1 Rotational energy levels of *ortho*H_2 – HCCCN in the ground vibrational state for the potential energy surfaces corresponding to the parallel, perpendicular and out-of-plane orientations. 201

B.2 Rotational energy levels of *ortho*H_2 – $HCCC^{15}N$ and *ortho*H_2 - DCCCN in the ground vibrational state for the potential energy surface corresponding to the parallel, orientation. 202

B.3 Rotational energy levels of *para*H_2 – HCCCN in the ground vibrational state for the averaged potential energy surface (equal weighting all three orientations). 203

B.4 Rotational energy levels of *para*H_2 – $HCCC^{15}N$ and *para*H_2 - DCCCN in the ground vibrational state for the averaged potential energy surface (equal weighting all three orientations). 204

List of Figures

Figure Page

2.1 A simplified schematic illustration of the setup of the Fourier transform microwave spectrometer used in our laboratory. 44

2.2 Illustration of the destructive MW-MW double resonance (DR) scheme used in this work. 45

2.3 A representative spectrum of the effect of destructive MW-MW DR experiment. 46

2.4 A schematic diagram showing the design of the para-hydrogen converter built for some studies in this thesis. 47

3.1 Experimental spectra of the $J_{KaKc} = 1_{01} - 0_{00}$ transition of *ortho*$H_2 - OC^{34}S$ and *para*$H_2 - OC^{34}S$. 62

3.2 Experimental spectrum of the $J_{KaKc} = 1_{10} - 1_{01}$ transition of *ortho*$H_2 - O^{13}CS$. 63

3.3 Experimental composite spectrum of the $J_{KaKc} = 1_{01} - 0_{00}$ transition of *para*$H_2 - O^{13}C^{33}S$. 64

3.4 The T-shaped geometry of the hydrogen-OCS complex. 65

4.1 A composite experimental spectrum of the $J_{KaKc} = 1_{01} - 0_{00}$ transition of *ortho*H_2 – HCCCN. 99

4.2 A composite experimental spectrum of the $J_{KaKc} = 1_{11} - 0_{00}$ transition of *ortho*H_2 – HCCCN. 100

4.3 A composite experimental spectrum of the $J_{KaKc} = 2_{12} - 1_{11}$ transition of *ortho*H_2 – HCCCN. 101

4.4 A composite experimental spectrum of the $J_{KaKc} = 1_{01} - 0_{00}$ transition of *para*H_2 – HCCCN. 102

4.5 The T-shaped geometry of the hydrogen-HCCCN complex. 103

4.6 The T-shaped geometry of the hydrogen-HCCCN complex used in the potential energy surface calculations. 104

5.1 $J_{KaKc} = 1_{01} - 0_{00}$ transitions of $($*ortho*$H_2)_2$ – OCS and $($*para*$H_2)($*ortho*$H_2)$ – OCS. 138

5.2 $J_{KaKc} = 1_{01} - 0_{00}$ transition of ($ortho$H$_2$)$_2$ – OC^{33}S. 139

5.3 $J = 1 - 0$ transitions of ($para$H$_2$)$_3$ – OCS and ($para$H$_2$)$_6$ – OCS. 140

5.4 $J = 1 - 0$ transitions of ($ortho$H$_2$)$_3$ – OCS and ($ortho$H$_2$)$_6$ – OCS. 141

5.5 $J = 1 - 0$ transitions of the mixed clusters found for $N = 3$. 142

5.6 $J = 1 - 0$ transitions of the structural isomers of ($para$H$_2$)$_2$($ortho$H$_2$)$_3$ – OCS. 143

5.7 Plot of rotational constants (B_o) in MHz versus the cluster size N for ($para$H$_2$)$_N$ – OCS clusters. 144

5.8 Plot of rotational constants (B_o) in MHz versus the cluster size N for ($ortho$H$_2$)$_N$ – OCS clusters. 145

6.1 Composite experimental autoscan spectrum showing the $J_{KaKc} = 1_{01} - 0_{00}$ transitions of (H$_2$)$_2$ – HCCCN clusters. 167

6.2 Experimental spectra of the $J_{KaKc} = 1_{01} - 0_{00}$ transition of ($para$H$_2$)$_2$ – HCCC^{15}N, ($para$H$_2$)($ortho$H$_2$) – HCCC^{15}N, and ($ortho$H$_2$)$_2$ – HCCC^{15}N. 168

6.3 Composite experimental autoscan spectrum showing the $J = 1 - 0$ transitions of (H$_2$)$_3$ – HCCCN clusters. 169

6.4 Plot of rotational constants, B_o, (in MHz) versus cluster size N for ($para$H$_2$)$_N$ – HCCCN clusters. 170

6.5 Plot of rotational constants, B_o, (in MHz) versus the cluster size N for ($ortho$H$_2$)$_N$ – HCCCN clusters. 171

6.6 The dependence of the observed normalized signal-to-noise ratio of three ($ortho$H$_2$)$_N$ – HCCCN clusters on sample pressure. 172

List of Abbreviations

aug-cc-pVTZ	Augmented correlation-consistent polarized triple-zeta basis set
BF	Bond functions
CC	Coupled cluster method
CCSD(T)	Coupled cluster method with single and double excitations and noniterative treatment of triple excitations as defined by J. D. Watts, J. Gauss, and R. J. Bartlett, *J. Chem. Phys.* **98** 8718 (1993).
c.m.	Centre of mass
DR	Double resonance
FTMW	Fourier transform microwave
MW	Microwave
MW-MW	Microwave-microwave
MW-MW DR	Microwave-microwave double resonance
$o\mathrm{H}_2$ or $ortho\mathrm{H}_2$	*ortho*-hydrogen molecule
$p\mathrm{H}_2$ or $para\mathrm{H}_2$	*para*-hydrogen molecule
PES(s)	Potential energy surface(s)
Ref.	Reference
Refs.	References
rms	Root-mean-square
VTZ	Correlation-consistent polarized triple-zeta basis set

Chapter 1

Introduction

Spectroscopy is the study of the interaction between light and matter. Various motions in molecules, complexes and clusters can be studied through their interactions with light at different frequencies. It is best to describe the interactions in molecules by the minimum energy necessary to excite motions.[1] The lower energy radio frequency region (3 MHz – 3 GHz) induces nuclear spin flipping (nuclear magnetic resonance (NMR)) in magnetic fields of a few Tesla. The next in energy, and most important region for the work in this thesis, is the microwave region (3 – 3000 GHz) with energies sufficient for excitation of rotational transitions in molecules and also for electron spin flips (electron spin resonance (ESR)). Infrared light (100 – 13,000 $\mathrm{cm}^{-1} \equiv 3 \times 10^3 - 3.9 \times 10^5$ GHz) excites the vibrational motions in molecules. The valence electron transitions in molecules are accessed by use of visible and ultraviolet (UV) radiation (10,000 – 100 Å $\equiv 3 \times 10^5 - 3 \times 10^7$ GHz). High energy x-ray wavelengths (100 – 0.1 Å $\equiv 3 \times 10^7 - 3 \times 10^{10}$ GHz) are responsible for transitions of core electrons. The boundaries are not clear and definite for which molecular motions are accessible by each frequency region. Since energy boundaries indicate the minimum energy required for excitation, higher energy radiation excites many motions simultaneously. For example, in ro-vibrational spectroscopy, infrared radiation excites the vibrational as well as the rotational motions.

There are some requirements of molecules to be able to observe the rotational motions and obtain a rotational spectrum. The main prerequisite is the presence of a permanent dipole moment. Microwave radiation exerts a torque on a molecule with a dipole moment which causes it to rotate.[2,3] In the complexes and clusters of interest in this thesis, the predominant rotation is the end-over-end rotation. The frequency at which the molecule rotates is related to its moment of inertia and, in general, lighter molecules rotate at a higher frequency than heavier molecules. Since the moment of inertia is related to the geometry of the molecule or complex studied, microwave spectroscopy is commonly used to determine molecular structure to a high precision in comparison to other methods of structural determination.[2,3]

High resolution microwave and infrared spectroscopy have been used to study van der Waals clusters containing helium atoms.[4-6] Helium clusters are the most weakly bound of the rare gas atom containing clusters and show very interesting behavior, including the manifestation of superfluidity in a finite system. Superfluidity is a phase of matter and is characterized by many interesting properties including an absence of viscosity.[7,8] Bulk helium is a superfluid when its temperature is dropped below 2.17 K (its λ-temperature, the transition temperature between normal fluid and superfluid ^{4}He). Above the λ-temperature, liquid helium acts as an ordinary fluid, named the He I phase.[9] When liquid helium is cooled to below its λ-temperature, it undergoes a phase transition to a superfluid (He II phase), which is unlike a classical fluid.[9] To explain the properties of superfluid helium a two-fluid model was proposed.[10-12] Briefly, the model suggests that He II phase consists of two fluids, a superfluid Bose-Einstein condensate and a normal fluid, both simultaneously present and interlocked. Due to the bosonic nature, atoms in a Bose-Einstein condensate occupy the lowest energy state and are described by a single wavefunction. Superfluidity is a manifestation of quantum behavior in a bulk system.

A demonstration of the two-fluid nature of a He superfluid is the Andronikashvili experiment.[13] In the experiment, a vessel of liquid helium containing a stack of thin plates was rotated and the effective moment of inertia of the vessel was measured. This experiment was repeated at various temperatures. When the liquid helium was cooled below 2.17 K, the effective moment of inertia decreased. Such an observation indicates increasing fractions of helium density were becoming frictionless and decoupling from the rotating vessel.[13]

Helium nanodroplets have provided one of the first observations of superfluidity outside of bulk helium. Nanodroplets contain ~1,000 - ~100,000 helium atoms and are confined in a skimmed molecular beam. Helium droplets alone cannot be studied via vibrational or rotational spectroscopy. The chemistry within a nanodroplet is probed by doping the droplet with a chromophore molecule on which spectroscopy is performed. Some of the chromophores investigated include, but are not exclusive to: OCS,[14-17] CO,[18] CO_2,[19,20] HCN,[21,22] HCCCN,[22-24] and N_2O.[19] The spectra obtained from infrared studies of chromophores such as with OCS in ^{4}He nanodroplets can show sharp, rotationally resolved spectral features like those expected in gas-phase spectroscopic studies.[14] Sharp spectral features suggest near free rotation of the OCS dopant within the droplet, which has been attributed to the superfluid nature of the nanodroplets. The effective moment of inertia of an OCS molecule embedded in a ^{4}He droplet is higher than that of the free molecule by a factor of 2.7.[14] Grebenev *et al.* proposed that the two-fluid nature of a superfluid could explain the experimental results. The superfluid density allowed the

OCS molecule to rotate freely, while the normal He II fraction was dragged by the rotor increasing its effective moment of inertia. The experiment was termed by the authors as the "microscopic Andronikashvili experiment."[14] The superfluid nature of ^{4}He nanodroplets has been supported by the observation of broader transitions in ^{3}He nanodroplets. The temperature of the ^{3}He droplets is not low enough to have superfluid behavior, since the λ-temperature of ^{3}He is 2.6 mK, significantly lower than in ^{4}He (2.17 K).[15] Studies were then carried out to determine if a specific number of ^{4}He atoms around a chromophore in a larger ^{3}He nanodroplet was needed to show these characteristic sharp spectral features. Sharp gas phase-like spectral features appeared for ~ 60 ^{4}He atoms around an OCS molecule in a ^{3}He nanodroplet.[5] Thus, the authors suggested that a minimum of 60 ^{4}He atoms are required for superfluidity.

A different approach to understanding doped helium clusters is the solvation of a molecule one helium atom at a time.[4-6,25] Such studies can be achieved in high resolution infrared and microwave, pulsed-jet spectroscopic experiments. Both techniques utilize a pulsed nozzle, which creates a near collision-free molecular expansion into a vacuum chamber. As a result, van der Waals clusters are stabilized and can be studied. The study of sequential solvation is aided by the fact that the distribution of the number of helium atoms around a chromophore can be controlled by sample pressure, chromophore concentration and nozzle temperature.[5,6,26] In these studies, the trends of spectroscopic constants, for example, the rotational constants of the clusters, with increasing number of helium atoms is followed. The rotational constant of a cluster is inversely proportional to its moment of inertia. When the cluster increases in size with the addition of a helium atom, the moment of inertia should increase in a classical picture and correspondingly the rotational constant should decrease. When a helium cluster shows superfluid behavior, the lack of viscosity of a superfluid causes some helium density to decouple from the rotation of the chromophore molecule. This decoupling is seen by a decrease in the moment of inertia and, therefore, an increase in the rotational constant with the addition of mass. Such a turn-around in the rotational constant is interpreted to be the onset of 'microscopic' superfluidity and has been observed for several helium clusters via infrared and/or microwave spectroscopy (He_N – OCS,[4,6,25,27-29] He_N – CO_2,[30] He_N – HCCCN,[5,31] He_N – CO,[32-37] and He_N – N_2O[38-40]).

This discussion will focus on two particular doped helium cluster systems: He_N – OCS and He_N – HCCCN. Both systems have been extensively studied via rotational spectroscopy.[5,6,31] The main requirements for suitable chromophores in clusters are large dipole moments, well known monomer spectra, and expected rotational transitions of the clusters in the operating range of the microwave spectrometer (3-26 GHz). Both chromophores, carbonyl sulfide (OCS) and cyanoacetylene (HCCCN), have been investigated in nanodroplet studies and infrared gas-phase studies exist for He_N - OCS.[4,14-17,25,28,29] Even though the chromophores have many similarities, they have one important difference: the length of the rotor. The cyanoacetylene rotor (4.83 Å) is nearly twice as long as the carbonyl sulfide rotor (2.72 Å).

The studies of He_N – OCS clusters studied via microwave[6] and infrared[4] spectroscopy show the feasibility of studying helium clusters by successive solvation one helium atom at a time. Larger clusters are generated by molecular collisions in the nozzle and then stabilized in the jet expansion into the cavity of the spectrometer. The size distribution of the clusters is controlled by the pressure and temperature at the nozzle and chromophore concentration in the gas sample. The small clusters ($N = 2$-8) behaved classically where the addition of a helium atom increased the moment of inertia. The vibrational shifts obtained from the infrared study[4] and the isotope shifts obtained in the microwave study[6] indicated that the first five helium atoms formed a ring around the OCS molecule. The sixth and seventh helium atoms were located near the oxygen end of the OCS molecule, while the eighth atom was located nearer the sulfur end. Spectroscopic constants, including rotational constants, for each cluster were determined. Interestingly, the observed rotational constant of the He_6 – OCS cluster was below the one obtained in the nanodroplet studies with OCS.[14] To eventually reach the nanodroplet limit at larger cluster sizes, a turn-around in the rotational constant would be necessary. The turn-around was not observed in the initial microwave[4,6] or infrared[25] studies due to experimental challenges in studying clusters larger than $N > 8$.

In subsequent experiments, the resolution of the pulsed-jet infrared spectrometer was significantly improved through the introduction of a skimmed jet. Spectra of He_N - OCS clusters with up to $N = 70$ helium atoms were resolved.[27,28] Complementary to this study, rotational spectra of He_N – OCS clusters up to $N = 39$ were measured.[27,28] The study was enabled by using high sample pressures and very low nozzle temperatures to generate the larger clusters. The trend in the rotational constants for the small-to-medium sized clusters show that the onset of superfluidity occurs at $N = 9$. Additionally, broad oscillations in the rotational constant show possible shell structures and variations in superfluid fractions as more helium atoms are added.[27,28]

The He_N-molecule cluster studies were extended to other dopants to observe the onset of superfluidity as the molecules are solvated with helium atoms. Cyanoacetylene

(HCCCN) was studied as a dopant in nanodroplets,[23,24,41,42] and was a promising dopant for microwave studies. An additional motivation for studying He_N – HCCCN clusters was to study the effect of a longer rotor on the onset of superfluidity. A first effect of the longer rotor was the observation of six helium atoms forming the ring around the dopant instead of the five atoms observed with OCS.[5] The study of cyanoacetylene doped helium clusters show that the onset of superfluidity occurs at $N = 10$.[5] The length of the rotor delayed the onset of superfluidity in the cluster compared to the He_N – OCS clusters.

Several groups have studied rotational and rovibrational properties of small to medium sized He_N – molecule clusters theoretically using different Quantum Monte Carlo (QMC) methods. Examples include He_N – OCS,[43-45] He_N – N_2O,[46-48] He_N – CO_2,[30] and He_N – HCCCN.[5] The accuracy of these computational results depends on both the choice of QMC method and the potential energy surfaces (PESs) used for the He-molecule and He-He interactions. The difficulty in reproducing experimental results can be seen in the studies done by K. B. Whaley *et al.* with He_N – OCS. The first studies[49-51] show that the rotational constants of growing clusters decrease smoothly to the nanodroplet rotational constant and reach the value at $N = 5$. Following the experimental studies of He_N – OCS ($N = 2$-8),[4,6,25] where the rotational constant of the clusters dipped below the nanodroplet value, Whaley *et al.* revisited their potential energy surface and calculations. Their new theoretical results[44,52] were able to reproduce the experimental data for $N = 2$-8 and predicted the rotational constants for larger clusters (up to $N = 20$). They predicted a single turn-around at $N = 6$, following which the rotational constants would increase asymptotically to the experimental nanodroplet value. The theoretical studies by Whaley and co-workers failed to predict the experimental results where broad oscillations in the rotational constants were observed.

Although theoretical studies of doped helium clusters are challenging, some groups have been able to produce results that agree nicely with experiments.[5,43,46] For example, the theoretical studies of cyanoacetylene doped helium clusters by Moroni *et al.* (He_N – HCCCN; $N = 1\text{-}31$) reproduce the experimentally observed turn-around in the rotational constants, as well as the broad oscillations for the larger clusters.[5] Impressively, this theoretical study captured small features in the trend of the rotational constants, which were observed in the experiments.

Helium becomes a superfluid because of several factors including the low atomic mass, very weak interatomic interactions, and the bosonic character.[7-9] Hydrogen molecules (H_2) are bosons with a mass half that of helium atoms which contributes to the possibility of seeing similar superfluid behavior in hydrogen molecules. Conversely, hydrogen molecules have van der Waals interactions which are twelve times stronger than within helium atoms and, in bulk, hydrogen solidifies at 13.8 K. Many attempts have been made to supercool bulk hydrogen to produce a superfluid, [53-57] but all attempts have been unsuccessful. Gas-phase studies, where solidification may not be an issue, could show potentially the onset of superfluidity in doped hydrogen clusters. Hydrogen atoms have a nuclear spin of ½ and the combination of two hydrogen atoms to form the hydrogen molecule gives rise to two spin isomers: *para*-hydrogen ($I_{total} = 0$) and *ortho*-hydrogen ($I_{total} = 1$). *Para*-hydrogen corresponds to a nuclear singlet state and is a spinless boson like the ^{4}He atom. Some studies have suggested that *para*-hydrogen would be the best candidate for superfluidity.[55,58] The λ-temperature for *para*-hydrogen has been estimated from the Bose-Einstein condensation temperature to be ~6 K.[55] All other forms of the hydrogen molecule (*ortho*H_2, *para*D_2, *ortho*D_2) are expected to have the transition occur at lower temperatures because of the degeneracy of their lowest energy level.[55] Therefore, *para*-hydrogen clusters are good candidates to show superfluid behavior in hydrogen molecules.

Grebenev *et al.* investigated $(paraH_2)_N$ – OCS clusters (N = 1-8, 14-16)[58-61] in ^4He and mixed $^4He/^3He$ nanodroplets. For the larger N = 14-16 clusters, the spectrum showed a disappearance of the Q-branch feature ($\Delta J = 0$) when the temperature was dropped from 0.38 K (in pure ^4He nanodroplets) to 0.15 K (in mixed $^4He/^3He$ nanodroplets). The disappearance of the Q-branch feature is associated with a vanishing of the angular momentum around the symmetry axis. When the transition to a superfluid occurs, both the effective moment of inertia and the angular momentum vanish.[60] The disappearance of the Q-branch in $(paraH_2)_{14\text{-}16}$ – OCS has been attributed to the onset of superfluidity in *para*H_2. In smaller clusters (N = 5-6), the disappearance of the Q-branch was attributed to the high symmetry permutation of the clusters causing the allowed energy levels to be too high in energy to be populated in the low temperature of the helium nanodroplet.[59]

To remove any matrix effects, it is best to study the doped hydrogen clusters in molecular expansions where the clusters are so-called 'bare', that is without any surrounding helium droplet. Infrared gas-phase studies have been done for the H_2 – OCS dimer[26] and larger $(H_2)_N$ – OCS (N = 2-7) bare clusters.[62] The vibrational band origin of the clusters shifts to the red (to lower wavenumbers) with increasing cluster size and a change in slope in the vibrational shifts at N = 5-7. This change of slope corresponds to the sixth and seventh hydrogen molecules occupying a different position (near the O end) compared to the ring formed by the first five hydrogen molecules about the waist of the OCS molecule. This is consistent with the results of He_N – OCS. For $N = 1$-7, the infrared study provided rotational constants to guide the spectral search for $(H_2)_N$ – OCS clusters in the microwave range. It also has shown the feasibility of gas-phase studies of doped hydrogen clusters by successive solvation as was done for doped helium clusters.

In two recent reports, Klemperer and coworkers have investigated the main OCS isotopologue of the hydrogen – OCS van der Waals dimer in the microwave region.[63,64] In the first report, they measured the *a*-type rotational transitions of five hydrogen – OCS (*ortho*H_2, *para*H_2, *ortho*D_2, *para*D_2 and HD) complexes.[63] Nuclear hyperfine structure was observed for all complexes except *para*H_2 – OCS, where $I(para\mathrm{H}_2)_{\mathrm{total}} = 0$ and no nuclear hyperfine structure is expected. To complete this study, the microwave spectra of the minor OCS isotopologues of *para*H_2 – OCS and *ortho*H_2 – OCS were investigated as a part of this thesis. The study of the minor isotopologues was motivated by the possibility to obtain better structural parameters for the complex. Additionally, the study would provide a means to test and improve PESs for the H_2 – OCS system. The observation of the hydrogen – OCS dimer in the microwave region, as well as the previously mentioned gas-phase infrared studies,[26,62] encouraged studies of larger hydrogen – OCS clusters as a part of this thesis.

Studies of hydrogen molecule clusters could show the onset of superfluidity in the similar way as the helium clusters, but such an observation is expected to occur at larger cluster sizes due to the stronger van der Waals interactions in hydrogen molecules. The observation of a turn-around in rotational constant as *N* increases would constitute a direct observation of superfluidity involving *para*-hydrogen molecules. In this thesis, I report the study of $(H_2)_N$ – OCS (N = 2-7) clusters containing *ortho*H_2 and *para*H_2 molecules. This is the first microwave study of hydrogen molecule clusters (larger than N = 1) seeded with a chromophore. Several isotopologues for OCS were measured for many cluster sizes. Mixed clusters containing both *ortho*H_2 and *para*H_2 molecules, some of which were also detected in the infrared study,[62] were observed and have aided the assignment of the pure *ortho*H_2 or pure *para*H_2 clusters. Microwave spectra are less spectrally crowded than infrared spectra and the mixed clusters do not overlap spectrally. The rotational constants from the current study agree very well with those from the infrared study.[62]

Theoretical investigations of H_2 – molecule systems, such as H_2 – OCS, are complicated by the spin isomers of the hydrogen molecules and the dependence on the orientation of the *ortho*H_2 molecule with respect to the molecule. Potential energy surface calculations have been performed for the H_2 – OCS system where three extreme orientations of the hydrogen molecule with OCS have been investigated.[65,66] The orientations are defined by the relative position of the molecular axes of the hydrogen and the OCS molecule when the dimer is in the T-shaped configuration. They are defined as parallel, perpendicular and out-of-plane. Bound state rotational energy levels supported by the potential have been determined for *ortho*H_2 – OCS and *para*H_2 – OCS dimers. The frequency for rotational transitions can be obtained by calculating the difference between the states of interest. Preliminary results show reasonable agreement with experimental transition frequencies.[65,66]

QMC studies have also been performed on the (*para*H_2)$_N$ – OCS system by Whaley and co-workers.[67-71] The rotational constants obtained in the studies show a smooth decrease as more hydrogen molecules are added up to $N = 8$.[71] These results agree with the rotational constants obtained from the infrared results up to $N = 7$.[62] For larger clusters (up to $N = 20$),[67] the vibrational shifts were calculated and showed reasonable agreement with infrared results up to $N = 7$.[62] The theoretical values were slightly above the experimental values for $N = 6$ and 7. From the chemical potentials of the $(pH_2)_N$ – OCS clusters, three cluster sizes, namely $N = 8$, 11, and 14, were considered "magic" number clusters since their chemical potentials were minima. The authors did not present the rotational constants for clusters larger than $N = 8$, therefore it can not be known whether a turn-around was predicted. Diffusion Monte Carlo (DMC) calculations of $(pH_2)_N$ – OCS clusters (up to $N = 30$) have been performed by Piccarreta and Gianturco to determine the structural parameters of the clusters.[72] The first five molecules formed a ring around the OCS molecule. Further molecules added to either side of the dopant species.[72] The DMC calculations did not provide rotational constants for comparison.

The rotor length effects observed in the helium cluster studies encouraged the investigations of the $(H_2)_N$ – HCCCN system. No previous experimental or theoretical results were available for the $(H_2)_N$ – HCCCN system and this thesis presents the rotational spectra of clusters up to $N = 6$. Potential energy surface calculations of three orientations of the H_2 molecule with respect to the HCCCN molecule are presented with the supported bound state rotational energy levels.

This thesis contains a brief background of the theory and the experimental set-up used in these studies in Chapter 2. The rotational spectra of minor isotopologues of hydrogen molecule – carbonyl sulfide dimers are presented in Chapter 3. The experimental study and the potential energy surface study of H_2 – HCCCN is presented in Chapter 4. Chapter 5 focuses on the results of the study of carbonyl sulfide (OCS) doped hydrogen clusters. The cyanoacetylene (HCCCN) doped hydrogen cluster results are presented in Chapter 6. A chapter summarizing the general findings of these doped hydrogen clusters studied via rotational spectroscopy with brief mention of future directions for similar studies concludes this thesis. The tables of single point energies for the H_2 – HCCCN potential energy surface are given in Appendix A found at the end of the thesis. Appendix B contains the bound state rotational energy levels supported by the potential energy surfaces. Due to the large number of tables generated by the analysis of the spectra in this thesis, the tables and figures are located at the end of the chapters for chapters dealing with spectral analysis. Bibliographies for chapters are independent and found at the end of each chapter.

1.1 References

[1] P. F. Bernath, *Spectra of Atoms and Molecules.* (Oxford University Press, New York, 1995).

[2] W. Gordy and R. L. Cook, *Microwave Molecular Spectra.* (Wiley-Interscience Publication, New York, 1984).

[3] C. H. Townes and A. L. Schawlow, *Microwave Spectroscopy.* (Dover Publications, New York, 1975).

[4] J. Tang, Y. Xu, A. R. W. McKellar, and W. Jäger, *Science* **297** (5589), 2030 (2002).

[5] W. Topic, W. Jäger, N. Blinov, P.-N. Roy, M. Botti, and S. Moroni, *J. Chem. Phys.* **125** (14), 144310 (2006).

[6] Y. Xu and W. Jäger, *J. Chem. Phys.* **119** (11), 5457 (2003).

[7] R. J. Donnelly, *Experimental Superfluidity*. (University of Chicago Press, Chicago, 1967).

[8] W. E. Keller, *Helium-3 and Helium-4*. (Plenum Press, New York, 1969).

[9] W. H. Keesom and M. Wolfke, in *Helium 4*, edited by Z. M. Galasiewicz (Pergamon Press, Oxford, 1971).

[10] F. London, *Nature* **141**, 643 (1938).

[11] L. Tisza, *Nature* **141**, 913 (1938).

[12] L. Tisza, *Phys. Rev.* **72** (9), 838 (1947).

[13] E. Andronikashvili, in *Helium 4*, edited by Z. M. Galasiewicz (Pergamon Press, Oxford, 1971).

[14] S. Grebenev, J. P. Toennies, and A. F. Vilesov, *Science* **279** (5359), 2083 (1998).

[15] S. Grebenev, M. Hartmann, M. Havenith, B. Sartakov, J. P. Toennies, and A. Vilesov, *J. Chem. Phys.* **112** (10), 4485 (2000).

[16] S. Grebenev, M. Havenith, F. Madeja, J. P. Toennies, and A. F. Vilesov, *J. Chem. Phys.* **113** (20), 9060 (2000).

[17] S. Grebenev, E. Lugovoi, B. G. Sartakov, J. P. Toennies, and A. F. Vilesov, *Faraday Discuss.* **118**, 19 (2001).

[18] K. von Haeften, S. Rudolph, I. Simanovski, M. Havenith, R. E. Zillich, and K. B. Whaley, *Phys. Rev. B* **73** (5) 054502 (2006).

[19] K. Nauta and R. E. Miller, *J. Chem. Phys.* **115** (22), 10254 (2001).

[20] R. Lehnig and W. Jäger, *Chem. Phys. Lett.* **424**, 146 (2006).

[21] A. Conjusteau, C. Callegari, I. Reinhard, K. K. Lehmann, and G. Scoles, *J. Chem. Phys.* **113** (12), 4840 (2000).

[22] P. L. Stiles, K. Nauta, and R. E. Miller, *Phys. Rev. Lett.* **90** (13), 135301 (2003).

[23] C. Callegari, I. Reinhard, K. K. Lehmann, G. Scoles, K. Nauta, and R. E. Miller, *J. Chem. Phys.* **113** (11), 4636 (2000).

[24] J. M. Merritt, G. E. Douberly, and R. E. Miller, *J. Chem. Phys.* **121** (3), 1309 (2004).

[25] J. Tang and A. R. W. McKellar, *J. Chem. Phys.* **119** (11), 5467 (2003).

[26] J. Tang and A. R. W. McKellar, *J. Chem. Phys.* **116** (2), 646 (2002).

[27] A. R. W. McKellar, Y. Xu, and W. Jäger, *Phys. Rev. Lett.* **97** (18), 183401 (2006).

[28] A. R. W. McKellar, Y. Xu, and W. Jäger, *J. Phys. Chem. A* **111** (31), 7329 (2007).

[29] J. Tang and A. R. W. McKellar, *J. Chem. Phys.* **115** (7), 3053 (2001).

[30] J. Tang, A. R. W. McKellar, E. Mezzacapo, and S. Moroni, *Phys. Rev. Lett.* **92** (14), 145503 (2004).

[31] W. C. Topic and W. Jäger, *J. Chem. Phys.* **123** (6), 064303 (2005).

[32] A. R. W. McKellar, *J. Chem. Phys.* **125** (16), 164328 (2006).

[33] A. R. W. McKellar, *J. Chem. Phys.* **121** (14), 6868 (2004).

[34] J. Tang and A. R. W. McKellar, *J. Chem. Phys.* **121** (1), 181 (2004).

[35] A. R. W. McKellar, Y. Xu, W. Jäger, and C. Bissonnette, *J. Chem. Phys.* **110** (22), 10766 (1999).

[36] M. C. Chan and A. R. W. McKellar, *J. Chem. Phys.* **105** (18), 7910 (1996).

[37] C. E. Chuaqui, R. J. Leroy, and A. R. W. McKellar, *J. Chem. Phys.* **101** (1), 39 (1994).

[38] X. G. Wang, T. Carrington, J. Tang, and A. R. W. McKellar, *J. Chem. Phys.* **123** (3), 034301 (2005).

[39] Y. Xu, W. Jäger, J. Tang, and A. R. W. McKellar, *Phys. Rev. Lett.* **91** (16), 163401 (2003).

[40] J. Tang and A. R. W. McKellar, *J. Chem. Phys.* **117** (6), 2586 (2002).

[41] C. Callegari, A. Conjusteau, I. Reinhard, K. K. Lehmann, and G. Scoles, *J. Chem. Phys.* **113** (23), 10535 (2000).

[42] I. Reinhard, C. Callegari, A. Conjusteau, K. K. Lehmann, and G. Scoles, *Phys. Rev. Lett.* **82** (25), 5036 (1999).

[43] S. Moroni, A. Sarsa, S. Fantoni, K. E. Schmidt, and S. Baroni, *Phys. Rev. Lett.* **90** (14), 143401 (2003).

[44] F. Paesani and K. B. Whaley, *J. Chem. Phys.* **121** (9), 4180 (2004).

[45] N. Blinov, X. G. Song, and P.-N. Roy, *J. Chem. Phys.* **120** (13), 5916 (2004).

[46] S. Moroni, N. Blinov, and P.-N. Roy, *J. Chem. Phys.* **121** (8), 3577 (2004).

[47] F. Paesani and K. B. Whaley, *J. Chem. Phys.* **121** (11), 5293 (2004).

[48] Y. Xu, N. Blinov, W. Jäger, and P.-N. Roy, *J. Chem. Phys.* **124** (8), 081101 (2006).

[49] Y. Kwon and K. B. Whaley, *J. Chem. Phys.* **115** (22), 10146 (2001).

[50] F. Paesani, F. A. Gianturco, and K. B. Whaley, *Europhys. Lett.* **56** (5), 658 (2001).

[51] F. Paesani, F. A. Gianturco, and K. B. Whaley, *J. Chem. Phys.* **115** (22), 10225 (2001).

[52] F. Paesani, A. Viel, F. A. Gianturco, and K. B. Whaley, *Phys. Rev. Lett.* **90** (7), 073401 (2003).

[53] G. M. Seidel, H. J. Maris, F. I. B. Williams, and J. G. Cardon, *Phys. Rev. Lett.* **56** (22), 2380 (1986).

[54] H. J. Maris, G. M. Seidel, and F. I. B. Williams, *Phys. Rev. B* **36** (13), 6799 (1987).

[55] H. J. Maris, G. M. Seidel, and T. E. Huber, *J. Low Temp. Phys.* **51** (5-6), 471 (1983).

[56] R. E. Grisenti, R. A. C. Fraga, N. Petridis, R. Dorner, and J. Deppe, *Europhys. Lett.* **73** (4), 540 (2006).

[57] E. L. Knuth, F. Schunemann, and J. P. Toennies, *J. Chem. Phys.* **102** (15), 6258 (1995).

[58] S. Grebenev, B. G. Sartakov, J. P. Toennies, and A. F. Vilesov, *J. Chem. Phys.* **114** (2), 617 (2001).

[59] S. Grebenev, B. Sartakov, J. P. Toennies, and A. Vilesov, *Phys. Rev. Lett.* **89** (22), 225301 (2002).

[60] S. Grebenev, B. Sartakov, J. P. Toennies, and A. F. Vilesov, *Science* **289** (5484), 1532 (2000).

[61] S. Grebenev, B. G. Sartakov, J. P. Toennies, and A. F. Vilesov, *J. Chem. Phys.* **118** (19), 8656 (2003).

[62] J. Tang and A. R. W. McKellar, *J. Chem. Phys.* **121** (7), 3087 (2004).

[63] Z. H. Yu, K. J. Higgins, W. Klemperer, M. C. McCarthy, and P. Thaddeus, *J. Chem. Phys.* **123** (22) (2005).

[64] Z. H. Yu, K. J. Higgins, W. Klemperer, M. C. McCarthy, P. Thaddeus, K. Liao, and W. Jäger, *J. Chem. Phys.* **127**, 054305 (2007).

[65] K. J. Higgins and W. Klemperer, *Private communication*.

[66] K. Liao and W. Jäger, *Unpublished results*.

[67] F. Paesani and K. B. Whaley, *J. Chem. Phys.* **124** (23), 234310 (2006).

[68] F. Paesani and K. B. Whaley, *Mol. Phys.* **104** (1), 61 (2006).

[69] Y. Kwon and K. B. Whaley, *J. Low Temp. Phys.* **140** (3-4), 227 (2005).

[70] F. Paesani, R. E. Zillich, Y. Kwon, and K. B. Whaley, *J. Chem. Phys.* **122** (18), 181106 (2005).

[71] F. Paesani, R. E. Zillich, and K. B. Whaley, *J. Chem. Phys.* **119** (22), 11682 (2003).

[72] C. Piccarreta and F. A. Gianturco, *Eur. Phys. J. D* **37** (1), 93 (2006).

Chapter 2

Basic theory and experimental techniques of rotational spectroscopy

This chapter summarizes the basic theory of microwave spectroscopy that is applicable to this thesis as well as the description of the experimental set-up. This chapter is presented to familiarize the reader with the notation that will be used in the following chapters. The theory has not been developed as a part of this thesis and has been explained in greater detail in several textbooks.[1,2] The experimental set-up for the Fourier transform microwave spectrometer was not developed during the course of this study. A brief description will be given to familiarize the reader with the set-up. A *para*-hydrogen converter was built as a part of this work and will be described in further detail within this chapter.

As a first part of this chapter, the theory relevant to the assignment and analysis of the pure rotational spectra of symmetric and asymmetric tops will be discussed. The theory discussion here will be as follows:

a. The rigid rotors;
b. Selection rules for asymmetric tops;
c. Centrifugal distortion;
d. Hyperfine structures;
e. Geometry determination.

As a second part to this chapter, pulsed excitation experiments will be described theoretically followed by a description of the microwave spectrometer used for the studies. The chapter will end with a description of the design of the *para*-hydrogen converter built and used for some studies.

2.1 Molecular rotational spectroscopy

The Born-Oppenheimer approximation states that the electrons can be considered to respond instantaneously to changes in nuclear position because of the large mass difference between the nucleus and the electrons.[3] The approximation allows for the electronic and nuclear components of the total Hamiltonian of the molecule, $\hat{H}_{total}$, to be separated. In addition, for these studies, interactions between the rotational and the various other motions in the Hamiltonian are neglected. The total Hamiltonian tunneling motions, all effects of nuclear and electronic spins, and all effects of external fields have also been neglected. With all these assumptions, the total Hamiltonian of the molecule is given by:

$$\hat{H}_{total} = \hat{H}_{trans} + \hat{H}_{elec} + \hat{H}_{vib} + \hat{H}_{rot} \quad [2.1]$$

where the components correspond to the translational, electronic, vibrational, and rotational components, respectively. The separation of the total Hamiltonian permits the simplification of the eigenfunctions, ψ, and eigenvalues, E, written as:

$$\Psi_{total} = \psi_{trans}\psi_{elec}\psi_{vib}\psi_{rot} \quad [2.2]$$

and:

$$E_{total} = E_{trans} + E_{elec} + E_{vib} + E_{rot}\,. \quad [2.3]$$

Of interest for this work is the rotational Hamiltonian and, thus, the discussion will be limited to it. The clusters and complexes studied in this work are subject to centrifugal distortion and, for some nuclei, nuclear spin interactions which lead to hyperfine structures in the rotational transitions need to be considered. The Hamiltonian, in these cases, becomes:

$$\hat{H} = \hat{H}_{rot} + \hat{H}_{distortion} + \hat{H}_{hyperfine} \qquad [2.4]$$

where $\hat{H}_{distortion}$ and $\hat{H}_{hyperfine}$ are the centrifugal distortion and hyperfine Hamiltonians, respectively, and will be discussed in more detail below. The Hamiltonian is used to determine the interaction energies and to fit spectroscopic parameters of the model Hamiltonian to the measured transition frequencies.

2.2 The rigid rotor

A starting point for obtaining approximate rotational energy levels is the assumption that molecules are rigid rotors. In this approximation, molecules are point masses connected by massless rigid rods. In general form, the rigid rotor Hamiltonian is given by:

$$\hat{H}_{rot} = B_a\hat{J}_a^2 + B_b\hat{J}_b^2 + B_c\hat{J}_c^2 \qquad [2.5]$$

where $\hat{J}_g$ and B_g are the rotational angular momentum operators and the rotational constants, respectively, along the *g*- principal inertial axes (*a*, *b*, or *c*). The rotational constants, $B_a \equiv A$, $B_b \equiv B$, and $B_c \equiv C$, are given by $B_g = \hbar^2/2I_g$, where I_g are the moments of inertia along the principal inertial axes. By convention, the principal inertial axes are chosen so that the rotational constants follow: $A \geq B \geq C$.

Molecules can be classified according to the relative values of the rotational constants. In a symmetric top, two of the rotational constants are equal. When $A = B > C$, the molecule is classified as a symmetric oblate top; when $A > B = C$, the molecule is a symmetric prolate top. The rotational Hamiltonian can be solved analytically in both of these cases. In the prolate case, which will be used in this discussion, the wave functions are designated $|JK\rangle$ where J and K are the quantum numbers associated with the total rotational angular momentum and its component along the principal inertial a-axis, respectively. The values that these quantum numbers can take are $J = 0, 1, 2, \ldots$ and $K = 0, \pm1, \pm2, \ldots, \pm J$.

The non-zero elements of the Hamiltonian matrix are given by:

$$\langle JK|\hat{H}_{rot}|JK\rangle = AK^2 + \frac{B+C}{2}\left[J(J+1) - K^2\right] \qquad [2.6]$$

and:

$$\langle JK \pm 2|\hat{H}_{rot}|JK\rangle = \frac{B-C}{4}\left[J(J+1) - K(K\pm1)\right]^{1/2}\left[J(J+1) - (K\pm1)(K\pm2)\right]^{1/2} \qquad [2.7]$$

where A, B, and C are the rotational constants of the molecule as described earlier. The rotational energy levels of the prolate symmetric top are given by:

$$E = BJ(J+1) + (A-B)K^2. \qquad [2.8]$$

The symmetric top wavefunctions form complete sets and can be used as basis sets for the treatment of asymmetric top molecules, where $A > B > C$. For asymmetric top molecules like many doped hydrogen molecule complexes, K is no longer a good quantum number and J_{KaKc} labels the energy levels where K_a and K_c are the prolate and oblate limits for the value of K, respectively.

2.3 Selection rules for asymmetric top molecules

The selection rules governing the allowed transitions for asymmetric top molecules are given in this section. The selection rules have been developed previously,[1,2] therefore only the main results will be presented here. The probability of a rotational transition occurring between energy levels m ($\equiv J'$, K_{-1}', K_1') and n ($\equiv J$, K_{-1}, K_1) is given by:

$$p_{m\rightarrow n} = \rho(\nu_{m\rightarrow n})B_{m\rightarrow n} \qquad [2.9]$$

where $\rho(\nu_{m\rightarrow n})$ is the density of the radiation at the transition frequency $\nu_{m\rightarrow n}$ and $B_{m\rightarrow n}$ is a "rate constant," known as the Einstein B coefficient.[4] $B_{m\rightarrow n}$, is given by:

$$B_{m\rightarrow n} = \frac{8\pi^3}{3h^2}\sum_F \left|\langle n|\mu_F|m\rangle\right|^2 . \qquad [2.10]$$

where the μ_F are the space-fixed F = X, Y, Z components of the molecular electric dipole moment. In a molecule, the dipole moment is given in the principal axis system ($g = a, b, c$). The principal axis system dipole moment is related to the space-fixed axis system since the radiation used in the experiments is defined in the space-fixed axis system. The coordinates of the molecular dipole moment in the principal axis system can be changed to the space-fixed axis system by:

$$\langle n|\mu_F|m\rangle = \sum_g \mu_g \langle n|\Phi_{Fg}|m\rangle \qquad [2.11]$$

where $g = a, b, c$ are the principal inertial axes of the molecule and Φ_{Fg} are the direction cosines between the spaced-fixed axes F and the principal axes g.

Since plane polarized radiation is used in microwave experiments, the molecular dipole will interact with only one space fixed axis defined here as the Z-axis. The direction cosines give rise to the selection rule $\Delta J = 0, \pm 1$. The selection rules for K_a and K_c can be reasoned using group theory. The wavefunctions of asymmetric rotors can be classified according to the irreducible representation D_2, the character table for which is given in Table 2.1.

Table 2.1: Character table for the D$_2$ point group

	E	C_2^a	C_2^b	C_2^c	K_a	K_c	Φ_{Fg}
A	1	1	1	1	e	e	
B_a	1	1	-1	-1	e	o	Φ_{Za}
B_b	1	-1	1	-1	o	o	Φ_{Zb}
B_c	1	-1	-1	1	o	e	Φ_{Zc}

The allowed transitions are those for which $\langle n|\mu_Z|m\rangle \neq 0$ and which are symmetric with respect to all operations of D$_2$. Since μ_Z can be separated as:

$$\langle n|\mu_Z|m\rangle = \mu_a\langle n|\Phi_{Za}|m\rangle + \mu_b\langle n|\Phi_{Zb}|m\rangle + \mu_c\langle n|\Phi_{Zc}|m\rangle, \qquad [2.12]$$

transitions can occur when μ_g is non-zero and when $\langle n|\Phi_{Zg}|m\rangle$ is totally symmetric. Table 2.2 summarizes the allowed transitions.

Table 2.2: Selection rules for rotational transitions

	ΔK_a	ΔK_c
a-type; $\mu_a \neq 0$	even; 0, ±2, …	odd; ±1, ±3, …
b-type; $\mu_b \neq 0$	odd; ±1, ±3, …	odd; ±1, ±3, …
c-type; $\mu_c \neq 0$	odd; ±1, ±3, …	even; 0, ±2, …

For the studies in this thesis, the largest dipole moment component is along the a-axis and a-type transitions are the most prominent in the doped hydrogen clusters.

2.4 Centrifugal distortion: The distortable rotor

The rigid rotor approximation gives a general description of the molecular rotational energy levels. This approximation neglects that bonds are flexible and spring-like. This flexibility results in distortions due to centrifugal force as the molecule rotates. The distortions change the moments of inertia and, consequently, the rotational constants. This is accounted for by the addition of centrifugal distortion terms into the rotational energy Hamiltonian in equation [2.1], as shown in equation [2.4]. The most common description of a semi-rigid molecule, and the one used in this thesis, is given by the Watson's A-reduction:[5]

$$\hat{H}_{rot} = B_x^{\prime(A)}\hat{J}_x^2 + B_y^{\prime(A)}\hat{J}_y^2 + B_z^{\prime(A)}\hat{J}_z^2 \qquad [2.13]$$

$$\hat{H}_{distortion} = -\Delta_J\hat{J}^4 - \Delta_{JK}\hat{J}^2\hat{J}_z^2 - \Delta_K\hat{J}_z^4 - 2\delta_J\hat{J}^2\left(\hat{J}_x^2 - \hat{J}_y^2\right) - \delta_K\left[\hat{J}_z^2\left(\hat{J}_x^2 - \hat{J}_y^2\right) + \left(\hat{J}_x^2 - \hat{J}_y^2\right)\hat{J}_x^2\right] + \ldots \qquad [2.14]$$

A less rigidly bound system, such as a weakly bound van der Waals complex, requires several centrifugal distortion constants to be fully described, even some higher order constants not explicitly given in equation [2.14].

2.5 Nuclear hyperfine interactions

The nuclear hyperfine interaction Hamiltonian used in some of the present studies can be expressed as:

$$\hat{H}_{hyperfine} = \hat{H}_{quadrupole} + \hat{H}_{spin-spin} + \hat{H}_{spin-rotation} \qquad [2.15]$$

where the nuclear quadrupolar component expresses the interaction of a nuclear electric quadrupole moment with the electric field gradient at the nucleus, the spin-spin Hamiltonian represents the interaction between two nuclear magnetic dipoles, and the spin-rotation component describes the interaction of a nuclear magnetic moment with the magnetic field produced by the rotating nuclei and electrons of the molecule. The components of the nuclear hyperfine Hamiltonian are only included in the total Hamiltonian when a nucleus (or nuclei) is present which can exhibit that type of interaction. For some complexes, all three hyperfine interactions will be present, while other complexes will have no hyperfine interactions.

Although each interaction will be discussed in more detail in turn, some considerations can be given in general. When a molecule contains at least one nucleus with a non-zero nuclear spin, the associated angular momentum can couple with the rotational angular momentum via the spin-rotation hyperfine interaction. The angular momentum coupling scheme when two (or more) nuclei are involved, such as in *ortho*H_2 – HCCCN (the *ortho*H_2 spin-spin interaction and the ^{14}N nuclear quadrupole coupling interaction) or $(oH_2)_2$-OCS (the spin-spin interaction of each of the two *ortho*H_2 molecules), can be expressed in two manners:

i. The 'parallel' scheme is most appropriate when the molecule has two equivalent coupling nuclei and is expressed as: $\mathbf{I}_1 + \mathbf{I}_2 = \mathbf{I}$; $\mathbf{I} + \mathbf{J} = \mathbf{F}$;

ii. The 'series' coupling scheme is used for molecules which contain two non-equivalent coupling nuclei and is expressed as: $\mathbf{I}_1 + \mathbf{J} = \mathbf{F}_1$; $\mathbf{I}_2 + \mathbf{F}_1 = \mathbf{F}$.

Here, $\mathbf{I}_1$, $\mathbf{I}_2$ are the spin angular momenta of the corresponding nuclei. A combination of parallel and series schemes can be applied for systems with more than two coupling nuclei. All spectroscopic fits for this thesis were done with the exact fitting program, SPFIT,[6] which utilises a complete diagonalisation procedure and, therefore, produces identical fits regardless of the coupling scheme used. The coupling schemes used in the analysis of the various complexes and clusters will be outlined in the appropriate chapters.

2.5.1 Nuclear electric quadrupole interaction

A quadrupolar nucleus with spin quantum number, *I*, greater than ½ has a nonspherical distribution of nuclear charge giving rise to a non-zero nuclear electric quadrupole moment, *eQ*. The nuclear electric quadrupole moment produces a nonspherical electric charge distribution around the nucleus and a resulting electric field gradient. The quadrupolar nucleus will try to orient itself in the electric field gradient. In gases, the field gradients at the nucleus are dependent on the rotational state of the molecule. For an external field free molecule, the nuclear spin, ***I***, is coupled to the molecular rotation angular momentum, ***J***, to produce the total angular momentum, ***F***. Transitions between the hyperfine levels are governed by the additional selection rule of $\Delta F = 0, \pm 1$.

The theory explaining nuclear electric quadrupole coupling has been developed in detail by several scientists including Zare,[7] Edmonds,[8] Gordy and Cook,[1] Cook and de Lucia,[9] and Slichter.[10] The important results will be given in this section.

The Hamiltonian can be expressed as the product of two second-rank spherical tensors:

$$\hat{H}_{Quad.} = \hat{V} \cdot \hat{Q} \qquad [2.16]$$

where $\hat{V}$ is the electric field gradient tensor at the location of the nucleus and $\hat{Q}$ is the nuclear quadrupole tensor of the coupling nucleus. These tensor operators are irreducible which means they transform under rotation like spherical harmonics.[1,2]

The nuclear quadrupole coupling constants, $e^2Q\left(q_J', q_J\right)$, are in the space-fixed axis system and can be expressed in terms of the elements in the principal inertial axis system by the following equation:

$$e^2Q\left(q_J^{'},q_J\right) = e^2Q\left\langle\frac{\partial^2 V}{\partial Z^2}\right\rangle = \left\langle\Phi_{Za}^2\right\rangle\chi_{aa} + \left\langle\Phi_{Zb}^2\right\rangle\chi_{bb} + \left\langle\Phi_{Zc}^2\right\rangle\chi_{cc} + 2\left\langle\Phi_{Za}\Phi_{Zb}\right\rangle\chi_{ab} + 2\left\langle\Phi_{Za}\Phi_{Zc}\right\rangle\chi_{ac} + 2\left\langle\Phi_{Zb}\Phi_{Zc}\right\rangle\chi_{bc} \qquad [2.17]$$

where $\left\langle\Phi_{Zg}\Phi_{Zg'}\right\rangle$ are the expectation values of the product of the direction cosines and the $\chi_{gg'} = e^2Q\frac{\partial^2 x}{\partial g \partial g'}$ are the nuclear quadrupole coupling constants in the principal inertial axis system. These $\chi_{gg'}$ constants are obtained directly from our spectroscopic data through the diagonalization program, SPFIT.[6] The off-diagonal quadrupole coupling interactions are negligible in all the complexes and clusters in this study. The nuclear quadrupole coupling constant is a tensor. The experiments do not contain information about the off-diagonal components.

For the complexes studied in this thesis, the chromophore molecule contains the nucleus with the electric quadrupole moment. The nuclear quadrupole coupling constants obtained for the hydrogen molecule complexes and clusters with the dopant molecule can be compared to the constants obtained for the bare chromophore. The weak van der Waals interaction holding the complexes together negligibly changes the electric field gradients at the chromophore molecule. Deviations in the nuclear quadrupole coupling constants between the monomer and the complex values can be attributed to the tilting of the inertial axis system, thus changing the projection of the space-fixed quadrupole interactions onto the inertial axis system. The van der Waals complexes studied in this thesis are non-rigid and have large amplitude motions which affect the quadrupole interaction. The average angle between the molecular axis of the chromophore and the *a*-inertial axis can be obtained by solving:

$$\chi_{aa} = \frac{1}{2}\chi_0\left\langle 3\cos^2\theta_a - 1\right\rangle \qquad [2.18]$$

and:

$$\chi_{bb} = \frac{1}{2}\chi_0\left\langle 3\sin^2\theta_a - 1\right\rangle \qquad [2.19]$$

where χ_0 is the quadrupole coupling constant of the isolated chromophore molecule. The angle, θ_a, obtained from this analysis is the average over the large amplitude motions in the complex. The nuclear quadrupole coupling interaction is normally the largest of the three hyperfine interactions presented here.

2.5.2 Nuclear magnetic spin-spin interaction

As mentioned in Chapter 1, hydrogen molecules exist as two spin isomer forms: *para*-hydrogen ($I_{H_2} = 0$; nuclear singlet state) and *ortho*-hydrogen ($I_{H_2} = 1$; nuclear triplet state). At room temperature and in equilibrium, a hydrogen gas sample consists of 75% *ortho*-hydrogen molecules and 25% *para*-hydrogen molecules. In spectroscopy, especially in the microwave region, complexes and clusters containing *ortho*-hydrogen molecules can be differentiated from those containing only *para*-hydrogen by the nuclear triplet state of the *ortho*H_2 molecule. Nuclear spin-spin interactions in *ortho*-hydrogen molecules give rise to the additional structure observed in the spectrum.

Nuclear spin-spin interaction occurs between two nuclei which both have a non-zero nuclear spin and an associated magnetic moment. This interaction has both a scalar and a tensor component. The scalar term is usually small (especially for light atoms) and no effect due to this term could be observed in the spectra analysed in this work. Therefore the scalar term has been neglected. The tensor component has two contributions: a direct and an indirect part. The direct contribution is the magnetic interaction between two dipoles k and l separated by a distance r_{kl}. The indirect part describes the indirect electron coupled interaction. The indirect term arises through the mechanism of each nucleus interacting with its own electron spin and the electron spins of the two nuclei interacting with each other. In general, the magnetic interaction of one nucleus with the electron of its atom causes the electron to align itself antiparallel to the nuclear spin. Since two electron spins in a triplet state (like in an *ortho*-hydrogen molecule) must be parallel to one another, the electron of the second atom will align itself antiparallel to the nuclear spin of the first nucleus. However, the second electron also interacts magnetically with its own nuclear spin. This combination of interactions thus gives rise an interaction between the magnetic dipoles of the two nuclei. In the case of light atoms, this interaction is normally negligible.[11-13] The indirect spin-spin constant has been neglected for all the complexes and clusters studied in this thesis.

The direct spin-spin interaction energy is given by:[14]

$$E_{spin-spin} = \frac{2\alpha_{J,K_a,K_c}}{J(J+1)} f(I,J,F) \qquad [2.20]$$

where:

$$\alpha_{J,K_a,K_c} = \frac{-3\mu_N^2 g_N^2}{r_{lk}^3}\left\{\alpha^2\langle J_a^2\rangle + \beta^2\langle J_b^2\rangle + \gamma^2\langle J_c^2\rangle - \frac{J(J+1)}{3}\right\} \qquad [2.21]$$

and $f(I,J,F)$ is the Casimir function, r_{lk} is the distance between the l^{th} and k^{th} nuclei involved in the interaction, μ_N is the nuclear magneton and g_N is the nuclear g factor of the protons. The α, β, and γ terms in equation [2.21] are the cosines of the angles between the H-H axis and the inertial a-, b-, and c-axes, respectively. $\langle J_a^2\rangle$, $\langle J_b^2\rangle$, and $\langle J_c^2\rangle$ are the expectation values of the squares of the components of the rotational angular momentum operators along the principal inertial axes. In these studies, the tensor spin-spin coupling constant along the *a*-inertial axis can be estimated from the geometry of the *ortho*H_2 molecule and by assuming $\alpha^2 = 1$ and $\beta^2 = \gamma^2 = 0$, giving S_{aa} from $S_{aa} = \alpha_{ss} = \frac{-3\mu_N^2 g_N^2}{r^3}$. The tensor spin-spin coupling constants can then be fit to the spectroscopic data allowing for non-zero β^2 and γ^2 terms corresponding to S_{bb} and S_{cc}, respectively.

2.5.3 Nuclear magnetic spin-rotation interaction

Nuclear magnetic spin-rotation interaction occurs when there is an interaction between the magnetic moment of a nucleus and the magnetic field generated by the rotation of the molecule. The magnetic field components along the nuclear rotational angular momentum, *J*, originate from two mechanisms: the rotation of the molecule as a rigid charge distribution and less directly, but more importantly, the electrons not following the molecular frame creating rotationally dependent magnetic fields.[1,2] The Hamiltonian describing this interaction is given by:

$$\hat{H}_{spin-rotation} = C_{J,K_aK_c}\,\mathbf{I}\cdot\mathbf{J} \qquad [2.22]$$

where $C_{J,K\,K_c}$ is the rotational state dependent spin-rotation coupling constant. The spin-rotation coupling constant that is independent of the rotational state (C_{gg}) is given by:

$$C_{gg} = -g_I \mu_N h_{gg} \qquad [2.23]$$

where g_I is the nuclear *g*-factor and h_{gg} is the component of the effective magnetic field along the g principal inertial axis.

Attempts have been made to relate the magnetic coupling constant to the electronic structure of the molecule.[2] Unfortunately, because the interaction between the electronic and the end-over-end rotation is a second-order effect, it is, in most cases, not possible to extract meaningful information from the nuclear spin-rotation coupling constant.[1]

2.6 Molecular structure

The spectroscopically obtained rotational constants are inversely proportional to the principal moments of inertia, I_{gg}, and can be related to the inertial defect of the molecule. The moments of inertia can be used to determine the structural parameters of the complex.

For the asymmetric top complexes studied in this thesis, all three rotational constants can in principle be obtained for a given isotopologue. For some isotopologues, the data set obtained was insufficient to determine all three rotational constants. For all complexes and clusters, the structural parameters of interest are the van der Waals bond length and the angle formed by the molecular axis of the dopant and each hydrogen molecule. In the dimer case, there are two structural parameters to determine: one bond length and one angle. In all cases, the structure of the chromophore molecule is assumed to not change upon complex formation since the van der Waals interaction is weak. Furthermore, the hydrogen molecule is considered as a point mass since no information about the orientation of the hydrogen molecule could be determined from the spectroscopic data. From the spectra and rotational constants for an isotopologue, one can calculate the two structural parameters needed:[15-17]

$$R = \left\{ 505379 \left[\frac{M_{H_2} + M_{chromophore}}{M_{H_2} M_{chromophore}} \right] \left(\frac{1}{B} - \frac{1}{b} \right) \right\}^{1/2} \qquad [2.24]$$

$$\sin\theta = \frac{b}{A}\left[\frac{A-B}{b-B}\right]^{1/2} \qquad [2.25]$$

where M_{H_2} is the mass of the H_2 molecule, $M_{chromophore}$ is the mass of the chromophore, A and B are the rotational constants (in MHz) of the H_2 – molecule complex and b is the rotational constant of the chromophore monomer. Additionally, isotopic data allow us to obtain the absolute positions of the atoms in the molecule (r_s structure). The treatment assumes that the bond lengths are unchanged by the isotopic substitution and that the changes in the moments of inertia are due to the changes in molecular mass.[18] An iterative program, MWSTR1, was used in this thesis to obtain the r_s structure of the complexes.[19,20]

In the analysis of the moments of inertia to yield structural parameters, it is necessary to establish the effects of zero-point vibrations. The effective moments of inertia have different vibrational effects which are dependent on the principal axes. This is shown by:[2]

$$\Delta_0 = I_c^0 - I_a^0 - I_b^0 \qquad [2.26]$$

where Δ_0 is the inertial defect and I_a^0, I_b^0, and I_c^0 are the moments of inertia along the *a*-, *b*-, and *c*-axes, respectively. In-plane and out-of-plane vibrations affect the sign and magnitude of the inertial defect. A rigid and planar molecule in its equilibrium structure would have an inertial defect of zero. A non-rigid and non-planar molecule has a nonzero inertial defect. A larger value for the inertial defect is evidence for a less rigidly bound complex and/or non-planarity of the complex.

Larger clusters ($N \geq 2$) contain more structural parameters to be determined and in general it is more difficult to extract the desired information. Isotopic substitution can provide general information from the moments of inertia regarding the positions of the hydrogen molecules with respect to the chromophore molecule. This was done in the study of doped helium clusters with OCS to determine the ring structure of five atoms as well as for relative positions of the sixth, seventh, and eighth helium atoms.[21]

2.7 Theoretical description of microwave spectroscopy

The interaction of an ensemble of molecular dipoles with a microwave pulse and the transient effects of such a pulse on the system will be discussed in this section. When a sample is irradiated with a microwave pulse of correct strength and duration, the microwave radiation induces a torque on the molecular dipole. Since many molecules are involved, a macroscopic dipole moment is induced. The macroscopic dipole moment oscillates in time with the microwave radiation. When the microwave pulse is removed, the macroscopic dipole moment is monitored as a function of time. A Fourier transform of the time domain signal provides the frequency domain signal.[22-24]

These phenomena of coherence transfer from the radiation to the sample and the decay of the coherence when the radiation is removed are best described using "optical Bloch equations" equivalent to those used in NMR.[25] Detailed derivations have been given by Flygare,[22-24,26] Shoemaker,[27] and Dreizler.[28,29] In this section I will provide some derivations and important results. As a first assumption, relaxation effects of the ensemble on the time frame of our experiment will be neglected in this treatment. To derive the Bloch equations, the time-dependent Schrödinger theory in a density matrix formalism is an appropriate description. The time-dependent Hamiltonian is:[28,29]

$$\hat{H}(t) = \hat{H}_o + \hat{H}^{(1)}(t) \qquad [2.27]$$

where $\hat{H}_o = \hat{H}_{rot}$, the time-independent rotational Hamiltonian and $\hat{H}^{(1)}(t)$ is a perturbation Hamiltonian. In this case, the perturbation is the interaction of the system with an external time-dependent electric field and is given by:

$$\hat{H}^{(1)}(t) = -\hat{\mu}E_o \cos\omega t \qquad [2.28]$$

where $\hat{\mu}$ is the dipole moment operator and $E_o \cos\omega t$ expresses the time-dependent electric field. ω is the angular frequency and not necessarily resonant with the rotational transition frequency. The space (q) and time (t) dependent wave functions for a two-level system are:

$$\Psi(q,t) = C_1(t)\psi_1(q) + C_2(t)\psi_2(q) \qquad [2.29]$$

where $C_1(t)$ and $C_2(t)$ are time-dependent coefficients. The functions $\psi_1(q)$ and $\psi_2(q)$ are solutions of:

$$\hat{H}_o\psi_i(q) = E_i\psi_i(q). \qquad [2.30]$$

The rotational transition between these levels occurs at $\omega_{12} = (E_2 - E_1)/\hbar$. The matrix elements for the full Hamiltonian are:

$$H_{11} = E_1,\ H_{22} = E_2 \text{ and } H_{12} = H_{21} = -\mu E_o \cos\omega t \qquad [2.31]$$

with $\mu = \int \psi_1 \hat{\mu} \psi_2 d\tau$. The elements of the density matrix $\rho(t)$ for the same system are given by:

$$\rho_{mn} = \frac{1}{N}\sum_{1}^{N} C_m^*(t)C_n(t) \qquad m,n = 1,2 \qquad [2.32]$$

where N is the number of molecules in the ensemble and equation [2.32] can be separated into the amplitude and phase factors:

$$\rho_{mn} = \left\{\frac{1}{N}\sum_{1}^{N}|C_m(t)|\cdot|C_n(t)|\right\}\cdot\left\{\frac{1}{N}\sum_{1}^{N}\exp\left[i(\gamma_n(t) - \gamma_m(t))\right]\right\}. \qquad [2.33]$$

The density matrix is diagonal at thermal equilibrium because the phase relation between particles is random. The population distributions of the stationary states are expressed by the diagonal elements. When external coherent radiation interacts with the system, a phase coherence develops between the wave functions of the individual particles and the off-diagonal elements may be nonzero.

The mean expectation value of the dipole moment operator $\hat{\mu}$, $\langle\mu\rangle$, can be calculated in terms of the density matrix using the following equation:

$$\langle\mu\rangle = Tr\{\mu \cdot \rho\} = \mu_{ab}\left[\rho_{ab}(t) + \rho_{ba}(t)\right] \qquad [2.34]$$

where *Tr* is the trace of the matrix. The macroscopic polarization, *P*, of the entire ensemble of *N* molecules is given by:

$$P = N \cdot Tr\{\mu \cdot \rho\} = N \cdot \mu_{ab}\left[\rho_{ab}(t) + \rho_{ba}(t)\right]. \qquad [2.35]$$

The necessary time-dependent density matrix elements, $\rho_{ab}(t)$ and $\rho_{ba}(t)$, can be obtained from the following relationship:

$$i\hbar\frac{\partial\rho}{\partial t} = \left[\hat{H},\rho\right] = \hat{H}\rho - \rho\hat{H}$$

$$i\hbar\frac{\partial\rho}{\partial t} = \begin{pmatrix} -\mu_{ab}(\rho_{ba}-\rho_{ab})\varepsilon_o\cos(\omega t) & -\rho_{ab}(E_b-E_a)-\mu_{ab}(\rho_{bb}-\rho_{aa})\varepsilon_o\cos(\omega t) \\ \rho_{ba}(E_b-E_a)-\mu_{ab}(\rho_{aa}-\rho_{bb})\varepsilon_o\cos(\omega t) & -\mu_{ab}(\rho_{ab}-\rho_{ba})\varepsilon_o\cos(\omega t) \end{pmatrix}$$

[2.36]

where $\hat{H}$ is the matrix representation of the Hamiltonian (equation [2.27]) in the $\psi_i(q)$ basis. The Rabi frequency is defined as $x = E_o\mu/\hbar$. The $(E_b - E_a)/\hbar$ can be simplified as ω_o and the matrix elements can be simplified by recognizing that $\rho_{ab} = \rho_{ba}^{*}$:

$$\frac{\partial\rho}{\partial t} = \begin{pmatrix} ix(\rho_{ba}-\rho_{ab})\cos(\omega t) & -i\rho_{ab}\omega_o + ix(\rho_{bb}-\rho_{aa})\cos(\omega t) \\ -i\rho_{ab}\omega_o - ix(\rho_{bb}-\rho_{aa})\cos(\omega t) & -ix(\rho_{ba}-\rho_{ab})\cos(\omega t) \end{pmatrix}. \qquad [2.37]$$

The Rabi frequency describes the strength of the interaction between the transition dipole moment of the molecular ensemble and the external radiation applied to the system. The density matrix elements can be transformed into a rotating coordinate system which rotates with the angular frequency ω:

$$\begin{aligned} \tilde{\rho}_{aa} &= \rho_{aa} \\ \tilde{\rho}_{bb} &= \rho_{bb} \\ \tilde{\rho}_{ab} &= \rho_{ab} e^{-i\omega t} \\ \tilde{\rho}_{ba} &= \rho_{ba} e^{i\omega t} \end{aligned} \qquad [2.38]$$

Some real variables connected with equation [2.38] are now introduced:

$$\begin{aligned} u &= \tilde{\rho}_{ba} + \tilde{\rho}_{ab} \\ v &= i(\tilde{\rho}_{ba} - \tilde{\rho}_{ab}) \\ w &= \tilde{\rho}_{aa} - \tilde{\rho}_{bb} \\ s &= \tilde{\rho}_{aa} + \tilde{\rho}_{bb} \end{aligned} \qquad [2.39]$$

Here, u and v describe the coherence set up by the microwave radiation. The coherence is proportional to the real and imaginary macroscopic polarization of the ensemble. The w and s variables are the difference and sum, respectively, of the populations of the two energy levels.

The experiment will be separated into the excitation and observation periods. Initially, the polarization is zero, so that $u(t_o) = v(t_o) = 0$, the population difference is $w(t_o) = \Delta N_o$. It is assumed, that a near-resonant, strong, short excitation pulse is used, such that $x\rangle\rangle\Delta\omega$. In this case, $\Delta\omega$ can be neglected to give:

$$\begin{aligned} \partial u/\partial t &= 0 \\ \partial v/\partial t &= -xw. \\ \partial w/\partial t &= xw \end{aligned} \qquad [2.40]$$

The solutions to the differential equations are:

$$\begin{aligned} u(t) &= u(t_o) = 0 \\ v(t) &= -\Delta N_o \sin(xt). \\ w(t) &= \Delta N_o \cos(xt) \end{aligned} \qquad [2.41]$$

These show an oscillation of $v(t)$ and $w(t)$ between ΔN_o and $-\Delta N_o$ with the Rabi frequency. The polarization reaches a maximum when the external radiation has a pulse length of $xt = \pi/2 = \frac{E_o \mu t}{\hbar}$ and describes the condition for a so-called $\pi/2$ pulse. The population difference is 'transferred' into polarization.

For the discussion of the observation period, it will be assumed that a $\pi/2$ pulse was applied to the system. When the pulse is switched off, the observation period begins. The system is no longer interacting with the applied field, therefore $x = E_o = 0$, and the equations become:

$$\begin{aligned} \partial u/\partial t &= -\Delta\omega \cdot v \\ \partial v/\partial t &= \Delta\omega \cdot u \\ \partial w/\partial t &= 0 \end{aligned} \qquad [2.42]$$

With maximum polarization transfer from the $\pi/2$ pulse, $u(\pi/2x) = 0$, $v(\pi/2x) = -\Delta N_o$, and $w(\pi/2x)=0$, the solutions are:

$$\begin{aligned} u(t') &= -\Delta N_o \cos(\Delta\omega t) \\ v(t') &= -\Delta N_o \sin(\Delta\omega t) \\ w(t') &= 0 \end{aligned} \qquad [2.43]$$

where $t' = t - \pi/2x$, the time after the excitation pulse.

The induced macroscopic dipole moment, P, is related to u and v by the following relationship which can be derived from equations [2.37] and [2.39]:

$$P = N\mu_{ab}\left[u(t)\cos(\omega t) - v(t)\sin(\omega t)\right] \qquad [2.44]$$

where from equation [2.44] it can be seen that u is the real part of P and is in-phase with the microwave perturbation and v is the imaginary part of P and is 90° out-of-phase.

The solutions of equations [2.43] are inserted into equation [2.44] to determine the polarization:

$$P = \Delta N_o \mu_{ab} \sin(xt')\sin(\omega_{12}t). \qquad [2.45]$$

The polarization oscillates with the rotational transition frequency ω_{12}; it is proportional to μ and the initial population difference ΔN_o. To increase the polarization of an ensemble, the dipole moment can be increased by changing the molecule investigated, or the initial population difference can be increased. There are methods available to increase the initial population difference, such as using the cooling properties of the molecular expansion.

2.8 General description of the Fourier transform microwave spectrometer

The experiments performed for the studies in this thesis were done using a Balle-Flygare type pulsed-jet Fourier transform microwave spectrometer.[30] A schematic diagram of this instrument is shown in Figure 2.1. The details of the spectrometer have been described elsewhere,[31,32] but will be given in brief here. Our spectrometer follows the design by Balle and Flygare.[30] The sample cell consists of a Fabry-Pérot microwave resonator contained in a vacuum chamber. The vacuum is maintained by a diffusion pump with a pumping speed of 2000 L s^{-1} which is backed by a rotary fore pump. The resonator consists of two spherical aluminum mirrors (26 cm in diameter; radius of curvature of 38 cm) separated by an adjustable distance of 20 to 40 cm. The distance between the mirrors is adjusted to tune the cavity into resonance with the external microwave frequency for each experiment.

In the centre of each mirror is a wire hook antenna which is used to couple the microwave radiation into and out of the resonator. The antenna on the stationary mirror is used to send the microwave pulses into the cavity, as well as to receive molecular emission signals from the sample. The antenna on the movable mirror is used to tune the cavity in order to create a standing wave pattern and to maximize the microwave power in the cavity. The length of the antennas can be varied for better frequency region coverage. The resonator is designed for optimal performance in the frequency range of 3-26 GHz.

Samples used in these studies contained trace concentrations (<0.03 %) of the chromophore molecule (OCS or HCCCN) with ~1-5% hydrogen or enriched *para*-hydrogen gas in helium backing gas. For the study of some *ortho*-hydrogen – molecule dimers, neon was used as a backing gas and an increase in signal intensity was observed consistent with the results of Klemperer *et al.*[15,16] A neon expansion has a higher translational temperature than a helium expansion. Higher temperatures in the expansion allow for additional population of more energetic energy levels.[33] In a neon expansion, signals due to *para*-H_2 containing complexes were no longer measurable due to a larger binding energy between neon and OCS as observed in References 15 and 16. The supersonic jet is generated with a General Valve Series 9 pulsed nozzle, mounted in the stationary mirror and connected to the gas supply. The molecular expansion is introduced into the sample cell maintained at low pressure. Weakly bound complexes and clusters are formed through collisions at the beginning of the expansion. As the density of atoms in the jet decreases, the expansion provides a collision-free environment where the clusters are free from interference with other species.[34] Specific sample pressures and concentrations used to study the complexes of interest will be discussed in the appropriate chapters.

The near collision-free property of the molecular expansion must be maintained by evacuating the cell completely after each pulse of gas. The vacuum chamber was pumped to < 1 mtorr by a diffusion pump backed by a rotary pump. The collisions in the throat of the nozzle convert rotational and vibrational energies (particularly the former) into translational energy, resulting in a cooling of the internal degrees of freedom.[34-39] Resulting rotational temperatures in the jet are ~2-3 K, with the vibrational temperatures being higher (~200 K). This very low rotational temperature ensures that only the lowest rotational energy levels are populated. The supersonic expansion reduces the translational temperature, resulting in a very narrow velocity range for the molecules and atoms in the jet.

In the setup used for these experiments, the molecular expansion and the direction of microwave propagation are coaxial. This arrangement optimizes the resolution and sensitivity of the spectrometer, but has the drawback of Doppler doubling for each transition line. This doubling occurs because the molecules emit radiation both forwards and backwards with respect to the direction of the jet. The antenna detects the splitting in the frequency due to the Doppler effect. The Doppler splitting increases as the transition frequency increases. The rest frequency of the transition is the average of the frequencies of the two Doppler components. The bandwidth of our spectrometer is ~1 MHz with the line widths in helium expansion being ~ 21 kHz full width at half maximum.

A heterodyne detection scheme was used to downconvert the molecular signal and aid with the digitization. Additionally, we use a 10 MHz clock to maintain the phase coherence of the experiments allowing for signal-averaging. We have a background signal and a sample signal for each averaging cycle.

2.9 Microwave-microwave decoherence double resonance experiments

To confirm spectroscopic assignments and to aid the search of further transitions, microwave – microwave double resonance (DR) experiments were used. A particular type of double resonance experiment, the so-called decoherence experiment,[31,40] was used for the studies described in this thesis. The pumping scheme used for the decoherence DR experiments is shown in Figure 2.2. The microwave radiation in the set-up is from a continuous source, which is broadcast into the cavity perpendicular to the molecular expansion. The molecular ensemble interacts with the second frequency after the ensemble has been prepared in a superposition state of the two energy levels ($|a\rangle$ and $|b\rangle$) from a $\pi/2$ pulse. A high power DR source ($\geq$ ~300 μW), like the powers used in our experiments, will cause decoherence of the emission signal.[31,40] This is illustrated for a connected *a*-type and a *b*-type transitions of *ortho*H_2 – $HCCC^{15}N$ dimer in Figure 2.3(a) and (b), respectively. The difference between the transitions is the dipole moment along the inertial axes associated with the pumped transition. The *a*-type transition, shown in Figure 2.3(a), requires much less pump power to achieve full decoherence as seen by the complete destruction of the signal for all frequencies near the connected transition. The *b*-type transition in Figure 2.3(b) on the other hand requires much stronger pump powers to achieve measurable decoherence. When the correct pump power is used, as in Figure 2.3(b), the decoherence effect is sharp. The observation of a decoherence effect between two transitions confirms their connectivity. The main advantage of the decoherence DR set-up is the ability to scan the pump frequency to find the frequency of an unknown transition while monitoring a strong transition.

2.10 Construction of the *para*-hydrogen converter

Although molecular hydrogen at room temperature and in equilibrium is only 25% *para*-hydrogen, a converter can easily be used to convert *ortho*-hydrogen to *para*-hydrogen. The lowest energy configuration is *para*-hydrogen and in the liquid and solid phases it is the preferred spin isomer. The conversion under normal conditions is theoretically forbidden since a singlet-triplet mixing would be necessary.[41] To induce the singlet-triplet mixing, a catalyst is used. The catalyst, chromium oxide on alumina, possesses an inhomogeneous magnetic field while hydrogen is liquefied and eventually solidified.

The converter containing the catalyst must be able to be put into a liquid helium dewar to achieve the temperature for liquefaction and solidification. The design of the converter was modeled from the *para*-hydrogen converter at the National Research Council (NRC) of Canada.[42] The measurements for the length and width of the converter were specific for the helium dewar which was to be used. After some initial tests with the converter, some changes were made to the design. Figure 2.4 shows the final design of the converter. The main change compared to the design at NRC made was the addition of a solid brass guide to the top of the copper cylinder. The guide was added to help with the safe and quick removal of the converter from the helium dewar and has no effect on the efficiency of the conversion.

2.11 Figures

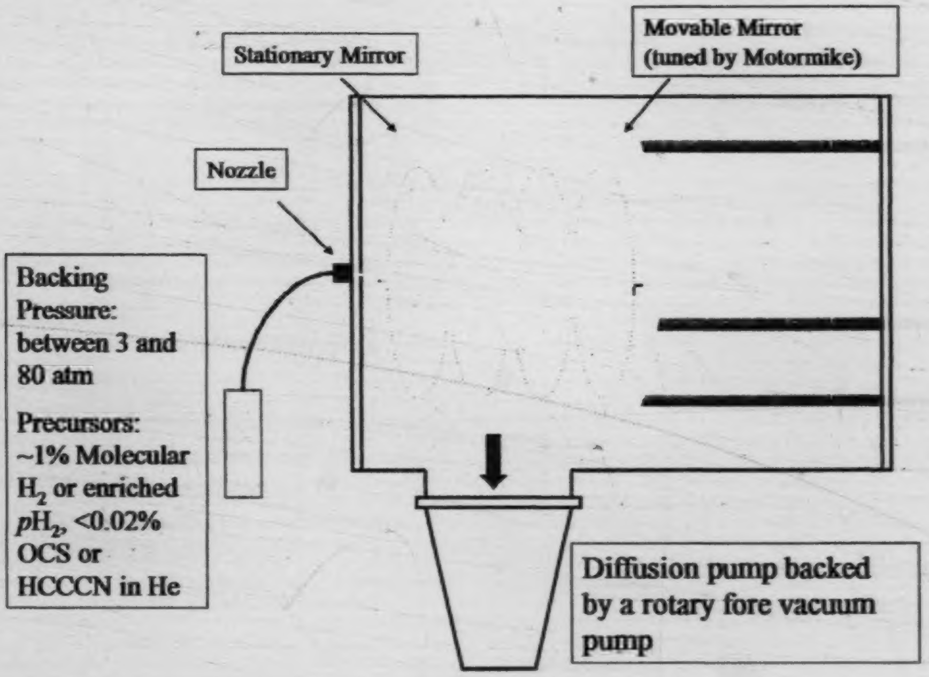
Stationary Mirror
Movable Mirror (tuned by Motormike)
Nozzle
Backing Pressure: between 3 and 80 atm
Precursors: ~1% Molecular H_2 or enriched pH_2, <0.02% OCS or HCCCN in He
Diffusion pump backed by a rotary fore vacuum pump

Figure 2.1: A simplified schematic illustration of the setup of the Fourier transform microwave spectrometer used in our laboratory.

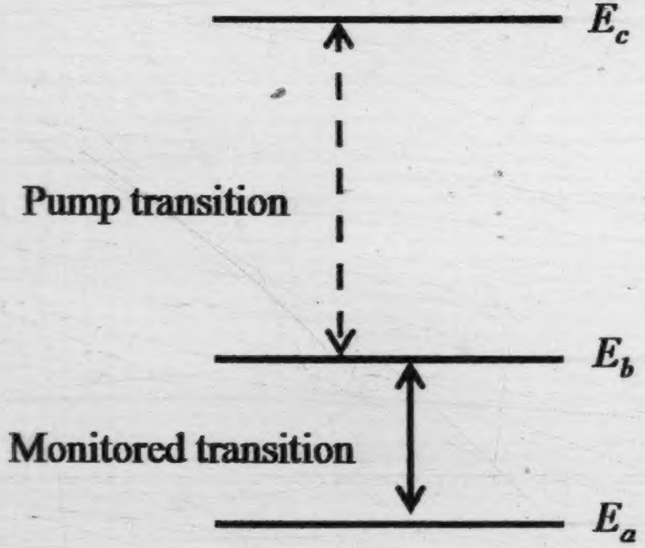
E_c
Pump transition
E_b
Monitored transition
E_a

Figure 2.2: Illustration of the destructive MW-MW double resonance (DR) scheme used in this work. The coherent emission MW signal at the transition frequency $((E_b\text{-}E_a)/\hbar)$ is destroyed when the pump radiation corresponds to the transition frequency of a connected transition $((E_c\text{-}E_b)/\hbar)$.

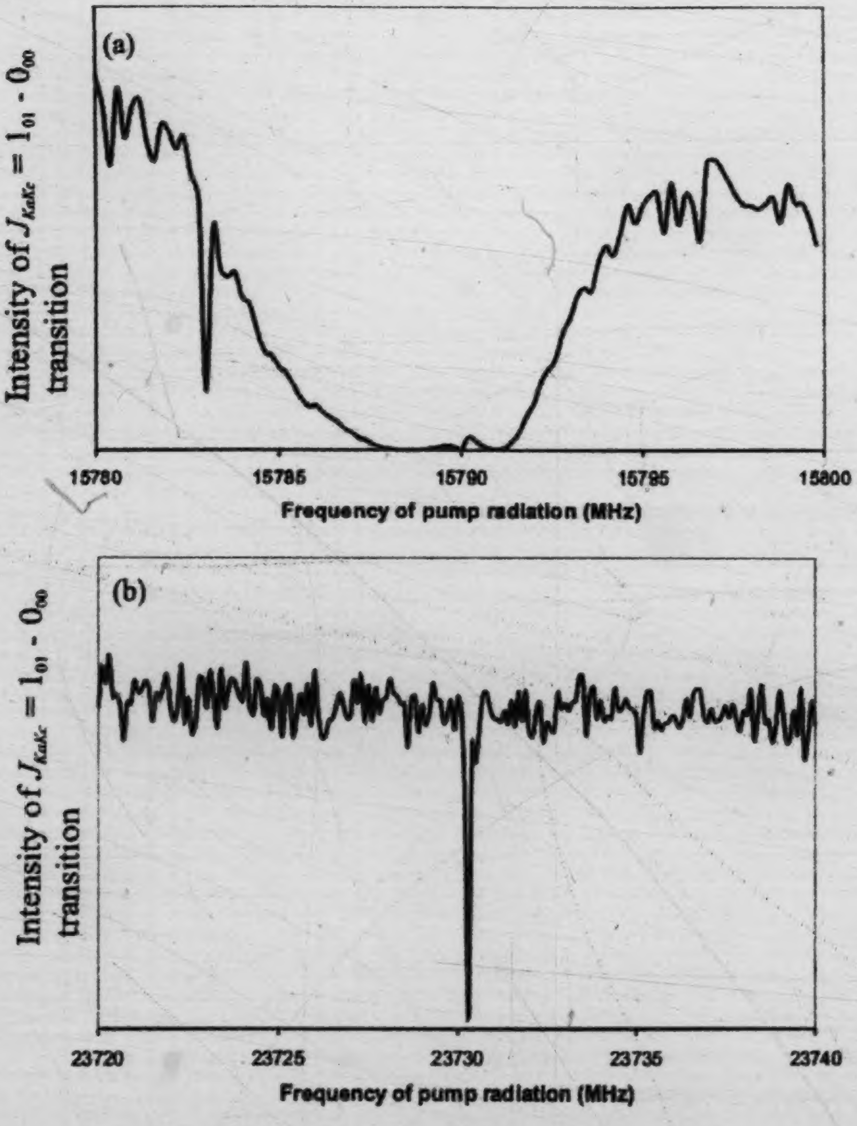

Figure 2.3: A representative spectrum of the effect of destructive MW-MW DR experiment. The emission signal of the F=2-1 nuclear hyperfine component of the *ortho*H_2 – $HCCC^{15}N$ $J_{KaKc} = 1_{01} - 0_{00}$ rotational transition was destroyed when the frequencies of two connected transitions were pumped. (a) The pump radiation was swept through the frequency region where $J_{KaKc} = 2_{02} - 1_{01}$ transition was predicted. (b) The pump radiation was swept through the frequency region where the $J_{KaKc} = 1_{11} - 0_{00}$ transition was predicted.

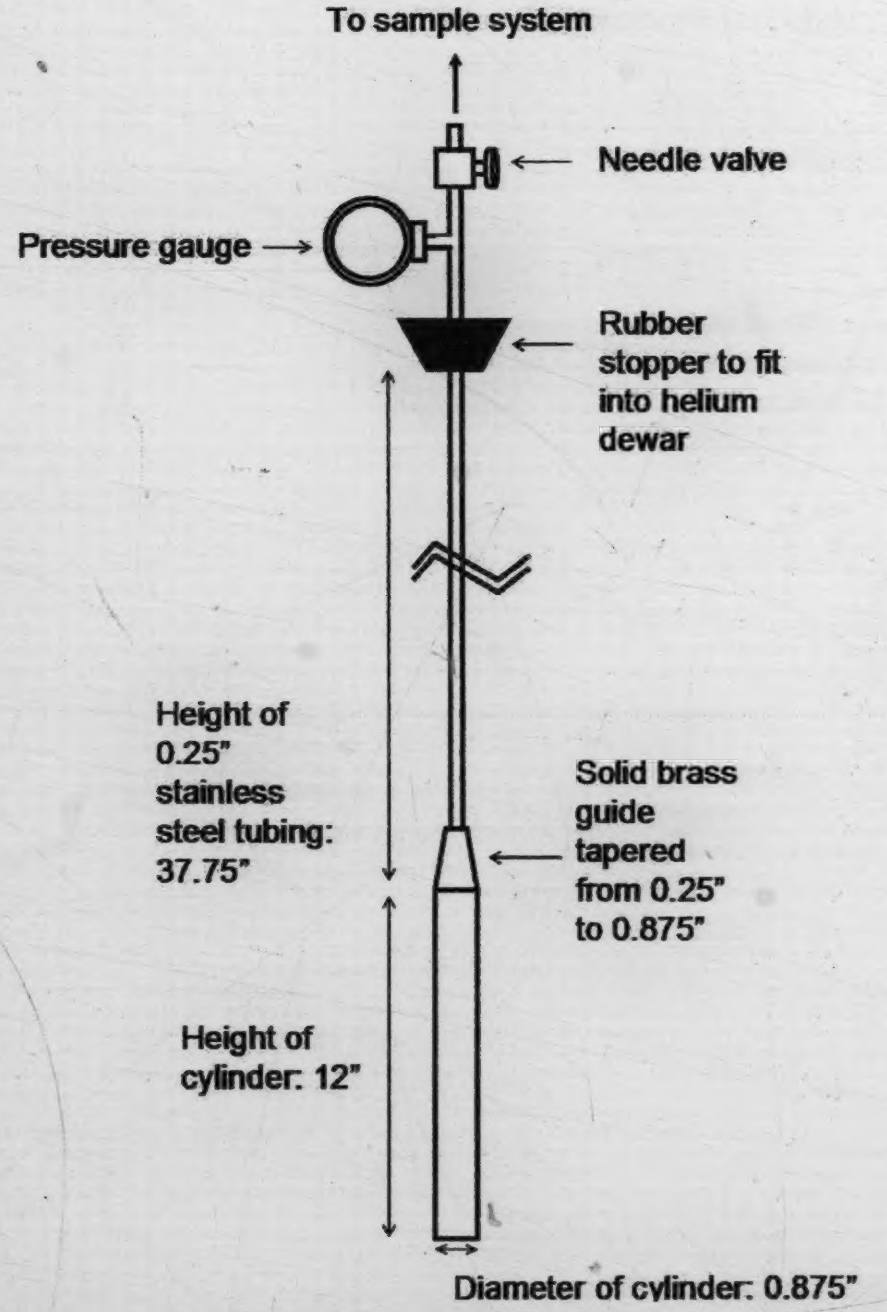

To sample system
Needle valve
Pressure gauge
Rubber stopper to fit into helium dewar
Height of 0.25" stainless steel tubing: 37.75"
Solid brass guide tapered from 0.25" to 0.875"
Height of cylinder: 12"
Diameter of cylinder: 0.875"

Figure 2.4: A schematic diagram showing the design of the para-hydrogen converter built for some studies in this thesis. The design was modeled from the converter at the National Research Council (NRC) of Canada.

2.12 References

[1] W. Gordy and R. L. Cook, *Microwave Molecular Spectra No. XVIII in Techniques of Chemistry*, 3rd ed. (Wiley-Interscience Publishers, New York, 1970).

[2] C. H. Townes and A. L. Schawlow, *Microwave Spectroscopy*. (Dover Publications, New York, 1975).

[3] D. A. McQuarrie, *Quantum Chemistry*. (University Science Books, California, 1983).

[4] P. F. Bernath, *Spectra of Atoms and Molecules*. (Oxford University Press, New York, 1995).

[5] J. K. G. Watson, *J. Chem. Phys.* **48** (10), 4517 (1968).

[6] H. M. Pickett, *J. Mol. Spectrosc.* **148** (2), 371 (1991).

[7] R. N. Zare, *Angular Momentum*. (Wiley, New York, 1988).

[8] A. R. Edmonds, *Angular Momentum in Quantum Mechanics*. (Princeton, New Jersey, 1974).

[9] R. L. Cook and F. C. DeLucia, *Am. J. Phys.* **39**, 1433 (1971).

[10] C. P. Slichter, *Principles of Magnetic Resonance*. (Springer Verlag, Berlin, 1978).

[11] N. F. Ramsey, *Phys. Rev.* **78**, 699 (1950).

[12] N. F. Ramsey, *Molecular Beams*. (Oxford University Press, London, 1953).

[13] C. Schlier, *Fortschr. Phys.* **9**, 455 (1961).

[14] N. Heineking and M. C. L. Gerry, *J. Mol. Spectrosc.* **158**, 62 (1993).

[15] Z. H. Yu, K. J. Higgins, W. Klemperer, M. C. McCarthy, and P. Thaddeus, *J. Chem. Phys.* **123** (22) 221106 (2005).

[16] Z. H. Yu, K. J. Higgins, W. Klemperer, M. C. McCarthy, P. Thaddeus, K. Liao, and W. Jäger, *J. Chem. Phys.* **127**, 054305 (2007).

[17] F. J. Lovas and R. D. Suenram, *J. Chem. Phys.* **87** (4), 2010 (1987).

[18] J. Kraitchman, *Am. J. Phys.* **21** (1), 17 (1953).

[19] V. Typke, *J. Mol. Spectrosc.* **69** (2), 173 (1978).

[20] V. Typke, *J. Mol. Spectrosc.* **72** (2), 293 (1978).

[21] Y. Xu and W. Jäger, *J. Chem. Phys.* **119** (11), 5457 (2003).

[22] W. H. Flygare, *Molecular Structure and Dynamics*. (Prentice-Hall, New Jersey, 1978).

[23] W. H. Flygare, *Pulsed Transform Microwave Spectroscopy*. (Plenum Press, New York, 1982).

[24] J. C. McGurk, T. G. Schmalz, and W. H. Flygare, *Adv. Chem. Phys.* **25**, 1 (1974).

[25] J. A. Shea, W. G. Read, and E. J. Campbell, *J. Chem. Phys.* **79**, 2559 (1983).

[26] J. Ekkers and W. H. Flygare, *Rev. Sci. Instrum.* **47**, 448 (1976).

[27] R. L. Shoemaker, *Laser and Coherent Spectroscopy*. (Plenum Press, New York, 1978).

[28] H. Dreizler, *Mol. Phys.* **59**, 1 (1986).

[29] H. Dreizler and B. Bunsenges, *Phys. Chem.* **99**, 1451 (1995).

[30] T. J. Balle and W. H. Flygare, *Rev. Sci. Instrum.* **52** (1), 33 (1981).

[31] V. N. Markov, Y. Xu, and W. Jäger, *Rev. Sci. Instrum.* **69** (12), 4061 (1998).

[32] Y. Xu and W. Jäger, *J. Chem. Phys.* **106** (19), 7968 (1997).

[33] J. B. Anderson and J. B. Fenn, *Phys. Fluids* **8**, 780 (1965).

[34] A. C. Legon, *Ann. Rev. Phys. Chem.* **34**, 275 (1983).

[35] D. H. Hevy, *Ann. Phys. Chem.* **31**, 197 (1980).

[36] C. E. Klots, *J. Chem. Phys.* **66**, 3965 (1980).

[37] H. W. Liepmann and A. Roshko, *Elements of Gas Dynamics*. (Wiley, New York, 1957).

[38] D. R. Miller, J. P. Toennies, and K. Winkelmann, *9th Symposium on Rarefied Gas Dynamics*. (DFVLR Press, 1974).

[39] T. A. Miller, *Science* **223**, 545 (1984).

[40] K. Brendal and H. Mäder, *Private Communication.*

[41] V. I. Tikhonov and A. A. Volkov, *Science* **296** (5577), 2363 (2002).

[42] A. R. W. McKellar, *Private Communication.*

Chapter 3

Study of H_2 – OCS dimer: Minor isotopologues of OCS

This chapter[*] details the rotational spectroscopic study of the hydrogen – carbonyl sulfide dimers with the minor isotopologues of OCS. These further experimental spectroscopic characterizations of the *ortho*H_2 – OCS and *para*H_2 – OCS dimers will lay the foundation for the study of larger $(H_2)_N$ – OCS clusters and can help in the assignment of *N*, the number of hydrogen atoms in these clusters. Furthermore, the spectroscopic study of complexes of minor isotopologues of OCS with hydrogen molecules can be used to test and improve *ab initio* potential energy surfaces (PESs). A good quality PES is particularly important for quantum Monte Carlo calculations of quantities related to larger doped hydrogen clusters.

3.1 Experimental details

The spectra were collected using a Balle-Flygare type[1] pulsed-jet Fourier transform microwave spectrometer and a microwave-microwave double resonance spectrometer[2,3] both described in Chapter 2. Our gas samples were composed of low concentrations of OCS, generally in the 0.05-0.2% range and 1-5% of hydrogen gas or enriched *para*-hydrogen gas. The backing gas used for the generation *ortho*-hydrogen dimers with OCS was neon or helium, while studies of *para*-hydrogen dimers with OCS required helium as backing gas. The use of neon as a carrier gas increased the signal intensity of some higher energy transitions. This is consistent with the order of binding energies of dimers with OCS (He < *para*H_2 < Ne < *ortho*H_2 < HD < *ortho*D_2 < *para*D_2) that was reported by Yu *et al.*[4] The enriched *para*-hydrogen was obtained using a home-built converter, details of which were described in Section 2.10. Although it is not possible to determine the conversion efficiency with our spectrometer, because of the different binding energies of *ortho*H_2 – OCS and *para*H_2 - OCS, we see a large increase in the signal intensity of *para*H_2 – OCS transitions and we estimate the enrichment to be > ~97% *para*-hydrogen. This estimate is conservative compared to the 99% conversion obtained for another similar catalytic converter measured using Raman spectroscopy.[5,6]

---

[*] A version of this chapter has been published: Michaud, J. M.; Liao, K.; Jäger, W. *Mol. Phys.* **106**, 23 (2007).

Rotational transitions of H_2 – OCS complexes with singly substituted isotopologues ($O^{13}CS$, $OC^{34}S$, and $OC^{33}S$) were visible using a non-enriched sample of OCS. Transitions of complexes with doubly substituted isotopologues, $O^{13}C^{34}S$ and $O^{13}C^{33}S$, were observed using an enriched $O^{13}CS$ sample (Cambridge Isotopes, 99% ^{13}C). The enriched $O^{13}CS$ sample was also used to resolve the hyperfine pattern of strong transitions and to measure weaker transitions of H_2 – $O^{13}CS$.

A microwave-microwave double resonance technique was used to search for weaker, higher *J* transitions and to confirm the connectivity between rotational transitions.[2,3] We used a destructive coherence double resonance technique where the microwave horn antenna is positioned outside the microwave resonator, as described in more detail in Section 2.9. This technique was also used to indirectly determine the frequency of a weaker *b*-type transition that falls outside the nominal operating range of our spectrometer (3 to 26 GHz).

3.2 Experimental results and spectroscopic analyses

Frequencies for the experimental searches for the H_2 - OCS dimer transitions of minor isotopologues of carbonyl sulfide were predicted based on the calculated change in moments of inertia from the main isotopologue, $H_2 - {}^{16}O^{12}C^{32}S$.[4] For the $J_{KaKc} = 1_{01} - 0_{00}$ *a*-type transition, these predictions were within ± 20 MHz of the subsequently measured transition frequencies. The measurement of the $J_{KaKc} = 1_{01}$ - 0_{00} transition for each isotopologue allowed for the determination of $(B+C)/2$. A decoherence double resonance experiment was then used to locate the frequency for the $J_{KaKc} = 1_{10} - 1_{01}$ *b*-type transition for *ortho*$H_2 - O^{13}CS$. The exact transition frequency was subsequently measured in a single resonance experiment. The quantum number assignments of all measured *ortho*$H_2 - O^{13}CS$ transitions are substantiated by the presence of a closed loop among the measured transitions. From the assignments of some *b*-type transitions, it was possible to predict where the $J_{KaKc} = 1_{11} - 0_{00}$ transition was located. Although this transition lies outside the frequency range of our spectrometer, we could use the double resonance technique to indirectly measure its frequency within ± 5 kHz. Unfortunately, the low signal intensity of the *b*-type transitions made it infeasible to observe them for dimers containing ^{34}S and ^{33}S.

The efficiency of decoherence double resonance technique depends mainly on the available pump power. High pump power is especially important for low dipole moment pump transitions, such as the *b*-type transitions in this work. Since the dipole moment along the *b*-inertial axis is smaller for the *para*H_2 – OCS complexes than the corresponding *ortho*H_2 – OCS complexes, the *b*-type transitions could not be observed for *para*$H_2 - O^{13}CS$ despite extensive double resonance searches.

The measured transition frequencies and the quantum number assignments of all the isotopically substituted dimers are listed in Tables 3.1, 3.2, 3.3, and 3.4. The spin angular momenta of the two equivalent protons (spin angular momentum quantum number $I_1 = I_2 = ½$) in *ortho*H_2 containing complexes are accounted for using the coupling scheme $\mathbf{I_1} + \mathbf{I_2} = \mathbf{I}$; $\mathbf{I} + \mathbf{J} = \mathbf{F}$; where $I_1 + I_2 = 1$ for *ortho*H_2 molecules. For the complexes containing both *ortho*H_2 and ^{33}S, the coupling scheme $\mathbf{I_{^{33}S}} + \mathbf{J} = \mathbf{F_1}$; $\mathbf{I_1} + \mathbf{I_2} = \mathbf{I}$; $\mathbf{I} + \mathbf{F_1} = \mathbf{F}$ was used. Data for each isotopologue were fit separately using Pickett's global least squares fitting program SPFIT[7] to obtain rotational constants and quartic and sextic centrifugal distortion constants using Watson's *A*-reduction Hamiltonian.[8] The spectral fits for *ortho*H_2 containing dimers also included contributions from the tensor proton-proton spin-spin coupling constants along the inertial *a*- and *b*- axes, S_{aa} and S_{bb}, and two sets of equal spin-rotation coupling constants, again along the inertial *a*- and *b*-axes, (one for each proton), $C_{aa}(1)$, $C_{aa}(2)$, $C_{bb}(1)$ and $C_{bb}(2)$, where the numerical designation denotes the hydrogen atom in question. For the $OC^{33}S$ containing species, a ^{33}S ($I = 3/2$) nuclear quadrupole coupling constant, $\chi_{aa}(^{33}S)$, was determined. We were also able to resolve the ^{33}S nuclear quadrupole hyperfine structure of the $J_{KaKc} = 1_{01} - 0_{00}$ transitions of *para*$H_2 - OC^{33}S$ and *para*$H_2 - O^{13}C^{33}S$, and could determine the corresponding ^{33}S nuclear quadrupole coupling constants, $\chi_{aa}(^{33}S)$. This allows for a direct comparison of the field gradient at the ^{33}S nucleus in the *ortho*H_2 – and *para*H_2 – OCS dimers. The ^{33}S nuclear quadrupole coupling constants obtained are listed in Tables 3.2 and 3.4. All other spectroscopic constants obtained for the *ortho*H_2 – and *para*H_2 – OCS dimers are listed in Tables 3.5 and 3.6.

Because of the limited data set available for analysis, some centrifugal distortion constants needed to be fixed at the values of the main isotopologues,[4] as indicated in Tables 3.5 and 3.6. The *A* rotational constants for some of the isotopologues were fixed at the reduced mass scaled values of the *A* constant of the main isotopologue.[4] This method of obtaining an approximate value for the *A* rotational constant yielded the *ortho*H_2 – $O^{13}CS$ value to within 0.035% of that obtained from the spectroscopic analysis. The limited data set for *para*H_2 – $O^{13}CS$ did not allow us to determine the *A* rotational constant; therefore it was varied within 0.1% of the reduced mass scaled *A* rotational constant of *para*H_2 – OCS (Reference 4) to optimize the fit. The inertial defects, $\Delta_0 = I_c^0 - I_a^0 - I_b^0$, as described in Section 2.6, are also included in Tables 3.5 and 3.6.

Spectra showing the different hyperfine patterns in the $J_{KaKc} = 1_{01} - 0_{00}$ transitions of *ortho*H_2 and *para*H_2 containing complexes are shown in Figure 3.1. The hyperfine pattern of the *ortho*H_2 – OCS transition is well resolved. The *para*H_2 – $OC^{34}S$ spectrum was obtained using an enriched *para*H_2 sample to achieve a sufficient signal to noise ratio. Figure 3.2 shows the *b*-type $J_{KaKc} = 1_{10} - 1_{01}$ transition of *ortho*H_2 - $O^{13}CS$. The signal intensity of this transition is much lower than that of the *a*-type $J_{KaKc} = 2_{02} - 1_{01}$ transition because of the smaller dipole moment along the *b*- than the *a*-axis. The *b*-type transitions in the H_2 – OCS complexes are weaker than the corresponding transitions in He – OCS (Reference 9) even though analogous *a*-type transitions have comparable or greater signal strengths. This is a result of the smaller mass of the H_2 molecule compared to the helium atom, resulting in the *a*-inertial axis to almost coincide with the OCS molecular axis in H_2 – OCS. Figure 3.3 shows the $J_{KaKc} = 1_{01}$ - 0_{00} transition of the *para*$H_2 - O^{13}C^{33}S$ dimer. The larger splitting is the ^{33}S nuclear quadrupole hyperfine structure.

3.3 Discussion

Both proton-proton spin-spin and proton spin-rotation interactions were included in the fitting procedures to account for the hyperfine structure introduced by the presence of the hydrogen molecule in *ortho*H_2 – OCS. In this thesis, the expression used for the spin-spin interaction energy of two equivalent nuclei with spin angular momentum quantum number I is given in equations [2.20] and [2.21].[10] The sign of the spin-spin coupling constant is chosen such that it is negative for homodiatomic molecules.[11] The measured $|K| = 1$ transitions required the inclusion of the S_{bb} spin-spin coupling constant, in addition to S_{aa}, in the fitting procedure. For the *ortho*$H_2 - O^{13}CS$ isotopologue, values of S_{aa}(*ortho*$H_2 - O^{13}CS$) = -121.6 kHz and $S_{bb}(12)$(*ortho*$H_2 - O^{13}CS$) = -9.5 kHz were obtained. The spin-spin coupling constants obtained for different isotopologues of OCS (see Tables 3.2 and 3.5) agree well; this is expected since the isotopologues of OCS should not have a significant effect on the geometry of the H_2 moiety. In Reference 12, Ramsey's nuclear hyperfine Hamiltonian[13] was used to fit the spin-spin hyperfine splittings. The value obtained in that work corresponds to negative one-fifth of the conventionally used spin-spin coupling constant in microwave spectroscopy, i.e. $-5D_{aa}$(ref. 12) = S_{aa} = -106 kHz. The constants obtained from both analyses differ by 12.8%; a possible reason is that the value in Reference 12 was obtained from *a*-type transitions in the $K = 0$ stack only. Comparing the spin-spin coupling constants in the *ortho*H_2 – OCS dimers to that of free *ortho*H_2 ($-5D_a$ = -288.4 kHz)[14] shows that the values are of the same order of magnitude although slightly smaller for *ortho*H_2 – OCS complexes. The spin-spin coupling constant is determined mainly by the distance between the spins in question, which would be relatively unchanged by the van der Waals bond with OCS. One consideration for the difference in the values between the complex and the free *ortho*H_2 molecule is the orientation dependence of the tensor spin-spin coupling constant, that is the necessity to include S_{bb} in the spectroscopic fit.

The spin-rotation coupling constants obtained here [C_{aa}(*ortho*H_2 – $O^{13}CS$) = 389.3 kHz; C_{bb}(*ortho*H_2 – $O^{13}CS$) = -2.26 kHz] are significantly different from the values obtained in Reference 12 (C_{aa} = -4.0 kHz). The discrepancy between the values from this study and Reference 12 is most likely a result of the additional transitions which were included in our fitting procedure. The values of the spin-rotation coupling constants obtained for different isotopologues are all of the same magnitude. Some hyperfine components of weaker isotopologues could not be resolved, which may be the cause for slight variations in value. The spin-rotation coupling constant obtained for free *ortho*H_2 is C_{aa} = 113.8 kHz (Reference 14) is in marginal agreement with the values obtained for *ortho*H_2 – OCS in this report, but in better agreement than with the values from Reference 12.

The ^{33}S nuclear quadrupole coupling constants obtained for the *ortho*H_2 – $O^{12/13}C^{33}S$ and *para*H_2 – $O^{12/13}C^{33}S$ complexes are very similar to the value of the $OC^{33}S$ monomer ($\chi_0(^{33}S)$ = -29.1184(12) MHz).[15] This is consistent with the result obtained for *ortho*H_2 – $OC^{33}S$ in Reference 12. The $\chi_{aa}(^{33}S)$ values obtained for *para*H_2 – $OC^{33}S$ and *ortho*H_2 – $OC^{33}S$ indicate only small differences in electric field gradients between the complexes. The similarities between the $\chi_{aa}(^{33}S)$ obtained for the van der Waals dimers and the $OC^{33}S$ monomer indicate that the OCS molecular axis is nearly parallel with the *a*-axis of the inertial frame. This can be shown by assuming that the electric field gradient of the free OCS is unchanged upon complex formation with an H_2 molecule. The average angle θ_a between the OCS molecular axis and the *a*-inertial axis is given in equation [2.19]. The nuclear quadrupole coupling constant, χ_0, of the isolated $OC^{33}S$ is -29.1184(12) MHz. Values for θ_a of 6.3° and 7.2° are obtained for *ortho*H_2 – $OC^{33}S$ and *para*H_2 – $OC^{33}S$, respectively. The angles obtained from the $\chi_{aa}(^{33}S)$ analysis can be compared to the ones from the structural analysis of the moments of inertia discussed in more detail below. The structural analysis provides the coordinates in the principal axis system from which the angle θ_a can be calculated. Values for θ_a of 9.0° and 5.9° are obtained for *ortho*H_2 – OCS and *para*H_2 – OCS, respectively. The values from both analyses are in reasonable agreement and corroborate that the OCS molecular axis is nearly parallel with the *a*-inertial axis. The remaining discrepancies between the values are due to the different averaged functions on which the respective spectroscopic observables depend and to the uncertainties in the determined coupling constants and coordinates.

The centrifugal distortion constant Δ_J of the *ortho*H_2 – $O^{13}CS$ dimer (Δ_J = -34.4 kHz) is within the error limits of the value for the main isotopologue obtained in Reference 4 (Δ_J = -34.8 kHz). The values for Δ_J of the minor isotopologues ($OC^{34}S$ or $O^{13}C^{34}S$) are also of similar magnitude. The negative value of the centrifugal distortion constant Δ_J is consistent with a Coriolis coupling with a low-lying excited state, as was suggested in Reference 4. The centrifugal distortion constant Δ_J for *para*H_2 – $O^{13}CS$ (Δ_J = 53.9 kHz) is quite similar to the value obtained for *para*H_2 – OCS in Reference 4 (Δ_J =

56.3 kHz). The large values for the Δ_J constant are consistent with large amplitude radial motions being present in the *para*H_2 – OCS complex.

The inertial defects for the dimers containing minor OCS isotopologues are given in Tables 3.5 and 3.6 [Δ_o(*ortho*H_2 – $O^{13}CS$) = 0.169 amu Å^2; Δ_o(*para*H_2 – $O^{13}CS$) = 2.94 amu Å^2] and are of the same order of magnitude as the inertial defects of the dimers containing the main OCS isotopologue[4] [$\Delta_{o,\,corr}$ (*ortho*H_2 – OCS) = 0.283 amu Å^2; $\Delta_{o,\,corr}$ (*para*H_2 – OCS) = 3.137 amu Å^2]. The values $\Delta_{o,\,corr}$ in Reference 4 are corrected for the contributions from the second moment, or planar moment, about the *c*-axis, while the values in this report do not. For comparison purposes, the planar moment of the *c*-axis can be removed from the values of Reference 4 to give Δ_o(*ortho*H_2 – OCS) = 0.165 amu Å^2 and Δ_o(*para*H_2 – OCS) = 2.94 amu Å^2 which agree very well with our values. The non-zero planar moments of *ortho*H_2 – OCS and *para*H_2 – OCS are mainly a result of the out-of-plane motion of the H_2 molecule and should therefore not change significantly with isotopic substitution of OCS. The inertial defects show that the *ortho*H_2 – OCS dimers are more rigid than the corresponding *para*H_2 – OCS dimers. This is consistent with the results obtained in Reference 4.

As discussed in Section 2.6, it is possible to calculate average geometries of the *ortho*H_2 – OCS and *para*H_2 – OCS van der Waals complexes from the experimental rotational constants. Figure 3.4 shows the definition of the structural parameters being determined. In particular, the isotopic data available allow us to obtain the absolute positions of the atoms in the molecule (r_s structure). It is assumed in this treatment that the bond lengths and angles are unchanged by the isotopic substitution and that the changes in rotational constants are solely due to the changes in molecular mass.[16,17] The complete r_s structure is obtained when isotopic substitution is done for each atomic position.[17] An iterative program, MWSTR1, developed by Typke[18,19] allows for the fitting of isotopologues with multiple substitutions (i.e. *ortho*H_2 - $O^{13}C^{34}S$) and was used in this report. The structural parameter, *R*, is defined as the distance between the centre of mass of the OCS and the centre of mass of the hydrogen molecule; θ is the obtuse angle between the OCS intermolecular axis and the *R* vector. The geometries obtained for *ortho*H_2 – OCS and *para*H_2 – OCS are shown in Table 3.7 along with the values obtained from Reference 4 and He – OCS.[9] The r_s geometry obtained in this study and the structural parameters obtained in Reference 4 are in good agreement. The discrepancy between the values is larger for *para*H_2 – OCS than for *ortho*H_2 – OCS which could be attributed to the more floppy nature of the *para*H_2 – OCS complex as seen with the large inertial defects and centrifugal distortion constants. A complete r_s structure could not be obtained in this study as no oxygen isotopologue was studied. The shorter bond lengths in the H_2 – OCS complexes compared to the He – OCS complex[9] is consistent with larger binding energies of the former. The calculated angle between the H_2 molecule and the OCS intermolecular axis depends sensitively on the *A* rotational constant of the complex. The *A* rotational constant could spectroscopically be determined only in the *ortho*H_2 – $O^{13}CS$ dimer case. Therefore, the angle obtained in the r_s structure of the *para*H_2 – OCS dimer should be considered less accurate than the *ortho*H_2 – $O^{13}CS$ value.

3.4 Conclusions

Rotational spectra of several OCS isotopologues of the *ortho*H_2 – OCS and *para*H_2 – OCS van der Waals complexes were observed. The high resolution capability of our spectrometer allowed us to determine rotational and centrifugal distortion constants, as well as the spin-spin (S_{aa}, S_{bb}) and spin-rotation (C_{aa}, C_{bb}) coupling constants of the *ortho*H_2 – OCS species. The spin-spin coupling constants were compared to previous results and to the values obtained for the free *ortho*H_2 molecule. The ^{33}S nuclear quadrupole coupling constants (χ_{aa}) were determined for both *ortho*H_2 – $OC^{33}S$ and *para*H_2 – $OC^{33}S$ complexes. An average angle between the OCS molecular axis and the *a*-inertial axis was obtained from the ^{33}S quadrupole coupling constants and compared to the angle obtained from the r_s substitution structure. The derived r_s structures of the complexes also indicate that the large amplitude vibrational bending motions in the *para*H_2 – OCS complex are greater than in *ortho*H_2 – OCS. The r_s structures and the rotational constants obtained for several isotopologues can be used to test and improve potential energy surfaces of H_2 – OCS.

3.5 Figures

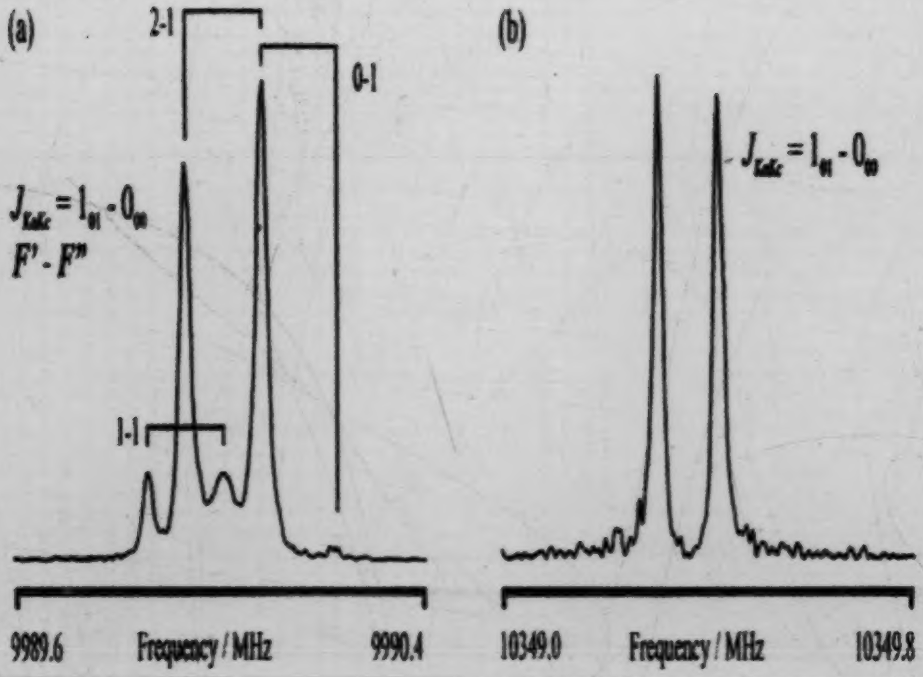

Figure 3.1: Experimental spectra of the $J_{KaKc} = 1_{01} - 0_{00}$ transition of (a) *ortho*H_2 – $OC^{34}S$ (50 averaging cycles) and (b) *para*H_2 – $OC^{34}S$ (100 averaging cycles). Spectrum (b) was obtained using an enriched *para*H_2 sample. The time domain signals were recorded at 10 ns sampling interval to obtain 8k data points. The data set was supplemented with 8k zeros before Fourier transformation. The difference in hyperfine patterns in the spectra is caused by the presence of proton-proton spin-spin and proton spin-rotation coupling in the *ortho*H_2 – OCS system.

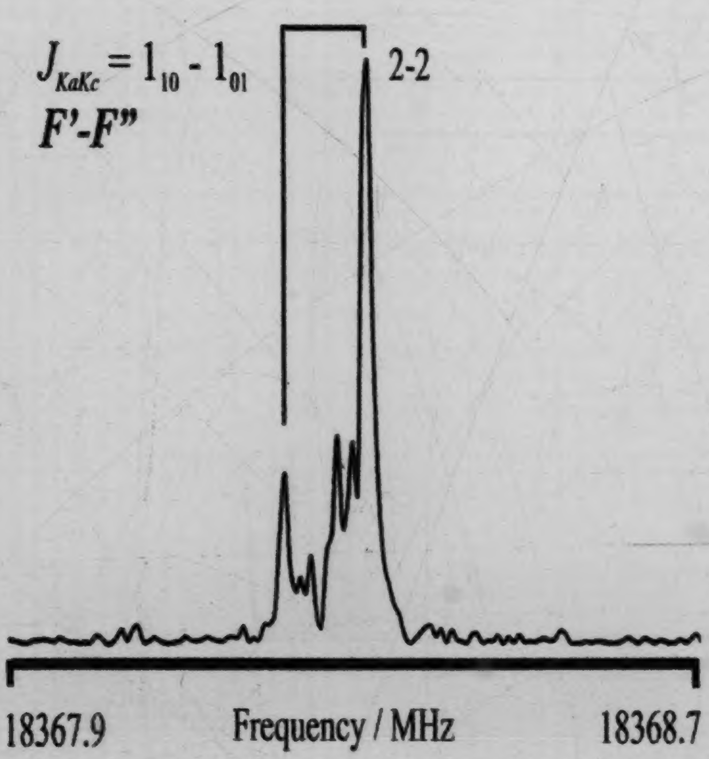

Figure 3.2: Experimental spectrum of the $J_{KaKc} = 1_{10} - 1_{01}$ transition of *ortho*$H_2 - O^{13}CS$, obtained with 2500 averaging cycles. The time domain signals were recorded at 10 ns sampling interval to obtain 8k data points. The data set was supplemented with 8k zeros before Fourier transformation. The lower intensity of this spectrum compared to the spectrum in Figure 3.1 (a) is the result of the smaller dipole moment along the *b*- compared to the *a*- axis in *ortho*H_2 – OCS. Because of the low intensity, only one Doppler component was resolved and used in the fitting procedure.

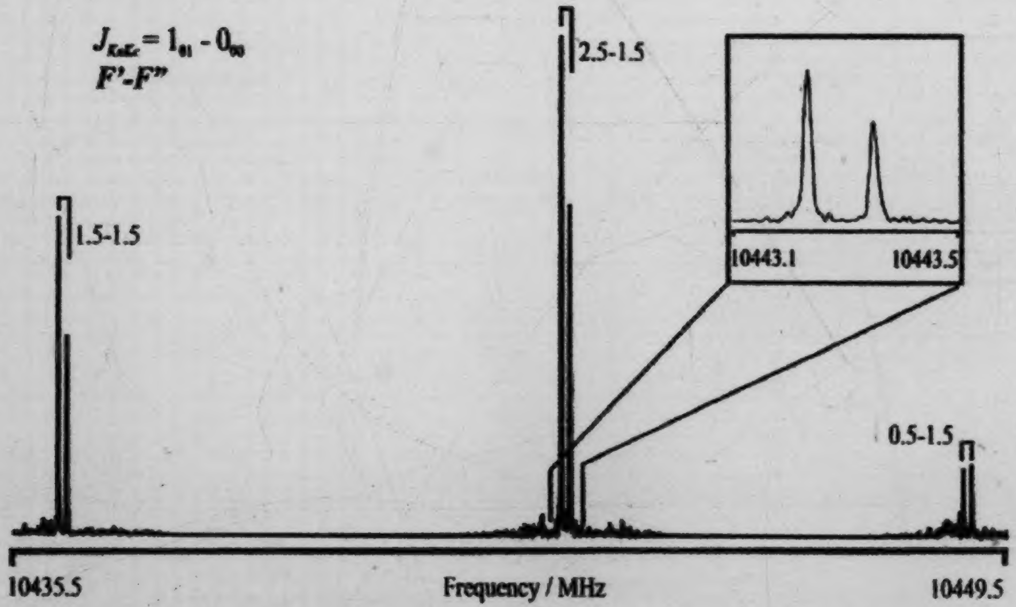

Figure 3.3: Experimental composite spectrum of the $J_{KaKc} = 1_{01} - 0_{00}$ transition of *para*$H_2 - O^{13}C^{33}S$, obtained with 500 averaging cycles. An enriched sample of $O^{13}CS$ was used to obtain these spectra. The inset shows an enlarged view of the strongest component of the hyperfine pattern. The time domain signals were recorded at 10 ns sampling interval to obtain 8k data points. The data set was supplemented with 8k zeros before Fourier transformation. The larger hyperfine splitting observed in this spectrum is the ^{33}S nuclear quadrupole hyperfine structure.

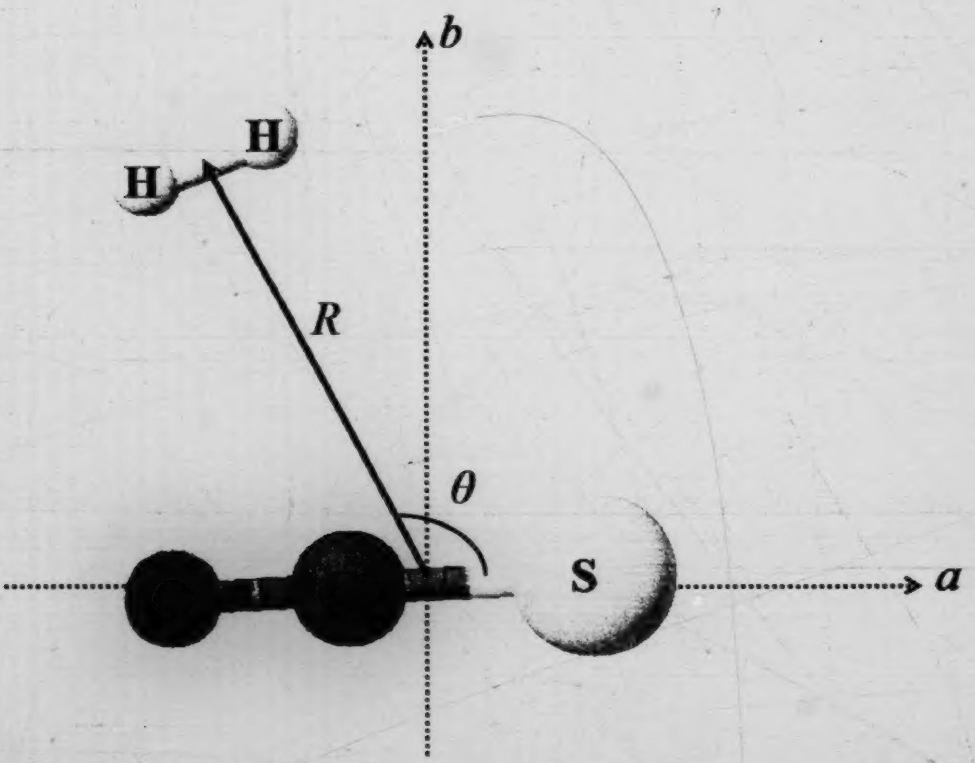

Figure 3.4: The T-shaped geometry of the hydrogen-OCS complex with the determined structural parameters marked. *R* is the van der Waals bond distance, θ is the angle between the OCS molecular axis and the ***R*** vector. The hydrogen moiety is considered a point mass in this study. The angle between the *a*-inertial axis and the OCS molecular axis is given by θ_a (not specifically shown in figure).

3.6 Tables

Table 3.1

Measured transition frequencies (in MHz) and quantum number assignments of isotopologues of the *ortho*H_2 – OCS dimer.

Transition (J'_{KaKc} – J''_{KaKc})	F'-F''	$o$$H_2$ – $O^{13}CS$	Δv[a] (kHz)	$o$$H_2$ – $OC^{34}S$	Δv (kHz)	$o$$H_2$ – $O^{13}C^{34}S$	Δv (kHz)
1_{01} - 0_{00}	1-1	10194.4766	4.3	9990.0419	3.3	9964.1133	7.4
	2-1	10194.5345	-6.5	9990.0994	-4.9	9964.1594	-12.1
	0-1	10194.6530	2.1	9990.2112	1.6	9964.2816	4.7
2_{02} - 1_{01}	3-2	20338.5171	0.5	19933.9271	-0.6	19882.3843	-0.5
	1-2	20338.5624	-1.1			19882.4305	0.5
	1-1	20338.6342	2.0	19934.0391	0.6		
2_{11} - 1_{10}	3-2	21494.8507	-6.7	21041.8079	0.1		
	1-1	21494.9022	-4.2	21041.8601	0.2		
	2-1	21494.9907	9.6				
1_{10} - 1_{01}	2-2	18368.2595	-1.4				
2_{11} - 2_{02}	3-3	19524.6031	1.4				
2_{12} - 1_{11}	3-2	19261.3056	11.4				
	1-1	19261.3484	-5.0				
	2-1	19261.4096	-6.5				
1_{11} - 0_{00}	2-1	27447.176[b]	1.9				

[a] $\Delta v = v_{ob.} - v_{calc}$

[b] Frequency obtained from double resonance experiment, uncertainty of ± 5 kHz.

Table 3.2

Measured transition frequencies (in MHz) with quantum number assignments and spectroscopic constants (in MHz) for *ortho*H_2 – $OC^{33}S$ and *ortho*H_2 – $O^{13}C^{33}S$ dimers.

Transition (J'_{KaKc} – J''_{KaKc})	F_1'-F_1'', F'-F''	$oH_2 - OC^{33}S$	$\Delta\nu$[a] (kHz)	$oH_2 - O^{13}C^{33}S$	$\Delta\nu$ (kHz)
1_{01} - 0_{00}	1.5-1.5, 0.5-0.5	10095.1445	4.1	10070.3059	5.7
	1.5-1.5, 2.5-2.5	10095.1643	-5.5	10070.3333	6.2
	1.5-1.5, 1.5-1.5	10095.2093	0.5	10070.3510	-11.8
	2.5-2.5, 2.5-1.5	10102.2965	-0.1	10077.4481	-10.8
	2.5-2.5, 3.5-2.5	10102.3358	0.5	10077.4939	-0.3
	2.5-2.5, 1.5-0.5	10102.3570	1.8	10077.5236	10.9
	0.5-1.5, 1.5-2.5	10108.0469	-1.2	10083.2104	0.1
2_{02} - 1_{01}	3.5-2.5, 3.5-2.5	20153.9595	-3.4		
	3.5-2.5, 4.5-3.5	20153.9778	3.4		
$S_{aa}(H_1\text{-}H_2)$		-0.1008(15)[b]		-0.0926(15)	
$S_{bb}(H_1\text{-}H_2)$		-0.00947[c]		-0.00947[c]	
$C_{aa}(H)$		0.38935[c]		0.38935[c]	
$C_{bb}(H)$		-0.00226[c]		-0.00226[c]	
$\chi_{aa}(^{33}S)$		-28.5973(23)		-28.6100(23)	
$\chi_{aa}(^{33}S)$[d]		-28.7			
θ_a[d](°)[e]		6.3		6.2	

[a] $\Delta\nu = \nu_{ob.} - \nu_{calc}$.

[b] Numbers in parenthesis are one standard deviation in units of the last significant figure.

[c] Fixed to value obtained for $oH_2 - O^{13}CS$.

[d] Reference 12.

[e] Obtained from the ^{33}S nuclear quadrupole coupling constant; see the text for detail.

Table 3.3

Measured transition frequencies (in MHz) of isotopologues of the *para*H_2 – OCS dimer.

Transition	$pH_2 - O^{13}CS$	$\Delta\nu$[a] (kHz)	$pH_2 - OC^{34}S$	$\Delta\nu$ (kHz)	$pH_2 - O^{13}C^{34}S$	$\Delta\nu$ (kHz)
1_{01} - 0_{00}	10569.7511	0.0	10349.3554	0.0[b]	10321.2067	0.0[b]
2_{02} - 1_{01}	21056.9903	-4.5	20623.3895	0.0	20567.7256	0.0
2_{11} - 1_{10}	22488.9257	2.0				
2_{12} - 1_{11}	19744.8145	2.5				

[a] $\Delta\nu = \nu_{ob.} - \nu_{calc}$.

[b] Two parameters, $(B+C)/2$ and Δ_J, were calculated from the two transition frequencies.

Table 3.4

Measured transition frequencies (in MHz) and spectroscopic constants (in MHz) for *para*$H_2 - OC^{33}S$ and *para*$H_2 - O^{13}C^{33}S$ dimers.

Transition	F"-F'	$pH_2 - OC^{33}S$	Δv^a (kHz)	$pH_2 - O^{13}C^{33}S$	Δv (kHz)
1_{01} - 0_{00}	1.5 – 1.5	10463.1822	-1.0	10436.1671	-0.9
	2.5 – 1.5	10470.2921	2.2	10443.2831	2.0
	0.5 – 1.5	10475.9753	-1.2	10448.9719	-1.1
$\chi_{aa}(^{33}S)$		-28.4289(31)[b]		-28.4548(31)	
θ_a^c		7.2		7.1	

[a] $\Delta v = v_{ob.} - v_{calc}$.

[b] Numbers in parenthesis are one standard deviation in units of the last significant figure.

[c] Obtained from the ^{33}S nuclear quadrupole coupling constant; see the text for detail.

Table 3.5

Spectroscopic constants (in MHz) of isotopologues of the *ortho*H_2 – OCS dimer.

	$oH_2 - O^{13}CS$	$oH_2 - OC^{34}S$	$oH_2 - O^{13}C^{34}S$
A	22921.46321(137)[a]	22918.17[b]	22906.63[b]
B	5661.29039(47)	5536.97486(71)	5521.74840(45)
C	4533.10401(47)	4452.95185(71)	4442.29[c]
Δ_J	-0.034377(52)	-0.034435(55)	-0.030754(56)
Δ_{JK}	2.923493(191)	2.934[d]	2.934[d]
Δ_K	8.145[d]	8.145[d]	8.145[d]
φ_J	-0.00017[d]	-0.00017[d]	-0.00017[d]
φ_{JK}	-0.001[d]	-0.001[d]	-0.001[d]
δ_J	-0.047805(213)	0.0177[d]	0.0177[d]
δ_K	3.235[d]	3.235[d]	3.235[d]
$S_{aa}(H_1\text{-}H_2)$	-0.1216(11)	-0.1180(79)	-0.1180(91)
$S_{bb}(H_1\text{-}H_2)$	-0.00947(12)	-0.00947[e]	-0.00947[e]
$C_{aa}(H)$	0.38935(231)	0.4047(85)	0.38935[c]
$C_{bb}(H)$	-0.00226(42)	-0.00226[e]	-0.00226[e]
Δ_0 (amu Å^2)	0.169	0.167	
#trans	7	3	2
rms (kHz)	5.3	2.3	6.7

[a] Numbers in parenthesis are one standard deviation in units of the last significant figure.

[b] The *A* rotational constant was fixed to a value obtained by reduced mass scaling of the *A* constant of the main isotopologue.[4]

[c] Fixed to the ratio of *B*/*C* rotational constants obtained from other isotopologues.

[d] Fixed at value of main isotopologue (Reference 4).

[e] Fixed at value obtained from the *ortho*$H_2 - O^{13}CS$ isotopologue.

Table 3.6

Spectroscopic constants (in MHz) of isotopologues of the *para*H_2 – OCS dimer.

	$pH_2 - O^{13}CS$	$pH_2 - OC^{34}S$	$pH_2 - O^{13}C^{34}S$
A	22372.961[a]	22378.36[b]	22367.14[b]
B	5978.19843(75)[c]		
C	4591.76816(76)		
$(B+C)/2$		5180.9507[d]	5166.8236[d]
Δ_J	0.053914(87)	3.1362[d]	3.1098[d]
Δ_{JK}	5.352[e]	5.352[e]	5.352[e]
Δ_K	9.161[e]	9.161[e]	9.161[e]
φ_J	0.000022[e]	0.000022[e]	0.000022[e]
φ_{JK}	0.00198[e]	0.00198[e]	0.00198[e]
δ_J	0.0177[e]	0.0177[e]	0.0177[e]
δ_K	3.452[e]	3.452[e]	3.452[e]
Δ_0 (amu Å^2)	2.94		
#trans	4	2	2
rms (kHz)	2.8		

[a] A rotational constant fixed to the value producing the best fit; see the text for details.

[b] The A rotational constant was fixed to a value obtained by reduced mass scaling of the A constant of the main isotopologue.[4]

[c] Numbers in parenthesis are one standard deviation in units of the last significant figure.

[d] Two parameters, $(B+C)/2$ and Δ_J, were calculated from the two transition frequencies.

[e] Fixed at value of the main isotopologue (Reference 4).

Table 3.7

Experimental structural parameters for *ortho*H_2 – OCS, *para*H_2 – OCS, and He – OCS van der Waals complexes.

	R(Å)	θ(°)[a]
pH_2 – OCS[b]	3.587	105.3
pH_2 – OCS[c]	3.69	103.0
oH_2 – OCS[b]	3.804	113.7
oH_2 - OCS[c]	3.78	113.0
He - OCS[d]	3.82	109.2

[a] Angle defined as the obtuse angle between the molecular axis of OCS and the R vector (π(sulfur atom – centre of mass of OCS – R vector)).

[b] r_s geometry obtained from all isotopologues studied, including the main isotopologue from Reference 4.

[c] Structural parameters from Reference 4.

[d] Reference 9.

3.7 References

[1] T. J. Balle and W. H. Flygare, *Rev. Sci. Instrum.* **52** (1), 33 (1981).

[2] V. N. Markov, Y. Xu, and W. Jäger, *Rev. Sci. Instrum.* **69** (12), 4061 (1998).

[3] U. Wötzel, W. Stahl, and H. Mäder, *Can. J. Phys.* **75** (11), 821 (1997).

[4] Z. H. Yu, K. J. Higgins, W. Klemperer, M. C. McCarthy, P. Thaddeus, K. Liao, and W. Jäger, *J. Chem. Phys.* **127**, 054305 (2007).

[5] B. Maté, F. Thibault, G. Tejeda, J. M. Fernández, and S. Montero, *J. Chem. Phys.* **122** (6), 064313 (2005).

[6] G. Tejeda, J. M. Fernández, S. Montero, D. Blume, and J. P. Toennies, *Phys. Rev. Lett.* **92** (22), 223401 (2004).

[7] H. M. Pickett, *J. Mol. Spectrosc.* **148** (2), 371 (1991).

[8] J. K. G. Watson, *J. Chem. Phys.* **48** (10), 4517 (1968).

[9] K. Higgins and W. Klemperer, *J. Chem. Phys.* **110** (3), 1383 (1999).

[10] N. Heineking and M. C. L. Gerry, *J. Mol. Spectrosc.* **158**, 62 (1993).

[11] H. S. P. Müller and M. C. L. Gerry, *J. Chem. Phys.* **103** (2), 577 (1995).

[12] Z. H. Yu, K. J. Higgins, W. Klemperer, M. C. McCarthy, and P. Thaddeus, *J. Chem. Phys.* **123** (22), 221106 (2005).

[13] N. F. Ramsey, *Molecular Beams*. (Oxford University Press, London, 1953).

[14] N. F. Ramsey, *Phys. Rev.* **85** (1), 60 (1952).

[15] J. M. Reinartz and A. Dymanus, *Chem. Phys. Lett.* **24** (3), 346 (1974).

[16] J. Kraitchman, *Am. J. Phys.* **21** (1), 17 (1953).

[17] C. C. Costain, *J. Chem. Phys.* **29** (4), 864 (1958).

[18] V. Typke, *J. Mol. Spectrosc.* **69** (2), 173 (1978).

[19] V. Typke, *J. Mol. Spectrosc.* **72** (2), 293 (1978).

Chapter 4

Spectroscopic and theoretical study of the weakly bound H_2 – HCCCN dimer

Previous studies of the He – HCCCN complex motivated the extension to H_2 - HCCCN complexes. The He – HCCCN dimer was studied using rotational spectroscopy and *ab initio* calculations.[1] Cyanoacetylene (HCCCN) has desirable qualities for a chromophore for these studies, such as the large dipole moment and the linear geometry of the rotor.

In this thesis, the weakly bound H_2 – HCCCN complex was studied by high-resolution microwave spectroscopy and by calculations of intermolecular potential energy surfaces. The rotational spectra of H_2 – HCCCN were observed with the pulsed-nozzle Fourier transform microwave spectrometer described in Chapter 2. Spectra of isotopologues of cyanoacetylene were measured ($HCCC^{15}N$, DCCCN and various ^{13}C containing isotopologues) in complexes with the two spin isomers of the H_2 molecule (*para*H_2 and *ortho*H_2). Transitions of complexes with HCCCN isotopologues containing ^{14}N and D nuclei were split by nuclear quadrupole hyperfine interactions, which were measured and analyzed. The *ortho*H_2 molecule containing complexes showed additional hyperfine structures due to nuclear magnetic spin-spin coupling of the hydrogen nuclei in the H_2 molecule, as was observed in H_2 – OCS dimers.[2,3] For *ortho*H_2 – HCCCN, both strong *a*- and weaker *b*-type transitions were measured and analyzed using a semi-rigid asymmetric rotor model. For the *para*H_2 – HCCCN complex, only *a*-type transitions with $K = 0$ were measured and analyzed. The dimer complexes are floppy and have a near T-shaped structure.

The intermolecular potential energy surfaces were calculated using the coupled-cluster method with single and double excitations and noniterative inclusion of triple excitations [CCSD(T)]. Three orientations of the hydrogen molecule with respect to the HCCCN molecular axis were considered. Bound-state rotational energy levels supported by the surfaces were determined for the different orientations as well as for an averaged surface. The quality of a potential energy surface can be assessed by comparing the experimentally measured transition frequencies with the transitions between the bound-state energy levels supported by the potential. Simple scaling of the surfaces improved the agreement with the experimental results.

4.1 Experimental details

The experimental details for the spectroscopic study of H_2 – HCCCN are quite similar to those of the H_2 – OCS studies.[2-4] There are some differences that will be discussed in more detail. Firstly, the synthesis of cyanoacetylene will be presented; it was performed independently by a former Ph.D. student in our laboratory.[1,5] Secondly, a discussion about the backconversion of *para*H_2 enrichment observed with HCCCN with a traditional gas mixture preparation will be presented. The new sample preparation method to limit backconversion will be presented. The spectrometer details are given in Chapter 2.

4.1.1 Synthesis of cyanoacetylene

Due to the reactive and poisonous nature of cyanoacetylene (HCCCN), it is no longer commercially available in North America. Cyanoacetylene has its boiling point at

5°C and polymerizes quickly at room temperature. The synthesis used in our laboratory follows the method of Moreau and Bongrand,[6] as modified by Miller and Lemmon.[7] The synthesis presented here is a summary of the total reaction scheme which has been presented in another thesis from our group.[5] In the first of the two steps, propiolamide is formed by adding methyl propiolate (Sigma-Aldrich Co.) to liquefied ammonia. The excess ammonia and alcohol side products were removed *in vacuo*. The propiolamide was then mixed with phosphorus oxide and sand (used for heat transfer) and heated to 200°C for a minimum of two hours. A liquid N_2 cooled cold trap was used to collect the resulting cyanoacetylene. Overall, the reaction scheme is:

$$H-C\equiv C-COOCH_3 \xrightarrow{NH_3(\ell)} H-C\equiv CONH_2 \xrightarrow{P_2O_5,\Delta} H-C\equiv C-C\equiv N. \quad [4.1]$$

The HCCCN, once trapped, can be stored for over two years at -35 °C without observable degradation.

The synthesis of isotopologues of cyanoacetylene can be done conveniently with the above reaction scheme. The deuterated cyanoacetylene (DCCCN) can be synthesized by modifying the reaction scheme [4.1] as reported by Mallinson and Fayt.[8] The propiolamide was dissolved in 25 mL of 99.77% D_2O (Columbia Organic Chemicals, Co. Inc.) and stirred for three days. After pumping off the D_2O, a second aliquot of 25 mL of D_2O was added and the mixture was stirred for an additional three days. After pumping off the D_2O again, the reaction proceeded as in [4.1]. The modified scheme produced highly pure DCCCN free of residual D_2O.

The ^{15}N enriched cyanoacetylene (HCCC^{15}N) utilized the reaction scheme [4.1] while using isotopically enriched NH_3 (10% $^{15}NH_3$, Cambridge Isotope Laboratories, Inc.). Through this method, a sample of cyanoacetylene enriched to 10% HCCC^{15}N was obtained.

4.1.2 *Para*H_2 enrichment

Initially, *para*H_2 enriched samples were prepared using the same procedure as in the H_2 – OCS studies. The gas sample was prepared by adding the chromophore gas to the sample cylinder followed by enriched *para*H_2 gas taken directly from the converter. The sample container was closed while the converter was emptied of remaining hydrogen through the forepump. The gas sample was then completed by the addition of helium gas to the desired pressure (3 – 8 atm). During this process, the *para*H_2 enriched gas interacted with the chromophore gas for several minutes (up to >10 minutes) prior to being diluted by helium. When this procedure was done with the HCCCN chromophore, the signal enhancement seen for the *para*H_2 – HCCCN transition was not as strong as expected from the OCS studies.[2,3] Even after preparing an enriched sample several times in hopes that the poor signal intensity was due to impurities in the sample system, the signal of the *para*H_2 – HCCCN transition did not increase as substantially as expected. The difference in the signal enhancement observed for both chromophores could be due to the nuclear spins of the main isotopologues and the interaction of the nuclear spin with the hydrogen molecules. The main isotopologue of carbonyl sulfide, $^{16}O^{12}C^{34}S$ (93.7% naturally abundant), has no nucleus with a non-zero nuclear spin, while the main isotopologue of $^{1}H^{12}C^{12}C^{12}C^{14}N$ (96.5% naturally abundant) contains a ^{14}N nucleus with a non-zero nuclear spin, $I(^{14}N) = 1$. The non-zero nuclear spin produces an inhomogeneous magnetic field which could backconvert the enriched *para*H_2 to *ortho*H_2 molecules.[9] Previous studies have been performed with chromophores with nuclear spins in the infrared region.[10,11] These studies used a high pressure sample containing the trace amount of chromophore gas in helium which was then added to a sample cylinder containing enriched *para*H_2 gas. An important aspect to this sample preparation method is that the chromophore and the enriched *para*H_2 gas are also in presence of an excess of helium. In the H_2 – HCCCN studies, substantial signal enhancement was achieved when a sample of trace HCCCN in high pressure helium was added to a gas cylinder containing the enriched *para*H_2 gas. Dilution with helium limits the interaction between the enriched *para*H_2 and HCCCN gases. Another experiment was required to confirm that the helium dilution helped maintain the enrichment from the catalytic converter. A sample of enriched *para*H_2 gas diluted in helium (10% enriched *para*H_2 in 90% helium) was added to a sample cylinder with the appropriate concentration of HCCCN. The gas sample was then quickly diluted with additional helium to the desired final pressure. This produces a signal enhancement comparable to that seen with H_2 – OCS dimers.

Cyanoacetylene has a ^{14}N nucleus with a nuclear spin of 1, which creates an inhomogeneous magnetic field around the molecule. The interaction of HCCCN with *para*H_2 molecule induces the backconversion to *ortho*H_2 through this inhomogeneous magnetic field. This is supported by the necessity that a catalyst used for the low temperature conversion of *ortho*H_2 to *para*H_2 be paramagnetic and therefore produces a magnetic field gradient.[12-14] This is necessary to promote the singlet-triplet mixing which is required for conversion. Additionally, a collision with a paramagnetic molecule such as O_2 is efficient for the conversion between *ortho*H_2 and *para*H_2.[9] The interaction of a magnetic field gradient with a spin isomer has been shown to induce spin conversion and collisions can have a major effect on the conversion rate.[15-17]

For all studies with enriched *para*H_2 samples with cyanoacetylene, a sample of ~10 % enriched *para*H_2 in helium (up to ~50 atm) was prepared. The gas mixture was prepared by adding the cyanoacetylene into an empty cylinder, adding the appropriate amount of diluted *para*H_2/helium and filling to the final pressure quickly with high pressure helium. The samples of 10% *para*H_2 gas in helium were kept in a sealed stainless steel container for up to a week without significant backconversion as measured by the signal of the *para*H_2 – HCCCN transitions.

4.2 Experimental results and analyses

The gas mixture for initial searches contained low concentrations (< 0.3 %) of HCCCN, DCCCN or a 10% $HCCC^{15}N$/90% HCCCN mixture with 1-3% H_2 gas in a helium expansion. Since no previous studies provided predictions for rotational constants of H_2 – HCCCN, a prediction was obtained by calculating the fractional changes for the $J_{KaKc} = 1_{01} - 0_{00}$ transitions of He – OCS (Ref. 18) and H_2 – OCS (Ref. 2) complexes and assuming this change is approximately the same for HCCCN complexes. Within 20 MHz, a transition was measured which had additional hyperfine structure consistent with spin-spin coupling due to a *ortho*H_2 molecule and it was assigned to be the $J_{KaKc} = 1_{01} - 0_{00}$ transition. The spectrum of the $J_{KaKc} = 1_{01} - 0_{00}$ transition is shown in Figure 4.1. DR decoherence experiments[19] as described in Chapter 2 were used to obtain the frequencies of connected *a*- and *b*-type transitions.

The *b*-type transitions for *ortho*H_2 – HCCCN and *ortho*H_2 – $HCCC^{15}N$ were observed first using DR decoherence experiments[19] as described in Chapter 2. The $J_{KaKc} = 1_{01} - 0_{00}$ transition was monitored while the frequency of the pump microwave radiation was swept through the region where the $J_{KaKc} = 1_{11} - 0_{00}$ transition was expected. A weak DR effect was observed, even though the DR effect observed for the *a*-type transition was quite strong when monitoring the same transition. This is consistent with the DR effect being dependent on the transition dipole moment of the pump transition and in this complex, the *a*-axis dipole moment is much stronger than the *b*-axis one. The transition frequency for the $J_{KaKc} = 1_{10} - 1_{01}$ transition was also determined with a decoherence DR experiment. The *b*-type transitions were measured with much longer microwave excitation pulse widths (~ 3 μs as opposed to 0.4 μs for the $J_{KaKc} = 1_{01} - 0_{00}$ transition). Longer pulse widths in the experiment indicate a smaller dipole moment for the transition. Additionally, an amplifier was used in the experiment to increase the power of the radiation coupled into the cavity. Amplifiers are necessary for studying transitions associated with low dipole moments. The $J_{KaKc} = 1_{11} - 0_{00}$ transition of *ortho*H_2 – HCCCN is shown in Figure 4.2. The weaker intensity of the signal, as well as the difference in the ^{14}N nuclear quadrupole hyperfine structure when compared to Figure 4.1, substantiates the assignment.

The $|K| = 1$ energy levels for *ortho*H_2 – HCCCN complexes are high in energy (~ 25-30 GHz higher than the ground state) and may only be sparsely populated in our molecular expansion where rotational temperatures can be on the order of a few Kelvin.[20] The use of lower sample pressures can facilitate the observation of transitions from these stacks since the temperature of the expansion is slightly higher thus increasing the populations of higher lying energy levels. Many efforts were made with a helium expansion to observe either of the $J_{KaKc} = 2_{12} - 1_{11}$ and $J_{KaKc} = 2_{11} - 1_{10}$ transitions, but without success. A final attempt was made with a low pressure sample containing neon as backing gas. In the H_2 – OCS dimer studies,[2-4] a neon expansion produced stronger signals for *ortho*H_2 – OCS transitions. As explained in Reference 4, the binding energy of neon with OCS is larger than that of *para*H_2 with OCS. Therefore, the *para*H_2 – OCS signals are destroyed in a neon expansion. A sample consisting of neon (3-5 atm) with 1.5% H_2 gas and < 0.2 % HCCCN was used and the transitions were successfully measured. The spectrum of the $J_{KaKc} = 2_{12} - 1_{11}$ transition is shown in Figure 4.3. The predictions for the transitions were obtained from bound-state calculations using the non-scaled potential energy surface. The energy difference between the K stacks was calculated from the potential and the prediction was within 180 MHz. Discussions in more detail regarding the potential energy surfaces will be presented later in this chapter. DR experiments were used to determine the frequencies of the connected $J = 3 - 2$ transitions for the $|K| = 1$ stacks and the transitions were subsequently measured in single resonance experiments. To substantiate the assignment of the measured transitions, one can measure transitions that form closed-loops with other measured transitions. In the *ortho*H_2 – HCCCN complex, despite experimental attempts at measuring closed-loop transitions (i.e. $J_{KaKc} = 2_{11} - 2_{02}$), no such transitions were measured. The inability to measure these transitions could be due to the very weak intensity of *b*-type transitions in the complex as well as the expected low population of the energy levels in the molecular expansion. The transition frequencies and quantum number assignments for *ortho*H_2 – HCCCN are tabulated in Table 4.1. Transition frequencies of minor isotopologues of *ortho*H_2 – HCCCN were predicted by calculating the changes in moments of inertia with the change of an atom. The measured transition frequencies are in Tables 4.2, 4.3 and 4.4 for all minor isotopologues studied (HCCC^{15}N; DCCCN; and H^{13}CCCN, HC^{13}CCN, HCC^{13}CN, respectively).

In searches with a non-enriched H_2 sample, a transition ~180 MHz higher than the $J_{KaKc} = 1_{01} - 0_{00}$ of *ortho*H_2 – HCCCN was measured which showed hyperfine patterns consistent with nuclear quadrupole coupling of a ^{14}N nucleus. It was therefore assigned to be the $J_{KaKc} = 1_{01} - 0_{00}$ transition of *para*H_2 – HCCCN. The signal intensity of the transition was consistent with the 25% content of *para*H_2 molecules in a non-enriched hydrogen gas sample. The presence of *para*H_2 was confirmed when the new preparation method was used to prepare the gas sample with enriched *para*H_2 and significant signal enhancement was observed. DR experiments were used to obtain the frequencies of connected *a*-type transitions in the $|K| = 0$ stack. DR experiments were also attempted in hopes of locating *b*-type transitions of the complex. Despite repeated searches over a large frequency region where both $J_{KaKc} = 1_{11} - 0_{00}$ and $1_{10} - 1_{01}$ transitions are predicted (over 10 GHz), no DR effect was observed and no *b*-type transitions for *para*H_2 – HCCCN were measured. This is consistent with the experimental findings in the H_2 – OCS study where the *b*-type transitions could not be located for the *para*H_2 – $O^{13}CS$ complex due to a small dipole moment along the *b*-axis. Transition frequencies of minor isotopologues of *para*H_2 – HCCCN were predicted by calculating the changes in moments of inertia and were measured with an enriched *para*H_2 sample. The $J_{KaKc} = 1_{01} - 0_{00}$ transition of *para*H_2 – HCCCN is shown in Figure 4.4 and the additional hyperfine structure due to the *ortho*H_2 molecule can be seen when compared to Figure 4.1. The transition frequencies of *para*H_2 – HCCCN and minor isotopologues are presented in Tables 4.5 and 4.6, respectively.

The spectra of the *ortho*H_2 – HCCCN complex contained ^{14}N nuclear quadrupole and magnetic nuclear spin-spin hyperfine structures which needed to be accounted for in the spectral fitting procedure. The coupling scheme used was: $\mathbf{J} + \mathbf{I}_{14N} = \mathbf{F}_1$, $\mathbf{I}_{H(1)} + \mathbf{I}_{H(2)} = \mathbf{I}$, $\mathbf{F}_1 + \mathbf{I} = \mathbf{F}$ where $\mathbf{I}_{H(1)} + \mathbf{I}_{H(2)} = 1$ for *ortho*H_2 molecules. The global least-squares fitting program, SPFIT,[21] was used to obtain rotational constants and quartic and sextic centrifugal distortion constants using Watson's *A*-reduction Hamiltonian.[22] The isotopologues were all fit separately. The contributions of both the nuclear quadrupole coupling constant and magnetic nuclear spin-spin coupling constant along both the *a*- and *b*-inertial axes were fit. Additionally, a magnetic spin-rotation contribution along the *a*-inertial axis for the *ortho*H_2 molecule was fit. From the limited data of the various ^{13}C containing complexes, only the $(B+C)/2$ rotational constant, the ^{14}N nuclear quadrupole coupling constants, and the spin-spin coupling constant of *ortho*H_2 could be obtained. The analysis of *ortho*H_2 – $HCCC^{15}N$ is simplified since ^{15}N has no nuclear quadrupole interaction ($I(^{15}N) = ½$). The coupling scheme is thus $\mathbf{I}_{H(1)} + \mathbf{I}_{H(2)} = \mathbf{I}$, $\mathbf{J} + \mathbf{I} = \mathbf{F}$ and again $\mathbf{I}_{H(1)} + \mathbf{I}_{H(2)} = 1$ for *ortho*H_2 molecules. Deuterated cyanoacetylene complexes have an additional quadrupolar nucleus ($I(D) = 1$) and the resulting coupling scheme is $\mathbf{J} + \mathbf{I}_{14N} = \mathbf{F}_1$, $\mathbf{F}_1 + \mathbf{I}_D = \mathbf{F}_2$, $\mathbf{I}_{H(1)} + \mathbf{I}_{H(2)} = \mathbf{I}$, $\mathbf{F}_2 + \mathbf{I} = \mathbf{F}$, where, again, $\mathbf{I}_{H(1)} + \mathbf{I}_{H(2)} = 1$ for *ortho*H_2 molecules. The data set for the deuterated complex is smaller and the deuterium nuclear quadrupole coupling constant only along the *a*-inertial axis could be obtained. In addition, the spin-spin coupling constant for *ortho*H_2 was fixed to the value obtained in the main isotopologue. Due to the experimental difficulty in resolving all components of the hyperfine patterns in the deuterated complexes, the error in the deuterium nuclear quadrupole coupling constant may be larger than that indicated by the fitting results. The spectroscopic constants from the minor isotopologues with *ortho*H_2 are given in Tables 4.2, 4.3, and 4.4, respectively.

For *para*H_2 – HCCCN complex, no information about the *A* rotational constant could be obtained from the measured transitions. In the spectral analysis, the *A* rotational constant was fixed at the value obtained from the bound-state energy levels supported by the potential. This will be discussed in further detail in Section 4.5. The analysis of *para*H_2 – HCCCN complexes is simplified since transitions are split only by the ^{14}N nuclear quadrupole interaction. Since only $|K| = 0$ transitions were measured, only the nuclear quadrupole coupling constant along the *a*-inertial axis could be determined. The coupling scheme used was $\mathbf{J} + \mathbf{I}_{14N} = \mathbf{F}$. The same coupling scheme was used for the ^{13}C containing isotopologues. Spectra of the ^{15}N containing complex show no hyperfine splittings. The *para*H_2 - DCCCN complex has the additional nuclear quadrupole interaction of the deuterium nucleus and the coupling scheme used is $\mathbf{J} + \mathbf{I}_{14N} = \mathbf{F}_1$, $\mathbf{F}_1 + \mathbf{I}_D = \mathbf{F}$. Again, only the *a*-inertial axis component of the deuterium quadrupole coupling constant could be determined due to the limited data set. The spectroscopic constants for *para*H_2 – HCCCN and the minor isotopologues are provided in Tables 4.7 and 4.8, respectively.

4.3 Discussion of experimental results

The nuclear quadrupole coupling constants along the *a*- and *b*-inertial axes were determined for ^{14}N and D containing complexes. For *ortho*H_2 – HCCCN, the ^{14}N nuclear quadrupole coupling constant along the *a*-inertial axis ($\chi_{aa}(^{14}N) = -4.28682$ MHz) is similar to the value of *para*H_2 – HCCCN ($\chi_{aa}(^{14}N) = -4.30299$ MHz). The deuterium nuclear quadrupole coupling constants for *ortho*H_2 – DCCCN ($\chi_{aa}(D) = 0.27764$ MHz) and *para*H_2 – DCCCN ($\chi_{aa}(D) = 0.1893$ MHz) are also in marginal agreement. Deviations between the values could be due to the limited data set for *para*H_2 – DCCCN compared to *ortho*H_2 – DCCCN. This agreement between the complex with different spin isomers of hydrogen is expected from previous H_2 – $OC^{33}S$ studies[3] because of the weak nature of the van der Waals interaction and that the interaction comparing the different spin isomers of hydrogen should be fairly similar. From the data set measured for the *ortho*H_2 – HCCCN complex, the nuclear quadrupole coupling constant could be determined along the *b*-inertial axis, $\chi_{bb}(^{14}N)$ =2.11299 MHz. The ^{14}N nuclear quadrupole coupling constants of the hydrogen complexes are in reasonable agreement with the values obtained for the He – HCCCN complex ($\chi_{aa}(^{14}N) = -4.2409$ MHz; $\chi_{bb}(^{14}N) = 2.0747$ MHz).[1] Similar agreement is seen for the D nuclear quadrupole coupling constants in *ortho*H_2 – DCCCN ($\chi_{aa}(D) = 0.2764$ MHz) and He – DCCCN ($\chi_{aa}(D) = 0.209$ MHz).[1] The small discrepancies could be due to the limited data set for H_2 – DCCCN complexes compared to He – DCCCN where both χ_{aa} and χ_{bb} could be resolved. The ^{14}N nuclear quadrupole coupling constants of isolated HCCCN and DCCCN molecules are $\chi_o(^{14}N) = -4.31924(1)$ MHz (Ref. 23) and $\chi_o(^{14}N) = -4.316(3)$ MHz (Ref. 24), respectively, which are in moderate agreement with the χ_{aa} values of the H_2 – HCCCN and H_2 - DCCCN complexes. The D nuclear coupling constant of an isolated DCCCN molecule is $\chi_o(D) = 0.2288(55)$ MHz (Reference 24) which is in decent agreement with the H_2 – HCCCN complex. The remaining discrepancies between the nuclear quadrupole coupling constants are assumed to be due to a tilting of the cyanoacetylene molecular axis thus changing the projection onto the inertial axes as discussed in Chapter 2. From the ^{14}N nuclear quadrupole coupling constants (χ_{aa} and χ_{bb}) and equations [2.18] and [2.19], we can calculate an average angle θ_a between the *a*-inertial axis and the molecular axis of HCCCN. For *ortho*H_2 – HCCCN, the θ_a values obtained from χ_{aa} and χ_{bb} are 3.9° and 5.1°, respectively. For *ortho*H_2 – DCCCN, the θ_a value obtained from the χ_{aa} coupling constant is 5.7°. For *para*H_2 – HCCCN, the θ_a value obtained from χ_{aa} is 2.9°. For *para*H_2 – DCCCN, the angle, θ_a, is 2.9°. The values from analyses of both hydrogen complexes are in reasonable agreement and corroborate that the HCCCN molecular axis is nearly parallel with the *a*-inertial axis. The difference between the angles obtained from the ^{14}N and D coupling constants is due to the floppy nature of the complex and due to the larger error in determining the constants in the DCCCN complexes. The larger experimental uncertainties in D nuclear quadrupole coupling constants make it a poor choice for determining the angle (i.e. θ_a(*ortho*H_2 – DCCCN) = 15.8° and θ_a(*para*H_2 – DCCCN) = 18.0°). The angles obtained from the same analysis in He – HCCCN are slightly larger (~6°) (Ref. 1) than the angles obtained for H_2 – HCCCN complexes which is consistent with the larger mass of helium causing the cyanoacetylene molecular axis to tilt further from the *a*-inertial axis.

Both proton-proton spin-spin and proton spin-rotation interactions were included in the fitting procedures to account for the hyperfine structure introduced by the presence of the hydrogen molecule in *ortho*H_2 – HCCCN. In this thesis, the expression used for the spin-spin interaction energy of two equivalent nuclei with spin angular momentum quantum number *I* is given in equations [2.20] and [2.21].[25] Again, the sign of the spin-spin coupling constant is chosen such that it is negative for homodiatomic molecules.[26] The measured $|K| = 1$ transitions required the inclusion of the S_{bb} spin-spin coupling constant, in addition to S_{aa}, in the fitting procedure. For the main *ortho*H_2 – HCCCN isotopologue, values of S_{aa}(*ortho*H_2 – HCCCN) = -45.6 kHz and S_{bb}(*ortho*H_2 – HCCCN) = 10.8 kHz were obtained. The spin-spin coupling constants obtained for different isotopologues of HCCCN (see Tables 4.2, 4.3, 4.4 and 4.5) agree well; this is expected since the isotopologues of HCCCN should not have a significant effect on the geometry of the H_2 moiety. In the study of the free *ortho*H_2 molecule, Ramsey's nuclear hyperfine Hamiltonian was used to fit the spin-spin hyperfine splittings.[27] The value obtained in that work corresponds to negative one-fifth of the conventionally used spin-spin coupling constant in microwave spectroscopy.[28] A comparison of the spin-spin coupling constants of the *ortho*H_2 – HCCCN dimers with that of free *ortho*H_2 ($-5D_a = -288.4$ kHz)[27] shows that the values are slightly smaller for the *ortho*H_2 – HCCCN complexes. The spin-spin coupling constant is determined mainly by the distance between the spins in question, which would be relatively unchanged by the van der Waals bond with HCCCN. One consideration for the difference in the values between the complex and the free *ortho*H_2 molecule is the orientation dependence of the tensor spin-spin coupling constant, as is shown by the necessity to include S_{bb} in the spectroscopic fit.

The spin-spin coupling constant of *ortho*H_2 molecule containing dimers can be compared as well. The constants of the *ortho*H_2 – $O^{13}CS$ isotopologues [S_{aa}(*ortho*H_2 – $O^{13}CS$) = -121.6 kHz and S_{bb}(12)(*ortho*H_2 – $O^{13}CS$) = -9.5 kHz][3] have slightly larger values than the constants obtained for the *ortho*H_2 – HCCCN complex. The discrepancy between the values could be due to a slightly different orientation of the *ortho*H_2 molecule in complexes with different dopant molecules. The S_{bb} spin-spin coupling constant is of opposite sign in the *ortho*H_2 – HCCCN dimer compared to *ortho*H_2 – $O^{13}CS$. The differences in the spin-spin coupling constants along the *b*-axis could also be due to a different orientation of the *ortho*H_2 molecule in the complex.

The values of the spin-rotation coupling constants obtained for different isotopologues are all of the same magnitude (C_{aa}(*ortho*H_2 – HCCCN) = -44.5 kHz). The limited data set of less abundant isotopologues may be the cause for slight variations in value. The spin-rotation coupling constant obtained for free *ortho*H_2 is C_{aa} = 113.8 kHz,[27] in marginal agreement with the values obtained for *ortho*H_2 – HCCCN in this report. As mentioned in Chapter 2, it is difficult to extract information about the electronic structure of the complex from the spin-rotation coupling constant because it is a second order interaction.[29,30]

The floppy nature of the *ortho*H_2 – HCCCN complex is demonstrated by the need to use six centrifugal distortion constants to fit the spectrum. The centrifugal distortion constants are of similar magnitude for the various isotopologues. The discrepancies are difficult to interpret due to the limited data sets for the minor isotopologues, as well as there being a mass-dependence of the centrifugal distortion constants.[30] The remainder of the discussion of centrifugal distortion constants will focus on the main HCCCN isotopologues. In *ortho*H_2 – HCCCN, of particular note is the negative sign of the Δ_J centrifugal distortion constant (Δ_J (*ortho*H_2 – HCCCN) = -0.1688 MHz); this could be the result of a Coriolis interaction with a low-lying excited state, similar to what was observed in the study of the *ortho*H_2 – OCS complex.[2,3] The magnitude of the Δ_J constant in the *ortho*H_2 – HCCCN complex cannot be easily interpreted because of the Coriolis effect. On the other hand, the centrifugal distortion constant Δ_J for *para*H_2 – HCCCN (Δ_J= 1.749 MHz) is quite large and is consistently large for all *para*H_2 - HCCCN isotopologues. The centrifugal distortion constant is obtained from an asymmetric semi-rigid rotor analysis of the spectrum by fixing the *A* rotational constant to the value obtained from the analysis of the bound-states supported by the potential energy surface. The large values for the Δ_J constant are consistent with large amplitude radial motions being present in the *para*H_2 – HCCCN complex. It is expected that the large amplitude radial motions are also present in *ortho*H_2 – HCCCN complexes, but this cannot be illustrated from the observed centrifugal distortion constant due to the Coriolis coupling which causes the negative Δ_J constant.

Another parameter that indicates the rigidity of a complex is the inertial defect, $\Delta_0 = I_c^0 - I_a^0 - I_b^0$, as described in Section 2.6, which is also included in Tables 4.6 and 4.7. The non-zero planar moments of *ortho*H_2 – HCCCN are mainly a result of the out-of-plane distribution of the H_2 molecule and large amplitude out-of-plane zero-point vibrational motions.[29,30] This is consistent with the analysis of the inertia defects determined from the analysis of the H_2 – OCS complexes.[2,3] Since the planar moments are primarily due to the hydrogen molecules, they should therefore not change significantly with isotopic substitution of HCCCN which can be seen by the reasonable agreement of the values from *ortho*H_2 – HCCCN (Δ_0 = 4.69 amu Å^2) and *ortho*H_2 - HCCC^{15}N (Δ_0 = 4.72 amu Å^2). Any discrepancy could be a result of the limited data set of *ortho*H_2 – HCCC^{15}N where no $|K| = 1$ *a*-type transitions were measured. The inertial defect for *para*H_2 –HCCCN cannot be determined for the experimental data since it is limited to *a*-type transitions in the $|K| = 0$ stack and only $(B+C)/2$ rotational constant could be resolved. The measurement of more transitions for the *para*H_2 – HCCCN complex would resolve more rotational constants and allow for a determination of the inertial defect. The relative rigidity of the complexes should follow the result of the H_2 – OCS study (Δ_0(*ortho*H_2 - OCS) = 0.165 amu Å^2; Δ_0(*para*H_2 – OCS) = 2.94 amu Å^2).[3]

Comparing the results of *ortho*H_2 complexes with different chromophore molecules, the HCCCN complexes are less rigid than the OCS complexes. This is again consistent with the results from the He – molecule studies.[1] The inertial defects in H_2 – HCCCN are much smaller than the values for He – HCCCN ((Δ_0 = 14.41 amu Å^2) (Reference 1) indicating that the hydrogen complexes are more rigidly bound than the He complexes. In fact, the hydrogen inertial defects are closer to those of the heavier rare gas atom dimers with HCCCN (Δ_0(Ne - HCCCN)[31] = 5.62 amu Å^2; Δ_0(Ar - HCCCN)[32] = 3.66 amu Å^2).

As discussed in Section 2.6, it is possible to calculate average geometries of the *ortho*H_2 – HCCCN and *para*H_2 – HCCCN van der Waals complexes from the experimental rotational constants. Figure 4.5 shows the definition of the structural parameters being determined. As described in Chapter 3, from the isotopic data we can obtain a r_s structure. The iterative program, MWSTR1, developed by Typke[33,34] was used in this report. The geometries obtained for *ortho*H_2 – HCCCN and *para*H_2 – HCCCN are shown in Table 4.10 along with the values obtained for He – HCCCN.[1] The shorter bond lengths in the H_2 – HCCCN complexes compared to the He – HCCCN complex are consistent with larger binding energies of the former. The calculated angle between the H_2 molecule and the HCCCN intermolecular axis depends sensitively on the *A* rotational constant of the complex. The *A* rotational constant could spectroscopically be determined only in the *ortho*H_2 – HCCCN and *ortho*H_2 – HCCC^{15}N dimers. In the structure determination of the *para*H_2 – HCCCN complex, the *A* rotational constant was taken from the analysis of the bound-state rotational energy levels supported by the calculated potential. Therefore, the angle obtained in the r_s structure of the *para*H_2 – HCCCN dimer should be considered less accurate than the *ortho*H_2 – HCCCN value.

4.4 Construction of potential energy surfaces

The construction of the potential energy surfaces follows the method successfully used with He – molecule complexes, such as He – HCCCN,[1] as well as with the H_2 – OCS complex.[35] The calculations were done on the CCSD(T)[36] level of theory with large basis sets and bond functions.[37] This is an established technique for the determination of the interaction energies of weakly bound systems.[38,39] Following the He – HCCCN potential energy calculations[1] and previous success by Dunning and co-workers, the augmented correlation-consistent (aug-cc)[40] basis sets were used. In this case, as in the He – HCCCN potentials, I used $3s3p2d1f1g$ bond functions with α coefficients (*sp* 0.9, 0.3, 0.1; *d* 0.3, 0.2; *fg* 0.3)[37,39] for the computation of the H_2 – HCCCN surfaces. These coefficients were chosen from the ab initio studies of the He – HCCCN[1] and Ne- and Ar-cyclopropane dimers, which resulted in potentials with microwave accuracy.[41]

The bond functions were located midway between the centres-of-mass of the hydrogen molecule and the HCCCN molecule. To be consistent with the He – HCCCN potential energy surface calculations,[1] the HCCCN structure was frozen at the equilibrium values from the calculation (CCSD(T), aug-cc-pVQZ) (*r*(H-C) = 1.0736 Å, *r*(C≡C) = 1.2094 Å, *r*(C-C) = 1.3810 Å, and *r*(C≡N) = 1.1637 Å).[1] The discrepancy between the equilibrium values and the ground-state effective structure of HCCCN[42] is on the order of 0.6% over the entire length. The discrepancy is insignificant compared to the frozen geometry approximation. The bond length of the hydrogen molecule was frozen at its ground state value, *r*(H-H) = 0.7414 Å.[43] This is consistent with the procedure in the CCSD(T) potential energy calculations of the H_2 – OCS dimer.[35] The supermolecule, single-point interaction energies were calculated using the MOLPRO 2002.6 package.[44] The basis set superposition error was corrected using the full counterpoise correction technique of Boys and Bernardi.[45]

In the related He – HCCCN complex,[1] the helium atom is spherical and a planar complex is obtained. The orientation of the hydrogen molecule, on the other hand, is described by two angles, α, and ϕ, with respect to the HCCCN molecule. The position of the hydrogen molecule is described by two parameters: the distance (R) between the centre of mass of the hydrogen and the HCCCN molecule and the angle (θ) between the HCCCN molecular axis and the vector **R**. Since the experimental orientation of the hydrogen subunit is unknown in the complexes, three potential energy surfaces with various orientations of the hydrogen molecule were calculated to help estimate any rotation of the H_2 subunit. The orientations and the description of the angles are shown in Figure 4.6. The orientations are described when the complex is T-shaped ($\theta = 90°$) and are named parallel, perpendicular, and out-of-plane orientations, following the study of H_2 - OCS.[35,46] The parallel orientation corresponds to $\phi = 0°$ and $\alpha = 90°$. The perpendicular orientation is at $\phi = 0°$ and $\alpha = 0°$. The out-of-plane orientation is when $\phi = 90°$ and $\alpha = 90°$. Single-point energies of the H_2 – HCCCN complex were calculated on a grid of points describing the relative positions of the hydrogen molecule and the HCCCN molecule. Calculations were done on three different grids (one for each hydrogen molecule orientation). The van der Waals bond between the centres-of-mass of the hydrogen moiety and the cyanoacetylene molecule was varied between 2.5 and 13 Å. The step size was varied between 0.25 and 1 Å depending on the steepness of the potential. Near the minima, a smaller step size was used, while long range effects were captured by 1 Å steps. The angle between the vector **R** and the HCCCN molecular axis (θ) ranged between 2° and 167°, in 11° steps. An angle of 0° corresponds to a linear configuration with the hydrogen molecule located at the N end of the cyanoacetylene molecule. In total, the potential energy surfaces corresponding to the three hydrogen orientations of H_2 – HCCCN were each composed of 400 single energy points. Rotational spectroscopy experiments of the dimer complex probe portions of the potential near the global minimum. The dense grid of the calculated potential allows for the possible determination of properties of larger $(H_2)_N$ – HCCCN clusters since clusters can probe other regions of the potential energy surface.

The energies of the surfaces could not be calculated at points located at shorter distances and near linear configurations (2°, 13°, 167°) because of the overlap of the hydrogen and the HCCCN molecules. It was ensured that the first point calculated was on the repulsive wall of the potential energy surface, above 0 cm^{-1}. For the configuration with $\theta = 178°$, it was not possible to calculate a first point on the repulsive wall without having a problem of convergence in the calculation, therefore the points on the potential energy surface end at 167°. All single point energies for the parallel, perpendicular and out-of-plane orientations are given in Appendix A.1 – A.3, respectively. Additionally, an averaged potential, where each orientation is given equal weight is tabulated in Appendix A.4.

Table 4.11 summarizes the main topological features of the potential energy surfaces calculated as a part of this thesis. The three orientations have varying features. The potential for the parallel orientation has a global minimum (E = -156.94 cm^{-1} at R =

3.30 Å and $\theta = 76.3°$) occurring at an approximately T-shaped configuration with a secondary minimum (E = -125.57 cm^{-1} at R = 5.45 Å and $\theta = 167°$) corresponding to a near linear H_2 – HCCCN configuration separated by a lower saddle point (E = -125.57 cm^{-1} at R = 4.65 Å and $\theta = 131.3°$) and an upper saddle point (E = -11.39 cm^{-1} at R = 5.56 Å and $\theta = 2°$). The potential for the out-of-plane orientation has a global minimum (E = -147.92 cm^{-1} at R = 5.38 Å and $\theta = 167°$) at a near linear configuration with a secondary minimum (E = -110.52 cm^{-1} at R = 3.37 Å and $\theta = 88.2°$) separated by a lower saddle point (E = -69.77 cm^{-1} at R = 3.95 Å and $\theta = 119.3°$) and an upper saddle point (E = -11.31 cm^{-1} at R = 5.57 Å and $\theta = 2°$). The potential for the perpendicular orientation has a global minimum (E = -188.78 cm^{-1} at R = 5.09 Å and $\theta = 2°$) at a near linear geometry with its secondary minimum (E = -110.83 cm^{-1} at R = 4.21 Å and $\theta = 128.5°$) at a near T-shaped configuration connected by a first saddle point (E = -76.35 cm^{-1} at R = 3.81 Å and $\theta = 72.6°$) and a second saddle point (E = -3.07 cm^{-1} at R = 5.67 Å and $\theta = 159.7°$). The averaged potential has a global minimum (E = -112.56 cm^{-1} at R = 3.41 Å and $\theta = 87.3°$) at a near T-shaped configuration with a broad secondary minimum (E = -72.56 cm^{-1} at R = 5.56 Å and $\theta = 167°$) at a near linear configuration separated by a lower saddle point (E = -68.32 cm^{-1} at R = 4.14 Å and $\theta = 121.2°$) and an upper saddle point (E = -60.50 cm^{-1} at R = 5.31 Å and $\theta = 2°$). The observed spectra for both complexes are consistent with an asymmetric top molecule in a near T-shaped configuration.

The energies of bound-state levels supported by the three orientations and the averaged potential energy surfaces were determined using the program JACOBI.[47] Radial basis sets of 150 tridiagonal Morse functions and angular basis sets of 150 Legendre polynomials were sufficient for convergence to within 0.0002 cm^{-1} for all calculated rotational energy levels. The eigenvalues and eigenvectors of the Hamiltonian matrix were obtained using 3000 Lanczos iterations. The ceiling of the potential in the program was set at 5000000 cm^{-1}. The details of the JACOBI program were reported in Ref. 47. Appendix B.1 shows the energies of the rotational energy levels, up to $J = 3$, for the ground vibrational state of *ortho*H_2 – HCCCN. The transition frequencies are obtained by calculating the difference between the rotational energy levels of interest. The energies of the rotational energy levels, up to $J = 3$, for the ground vibrational state of *para*H_2 – HCCCN are given in Appendix B.3.

4.5 Properties and accuracy of the H_2 – HCCCN potential energy surfaces

The bound-state energies supported by the potentials were obtained from the JACOBI program[47] and compared to the experimental transition frequencies. First, this procedure was performed on the potential energy surface for each orientation separately. The transition frequencies obtained from the parallel orientation potential corresponds to the spectral pattern of an asymmetric top molecule as was observed experimentally. The patterns obtained from both the out-of-plane and perpendicular orientations were of linear type molecules with very high frequency $J = 1 - 0$ *b*-type transition (~550 GHz). The transition frequencies obtained from the averaged potential energy surface were consistent with the spectral pattern of an asymmetric top molecule. In the H_2 – OCS MP4 calculations, an averaged potential was used to describe the *para*H_2 – OCS system while the potential for the parallel orientation was able to reproduce the *ortho*H_2 – OCS experimental results.[46] The same analysis was followed in this thesis.

The transition frequencies obtained from the bound-state energy levels were in moderate agreement ($|\%\Delta\nu_{av}| = 4.8\%$) with the experimental frequencies. The agreement between theoretical and experimental frequencies of *b*-type transitions was much less accurate ($|\%\Delta\nu_{av}| = 8.2 - 10.3\%$) compared to *a*-type transitions ($|\%\Delta\nu_{av}| = 1.4 - 3.0\%$). Simple scaling techniques were applied to the potential energy surfaces to improve the agreement of calculated and experimental rotational transition frequencies. Following the He – HCCCN potential energy surfaces studies,[1] a simple scaling of the potential to deepen the well slightly was tried, but the results did not improve the agreement with experiment. When the parallel potential was made shallower by 3%, the agreement between transition frequencies of *a*-type transitions was virtually unchanged while the agreement with *b*-type transitions was improved by only 0.2%. By making the parallel potential shallower by 10%, the agreement between the experimental and theoretical transitions frequencies of *b*-type transitions was improved by only an additional 0.4%. This scaling method was not feasible to achieve good agreement with experimental results. Other scaling procedures to reproduce the experimentally determined van der Waals bond length by shifting the potential to longer bond lengths yielded better agreement of the transitions frequencies with the measured frequencies. The agreement for *b*-type transition frequencies improved substantially ($|\%\Delta\nu_{av}| = 0.8 - 2.5\%$) with the scaling procedure. The results of the various scaled and the un-scaled potentials for *ortho*H_2 – HCCCN are shown in Table 4.12 and compared to the unsplit, that is where the hyperfine splittings have been removed, experimental line frequencies.

The scaling procedure to reproduce the experimental results of *para*H_2 – HCCCN involved shortening the van der Waals bond length. For *para*H_2 – HCCCN, the averaged potential energy surface was scaled by shortening the van der Waals bond by 0.15 Å without any variation in the depth of the well. The transition frequencies from this scaled potential are shown in Table 4.13 and are compared to the unsplit experimental line frequencies.

The scaled potentials for both *ortho*H_2 – HCCCN and *para*H_2 – HCCCN complexes have been used to predict the rotational transition frequencies for the $HCCC^{15}N$ and DCCCN complexes. The transition frequencies are given in Tables 4.14 and 4.15, respectively, along with the hyperfine-free experimental transition frequencies. For the *ortho*H_2 – HCCCN complexes, the PES results predict the rotational transitions of minor isotopologues within 2% of the experimental results. The *para*H_2 – HCCCN complexes predict the minor isotopologue transitions within less than 1% of the experimentally measured frequencies.

The rotational transition frequencies obtained from the bound-state rotational energy levels supported by the unscaled and scaled potentials can be fit to the spectroscopic constants using SPFIT[21] are shown for *ortho*H_2 – HCCCN and *para*H_2 – HCCCN complexes in Tables 4.12 and 4.13, respectively. The experimental rotational constants are in better agreement with the results from the scaled potentials. The centrifugal distortion constants are in marginal agreement with the experimental results. For the *ortho*H_2 – HCCCN complexes, the negative Δ_J reproduces the experimental results. The magnitude of the value is less well reproduced, the value obtained from the analysis of the theoretical results is over three times smaller than the experimentally determined result. The effect on the experimental spectra of the large amplitude motions and Coriolis interactions can be difficult to capture in the potential energy surfaces. The scaling of the potential does improve the agreement of some of the constants with experimental results. For the *para*H_2 – HCCCN complex, the agreement of the experimental results with the results from the analysis of the theoretical energy levels is more difficult due to the limited data set obtained experimentally. The $(B+C)/2$ rotational constant is well reproduced, especially for the scaled potential. The centrifugal distortion constants are obtained from an asymmetric rotor model using the nine transitions obtained from the theoretical results. The centrifugal distortion constants cannot be compared from the analyses. By fitting only the same three transitions as the experimental results for the *para*H_2 – HCCCN complexes, the results can be better compared. The centrifugal distortion constant from a linear rotor analysis of the theoretical transition frequencies (D_J = 1.35414 MHz) is in better agreement with the experimental results of the *para*H_2 – HCCCN complex (D_J = 1.56990 MHz). Both results are consistent with the *para*H_2 – HCCCN complex being weakly bound with large amplitude motions.

The transition frequencies of $HCCC^{15}N$ and DCCCN containing complexes were fit using SPFIT[21] in the same manner as the previous analyses and the results are given in Tables 4.14 and 4.15, respectively. Similar agreement with experimental results is seen for the minor isotopologues as for the main isotopologues for both complexes with *ortho*H_2 and *para*H_2. This substantiates the scaling methods as being appropriate ones to describe both of the H_2 – HCCCN systems.

The analysis of the supported bound-state energy levels could determine all rotational constants and can provide an inertia defect for comparison with the experimentally determined one of the *ortho*H_2 – HCCCN complex. A nice illustration of the dependence of the inertial defect on the hydrogen molecule is the comparison between the *ortho*H_2 – and *para*H_2 – HCCCN complexes. The inertial defect for the *ortho*H_2 – HCCCN complex ($\Delta_0 = 2.7$ amu Å^2) is smaller than that of *para*H_2 – HCCCN ($\Delta_0 = 4.0$ amu Å^2). The larger inertial defect indicates that the *para*H_2 – HCCCN complex is less rigid than the *ortho*H_2 – HCCCN dimer. This is consistent with the trend observed in the H_2 – OCS complexes study.[3,4] The inertial defects obtained from the theoretical analysis of minor isotopologues are in agreement with the main isotopologues values. An isotopic substitution on the HCCCN molecule should not affect the inertial defect since the inertial defect is mainly due to the out-of-plane motions and large amplitude motions of the hydrogen molecule.

4.6 Conclusions

The *ortho*H_2 – HCCCN and *para*H_2 – HCCCN complexes were investigated using rotational spectroscopy. Three isotopologues (HCCCN, DCCCN and HCCC^{15}N) were studied for both complexes with *a*-type transitions in the $|K| = 0$ stack measured for each isotopologue, with more extensive study of *ortho*H_2 – HCCCN and *ortho*H_2 – HCCC^{15}N complexes. Additionally, the $J_{KaKc} = 1_{01} - 0_{00}$ transition of various ^{13}C containing isotopologues have been measured. The spectra observed for the complexes are consistent with a T-shaped complex. The analysis of the spectra yielded the spectroscopic parameters including many centrifugal distortion constants consistent with a floppy complex. An analysis of the rotational constants provided structural parameters for both *ortho*H_2 – HCCCN ($R = 3.68$ Å; $\theta = 102.2°$) and *para*H_2 – HCCCN ($R = 3.59$ Å; $\theta = 105.3°$). The rotational constants were analysed and showed large inertial defects for the *ortho*H_2 – HCCCN complex. The data set for the *para*H_2 – HCCCN complex was insufficient to determine the inertial defect for the complex.

Potential energy surface calculations were performed on the H_2 – HCCCN system using the CCSD(T) method and aug-cc-pVTZ basis sets supplemented by midbond functions. Three orientations (parallel, perpendicular and out-of-plane) of the H_2 molecule moiety were calculated on the PES. The bound-state rotational energy levels supported by the potential energy surface were obtained and the transition frequencies were compared to the experimental results. The *ortho*H_2 – HCCCN experimental results were best reproduced using the potential corresponding to the parallel orientation of the H_2 molecule. A simple scaling technique of lengthening the bond length by 0.15 Å improved the agreement, especially for the *b*-type transitions. The experimental results of the *para*H_2 – HCCCN complex were best reproduced by the averaged potential where all three orientations have equal weight. A similar scaling technique as with the previous potential was used for improving the agreement with experimental results, but by shortening the bond length by 0.15 Å. The scaled potentials for *ortho*H_2 – HCCCN and *para*H_2 – HCCCN complexes were used to determine the transition frequencies for DCCCN and $HCCC^{15}N$ isotopologues. The agreement with the experimental results of the isotopologues substantiates the scaling method.

4.7 Figures

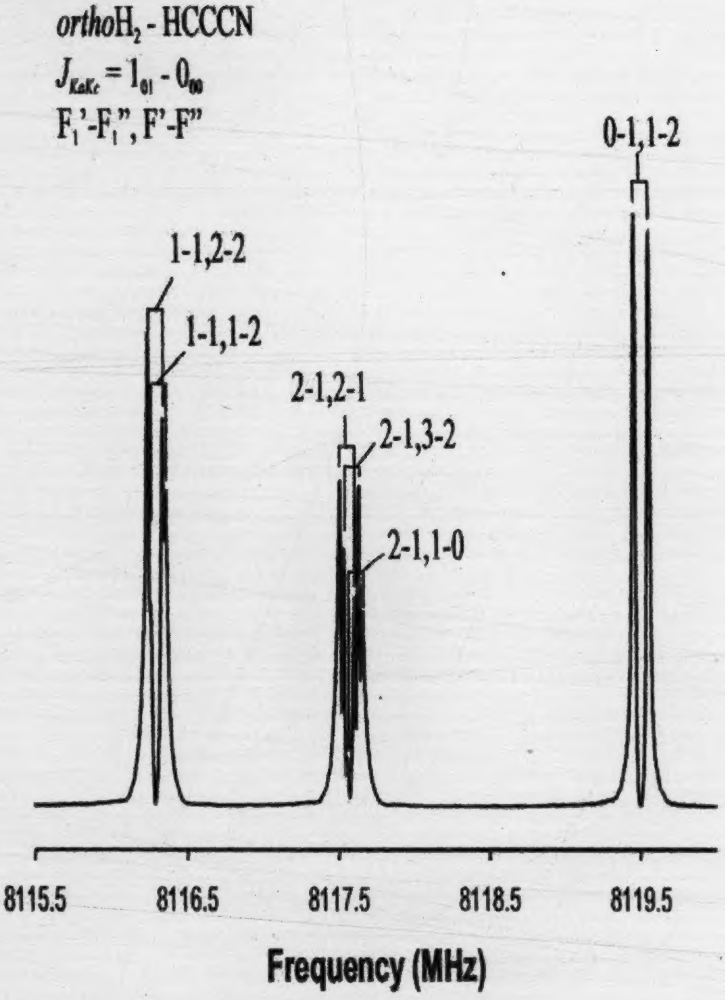

Figure 4.1: A composite experimental spectrum of the $J_{KaKc} = 1_{01} - 0_{00}$ transition of *ortho*H$_2$ – HCCCN, obtained with 100 averaging cycles. Each ^{14}N component is obtained in a separate experiment due to the small bandwidth of the spectrometer. The time domain signals were recorded at 10 ns sampling interval to obtain 8k data points. The data set was supplemented with 8k zeros before Fourier transformation. The Doppler pairs are shown with the quantum number assignments of each component.

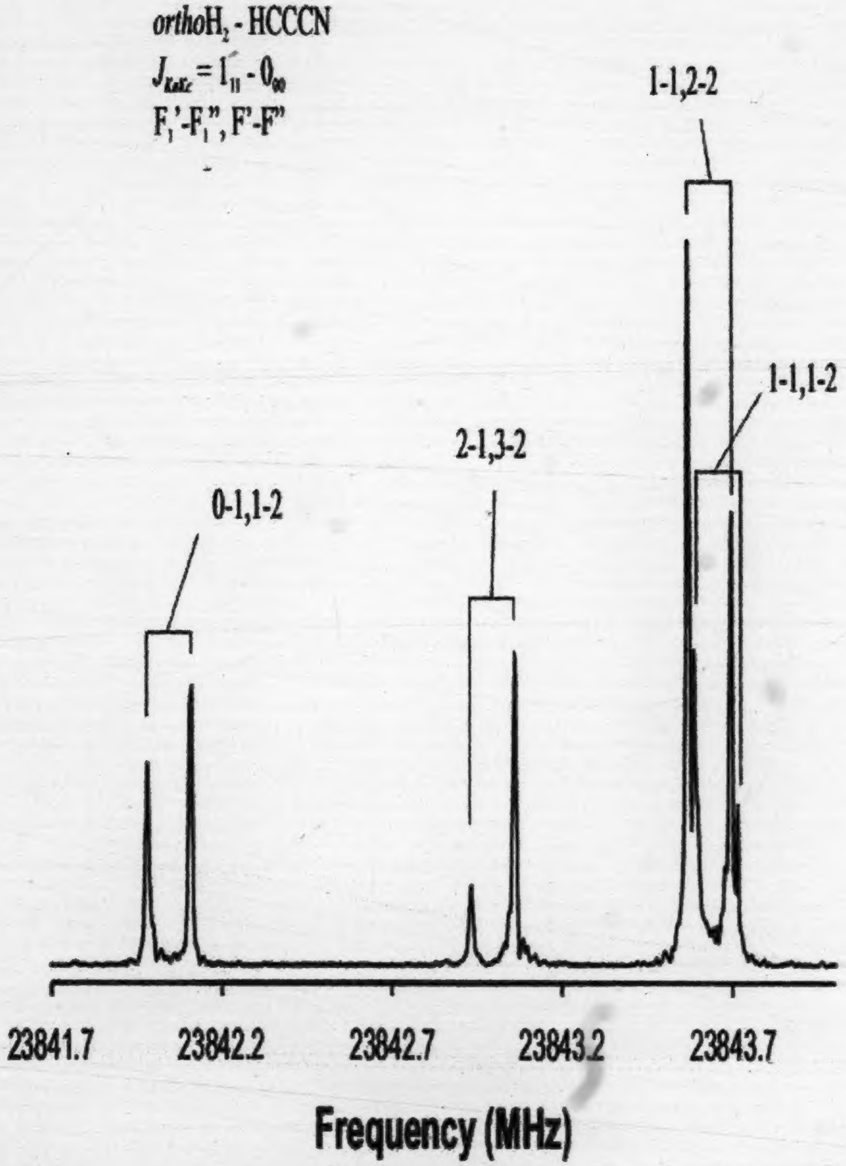

Figure 4.2: A composite experimental spectrum of the $J_{KaKc} = 1_{11} - 0_{00}$ transition of *ortho*H_2 – HCCCN, obtained with 250 averaging cycles in a neon expansion and with a power amplifier. The time domain signals were recorded at 10 ns sampling interval to obtain 8k data points. The data set was supplemented with 8k zeros before Fourier transformation. The Doppler pairs are shown in the Figure along with the quantum number assignments of each component.

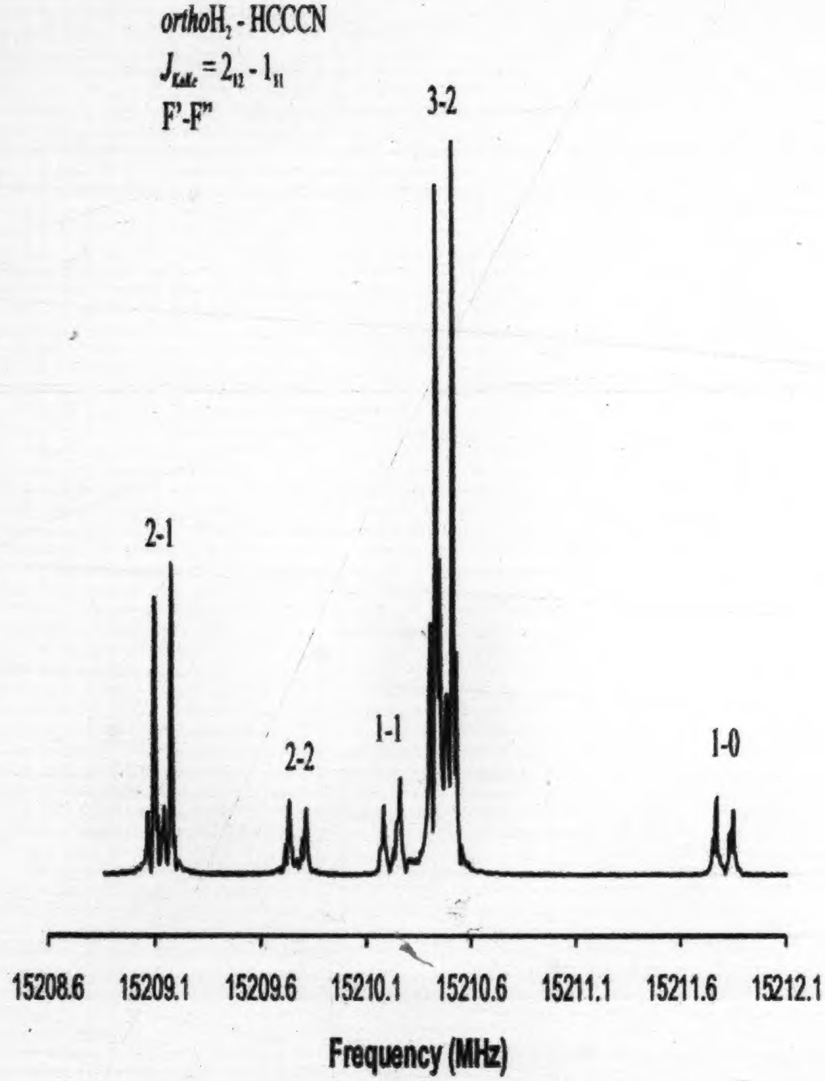

Figure 4.3: A composite experimental spectrum of the $J_{KaKc} = 2_{12} - 1_{11}$ transition of *ortho*H_2 – HCCCN, obtained with 100 averaging cycles. The time domain signals were recorded at 10 ns sampling interval to obtain 8k data points. The data set was supplemented with 8k zeros before Fourier transformation. The spectrum was obtained in a neon expansion. The quantum number assignments for the ^{14}N components are shown in the figure.

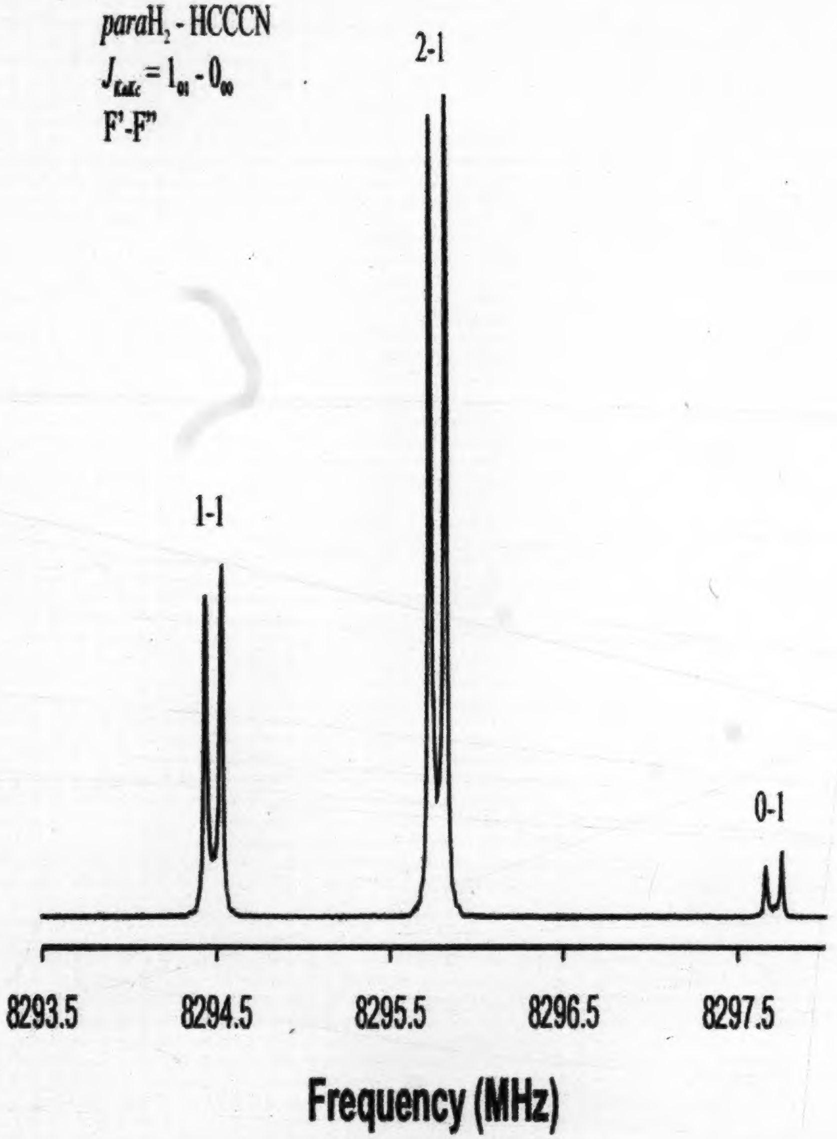

Figure 4.4: A composite experimental spectrum of the $J_{KaKc} = 1_{01} - 0_{00}$ transition of *para*H_2 – HCCCN, obtained with 100 averaging cycles. An enriched *para*H_2 sample was used to obtain this spectrum. The time domain signals were recorded at 10 ns sampling interval to obtain 8k data points. The data set was supplemented with 8k zeros before Fourier transformation. The quantum number assignments of each component are shown in the figure.

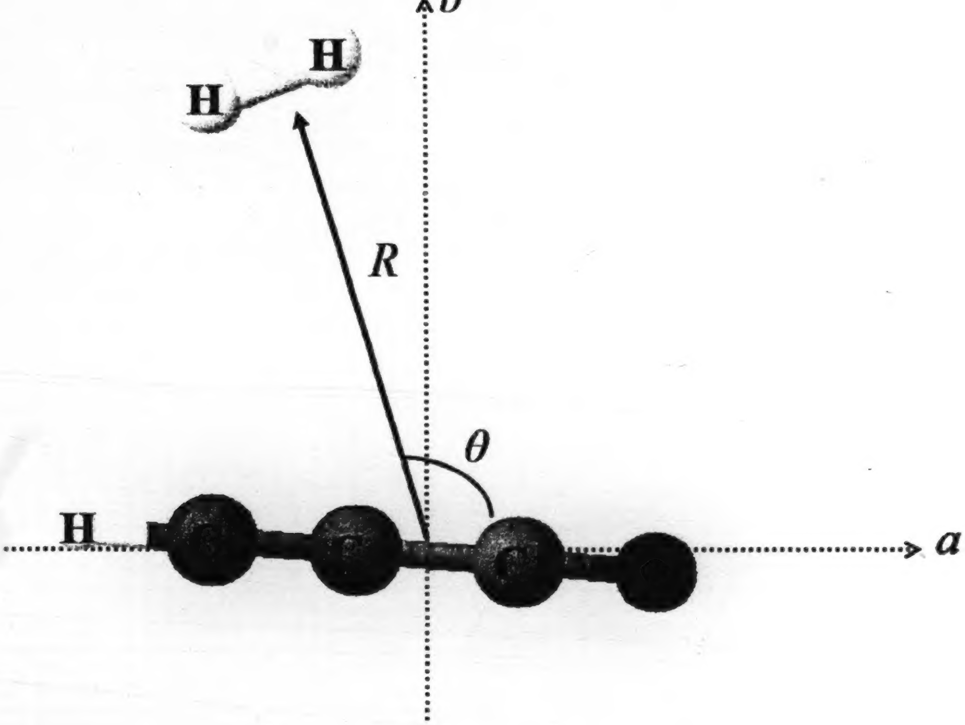

Figure 4.5: The T-shaped geometry of the hydrogen-HCCCN complex with the determined structural parameters marked. *R* is the van der Waals bond distance, θ is the angle between the HCCCN molecular axis and the ***R*** vector. The hydrogen moiety is considered a point mass in this analysis. The angle between the *a*-inertial axis and the HCCCN molecular axis is given by θ_a (not specifically shown in the figure).

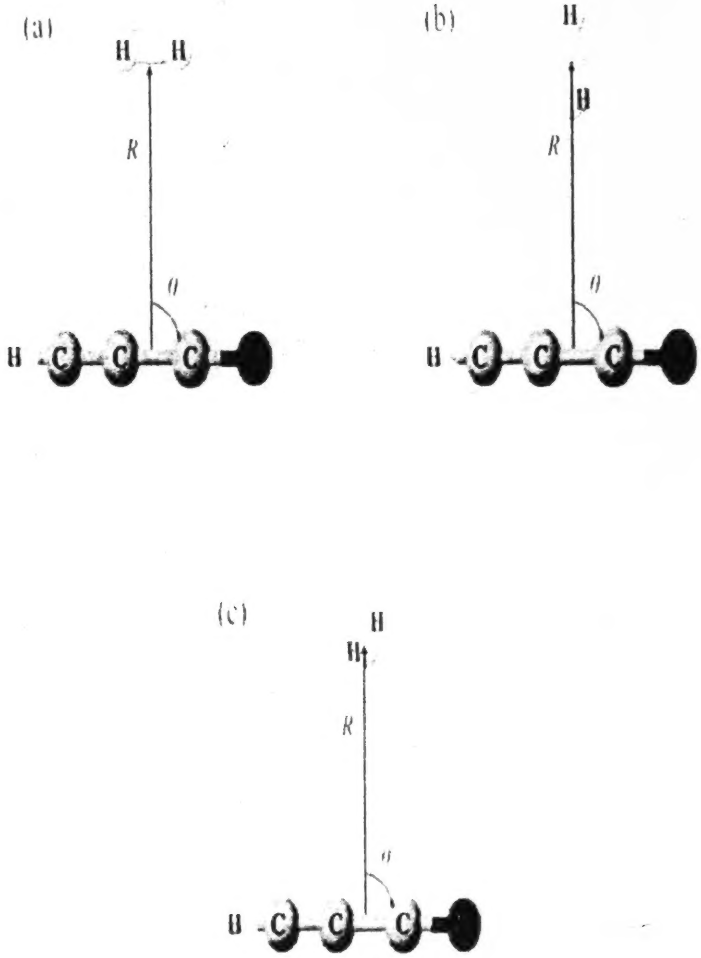

Figure 4.6: The T-shaped geometry of the hydrogen-HCCCN complex used in the potential energy surface calculations with the structural parameters marked. R is the van der Waals bond distance, θ is the angle between the HCCCN molecular axis and the $\boldsymbol{R}$ vector. The parallel orientation, shown in (a), corresponds to $\phi = 0°$ and $\alpha = 90°$. The perpendicular orientation, shown in (b), is described by $\phi = 0°$ and $\alpha = 0°$. The out-of-plane orientation, shown in (c), corresponds to $\phi = 90°$ and $\alpha = 90°$.

4.8 Tables

Table 4.1

Measured rotational transition frequencies (in MHz) and quantum number assignments for the *ortho*H_2 – HCCCN dimer.

Transition (J'_{KaKc} – J''_{KaKc})	F_1'-F_1''	F'-F''	ν_{obs}	$\Delta\nu^a$ (kHz)
1_{01} - 0_{00}	1-1	2-2	8116.2725	-6.0
		1-2	8116.2965	-0.2
	2-1	2-1	8117.5420	-7.9
		3-2	8117.5716	4.2
		1-0	8117.5966	6.9
	0-1	1-2	8119.4937	2.9
2_{12} - 1_{11}	2-1	3-2	15209.0971	-21.7
		2-1	15209.1293	3.4
		1-1	15209.1441	-8.0
	2-2	2-2	15209.7249	-16.6
		2-1	15209.7495	10.1
		3-3	15209.7675	-3.7
	1-1	2-2	15210.2152	12.8
	3-2	3-2	15210.4404	7.8
		4-3	15210.4656	1.1
		3-3	15210.4834	1.1
	1-0	2-1	15211.7877	-8.9
		1-1	15211.8041	-1.0
		0-1	15211.8390	5.6
2_{02} - 1_{01}	2-2	3-3	16194.8387	-5.7
	1-0	2-1	16195.0566	-0.4
	2-1	3-2	16196.1361	2.8
	3-2	4-3	16196.2234	3.3
	1-1	1-2	16198.2718	-13.3
1_{10} - 1_{01}	1-0	1-1	16669.3999	28.0
	2-2	2-1	16670.6644	31.5
	1-2	1-2	16671.3228	10.0
	2-1	2-2	16671.9388	-5.3
		1-0	16671.9701	-4.4
	1-1	2-2	16672.5214	-44.5
		1-2	16672.5687	-15.5
2_{11} - 1_{10}	2-1	3-2	17096.1244	-12.1
		1-1	17096.1650	-2.1
	2-2	2-2	17096.7713	-1.7
		3-3	17096.7943	-7.0
		1-2	17096.8129	5.7
	1-1	2-2	17097.1910	-3.3
		1-2	17097.2115	-4.4
	3-2	3-2	17097.4522	7.2
		4-3	17097.4724	-7.0
		2-1	17097.4943	15.0
	1-0	2-1	17098.8136	6.2
		1-1	17098.8327	3.7
3_{13} - 2_{12}	3-3	4-4	22802.8020	-8.7

	3-2	3-2	22803.4856	-8.8
		4-3	22803.5086	4.6
		2-2	22803.5418	7.9
	2-1	3-2	22803.8749	-0.1
	4-3	5-4	22803.8909	3.5
	2-2	3-3	22804.9601	1.5
$1_{11} - 0_{00}$	0-1	1-2	23842.0388	-13.3
	2-1	3-2	23842.9910	14.9
	1-1	2-2	23843.6249	-3.6
		1-2	23843.6435	2.0
$3_{03} - 2_{02}$	3-3	4-4	24195.5996	-3.7
	2-1	3-2	24196.7626	-0.1
	3-2	2-1	24196.9876	4.6
	4-3	4-3	24197.0294	1.1
	2-2	3-3	24198.9010	2.3
$3_{12} - 2_{11}$	3-3	3-3	25624.2633	-4.3
	3-2	4-3	25624.9463	-5.6
	2-1	3-2	25625.3308	5.2
	2-2	3-3	25626.3882	4.8

[a] $\Delta\nu = \nu_{obs.} - \nu_{calc.}$

Table 4.2

Measured rotational transition frequencies (in MHz) and quantum number assignments for the *ortho*H_2 – $HCCC^{15}N$.

Transition (J'_{KaKc} – J''_{KaKc})	F'-F''	*ortho*H_2 – $HCCC^{15}N$ ν_{obs}	$\Delta\nu^a$ (kHz)
1_{01} - 0_{00}	1-1	7911.6803	4.5
	2-1	7911.7039	3.3
	0-1	7911.7299	-7.9
2_{02} - 1_{01}	1-0	15788.4720	-5.6
	3-2	15788.5055	5.6
1_{10} - 1_{01}	2-2	16718.9888	-11.4
	1-2	16179.0193	3.5
	2-1	16719.0328	7.8
3_{03} - 2_{02}	4-3	23594.8218	0.0[b]
1_{11} - 0_{00}	0-1	23730.2693	-2.2
	2-1	23730.2875	2.2

[a] $\Delta\nu = \nu_{obs.} - \nu_{calc.}$.

[b] Small $\Delta\nu$ since fit calculated the rotational constants and centrifugal distortion constants from the five transitions.

Table 4.3

Measured rotational transition frequencies (in MHz), quantum number assignments, and determined spectroscopic constants (in MHz) for various ^{13}C dimers of *ortho*H_2 – HCCCN.

Transition (J'_{KaKc} – J''_{KaKc})	F_1'- F_1''	F'- F''	*ortho*H_2 – $H^{13}CCCN$ ν_{obs}	*ortho*H_2 – $HC^{13}CCN$ ν_{obs}	*ortho*H_2 – $HCC^{13}CN$ ν_{obs}
1_{01} - 0_{00}	1-1	2-2	7881.3438(-2.2)[a]	8081.6726(-3.4)	8088.5690(-2.2)
		1-2	7881.3642(0.3)	8081.6969(0.7)	8088.5900(-4.4)
	2-1	2-1	7882.6161(2.1)	8082.9441(3.2)	8089.8408(6.6)
		3-2	7882.6414(-0.5)	8082.9713(-1.1)	8089.8653(-5.4)
		1-0	7882.6598(1.6)	8082.9933(2.4)	8089.9019(9.7)
	0-1	1-2	7884.5645(-1.3)	8084.8927(-1.8)	8091.7893(-4.4)
$(B+C)/2$			3940.8750(2)[b]	4041.0399(2)	4044.4883(2)
$\chi_{aa}(^{14}N)$			-4.28797(163)	-4.28545(163)	-4.28973(163)
$S_{aa}(oH_2)$			-0.0624(18)	-0.0707(18)	-0.0819(18)

[a] The numbers in the parentheses are the $\Delta\nu = \nu_{obs.} - \nu_{calc.}$ in kHz.

[b] Numbers in parenthesis are one standard deviation in units of the last significant figure.

Table 4.4

Measured rotational transition frequencies (in MHz) and quantum number assignments for the *ortho*H_2 – DCCCN dimer.

Transition (J'_{KaKc} – J''_{KaKc})	F_2'-F_2''	F_1'-F_1''	F' – F''	*ortho*H_2 – DCCCN ν_{obs}	$\Delta\nu^a$ (kHz)
1_{01} - 0_{00}	1-1	1-2	2-3	7575.0437	-73.0
		2-2	3-3	7575.0800	-80.4
		0-1	1-2	7575.1258	-101.5
	2-1	1-0	2-1	7576.3210	-72.0
		3-2	4-3	7576.3552	-72.7
		2-1	3-2	7576.4072	-82.2
	0-1	1-1	2-2	7578.2949	-65.5
2_{02} - 1_{01}	2-2	2-2	3-3	15122.0745	64.1
		3-3	4-4	15122.0919	61.7
	1-0	2-1	3-2	15122.2694	33.8
		1-1	2-2	15122.3221	46.4
	2-1	3-2	4-3	15123.3215	23.7
		2-1	3-2	15123.4401	57.0
	3-2	4-3	5-4	15123.4980	101.8
	1-1	1-0	2-1	15125.4035	-5.2
		2-2	3-3	15125.4637	28.1
		1-2	3-2	15125.5033	27.6
		1-1	2-2	15125.5183	-1.1
3_{03} - 2_{02}	3-3	4-4	5-5	22610.7115	-33.8
	3-2	4-3	5-4	22612.0595	-51.8
	4-3	5-4	6-5	22612.1393	-25.4
	2-2	3-3	4-4	22614.0358	1.6

[a] $\Delta\nu = \nu_{obs.} - \nu_{calc.}$

Table 4.5

Measured rotational transition frequencies (in MHz) and quantum number assignments for the *para*H_2 – HCCCN dimer and *para*H_2 – $HCCC^{15}N$.

Transition (J'_{KaKc} – J''_{KaKc})	F' – F''	*para*H_2 – HCCCN ν_{obs}	$\Delta\nu^{a}$ (kHz)	*para*H_2 – $HCCC^{15}N$ ν_{obs}	$\Delta\nu$ (kHz)
1_{01} - 0_{00}	1-1	8294.4725	4.8	8075.8056	-8.4
	2-1	8295.7655	6.9		
	0-1	8297.6989	3.9		
2_{02} - 1_{01}	2-2	16547.8251	5.2	16113.9571	6.7
	1-0	16548.0354	-10.0		
	2-1	16549.1239	2.8		
	3-2	16549.2242	10.9		
	1-1	16551.2618	-10.9		
3_{03} - 2_{02}	4-3	24718.8219	3.1	24076.7297	-1.7

[a] $\Delta\nu = \nu_{obs.} - \nu_{calc.}$.

Table 4.6

Measured rotational transition frequencies (in MHz), quantum number assignments, and determined spectroscopic constants (in MHz) for various ^{13}C dimers of *para*H_2 – HCCCN.

Transition ($J'_{KaKc} - J''_{KaKc}$)	$F' - F''$	*para*H_2 – $H^{13}CCCN$ ν_{obs}	*para*H_2 – $HC^{13}CCN$ ν_{obs}	*para*H_2 – $HCC^{13}CN$ ν_{obs}
1_{01} - 0_{00}	1-1	8053.5610(-2.4)[a]	8260.2231(0.1)	8263.6884(-0.5)
	2-1	8054.8585(4.0)	8261.5194(0.1)	8264.9806(0.8)
	0-1	8056.7896(-1.6)	[b]	8266.9159(-0.3)
$(B+C)/2$		4030.8167(3)[c]	4134.1487[d]	4135.8794(3)
$\chi_{aa}(^{14}N)$		-4.30373(187)	-4.321(39)	-4.30311(187)

[a] The numbers in the parentheses are the $\Delta\nu = \nu_{obs.} - \nu_{calc.}$ in kHz.

[b] The component F'-F'' = 0-1 was unmeasurable due to accidental overlap with the F'-F'' = 1-1 component of *para*H_2 – $HCC^{13}CN$.

[c] Numbers in parenthesis are one standard deviation in units of the last significant figure.

[d] Fixed at value that provides best fit due to limited data.

Table 4.7

Measured rotational transition frequencies (in MHz) and quantum number assignments for the *para*H_2 – DCCCN dimer.

Transition (J'_{KaKc} – J''_{KaKc})	F_1'-F_1''	$F' - F''$	*para*H_2 – DCCCN ν_{obs}	$\Delta\nu^a$ (kHz)
1_{01} - 0_{00}	1-1	1-2	7735.4018	2.5
		2-2	7735.4323	-3.6
	2-1	3-2	7736.7117	-0.5
		2-1	7736.7577	2.4
	0-1	1-2	7738.6572	-0.7
2_{02} - 1_{01}	3-3	4-3	15441.7024	0.0[b]

[a] $\Delta\nu = \nu_{obs.} - \nu_{calc.}$.

[b] Small $\Delta\nu$ since the centrifugal distortion constant is calculated from the two transitions.

Table 4.8

Determined spectroscopic parameters for the *ortho*H_2 – HCCCN, *ortho*H_2 – $HCCC^{15}N$, and *ortho*H_2 – DCCCN dimers. All values are in MHz, unless stated otherwise.

	oH_2 – HCCCN	oH_2 – DCCCN	oH_2 – $HCCC^{15}N$
A	20434.84172(53)[a]	19947.467[b]	20402.48976(64)
B	4531.23799(81)		4406.07907(247)
C	3585.44274(53)		3505.01923(171)
$(B+C)/2$		3790.4995(36)	
Δ_J	-0.168862(73)	1.2045851(241)	-0.150575(82)
Δ_{JK}	21.589188(273)	21.589188[d]	-21.589188[d]
Δ_K	135.1389[c]	135.1389[c]	135.1389[c]
Φ_J	-0.0005214(41)	-0.0005214[d]	-0.0005214[d]
Φ_{JK}	0.043841(17)	0.043841[d]	0.043841[d]
δ_J	0.074902(59)	0.074902[d]	0.08146(43)
δ_K	0.0000034[c]	0.0000034[c]	0.0000034[c]
ϕ_J	0.0005254(31)	0.0005254[d]	0.0005254[d]
$\chi_{aa}(^{14}N)$	-4.27682(63)	-4.2690(71)	-
$\chi_{bb}(^{14}N)$	2.11299(68)	-	-
$\chi_{aa}(D)$	-	0.27764(173)	-
$S_{aa}(H_1\text{-}H_2)$	0.04564(87)	0.04564[d]	-0.0449(13)
$S_{bb}(H_1\text{-}H_2)$	0.01080(264)	-	-0.0521(17)
$C_{aa}(H)$	-0.04453(65)	-	-
$C_{bb}(H)$	-0.003587(134)	-	-
Δ_0[e] (amu Å^2)	4.69		4.72
#trans	9	3	5
rms (kHz)	10.7	58.4	5.8

[a] Numbers in parenthesis are one standard deviation in units of the last significant figure.

[b] Fixed to the value obtained from the analysis of transitions between Bound-state rotational energy levels.

[c] Fixed to the value of He – HCCCN complex (Ref. 1).

[d] Fixed at value of main isotopologue.

[e] $\Delta_0 = I_c - I_a - I_b$.

Table 4.9

Experimental structural parameters for *ortho*H_2 – HCCCN, *para*H_2 – HCCCN, and He – HCCCN van der Waals complexes.

	R(Å)	θ(°)[a]
$p$$H_2$ –HCCCN[b]	3.59	105.3
$o$$H_2$ – HCCCN	3.68	102.2
Averaged potential[c]	3.68	
Parallel potential[c]	3.49	
He – HCCCN[d]	3.93	80.1

[a] Angle defined as the angle between the molecular axis of HCCCN and the **R** vector (∠ (nitrogen atom – centre of mass of HCCCN – **R** vector)).

[b] Structural parameters obtained from rotational constants from analysis of bound-states supported by the potential energy surface with the isotopic data $(B+C)/2$ from experiment.

[c] Obtained from the ground state radial wavefunction calculated with the JACOBI program.

[d] Reference 1.

Table 4.10

Determined spectroscopic parameters for the *para*H_2 – HCCCN, *para*H_2 – $HCCC^{15}N$, and *para*H_2 – DCCCN dimers. All values are in MHz, unless stated otherwise.

	pH_2 – HCCCN	pH_2 – DCCCN	pH_2 – $HCCC^{15}N$
A	21698.80[a]	21677.587[a]	21682.649[a]
$(B+C)/2$	4151.268825(198)[b]	3870.877232(310)	4041.04681(36)
Δ_J	1.7485679(173)	1.311951(56)	1.5699028(241)
δ_J	0.0130[a]	-	-
$\chi_{aa}(^{14}N)$	-4.30299(119)	-4.30053(170)	-
$\chi_{aa}(D)$	-	0.1893(43)	-
#trans	3	2	3
rms (kHz)	7.2	2.1	6.3

[a] Fixed to value obtained from analysis of transitions between Bound-state rotational levels.

[b] Numbers in parenthesis are one standard deviation in units of the last significant figure.

Table 4.11

Topographical features of various H_2 – HCCCN potential energy surfaces, calculated at a resolution of $R = 0.08$ Å and $\theta = 0.9°$. Entries are given as [R(Å), θ(°), E (cm^{-1})].

	Saddle point 1	Global minimum	Saddle point 2	Secondary minimum
Parallel	4.65,131.3,-38.25	3.30,76.3,-156.95	5.65,2,-11.39	5.45,167,-125.57
Perpendicular	3.81,72.6,-76.35	5.09,2,-188.78	5.67,159.7,-3.07	4.21,128.5,-110.83
Out-of-plane	3.95,119.3,-69.77	5.38,167,-147.92	5.57,2,-11.31	3.37,88.2,-110.52
Averaged	4.14,121.2,-68.32	3.41,87.3,-112.56	5.31,2,-60.50	5.56,167,-72.56

Table 4.12

Hypothetical unsplit centre line frequencies and spectroscopic parameters of the *ortho*H_2 – HCCCN complex from potential energy surfaces compared with experimental values. All values are in MHz, unless specified.

J'_{KaKc} – J''_{KaKc}	Experiment	Parallel orientation		Parallel orientation (R = r + 0.15 Å)	
	ν_{obs}[a]	ν_{PES}	$\%\Delta\nu$[b]	ν_{PES}	$\%\Delta\nu$[b]
$1_{01} - 0_{00}$	8117.3520	8257.3	1.7	8201.4	1.0
$2_{12} - 1_{11}$	15210.1951	15663.3	3.0	15499.7	1.9
$2_{02} - 1_{01}$	16196.1303	16485.6	1.8	16366.5	1.1
$1_{10} - 1_{01}$	16670.9616	18388.6	10.3	16712.9	2.5
$2_{11} - 1_{10}$	17097.2104	17341.8	1.4	17283.1	1.1
$3_{13} - 2_{12}$	22803.7703	23477.1	3.0	23227.3	1.9
$1_{11} - 0_{00}$	23843.1092	25806.7	8.2	24022.6	0.8
$3_{03} - 2_{02}$	24196.9788	24655.1	1.9	24458.5	1.1
$3_{12} - 2_{11}$	25625.2174	25994.2	1.4	25917.6	1.1
$\lvert\%\Delta\nu_{av}\rvert$[c]			4.8		1.5
Rotational parameters					
A	20434.84172(53)	22239.162(1)		20510.498(1)	
B	4531.23799(81)	4548.212(2)		4546.728(2)	
C	3585.44274(53)	3708.946(1)		3654.478(1)	
Δ_J	-0.168862(73)	-0.0482(2)		-0.0499(2)	
Δ_{JK}	21.589188(273)	3.2252(6)		4.0770(6)	
Δ_K	135.1390[d]	135.1390[d]		135.1390[d]	
Φ_J	-0.0005214(41)	-0.000898(7)		0.000509(9)	
Φ_{JK}	0.043841(17)	-0.00560(4)		0.11212(4)	
δ_J	0.07490(6)	0.00112(1)		0.0919(1)	
δ_K	0.0000034[d]	0.0000034[d]		0.0000034[d]	
ϕ_J	0.00052543(306)	0.000097(7)		0.011421(7)	
Δ_0[e]	4.69	2.43		2.50	

[a] ν_{obs} is the hyperfine free centre frequency obtained from the spectroscopic fit.

[b] $\%\Delta\nu = 100\times(\nu_{PES} - \nu_{obs})/\nu_{obs}$.

[c] $\lvert\%\Delta\nu_{av}\rvert = [\Sigma_i(\%\Delta\nu_i)^2/n]^{1/2}$, where n is the number of transitions.

[d] Fixed at value from He – HCCCN dimer [ref. 1].

[e] $\Delta_0 = I_c - I_a - I_b$.

Table 4.13

Hypothetical unsplit centre line frequencies and spectroscopic parameters of the *para*H_2 – HCCCN complex from potential energy surfaces compared with experimental values. All values are in MHz, unless specified.

J_{KaKc} – J_{KaKc}	Experiment	Averaged potential		Averaged potential (R = r - 0.15 Å)	
	ν_{obs}[a]	ν_{PES}	$\%\Delta\nu$[b]	ν_{PES}	$\%\Delta\nu$[b]
$1_{01} - 0_{00}$	8295.5435	8240.0	-0.7	8294.1	-0.02
$2_{12} - 1_{11}$		15497.7		15637.6	
$1_{10} - 1_{01}$		16248.4		17857.8	
$2_{02} - 1_{01}$	16549.1211	16436.5	-0.7	16553.0	0.02
$2_{11} - 1_{10}$		17418.2		17471.9	
$3_{13} - 2_{12}$		23195.3		23437.1	
$1_{11} - 0_{00}$		23518.9		25234.5	
$3_{03} - 2_{02}$	24718.7675	24545.3	-0.7	24740.8	0.09
$3_{12} - 2_{11}$		26100.6		26186.4	
$\|\%\Delta\nu_{av}\|$[c]			0.7		0.05
Rotational parameters					
A	21698.800[d]	20035.226(1)		21698.800(1)	
B		4604.581(1)		4605.613(2)	
C		3534.9836(7)		3688.111(1)	
$(B+C)/2$	4151.268825(198)	4123.69552(36)[e]		4150.05628(36)[e]	
Δ_J	1.7485679(173)	-0.1128(1)		-0.0946(2)	
Δ_J^{f}		1.8230292(241)		1.4772278(241)	
Δ_{JK}	-	8.3547(6)		8.8576(6)	
Δ_K	-	135.1390[g]		135.1390[g]	
Φ_J	-	-0.001189(8)		-0.001173(9)	
Φ_{JK}	-	-0.00512(4)		-0.00202(4)	
δ_J	0.0130[e]	0.01294(2)		0.0130(1)	
δ_K	-	0.0000034[g]		0.0000034[g]	
ϕ_J	-	0.000292(6)		0.00238(7)	
Δ_0[h]		4.05		4.01	

[a] ν_{obs} is the hyperfine free centre frequency obtained from the quadrupole fit.

[b] $\%\Delta\nu = 100\times(\nu_{PES} - \nu_{obs})/\nu_{obs}$.

[c] $|\%\Delta\nu_{av}| = [\Sigma_i(\%\Delta\nu_i)^2/n]^{1/2}$, where n is the number of transitions.

[d] fixed at value obtained from the analysis of the bound-states supported by the scaled potential.

[e] (B+C)/2 obtained from a fit of the three transitions experimentally determined with only Δ_J as centrifugal distortion constant.

[f] Centrifugal distortion constant (Δ_J) obtained by fitting only the three transitions experimentally determined.

[g] Fixed at value from He – HCCCN dimer [ref. 1].

[h] $\Delta_0 = I_c - I_a - I_b$.

Table 4.14

Hypothetical unsplit centre line frequencies and spectroscopic parameters of the *ortho*H_2 – DCCCN and *ortho*H_2 – $HCCC^{15}N$ complexes from potential energy surfaces compared with experimental values. All values are in MHz, unless specified.

	oH_2 – $HCCC^{15}N$			oH_2 - DCCCN		
J'_{KaKc} – J''_{KaKc}	Experiment	Parallel orientation (R = r + 0.15 Å)		Experiment	Parallel orientation (R = r + 0.15 Å)	
	ν_{obs}	ν_{PES}	$\%\Delta\nu^b$	$\nu_{obs}{}^a$	ν_{PES}	$\%\Delta\nu^b$
$1_{01} - 0_{00}$	7911.7137	8011.1	1.3	7576.2237	7637.6	0.8
$2_{12} - 1_{11}$		15138.4			14468.7	
$2_{02} - 1_{01}$	15788.5040	15986.3	1.3	15123.3087	15244.0	0.8
$1_{10} - 1_{01}$	16719.0075	16246.1	-2.8		16386.1	
$2_{11} - 1_{10}$		16884.3			16058.3	
$3_{13} - 2_{12}$		22685.6			21684.9	
$1_{11} - 0_{00}$	23730.2733	23384.2	-1.5		23228.0	
$3_{03} - 2_{02}$	23594.8201	23889.5	1.3	22612.1161	22792.1	0.8
3_{12} - 2_{11}		25303.6			24068.4	
$\lvert\%\Delta\nu_{av}\rvert^c$			1.7			0.8
Rotational parameters						
A	20402.48123(71)	19956.146(1)		19947.467^d	19947.467(1)	
B	4406.05966(97)	4441.884(1)			4215.621(1)	
C	3505.03635(72)	3568.9337(7)			3420.8479(7)	
$(B+C)/2$				3790.54009(36)	3820.81905(36)^e	
Δ_J	-0.1516116(226)	-0.0637(1)		1.2141153(241)	-0.0508(1)	
Δ_J^f					1.2300236(241)	
Δ_{JK}	21.589188^g	2.9588(6)			2.6615(6)	
Δ_K	135.1390^h	135.1390^h			135.1390^h	
Φ_J	-0.0005214^g	-0.001049(8)			-0.000889(8)	
Φ_{JK}	0.043841^g	-0.00787(4)			-0.00783(4)	
δ_J	0.074902^g	-0.00107(2)			0.000125(2)	
δ_K	0.0000034^h	0.0000034^h			0.0000034^h	
$\Delta_0{}^i$		2.50			2.52	

[a] ν_{obs} is the hyperfine free centre frequency obtained from the fit.

[b] $\%\Delta\nu = 100\times(\nu_{PES} - \nu_{obs})/\nu_{obs}$.

[c] $\lvert\%\Delta\nu_{av}\rvert = [\Sigma_i(\%\Delta\nu_i)^2/n]^{1/2}$, where n is the number of transitions.

[d] Fixed at value obtained from analysis of transitions between Bound-state rotational levels.

[e] (B+C)/2 obtained from a fit of the three transitions experimentally determined with only Δ_J as centrifugal distortion constant.

[f] Centrifugal distortion constant (Δ_J) obtained by fitting only the three transitions experimentally determined.

[g] Fixed at the values obtained from the analysis of *ortho*H_2 – HCCCN.

[h] Fixed at value from He – HCCCN dimer [ref. 1].

[i] $\Delta_0 = I_c - I_a - I_b$.

Table 4.15

Hypothetical unsplit centre line frequencies and spectroscopic parameters of the *para*H_2 – DCCCN and *para*H_2 – $HCCC^{15}N$ complexes from potential energy surfaces compared with experimental values. All values are in MHz, unless specified.

	pH_2 – $HCCC^{15}N$			pH_2 - DCCCN		
J_{KaKc} – J_{kaKc}	Experiment	Averaged orientation (R = r + 0.15 Å)		Experiment	Averaged orientation (R = r + 0.15 Å)	
	ν_{obs}	ν_{PES}	%Δν[a]	ν_{obs}[b]	ν_{PES}	%Δν[a]
$1_{01} - 0_{00}$	8075.8056	8118.2	0.5	7735.5064	7734.0	-0.02
$2_{12} - 1_{11}$		15324.5			14638.8	
$2_{02} - 1_{01}$	16113.9571	16204.2	0.6	15441.6146	15441.7	0.001
$1_{10} - 1_{01}$		17911.6			18060.2	
$2_{11} - 1_{10}$		17084.1			16238.5	
$3_{13} - 2_{12}$		22969.0			21943.7	
$1_{11} - 0_{00}$		25149.8			24994.2	
$3_{03} - 2_{02}$	24076.7297	24224.9	0.6		23095.9	
$3_{12} - 2_{11}$		25606.5			24341.8	
$\|\%\Delta\nu_{av}\|$[c]			0.6			0.01
Rotational parameters						
A	21682.649[d]	21682.649(1)		21677.587[d]	21677.587(1)	
B		4498.946(1)			4266.879(1)	
C		3618.8737(7)			3466.7890(7)	
$(B+C)/2$[e]	4041.04681(36)	4061.85585(36)		3870.877232(310)	3869.17399(67)	
Δ_J	1.5699028(241)	-0.0900(1)		1.311951(56)	-0.0761(1)	
Δ_J[f]		1.3541458(241)			1.094746(93)	
Δ_{JK}		8.4803(6)			7.6970(6)	
Δ_K		135.1390[g]			135.1390[g]	
Φ_J		-0.001271(8)			-0.001229(8)	
Φ_{JK}		-0.00181(4)			-0.00137(4)	
δ_J		-0.00797(2)			0.000690(2)	
δ_K		0.0000034[g]			0.0000034[g]	
Δ_0[h]		4.01			4.02	

[a] $\%\Delta\nu = 100\times(\nu_{PES} - \nu_{obs})/\nu_{obs}$.

[b] ν_{obs} is the hyperfine free centre frequency obtained from the fit.

[c] $|\%\Delta\nu_{av}| = [\Sigma_i(\%\Delta\nu_i)^2/n]^{1/2}$, where n is the number of transitions.

[d] Fixed at value obtained from analysis of bound-state levels.

[e] (B+C)/2 obtained from a fit of the three transitions experimentally determined with only Δ_J as centrifugal distortion constant.

[f] Centrifugal distortion constant (Δ_J) obtained by fitting only the three transitions experimentally determined.

[g] Fixed at value from He – HCCCN dimer [ref. 1].

[h] $\Delta_0 = I_c - I_a - I_b$.

4.9 References

[1] W. C. Topic and W. Jäger, *J. Chem. Phys.* **123**, 064303 (2005).

[2] Z. H. Yu, K. J. Higgins, W. Klemperer, M. C. McCarthy, and P. Thaddeus, *J. Chem. Phys.* **123**, 221106 (2005).

[3] J. M. Michaud, K. Liao, and W. Jäger, *Mol. Phys.* **106**, 23 (2008).

[4] Z. H. Yu, K. J. Higgins, W. Klemperer, M. C. McCarthy, P. Thaddeus, K. Liao, and W. Jäger, *J. Chem. Phys.* **127**, 054305 (2007).

[5] W. Topic, University of Alberta, 2006.

[6] C. Moreau and C. J. Bongrand, *Ann. Chim.* (Paris) **14**, 47 (1920).

[7] F. A. Miller and D. H. Lemmon, *Spectrochim. Acta, Part A* **23**, 1415 (1967).

[8] P. D. Mallinson and A. Fayt, *Mol. Phys.* **32**, 473 (1976).

[9] P. L. Chapovsky and L. J. F. Hermans, *Ann. Rev. Phys. Chem.* **50**, 315 (1999).

[10] J. Tang and A. R. W. McKellar, *J. Chem. Phys.* **117**, 8308 (2002).

[11] J. Tang and A. R. W. McKellar, *J. Chem. Phys.* **123**, 114314 (2005).

[12] P. W. Selwood, *J. Am. Chem. Soc.* **88**, 2676 (1966).

[13] M. Misono and P. W. Selwood, *J. Am. Chem. Soc.* **91**, 1300 (1968).

[14] E. Ilisca and S. Sugano, *Phys. Rev. Lett.* **57**, 2590 (1986).

[15] M. Tudorie, M. Khelkhal, J. Cosleou, and P. Cacciani, *Surface Science* **601**, 1630 (2007).

[16] P. Cacciani, J. Cosleou, F. Herlemont, M. Khelkhal, C. Boulet, and J. M. Hartmann, *J. Mol. Struct.* **780-81**, 277 (2006).

[17] C. Puzzarini, J. Cosleou, P. Cacciani, F. Herlemont, and M. Khelkhal, *Chem. Phys. Lett.* **401**, 357 (2005).

[18] K. Higgins and W. Klemperer, *J. Chem. Phys.* **110**, 1383 (1999).

[19] V. N. Markov, Y. Xu, and W. Jäger, *Rev. Sci. Instrum.* **69**, 4061 (1998).

[20] D. R. Miller, J. P. Toennies, and K. Winkelmann, *9th Symposium on Rarefied Gas Dynamics*. (DFVLR Press, 1974).

[21] H. M. Pickett, *J. Mol. Spectrosc.* **148**, 371 (1991).

[22] J. K. G. Watson, *J. Chem. Phys.* **48**, 4517 (1968).

[23] R. L. DeLeon and J. S. Muenter, *J. Chem. Phys.* **82**, 1702 (1985).

[24] E. Fliege, H. Dreizler, and B. Kleibömer, *J. Mol. Struct.* **97**, 225 (1983).

[25] N. Heineking and M. C. L. Gerry, *J. Mol. Spectrosc.* **158**, 62 (1993).

[26] H. S. P. Müller and M. C. L. Gerry, *J. Chem. Phys.* **103**, 577 (1995).

[27] N. F. Ramsey, *Phys. Rev.* **85**, 60 (1952).

[28] N. F. Ramsey, *Molecular Beams*. (Oxford University Press, London, 1953).

[29] W. Gordy and R. L. Cook, *Microwave Molecular Spectra No. XVIII in Techniques of Chemistry*, 3rd ed. (Wiley-Interscience Publishers, New York, 1970).

[30] C. H. Townes and A. L. Schawlow, *Microwave Spectroscopy*. (Dover Publications, New York, 1975).

[31] A. Huckauf and W. Jäger, Manuscript in Preparation.

[32] A. Huckauf and W. Jäger, *J. Chem. Phys.* **119**, 7749 (2003).

[33] V. Typke, *J. Mol. Spectrosc.* **69**, 173 (1978).

[34] V. Typke, *J. Mol. Spectrosc.* **72**, 293 (1978).

[35] K. Liao and W. Jäger, Unpublished results.

[36] K. Raghavachari, G. W. Trucks, J. A. Pople, and M. Head-Gordon, *J. Chem. Phys.* **115**, 8431 (2001).

[37] F.-M. Tao and Y.-K. Pan, *J. Chem. Phys.* **97**, 4989 (1992).

[38] S. M. Cybulski and R. R. Toczylowski, *J. Chem. Phys.* **111**, 10520 (1999).

[39] T. B. Pederson, B. Fernández, H. Koch, and J. Makarewicz, *J. Chem. Phys.* **115**, 8431 (2001).

[40] T. H. Dunning Jr., *J. Chem. Phys.* **90**, 1007 (1989).

[41] Y. Xu and W. Jäger, *J. Chem. Phys.* **106**, 7968 (1997).

[42] J. K. Tyler and J. Sheridan, *Trans. Faraday Soc.* **59**, 266 (1963).

[43] G. Herzberg, *Can. J. Res. A* **28**, 144 (1950).

[44] H.-J. Werner, P. J. Knowles, R. Lindh *et al.*, MOLPRO, a package of *ab initio* programs (Cardiff, UK).

[45] S. F. Boys and F. Bernardi, *Mol. Phys.* **19**, 553 (1970).

[46] K. J. Higgins and W. Klemperer, *Private communication.*

[47] X. G. Song, Y. Xu, P.-N. Roy, and W. Jäger, *J. Chem. Phys.* **121**, 12308 (2004).

Chapter 5

Spectroscopic investigations of $(H_2)_N - OCS$ clusters ($N = 2$-7)

The study of bare hydrogen molecule clusters would remove any matrix effects due to the surrounding helium droplet and would aid in the study of possible superfluidity in *para*-hydrogen. This would be a direct observation of superfluidity in *para*-hydrogen molecules. Infrared studies have been performed for the $H_2 - OCS$ dimer[1] and larger $(H_2)_N - OCS$ ($N = 2$-7) clusters.[2] The band origins red shift as the cluster increases in size with a change in slope for $N = 5$-7. This change in slope corresponds to the 6th and 7th hydrogen molecules taking a different location (near the O end) compared to the ring formed by the 1st through the 5th hydrogen molecules. This is consistent with the $He_N - OCS$ results from the infrared and microwave studies.[3-6] For $N = 1$-7, the infrared study provided rotational constants to guide the spectral search in the microwave study.[1,2] It also showed the feasibility of studying the bare hydrogen clusters using pulsed-jet experiments much like the doped helium clusters studies.

This current study reports the $(H_2)_N - OCS$ ($N = 2$-7) clusters containing *ortho*H_2 and *para*H_2 molecules. This is the first microwave study of hydrogen molecule clusters (larger than $N = 1$) seeded with a chromophore. Several isotopologues for OCS were measured for many of the clusters. Mixed clusters, some of which were also observed in the infrared study,[2] containing a combination of *ortho*H_2 and *para*H_2 molecules were also assigned and have supported the assignment of the pure *ortho*H_2 or pure *para*H_2 clusters.

Microwave spectra are less spectrally crowded than infrared spectra and the mixed clusters do not overlap in the same way. To help simplify the notation of these molecular formula of the clusters, *para*H_2 will be abbreviated to pH_2 and similarly, *ortho*H_2 to oH_2. Outside of the molecular formulas, no abbreviations will be made.

Rotational spectra of small-sized $(H_2)_N$ – OCS clusters with N = 2-7 were observed via rotational spectroscopy using the pulsed-jet Fourier transform microwave spectrometer described in Chapter 2. Spectra of pure $(pH_2)_N$ – OCS clusters, pure $(oH_2)_N$ – OCS clusters, and mixed *ortho*H_2 and *para*H_2 containing clusters were measured. The rotational lines of *ortho*H_2 molecules containing clusters show spin-spin hyperfine structure and the pattern evolves as the number of *ortho*H_2 molecules increases. Nuclear quadrupole hyperfine structures were observed for ^{33}S (nuclear spin quantum number I = 3/2) containing isotopologues. The nuclear quadrupole coupling constants of ^{33}S are compared to the values of the OCS monomer and the He_N – OCS clusters. The assignment of the number of solvating hydrogen molecules, N, is supported by the analyses of the spin-spin hyperfine structures of the mixed clusters, the dependence of line intensities on sample conditions (pressure and concentrations), and the agreement of the $(pH_2)_N$ – OCS and $(oH_2)_N$ – OCS rotational constants with those from previous infrared studies.[2]

5.1 Experimental details

The results from the current study were obtained from a Balle-Flygare pulsed molecular beam Fourier transform microwave spectrometer.[7] Details of our spectrometer have been described previously[8] and given in Chapter 2.

The gas sample to study the hydrogen – OCS clusters consisted of trace amounts (<0.5 %) of OCS and ~1-5 % hydrogen gas or enriched *para*-hydrogen gas in helium as a carrier gas. The backing gas pressures varied from 8-85 atm with the higher pressures favoring generation of larger clusters. Enriched *para*-hydrogen was generated using a home-built catalytic converter (chromium oxide on alumina catalyst) which has been described in Chapter 2.

Enriched *para*-hydrogen samples allowed us to study pure $(pH_2)_N$ – OCS clusters and mixed clusters containing predominately *para*-hydrogen molecules (for example, $(pH_2)_4(oH_2)$ – OCS). Over time, we observed some back-conversion of the enriched *para*-hydrogen to *ortho*-hydrogen. This is consistent with the results seen by McKellar *et al.* in their infrared study.[2] As a result, the mixed clusters containing more *ortho*-hydrogen molecules gained significant signal intensity, since *ortho*-hydrogen molecules bind more strongly to OCS than *para*-hydrogen molecules.[9-11]

In addition to the normal isotopologues of $(H_2)_N$ – OCS ($N = 2$-7), other isotopologues were also investigated, namely those containing $O^{13}CS$, $OC^{33}S$, $OC^{34}S$, and $O^{13}C^{34}S$. Spectra of complexes containing $O^{13}CS$ and $O^{13}C^{34}S$ were obtained using an enriched sample (Cambridge Isotopes Laboratories, 99% ^{13}C).

Microwave-microwave double resonance experiments as described in Chapter 2 were done in attempts to measure the frequencies of higher J transitions.[12] Pump radiation was introduced perpendicularly to the excitation radiation using a horn antenna. The set-up, described in more detail previously,[12] used was a decoherence DR experiment where a strong transition is monitored, while the pumped frequency is swept through the region where a connected transition is predicted.[13] This set-up has been successfully used with He_N – molecule clusters[6,14,15] and with H_2 – molecule dimers.[16]

5.2 Results and analyses

Predictions from the infrared work on clusters with $N = 2\text{-}7$ (pure *para*H_2 and pure *ortho*H_2) were used to search for the rotational transitions. The measured transition frequencies of $(pH_2)_N$ – OCS, $(oH_2)_N$ – OCS, and mixed clusters are given in Tables 5.1, 5.2 and 5.3, respectively. The hyperfine structure due to the proton spin-spin coupling was resolved for many $(oH_2)_N$ – OCS and for $(pH_2)_{N-x}(oH_2)_x$ – OCS clusters. Figure 5.1 shows the difference in the hyperfine patterns of the $(oH_2)_2$ – OCS and the $(pH_2)(oH_2)$ – OCS spectra. The complexity of the hyperfine pattern was observed to increase as the number of *ortho*H_2 molecules increase. The frequencies of the hyperfine components in clusters with less than five *ortho*H_2 molecules were fit to obtain spin-spin coupling constants, one for each *ortho*H_2 molecule present in the cluster. In most cases where more than one *ortho*H_2 molecule is present in a cluster, the spin-spin coupling constants were constrained to all being equal in the fitting procedure. This assumes that the *ortho*H_2 molecules are all in a similar environment within a given cluster and that the spin-spin interactions are equivalent. The spectroscopic fits were done for each isotopologue and each cluster separately using Pickett's global least squares fitting program, SPFIT,[17] to obtain the hyperfine coupling constants.

Some mixed clusters containing a combination of *para*H_2 and *ortho*H_2 molecules were observed such as $(pH_2)_2(oH_2)$ - OCS, but not all could be resolved, in the infrared study.[2] In the search procedure we assumed that the transitions of the mixed clusters occur at equidistant frequency intervals between the pure *para*H_2 and pure *ortho*H_2

molecule clusters. For example, in $N = 2$, the $(p\mathrm{H_2})(o\mathrm{H_2})$ – OCS cluster should lie nearly equidistant from the $(p\mathrm{H_2})_2$ – OCS and $(o\mathrm{H_2})_2$ – OCS transition frequencies. The transition assigned to $(p\mathrm{H_2})(o\mathrm{H_2})$ – OCS ($J_{KaKc} = 1_{01} - 0_{00}$) was observed within 2.5 MHz of the expected frequency.

Despite extensive MW-MW DR experiments, no $J = 2$-1 transitions could be observed for any of the clusters. Additionally, transitions observed at higher frequencies could not be linked via DR to any $J = 1$-0 transition.

5.2.1 $N = 2$

All $N = 2$ clusters with $^{16}\mathrm{O}^{12}\mathrm{C}^{32}\mathrm{S}$ were found and initially measured without the use of an enriched *para*$\mathrm{H_2}$ sample. The $J_{KaKc} = 1_{01} - 0_{00}$ transitions of $(p\mathrm{H_2})_2$ – OCS, $(o\mathrm{H_2})_2$ – OCS and $(p\mathrm{H_2})(o\mathrm{H_2})$ – OCS were found and measured for OCS, $\mathrm{O}^{13}\mathrm{CS}$ and $\mathrm{OC}^{34}\mathrm{S}$, as well as for $\mathrm{O}^{13}\mathrm{C}^{34}\mathrm{S}$ of the $(o\mathrm{H_2})_2$ – OCS cluster. The signal intensity of the clusters was sufficient to observe the $J_{KaKc} = 1_{01} - 0_{00}$ transition of $(p\mathrm{H_2})_2$ – OCS with 10 averaging cycles. The signal did increase correspondingly 15 fold when an enriched *para*$\mathrm{H_2}$ sample was used, thus confirming the presence of *para*$\mathrm{H_2}$ in the cluster. The use of enriched *para*-$\mathrm{H_2}$ samples allowed us to measure the spectra of less abundant isotopologues.

Additionally, the $J_{KaKc} = 1_{01} - 0_{00}$ transition frequencies of $(o\mathrm{H_2})_2$ – $\mathrm{OC}^{33}\mathrm{S}$ were measured and are given in Table 5.4. The spectrum of the $J_{KaKc} = 1_{01} - 0_{00}$ transition of $(o\mathrm{H_2})_2$ – $\mathrm{OC}^{33}\mathrm{S}$ (Figure 5.2) shows additional hyperfine structure as a result of $^{33}\mathrm{S}$ ($I = 3/2$) nuclear quadrupolar coupling. The spectrum was fit to a $^{33}\mathrm{S}$ nuclear quadrupole coupling constant and two equivalent spin-spin coupling constants, one for each *ortho*$\mathrm{H_2}$ molecule in the cluster. The corresponding nuclear quadrupole coupling constant, χ_{aa}, (Table 5.4) differs by only 2.2% from that of the OCS monomer.[18] This indicates that the OCS unit lies approximately along the *a*-principal inertial axis of the complex; and from equation [2.18] an average excursion angle, θ_a, of 6.9° is obtained from χ_{aa}.

5.2.2 $N = 3,4,5$

The predicted rotational constants for the $N = 3$-5 clusters from the infrared study[2] were quite close for both the pure *para*H_2 and *ortho*H_2 clusters. Gas mixtures with backing pressures of ~14-35 atm were required to produce the clusters in this size regime. These pressures are significantly higher than those needed for the study of the helium clusters of the same size.[6] Additionally, very low concentrations of OCS (< 0.2 %) and hydrogen gas (< 0.5%) were used.

5.2.2.1 $(pH_2)_{3,4,5}$ – OCS clusters

The $J = 1 - 0$ transition of $(pH_2)_3$ – OCS could be measured without an enriched *para*H_2 sample, but the signal intensity improved significantly when an enriched sample was used confirming that presence of *para*H_2 molecules in the clusters. The $(pH_2)_4$ – OCS signal was quite weak and only transitions of the normal isotopologue could be observed. The assignment for $N = 4$ was solidified by the observation of all possible mixed clusters. Transitions of the $N = 5$ cluster were measured using an enriched sample but can be seen very weakly with a non-enriched sample. The $J = 1$ - 0 transitions for $(pH_2)_3$ – OCS and $(pH_2)_5$ - OCS were measured for OCS, $O^{13}CS$ and $OC^{34}S$ isotopologues. The $J = 1 - 0$ transition of $(pH_2)_5$ – $O^{13}C^{34}S$ was also measured. Examples of typical spectra obtained for the $(pH_2)_3$ – OCS and $(pH_2)_6$ – OCS clusters are shown in Figure 5.3. The measured transition frequencies for the pure $(pH_2)_{3\text{-}5}$ – OCS clusters are given in Table 5.1.

5.2.2.2 $(o\mathrm{H}_2)_{3,4,5}$ – OCS clusters

The $J = 1$ - 0 transitions of the $(o\mathrm{H}_2)_{3\text{-}5}$ – OCS clusters were measured for OCS and $\mathrm{O}^{13}\mathrm{CS}$ isotopologues. Additionally, the $J = 1 - 0$ transitions of $(o\mathrm{H}_2)_{3,4}$ – $\mathrm{OC}^{34}\mathrm{S}$ and $(o\mathrm{H}_2)_4$ – $\mathrm{O}^{13}\mathrm{C}^{34}\mathrm{S}$ were measured. The transition frequencies for $(o\mathrm{H}_2)_{3\text{-}5}$ – OCS clusters are given in Table 5.2. Hyperfine structure due to the protons in these clusters was observed and measured. Figure 5.4 shows the spectra of the $J = 1 - 0$ transitions of $(o\mathrm{H}_2)_3$ – OCS, as well as $(o\mathrm{H}_2)_6$ – OCS for comparison. The hyperfine structure of these transitions becomes more complex as the number of *ortho*H_2 molecules in the cluster increases. The analysis was possible for clusters containing less than five *ortho*H_2 molecules and provided spin-spin coupling constants for $(o\mathrm{H}_2)_3$ – OCS and $(o\mathrm{H}_2)_4$ – OCS clusters. Due to the complexity of the spectrum and restrictions of the SPFIT[17] program, analysis of $(o\mathrm{H}_2)_5$ – OCS and any cluster containing five *ortho*H_2 molecules or more was not feasible. The coupling constants that could be determined are presented in Table 5.2. The Doppler pairs for transitions where the analysis was not possible are presented in Table 5.2.

The $J = 1 - 0$ transitions for $(o\mathrm{H}_2)_3$ – $\mathrm{OC}^{33}\mathrm{S}$ and $(o\mathrm{H}_2)_4$ – $\mathrm{OC}^{33}\mathrm{S}$ were measured and the frequencies are given in Table 5.4, together with the $^{33}\mathrm{S}$ nuclear quadrupole coupling constants, χ_{aa}, obtained from the spectroscopic analysis. The χ_{aa} values remain quite close to the monomer value,[18] indicating that the OCS unit lies relatively rigid along the principal a-inertial axis. The average excursion angle, θ_a, can again be obtained from χ_{aa} and equation [2.18]. For the $(o\mathrm{H}_2)_3$ – $\mathrm{OC}^{33}\mathrm{S}$ cluster, a value of 4.2° is obtained, while a value of 5.6° is obtained for the $(o\mathrm{H}_2)_4$ – $\mathrm{OC}^{33}\mathrm{S}$ cluster.

5.2.2.3 $(pH_2)_x(oH_2)_{N-x}$ – OCS mixed clusters ($N = 3,4,5$)

For $N = 3$ and 4, the spectral searches for mixed clusters were straightforward and transitions were found quite close to the expected values. The evolution of the hyperfine structure in the mixed clusters as a result of the changing number of *ortho*H_2 molecules is shown in Figure 5.5 for clusters with $N = 3$.

For $N = 5$, the mixed clusters were also found near the predicted frequencies with evolving hyperfine structures. However, for the $J = 1 - 0$ transition of the $(pH_2)_2(oH_2)_3$ – OCS cluster, two transitions were found on either side of the expected frequency. Both transitions require similar sample conditions to be observed and have hyperfine structures consistent with multiple *ortho*H_2 molecules in the system. The transition at higher frequency is stronger in intensity by at least an order of magnitude. The proposed reason for the observation of two transitions for this mixed cluster is the occurrence of two structural isomers. The *para*H_2 and *ortho*H_2 molecules can be arranged in two different ways in the $(pH_2)_2(oH_2)_3$ – OCS cluster and these two isomers would have slightly different rotational constants. Figure 5.6 shows the two spectra found for the structural isomers together with the proposed cluster geometries. The proposed geometries are assigned based on the signal intensities of the observed transitions and the spin-spin coupling constants obtained from the analysis. A more thorough discussion of the proposed geometries will be provided in a later section.

5.2.3 $N = 6, 7$

5.2.3.1 $(pH_2)_{6,7}$ – OCS clusters

The $J = 1 - 0$ transitions of $(pH_2)_6$ – OCS and $(pH_2)_7$ – OCS were observed by using very low concentrations of OCS (< 0.1%) and low concentrations of enriched *para*H_2 gas (0.2-1%) in high pressures of helium backing gas (50-80 atm). The transitions are not visible without the use of an enriched sample, which confirms the presence of *para*H_2 molecules in the clusters. Transitions were also measured for clusters containing $O^{13}CS$, as well as for $(pH_2)_6 - OC^{34}S$. Figure 5.3 shows the spectrum of $(pH_2)_6 - OCS$ compared with $(pH_2)_3 - OCS$. The transition frequencies are given in Table 5.1.

5.2.3.2 $(oH_2)_{6,7}$ – OCS clusters

The $J = 1 - 0$ transition was measured for the main isotopologue and for $(oH_2)_6 - O^{13}CS$. The spectrum of $(oH_2)_6 - OCS$ is shown in Figure 5.4 next to the spectrum of $(oH_2)_3 - OCS$ for comparison. The transition frequencies, including the Doppler pairs of the spin-spin hyperfine components, are given in Table 5.2. The spin-spin hyperfine patterns due to six and seven *ortho*H_2 molecules are too complicated and a hyperfine structure analysis was not feasible using SPFIT.[17] The analysis is further complicated by the placement of the sixth and seventh H_2 molecules off of the ring around the OCS molecule, as was observed by a change in slope of the vibrational shifts.[2] Due to the different placement of the hydrogen molecules, the spin-spin coupling constants of all the hydrogen molecules can not be constrained to being equal as not all of the molecules are in similar environments.

5.2.3.3 $(pH_2)_{N-x}(oH_2)_x$ – OCS mixed clusters ($N = 6,7$)

The $J = 1 - 0$ transitions of all possible mixed clusters for $N = 6$ and 7 were observed using similar conditions as for the pure clusters and assigned utilizing the evolving hyperfine structure. The transition frequencies are given in Table 5.3, together with the spin-spin coupling constants for clusters containing fewer than five *ortho*H_2

molecules. Structural isomers were found for the $J = 1 - 0$ transition of the $(pH_2)_3(oH_2)_3$ – OCS cluster, where two transitions were detected within a ~75 MHz range, similar to the case of the structural isomers observed in the $(pH_2)_2(oH_2)_3$ – OCS cluster. The transitions require similar sample conditions and show hyperfine structures consistent with the presence of several *ortho*H_2 molecules. Unfortunately, an analysis of the spin-spin coupling constants was not possible for the $(pH_2)_3(oH_2)_3$ – OCS structural isomers since the data set was insufficient to fit the necessary number of coupling constants. The hyperfine components of the transition corresponding to the $(pH_2)_4(oH_2)_2$ – OCS cluster could not be resolved. The components appeared to have collapsed and no Doppler pairs could be assigned. The transition frequency was taken as the centre of the unresolvable component.

For $N = 7$, transitions corresponding to two mixed clusters, namely $(pH_2)_2(oH_2)_5$ – OCS and $(pH_2)_3(oH_2)_4$ – OCS, could not be observed despite extensive searches. As the number of H_2 molecules increase in the cluster, the number of mixed clusters over which intensity is spread also increases. It is also difficult to predict the geometry of the larger mixed clusters, where H_2 molecules begin to spill off the equatorial ring to the poles. There is no indication of whether *para*H_2 or *ortho*H_2 molecules would prefer to be on the ring or at the pole. For example, in $(pH_2)_3(oH_2)_4$ – OCS, it is unknown which spin isomers would assemble to make the ring. Additionally, the composition of the ring could change as the number of *para*H_2 and *ortho*H_2 molecules is changed in the cluster. For example, in $(pH_2)_5(oH_2)_2$ – OCS, the ring could be expected to be comprised of five *para*H_2 molecules. In $(pH_2)_2(oH_2)_5$ – OCS, the ring could be entirely *ortho*H_2 molecules. The question becomes: "at which mixed cluster would the composition of the ring change?" Due to this uncertainty, the number of additional structural isomers would increase and the signal intensity for a specific cluster size would be distributed amongst them. This could help explain why transitions for some mixed clusters were not observed.

5.3 Discussion

5.3.1 Cluster size assignment

The isotopic data helps to confirm assignments of individual transitions to a certain cluster size, but determining the actual number N of hydrogen molecules is more difficult. In the case of He_N – OCS, extensive studies about pressure, sample concentration, and nozzle temperature dependence of the signal intensities gave a relative sizing of the clusters.[6] Important additional information is available in the $(H_2)_N$ – OCS studies with the observation of the mixed clusters. The evolution of the hyperfine structure due to the number of *ortho*H_2 molecules in the mixed clusters and the relative spacing of the clusters allows for relatively confident assignments of the absolute cluster sizes. The assignment of the mixed clusters is substantiated by the similarity of the hyperfine patterns of clusters with the same number of *ortho*H_2 molecules. This can be seen in the spin-spin coupling constants being in reasonable agreement as will be discussed in the next section. Comparison with the data from the infrared study[2] further substantiates the N number assignments.

5.3.2 Spin-spin hyperfine patterns from *ortho*H_2 molecules

Transitions of *ortho*H_2 molecule containing clusters show hyperfine patterns due to the nuclear magnetic spin-spin coupling of the hydrogen nuclei. The spin-spin interaction energy of two equivalent nuclei with spin angular momentum quantum number I is given by equations [2.20] and [2.21].[19] In the present studies, only a-type, $J = 1 - 0$ transitions were measured and only S_{aa} constants were determined from the data. A first estimate for the tensor spin-spin coupling constant can be obtained, as in the previous studies, from the geometry of the *ortho*H_2 molecule. The sign of the spin-spin coupling constant is chosen such that it is negative for homodiatomic molecules.[20] One S_{aa} coupling constant is obtained for each *ortho*-hydrogen molecule in the cluster (see Tables 5.2 and 5.3). Unless specified, the S_{aa} coupling constants in clusters containing more than one *ortho*-hydrogen molecule were constrained to be equal.

When comparing clusters which contain only one *ortho*H_2 molecule, the spin-spin coupling constants S_{aa} are between -88.6 – -121.2 kHz. The coupling constants for the isotopologues of a specific cluster are in better agreement, within 13 kHz. The deviation in S_{aa} between different cluster sizes could be due to the effect of the increasing number of *para*H_2 molecules in the cluster. As the cluster size increases, the motion of the hydrogen molecules could perhaps be restricted. In the He_N – OCS clusters, this increased rigidity is observed by a decrease in the centrifugal distortion constant with the first five helium atoms.[6] The hydrogen clusters could be expected to behave similarly. The *ortho*H_2 – OCS dimer has a spin-spin coupling constant of $S_{aa} = -5D_{aa} = -106$ kHz.[10] Other isotopologues of OCS in the *ortho*H_2 – OCS dimer have $S_{aa} = -121.6$ kHz ($O^{13}CS$).[16] The spin-spin coupling constants obtained for the larger mixed clusters $(pH_2)_{N-1}(oH_2)$ – OCS are in good agreement with the values obtained in the dimer studies.[10,16] The free *ortho*H_2 molecule has a spin-spin constant of $S_{aa} = -5D_{aa} = -288.4$ kHz.[21] The values of S_{aa} of the mixed clusters containing one *ortho*H_2 molecule and the free *ortho*H_2 molecule are on the same order of magnitude, but smaller by a factor of ~2 for the clusters.

In most cases, when a cluster contained two *ortho*H_2 molecules, two S_{aa} constants were fit and they were constrained to being equal. The spin-spin coupling constants for $(oH_2)_2$ – OCS and the minor isotopologues of OCS are $S_{aa} \cong$ -185 kHz. The mixed clusters containing two *ortho*H_2 molecules ($(pH_2)_{N-2}(oH_2)_2$ – OCS) are in good agreement with the $(oH_2)_2$ – OCS results with the largest deviation being 22% for $(pH_2)_2(oH_2)_2$ – $OC^{34}S$ where only two components were resolved. For the main isotopologue, the largest deviation is 15.5% or 29.4 kHz for $(pH_2)_3(oH_2)_2$ - OCS.

For clusters containing three *ortho*H_2 molecules, three S_{aa} constants were fit and were constrained to being equal. The spin-spin coupling constants obtained for the $(oH_2)_3$ – OCS clusters are in agreement for the main isotopologue (S_{aa} = -152.3 kHz) and $O^{13}CS$ (S_{aa} = -159.8 kHz). The transition corresponding to $(oH_2)_3$ – $OC^{34}S$ was not as resolved due to the lower signal intensity and the spin-spin coupling constant is less in agreement (S_{aa} = -182.2 kHz). The mixed clusters which were analysed with three equivalent spin-spin coupling constants are in agreement with the main isotopologue (S_{aa} = -141.3 – -158.6 kHz). Some of the minor isotopologues have spin-spin coupling constants which do not agree as well (S_{aa} = -113.3 – -179.7 kHz) which could be due to some hyperfine components not being resolved.

The analysis of clusters containing four *ortho*H_2 molecules included four equal spin-spin coupling constants. For the $(oH_2)_4$ – OCS clusters, all the spin-spin coupling constants are in good agreement with the maximum deviation of 5.4% from the main isotopologue value (S_{aa} = -214.2 kHz). The mixed clusters with four *ortho*H_2 molecules were analysed in the same manner, but the agreement with $(oH_2)_4$ – OCS clusters is fair at best. The spin-spin coupling constants of the $(pH_2)(oH_2)_4$ – OCS clusters (S_{aa}(OCS) = -151.2 kHz; S_{aa}(O^{13}CS) = -167.9 kHz) are in better agreement with the values obtained for $(pH_2)_2(oH_2)_4$ – OCS clusters (S_{aa}(OCS) = -162.4 kHz; S_{aa}(O^{13}CS) = -151.0 kHz). The assignment of the mixed clusters containing four *ortho*H$_2$ molecules is substantiated by the transition frequency compared to the other clusters of the same *N* number. The agreement between the spin-spin coupling constants of the mixed clusters suggests that the *para*H$_2$ molecule(s) in the cluster have a similar effect on the spin-spin coupling of the *ortho*H$_2$ molecules in both clusters.

Clusters containing five or more *ortho*H$_2$ molecules were not analyzed for spin-spin coupling constants, but do show a complex hyperfine pattern. The pattern continues to evolve as the number of *ortho*H$_2$ molecules increases in the cluster. Although the analysis was not done in this study, it can be seen from the transition frequencies that the hyperfine pattern is collapsing as more *ortho*H$_2$ molecules are added. This is expected since the spin-spin coupling constant of the *ortho*H$_2$ molecule is quite small and the splittings of the hyperfine components would no longer be resolved within the linewidths in a helium expansion (FWHM = ~21 kHz).

The analysis of the structural isomers of $(pH_2)_2(oH_2)_3$ – OCS allowed for non-equal spin-spin coupling constants for the three *ortho*H$_2$ molecules. Due to the symmetry of both structural isomers as seen in Figure 5.6, two of the spin-spin coupling constants were constrained to be equal. The spin-spin coupling constants for structural isomer 1 are: $S_{aa}(1)$ = -174.3 kHz; $S_{aa}(2) = S_{aa}(3)$ = -147.1 kHz. In the structural isomer 1, all three *ortho*H$_2$ molecules are next to each other on the ring. The centre *ortho*H$_2$ molecule has two neighbouring *ortho*H_2 molecules, such as in $(oH_2)_3$ – OCS with S_{aa} = -152.3 kHz. The other two *ortho*H_2 molecules only have one neighbouring *ortho*H_2 molecule, similar to $(oH_2)_2$ – OCS with S_{aa} = -189.4 kHz. The spin-spin coupling constants agree fairly well with the expected values from the geometry. The spin-spin coupling constants for structural isomer 2 are: $S_{aa}(1)$ = -130.0 kHz; $S_{aa}(2) = S_{aa}(3)$ = -196.2 kHz. Structural isomer 2 has an isolated *ortho*H_2 molecule which is surrounded by *para*H_2 molecules, such as $(pH_2)_4(oH_2)$ – OCS with S_{aa} = -110.7 kHz. The other two *ortho*H_2 molecules have only one neighbouring *ortho*H_2 molecule, again similar to $(oH_2)_2$ – OCS with S_{aa} = -189.4 kHz. The decent agreement between the expected values by comparison to similar clusters and the determined spin-spin coupling constants solidifies the assignment of the structural isomers, as well as the proposed geometries given in Figure 5.4.

5.3.3 ^{33}S nuclear quadrupole hyperfine pattern

The ^{33}S nuclear quadrupole coupling constants of the $(oH_2)_N$ – $OC^{33}S$ (N = 2-4) clusters are similar to the value of the $OC^{33}S$ monomer ($\chi_0(^{33}S)$ = -29.1184(12) MHz).[18] The values are also comparable to the corresponding coupling constants in He_N-OCS clusters of the same size.[6] The similarity between all these values is consistent with the OCS molecular axis being nearly coincident with the a-inertial axis. An effective angle θ_a between the a-inertial axis and the OCS molecular axis[18] can be obtained from Equation [2.18]. The values for θ_a obtained are given in Table 4, and are at most 6.9° for the $(oH_2)_2$ – OCS cluster.

5.3.4 Trend in rotational constant with increasing cluster size

In the helium cluster studies, the onset of superfluidity has been observed by examining the trend in the rotational constant as the cluster size increases.[5,6,14,22-24] In

He_N – OCS, the rotational constant B_o decreases[6,14,23] from N=1 to 9 and an increase in B_o is observed between N = 9 and 10. For the hydrogen clusters, it is interesting to look at similar trends in the rotational constant with increased cluster size. Figures 5.7 and 5.8 show the plots of rotational constants (B_o) from the current studies versus the size of the clusters (N) for $(pH_2)_N$ – OCS and $(oH_2)_N$ – OCS, respectively. For comparison, the plots also show the rotational constants obtained from the infrared studies.[1,2] For the $(pH_2)_N$ – OCS clusters, the theoretical rotational constants obtained by Whaley *et al.* are also shown for comparison.[25] The rotational constants steadily decrease with the addition of hydrogen molecules, similar to the trend in the He_N – OCS clusters.[6,14,23] The rotational constants obtained in this study agree quite well with the values from the infrared studies.[1,2] The theoretically obtained rotational constants[25] predict the correct trend of the rotational constants, but are consistently lower than the experimental values.

The rotational constants from microwave and infrared results for the *ortho*H_2 molecule agree within 3.6% until N = 6, where the infrared study ended.[2] The agreement is also quite good (1.8%) for the *para*H_2 molecule cluster case until N = 6. At N = 7, there is a difference of 11.5% between the microwave and the infrared values. This is a result of a larger error in B_o for N=7 in the infrared study, where only two transitions (P(1) and R(0)) of $(pH_2)_7$ – OCS were measured.[2]

It is difficult to compare the microwave results with those of the helium nanodroplet experiments[26-29] since the helium atoms in the droplet appears to affect structure and energetics of the $(pH_2)_N$ – OCS cluster. The nanodroplet geometry shows six *para*H_2 molecules forming a ring around the OCS molecule,[26,29] but the infrared results predict only five *para*H_2 molecules on a ring in the bare hydrogen clusters.[2] There is insufficient microwave data to determine the geometry of the clusters. The agreement between the rotational constant of the infrared[2] and microwave studies suggests that the vibrational shifts suggesting five molecules on the ring is accurate.

5.4 Summary

The pure rotational transitions of $(pH_2)_N$ – OCS and $(oH_2)_N$ - OCS for $N = 2$ to 7 were investigated by microwave spectroscopy. Additionally, mixed clusters were investigated and showed the evolving hyperfine patterns consistent with an increasing number of *ortho*H_2 molecules. While the OCS and $O^{13}CS$ isotopologues were primarily investigated, the $J = 1 - 0$ rotational transitions of some $OC^{34}S$, $O^{13}C^{34}S$, and $OC^{33}S$ isotopologues were also measured. Unfortunately, only $J = 1 - 0$ transitions were measured for all clusters despite extensive MW-MW DR studies, therefore the rotational constant (B) corresponds to ½ the $J = 1 - 0$ transition frequency. The rotational constants obtained from this study agree well with the rotational constants obtained from the infrared study of $(H_2)_N$ – OCS clusters.[2] The theoretical rotational constants by Whaley *et al.*[25] show similar agreement, although the values consistently underestimate the rotational constant observed. The spin-spin hyperfine constants for *ortho*H_2 molecules were obtained for clusters containing less than five *ortho*H_2 molecules. The evolving hyperfine pattern in mixed clusters was analysed and the spin-spin coupling constants obtained. The analysis of the hyperfine patterns of the structural isomers of $(pH_2)_2(oH_2)_3$ - OCS provided spin-spin coupling constants which were compared to the values obtained for *ortho*H_2 molecules in similar environments. This analysis solidified the assignment and proposed geometries of the structural isomers. Clusters with $OC^{33}S$ were also analysed for the ^{33}S nuclear quadrupole coupling constant. The evolution of B with N for $(H_2)_N$ - OCS clusters shows an increase in the moment of inertia as the number of solvating hydrogen molecules increases. This is consistent with a classical physics picture for these smaller doped hydrogen clusters. Manifestations of quantum effects in hydrogen molecule clusters are expected to occur at larger cluster sizes than in He_N – molecule clusters due to increased intermolecular interactions between hydrogen molecules as compared to helium atoms. The feasibility of studying small doped hydrogen clusters with rotational spectroscopy has been shown by this study.

5.5 Figures

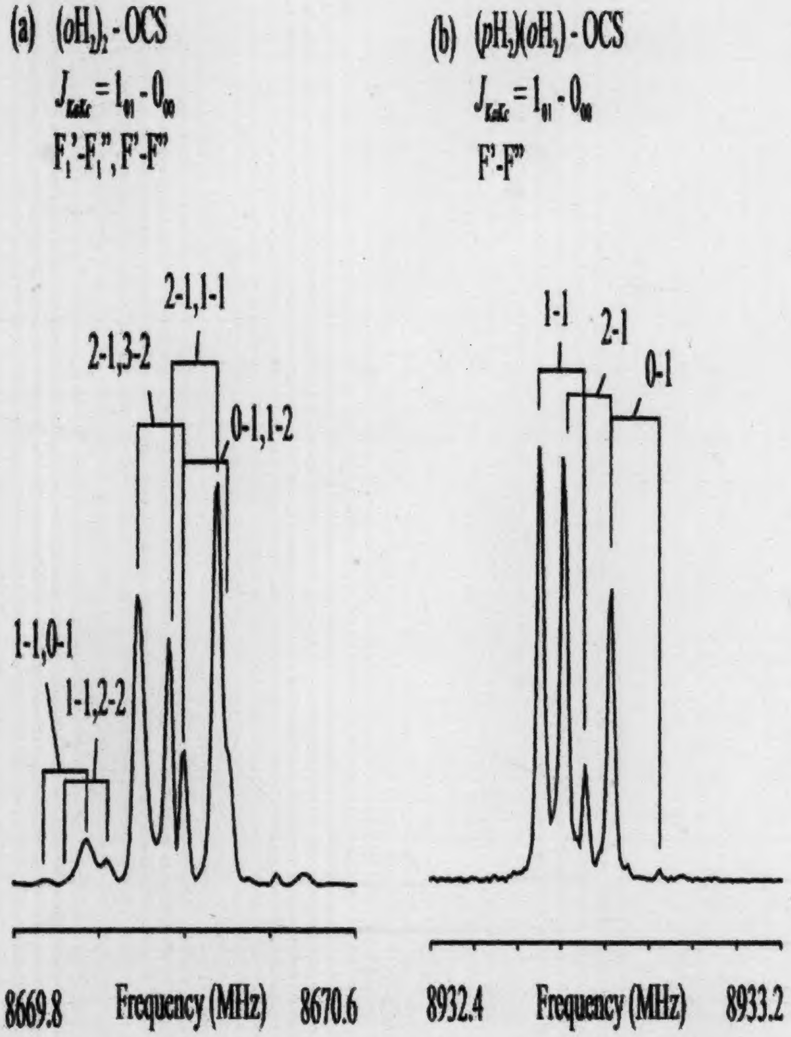

Figure 5.1: $J_{KaKc} = 1_{01} - 0_{00}$ transitions of (a) $(o\mathrm{H}_2)_2 - \mathrm{OCS}$, 8k data points at 10 ns interval, 10 averaging cycles, the data set was supplemented with 8k zeros before Fourier transformation. (b) $(p\mathrm{H}_2)(o\mathrm{H}_2) - \mathrm{OCS}$, 8k data points at 10 ns interval, 100 averaging cycles, the data set was supplemented with 8k zeros before Fourier transformation. The differences in the hyperfine structures of the two transitions are due to the additional $o\mathrm{H}_2$ molecule in (a).

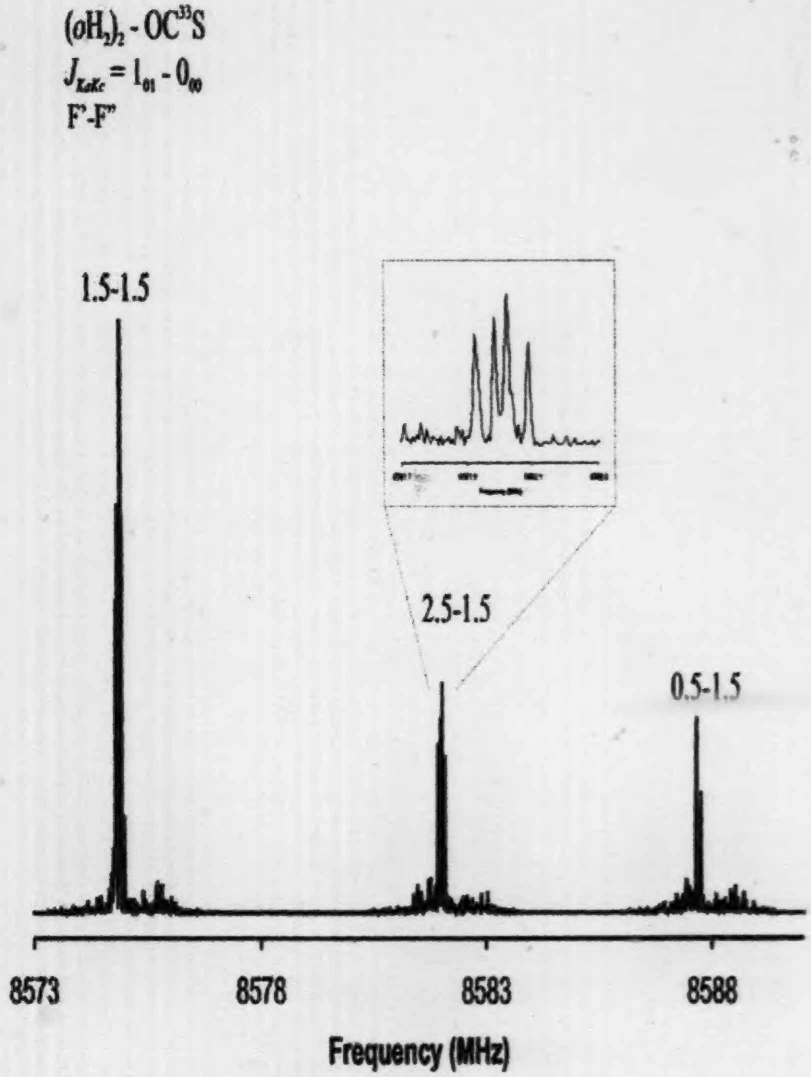

Figure 5.2: $J_{KaKc} = 1_{01} - 0_{00}$ transition of $(o\mathrm{H}_2)_2 - \mathrm{OC}^{33}\mathrm{S}$, 8k data points at 10 ns interval, 5000 averaging cycles, the data set was supplemented with 8k zeros before Fourier transformation. This spectrum is a composite of three separate experiments due to the small bandwidth of our spectrometer. The larger hyperfine splitting in this spectrum is due nuclear quadrupole coupling interactions with the ^{33}S quadrupolar nucleus ($I(^{33}\mathrm{S}) = 3/2$).

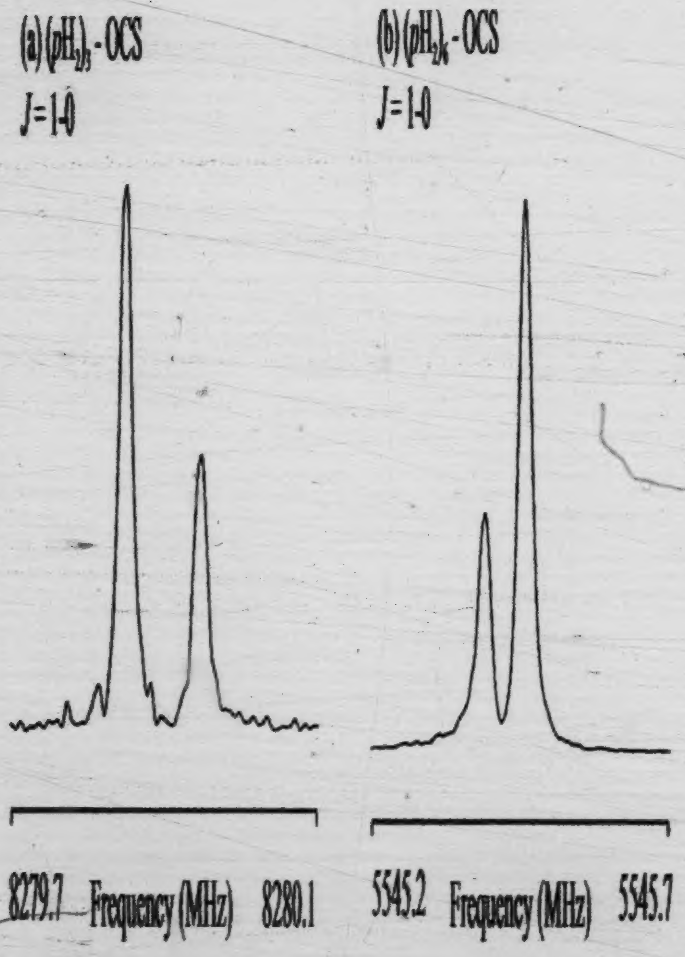

Figure 5.3: $J = 1 - 0$ transitions of (a) $(pH_2)_3$ – OCS, 8k data points at 10 ns interval, 100 averaging cycles, the data set was supplemented with 8k zeros before Fourier transformation with a non-enriched *para*H_2 sample, and (b) $(pH_2)_6$ – OCS, 8k data points at 10 ns interval, 10 averaging cycles, the data set was supplemented with 8k zeros before Fourier transformation with an enriched *para*H_2 sample.

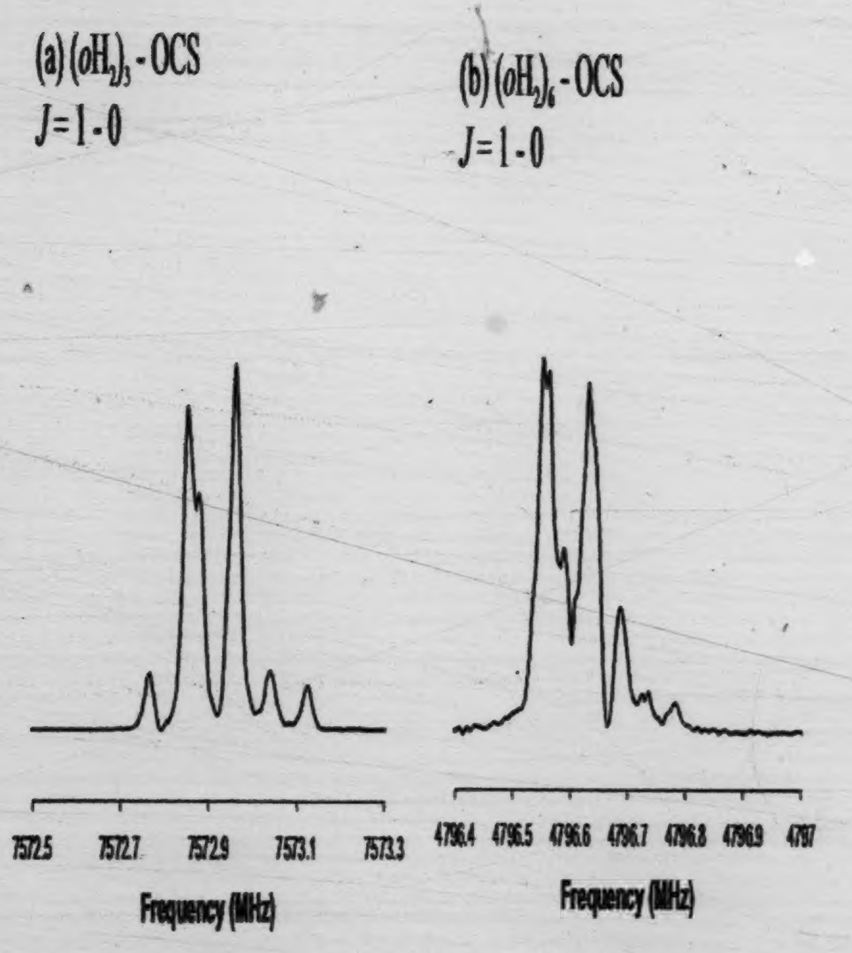

Figure 5.4: $J = 1 - 0$ transitions of (a) $(oH_2)_3$ – OCS, 8k data points at 10 ns interval, 250 averaging cycles, the data set was supplemented with 8k zeros before Fourier transformation, and (b) $(oH_2)_6$ – OCS, 8k data points at 10 ns interval, 100 averaging cycles, the data set was supplemented with 8k zeros before Fourier transformation. The hyperfine structure in each of these transitions is dependent on the number of *ortho*H_2 molecules in the cluster. The hyperfine can aid in the assignment of the relative cluster size.

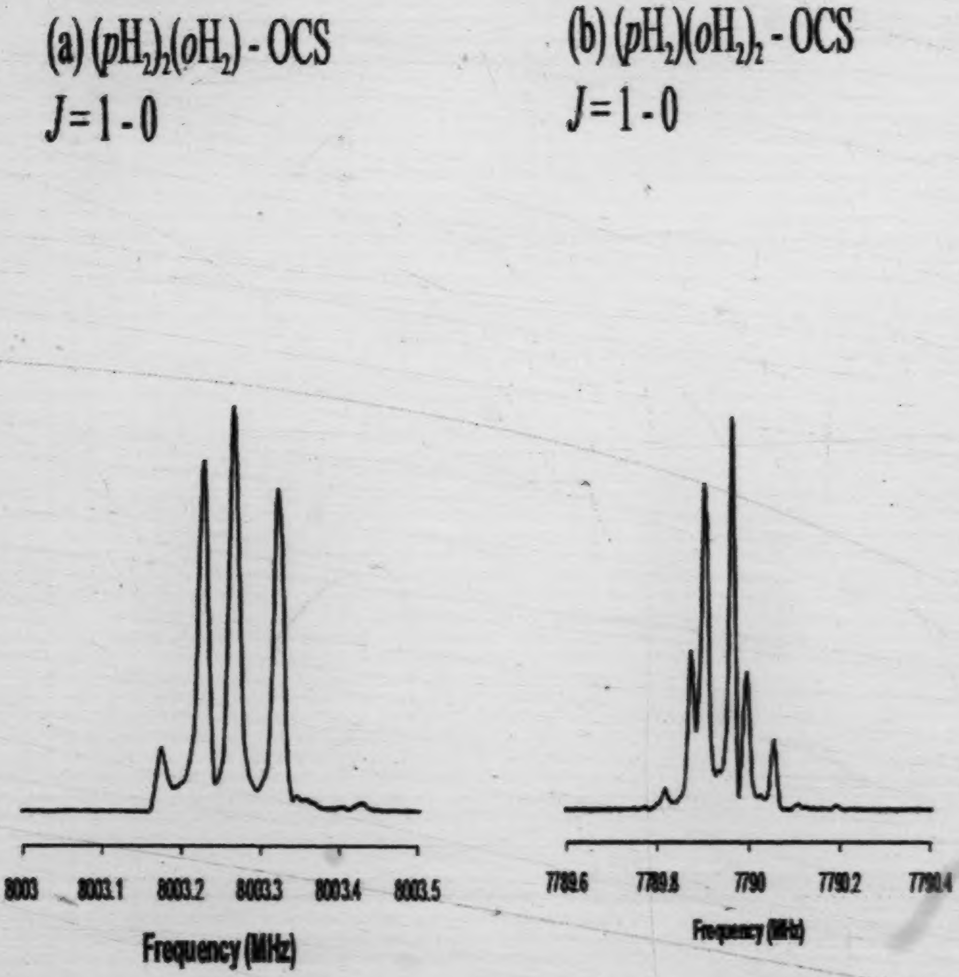

Figure 5.5: $J = 1 - 0$ transitions of the mixed clusters found for $N = 3$, (a) $(pH_2)_2(oH_2)$ – OCS, 100 averaging cycles taken at 8k points and 16k points Fourier transform, and (b) $(pH_2)(oH_2)_2$ – OCS, 150 averaging cycles taken at 8k points and 16k points Fourier transform with an enriched *para*H_2 sample. The evolution of the hyperfine structure, comparing with Figures 3(a) and 4(a) also, is due to the change in the number of *ortho*H_2 molecules in the clusters.

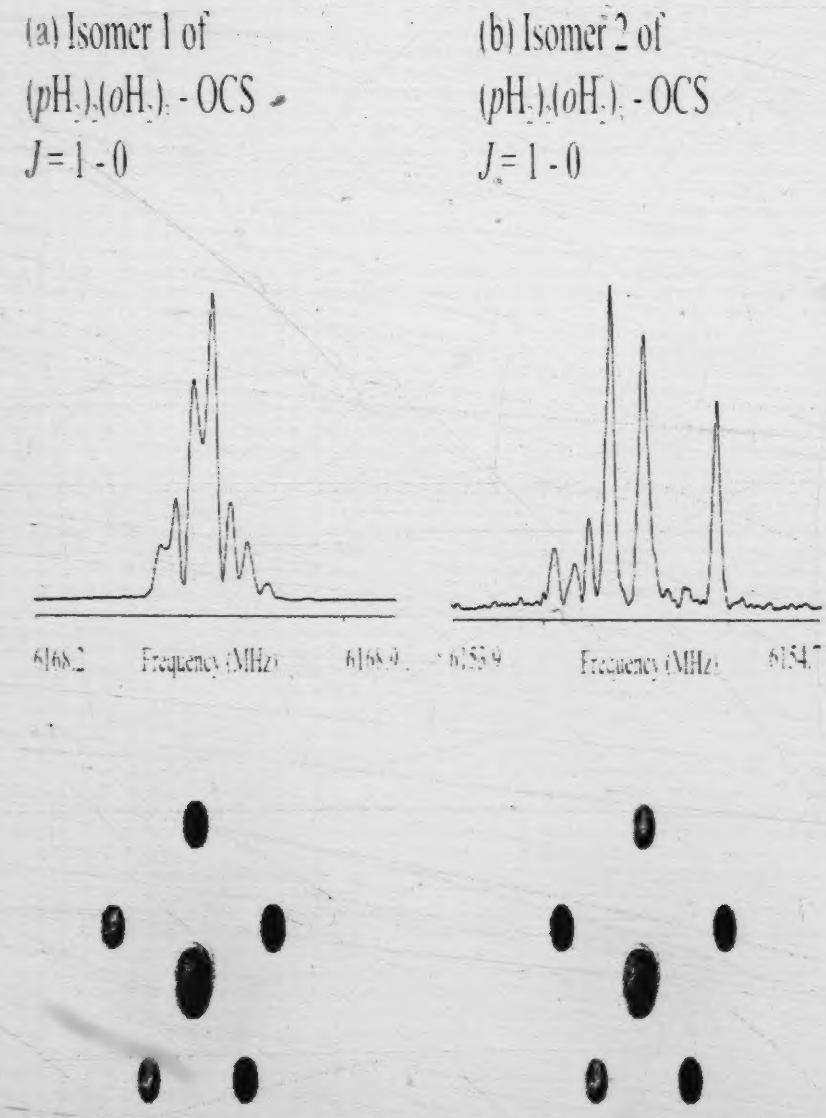

Figure 5.6: $J = 1 - 0$ transitions of the structural isomers of $(pH_2)_2(oH_2)_3 - OCS$, (a) Isomer 1, 8k data points at 10 ns interval, 50 averaging cycles, the data set was supplemented with 8k zeros before Fourier transformation, and (b) Isomer 2, 8k data points at 10 ns interval, 300 averaging cycles, the data set was supplemented with 8k zeros before Fourier transformation. Below each transition is the proposed geometry of the structural isomer with simple balls representing the H_2 molecules (green = *para*H_2; blue = *ortho*H_2).

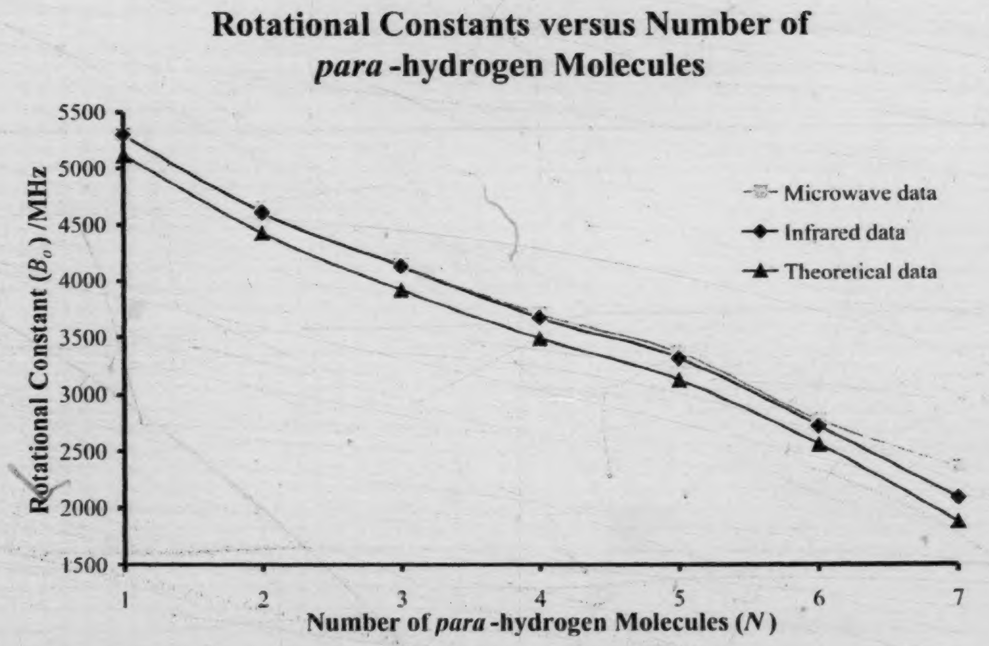

Figure 5.7: Plot of rotational constants (B_o) in MHz versus the cluster size N for $(pH_2)_N$ – OCS clusters. The microwave data is compared to the B_o values obtained in the infrared study [Reference 2] and to a theoretical study [Reference 25].

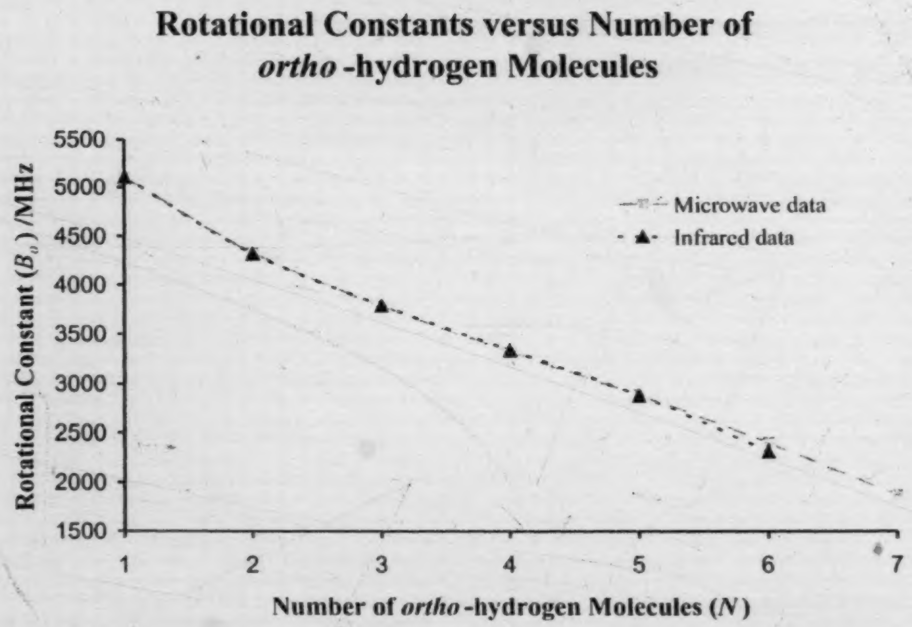

Figure 5.8: Plot of rotational constants (B_o) in MHz versus the cluster size N for $(o\text{H}_2)_N - \text{OCS}$ clusters. The microwave data is compared to the B_o values obtained in the infrared study.[2]

5.6 Tables

Table 5.1

Measured frequencies (MHz) of the $J = 1\text{-}0$ rotational transitions of $(p\mathrm{H}_2)_N$ – OCS clusters.

Size	$^{16}\mathrm{O}^{12}\mathrm{C}^{32}\mathrm{S}$	$^{16}\mathrm{O}^{12}\mathrm{C}^{34}\mathrm{S}$	$^{16}\mathrm{O}^{13}\mathrm{C}^{32}\mathrm{S}$	$^{16}\mathrm{O}^{13}\mathrm{C}^{34}\mathrm{S}$
$(p\mathrm{H}_2)_2$	9190.2949	8993.6855	9173.1871	
$(p\mathrm{H}_2)_3$	8279.8940	8117.5594	8268.5515	
$(p\mathrm{H}_2)_4$	7354.8633			
$(p\mathrm{H}_2)_5$	6727.0838	6598.7433	6722.3586	6594.4960
$(p\mathrm{H}_2)_6$	5545.4195	5441.0913	5543.7664	
$(p\mathrm{H}_2)_7$	4693.7457		4693.4178	

Table 5.2

Rotational transition frequencies (in MHz) of $(oH_2)_N$ – OCS clusters.

Size	$^{16}O^{12}C^{32}S$	$^{16}O^{12}C^{34}S$	$^{16}O^{13}C^{32}S$	$^{16}O^{13}C^{34}S$
$(oH_2)_2$				
1-0	8669.9163			
	8669.9682			
	8670.1364	8495.6329	8655.2902	8479.2038
	8670.2149	8495.7064	8655.3606	8479.2746
	8670.3465	8495.8442	8655.4950	8479.4103
$S_{aa}(oH_2)^a$	-0.1894(11)	-0.1860(25)	-0.1805(25)	-0.1821(25)
$(oH_2)_3$				
1-0	7572.7344	7433.0685	7563.1689	
	7572.8041	7433.1589	7563.2638	
	7572.8317		7563.2836	
	7572.9171	7433.2753	7563.3658	
	7572.9878		7563.4453	
$S_{aa}(oH_2)^a$	-0.1523(15)	-0.1822(23)	-0.1598(15)	
$(oH_2)_4$				
1-0	6638.6794		6632.6792	
	6638.7557	6527.2553	6632.7495	
	6638.8706	6527.3653	6632.8807	6520.2137
	6639.0037	6527.4873	6633.0053	6520.3416
	6639.0337	6527.5176	6633.0360	
$S_{aa}(oH_2)^a$	-0.2142(12)	-0.2026(19)	-0.2177(14)	-0.2095(45)
$(oH_2)_5$				
1-0	5780.1202[b]		5776.5431[b]	
	5780.1965		5776.6505	
	5780.2677		5776.6989	
	5780.3470		5776.8334	
	5780.4224			
$(oH_2)_6$				
1-0	4796.5800[b]		4795.9955[b]	
	4796.6046		4796.0237	
	4796.6471		4796.1163	
	4796.7479			
$(oH_2)_7$				
1-0	3739.9990[b]			
	3740.0583			
	3740.1413			

[a] Spectrum fit with one spin-spin coupling constant for each *ortho*H_2 molecule in the cluster, the coupling constants were constrained to be equal.

[b] Hyperfine components not fit due to the complexity of the spectrum associated with five or more *ortho*H_2 molecules in the cluster.

Table 5.3

Rotational transition frequencies and *ortho*H_2 spin-spin coupling constants (in MHz) of the mixed $(pH_2)_x(oH_2)_{N-x}$ – OCS clusters.

Size	$^{16}O^{12}C^{32}S$	$^{16}O^{12}C^{34}S$	$^{16}O^{13}C^{32}S$	$^{16}O^{13}C^{34}S$
$N = 2$				
$(pH_2)(oH_2)$				
1-0	8932.6979	8747.1300	8916.7211	
	8932.7554	8747.1907	8916.7794	
	8932.8681		8916.8803	
$S_{aa}(oH_2)$	-0.1144(19)	-0.1012(47)	-0.1067(19)	
$N = 3$				
$(pH_2)(oH_2)_2$				
1-0	7789.8536	7641.7682	7779.4686	
	7789.9119	7641.8326	7779.5353	
	7790.0608		7779.6694	
$S_{aa}(oH_2)^a$	-0.1860(25)	-0.2147(94)	-0.1776(25)	
$(pH_2)_2(oH_2)$				
1-0	8003.2117	7841.3836	7994.0753	
	8003.2742	7841.4293	7994.1369	
	8003.3826	7841.5455	7994.2557	
$S_{aa}(oH_2)$	-0.1144(19)	-0.1096(19)	-0.1212(19)	
$N = 4$				
$(pH_2)(oH_2)_3$				
1-0	6823.5705	6685.3639	6820.9808	6683.0490
	6823.6453	6685.4029	6821.1212	6683.0715
	6823.6773	6685.4516	6821.2006	
	6823.7619	6685.5371	6821.2784	
$S_{aa}(oH_2)^a$	-0.1586(23)	-0.1509(23)	-0.1797(17)	-0.1133(67)
$(pH_2)_2(oH_2)_2$				
1-0	7034.6088	6908.2016	7028.8329	
	7034.6759	6908.2709	7028.9092	
	7034.8133		7029.0439	
$S_{aa}(oH_2)^a$	-0.1811(25)	-0.2310(28)	-0.1850(25)	
$(pH_2)_3(oH_2)$				
1-0	7229.7444		7223.2965	
	7229.8085		7223.3543	
	7229.8786		7223.4460	
$S_{aa}(oH_2)$	-0.0886 (19)		-0.0998(19)	
$N = 5$				
$(pH_2)(oH_2)_4$				
1-0	5965.8446		5961.7676	
	5965.9146		5961.8381	
	5966.0153		5961.9568	
$S_{aa}(oH_2)^a$	-0.1512(25)		-0.1679(25)	
$(pH_2)_2(oH_2)_3$ (isomer 1)				

1-0	6168.4700	6165.0797
	6168.5033	6165.1102
	6168.5735	
$S_{aa}(o\mathrm{H}_2(1))$	-0.1743(68)	-0.166(73)
$S_{aa}(o\mathrm{H}_2(2))$	-0.1471(27)	-0.1482(27)
$S_{aa}(o\mathrm{H}_2(3))$	-0.1471^b	-0.1482^b
$(p\mathrm{H}_2)_2(o\mathrm{H}_2)_3$ (isomer 2)		
1-0	6154.1590	6149.5451
	6154.2045	6149.6163
	6154.2748	
$S_{aa}(o\mathrm{H}_2(1))$	-0.1300(47)	-0.1396(47)
$S_{aa}(o\mathrm{H}_2(2))$	-0.1962(92)	-0.177(18)
$S_{aa}(o\mathrm{H}_2(3))$	-0.1962^b	-0.177^b
$(p\mathrm{H}_2)_3(o\mathrm{H}_2)_2$		
1-0	6345.8499	
	6345.9384	6342.1233
	6346.0383	6342.2306
$S_{aa}(o\mathrm{H}_2)$	-0.1600(25)	-0.1324(35)
$(p\mathrm{H}_2)_4(o\mathrm{H}_2)$		
1-0	6577.5778	6573.2301
	6577.6322	6573.2941
	6577.7424	6573.4074
$S_{aa}(o\mathrm{H}_2)$	-0.1107 (19)	-0.1188 (19)
$N = 6$		
$(p\mathrm{H}_2)(o\mathrm{H}_2)_5$		
1-0	4876.9441^c	4876.2976^c
	4877.0292	4876.3402
	4877.0688	4876.4380
$(p\mathrm{H}_2)_2(o\mathrm{H}_2)_4$		
1-0	5013.585	5013.0563
	5013.6935	5013.1572
	5013.7697	5013.2280
$S_{aa}(o\mathrm{H}_2)^a$	-0.1624(23)	-0.1510(25)
$(p\mathrm{H}_2)_3(o\mathrm{H}_2)_3$ (isomer 1)		
1-0	5121.0575^d	5120.4256^d
	5121.1426	5120.4610
		5120.5191
$(p\mathrm{H}_2)_3(o\mathrm{H}_2)_3$ (isomer 2)		
1-0	5197.1136^d	5196.4994^d
	5197.2131	5196.5325
	5197.2377	5196.5668
		5196.5932
$(p\mathrm{H}_2)_4(o\mathrm{H}_2)_2$		
1-0	5380.0006^e	
$(p\mathrm{H}_2)_5(o\mathrm{H}_2)$		
1-0	5453.1773	5451.6124

	5453.2356	5451.6836
	5453.3484	5451.7992
$S_{aa}(oH_2)$	-0.1150(19)	-0.1248(19)
$N = 7$		
$(pH_2)(oH_2)_6$		
1-0	3820.2597[c]	
	3820.3387	
	3820.4616	
$(pH_2)_4(oH_2)_3$		
1-0	4283.7599	
	4283.8272	
	4283.9823	
$S_{aa}(oH_2)$[a]	-0.1413(18)	
$(pH_2)_5(oH_2)_2$		
1-0	4487.0463	
	4487.1286	
	4487.2539	
$S_{aa}(oH_2)$[a]	-0.1802(25)	
$(pH_2)_6(oH_2)$		
1-0	4637.3855	4637.0496
	4637.4375	4637.1074
	4637.5382	4637.1933
$S_{aa}(oH_2)$	-0.1026(19)	-0.0957(19)

[a] One spin-spin coupling constant is included in the fit for each *ortho*H_2 molecule and they are constrained to be equal.

[b] $S_{aa}(oH_2(3))$ constrained to being equal to $S_{aa}(oH_2(2))$, since two *ortho*H_2 molecules are in the same environment (due to the symmetry of the cluster) and should have the same spin-spin coupling constant.

[c] Hyperfine components not fit due to the complexity of the spectrum associated with five or more *ortho*H_2 molecules in the cluster.

[d] Hyperfine components not analysed since the data set is insufficient to resolve the three spin-spin coupling constants necessary.

[e] Hyperfine components could not be resolved for this cluster, hyperfine pattern appeared to be collapsed. Transition frequency obtained by determining the centre frequency of the measured component as no Doppler pairs could be assigned.

Table 5.4

Rotational transition frequencies of the nuclear quadrupole hyperfine components (MHz) of the $J = 1\text{-}0$ transitions and nuclear quadrupole coupling constants (in MHz) of the $(o\mathrm{H}_2)_N - \mathrm{OC}^{33}\mathrm{S}$ clusters.

Size F'-F"	$^{16}\mathrm{O}^{12}\mathrm{C}^{33}\mathrm{S}$ ν_{obs}	 $\Delta\nu^a$
$N = 2$	$(o\mathrm{H}_2)_2$	
1.5-1.5	8574.8446	0.01
	8574.8629	-2.5
	8574.9409	3.4
2.5-1.5	8581.9656	2.4
	8582.0282	-4.7
0.5-1.5	8587.7079	1.3
$S_{aa}(o\mathrm{H}_2)$	-0.1297(31)	
$\chi_{aa}(^{33}\mathrm{S})$	-28.4861(47)	
θ_a	6.9°	
$\chi_{aa}(^{33}\mathrm{S})$ in $\mathrm{He}_2 - \mathrm{OC}^{33}\mathrm{S}$	-26.9344(32)[b]	
$N = 3$	$(o\mathrm{H}_2)_3$	
1.5-1.5	7495.4509	6.9
	7495.4661	12.2
2.5-1.5	7502.5742	-10.9
	7502.6413	-16.7
	7502.6741	-15.2
0.5-1.5	7508.4350	23.8
$S_{aa}(o\mathrm{H}_2)$	-0.0857(23)	
$\chi_{aa}(^{33}\mathrm{S})$	-28.8819(56)	
θ_a	4.2°	
$\chi_{aa}(^{33}\mathrm{S})$ in $\mathrm{He}_3 - \mathrm{OC}^{33}\mathrm{S}$	-27.9036(36)[b]	
$N = 4$	$(o\mathrm{H}_2)_4$	
1.5-1.5	6575.8964[c]	
	6575.9409	
	6575.9782	
2.5-1.5	6583.0660	
	6583.1049	
	6583.1423	
0.5-1.5	6588.8526	
$\chi_{aa}(^{33}\mathrm{S})$	-28.6955(63)	
θ_a	5.6°	
$\chi_{aa}(^{33}\mathrm{S})$ in $\mathrm{He}_4 - \mathrm{OC}^{33}\mathrm{S}$	-28.2449(33)[b]	
$S_{aa}(o\mathrm{H}_2)$ in $o\mathrm{H}_2$ - OCS	-0.106[d]	
$S_{aa}(o\mathrm{H}_2)$ in $o\mathrm{H}_2 - \mathrm{O}^{13}\mathrm{CS}$	-0.121[e]	
$\chi_{aa}(^{33}\mathrm{S})$ in $\mathrm{OC}^{33}\mathrm{S}$	-29.1184(12)[f]	

[a] $\Delta\nu = \nu_{obs.} - \nu_{calc.}$ [b] Reference 6. [c] Spin-spin coupling constant could not be fit, the average of the *ortho*H_2 component was fit to the $^{33}\mathrm{S}$ nuclear quadrupole coupling constant. [d] Reference 10, $S_{aa} = -5D_{aa}$. [e] Reference 16. [f] Reference 18.

5.7 References

[1] J. Tang and A. R. W. McKellar, *J. Chem. Phys.* **116** (2), 646 (2002).

[2] J. Tang and A. R. W. McKellar, *J. Chem. Phys.* **121** (7), 3087 (2004).

[3] J. Tang and A. R. W. McKellar, *J. Chem. Phys.* **115** (7), 3053 (2001).

[4] J. Tang and A. R. W. McKellar, *J. Chem. Phys.* **119** (11), 5467 (2003).

[5] J. Tang, Y. Xu, A. R. W. McKellar, and W. Jäger, *Science* **297** (5589), 2030 (2002).

[6] Y. Xu and W. Jäger, *J. Chem. Phys.* **119** (11), 5457 (2003).

[7] T. J. Balle and W. H. Flygare, *Rev. Sci. Instrum.* **52** (1), 33 (1981).

[8] Y. Xu and W. Jäger, *J. Chem. Phys.* **106** (19), 7968 (1997).

[9] K. J. Higgins and W. Klemperer, *Private communication.*

[10] Z. H. Yu, K. J. Higgins, W. Klemperer, M. C. McCarthy, and P. Thaddeus, *J. Chem. Phys.* **123** (22), 221106 (2005).

[11] Z. H. Yu, K. J. Higgins, W. Klemperer, M. C. McCarthy, P. Thaddeus, K. Liao, and W. Jäger, *J. Chem. Phys.* **127**, 054305 (2007).

[12] V. N. Markov, Y. Xu, and W. Jäger, *Rev. Sci. Instrum.* **69** (12), 4061 (1998).

[13] K. Brendal and H. Mäder *Private Communication.*

[14] A. R. W. McKellar, Y. Xu, and W. Jäger, *Phys. Rev. Lett.* **97** (18), 183401 (2006).

[15] W. Topic, W. Jäger, N. Blinov, P.-N. Roy, M. Botti, and S. Moroni, *J. Chem. Phys.* **125** (14), 144310 (2006).

[16] J. M. Michaud, K. Liao, and W. Jäger, *Mol. Phys.* **106**, 23 (2008).

[17] H. M. Pickett, *J. Mol. Spectrosc.* **148** (2), 371 (1991).

[18] J. M. Reinartz and A. Dymanus, *Chem. Phys. Lett.* **24** (3), 346 (1974).

[19] N. Heineking and M. C. L. Gerry, *J. Mol. Spectrosc.* **158**, 62 (1993).

[20] H. S. P. Müller and M. C. L. Gerry, *J. Chem. Phys.* **103** (2), 577 (1995).

[21] N. F. Ramsey, *Phys. Rev.* **85** (1), 60 (1952).

[22] A. R. W. McKellar, *J. Chem. Phys.* **125** (16), 164328 (2006).

[23] A. R. W. McKellar, Y. Xu, and W. Jäger, *J. Phys. Chem. A* **111** (31), 7329 (2007).

[24] W. C. Topic and W. Jäger, *J. Chem. Phys.* **123** (6), 064303 (2005).

[25] F. Paesani, R. E. Zillich, and K. B. Whaley, *J. Chem. Phys.* **119** (22), 11682 (2003).

[26] S. Grebenev, E. Lugovoi, B. G. Sartakov, J. P. Toennies, and A. F. Vilesov, *Faraday Discuss.* **118**, 19 (2001).

[27] S. Grebenev, B. Sartakov, J. P. Toennies, and A. F. Vilesov, *Science* **289** (5484), 1532 (2000).

[28] S. Grebenev, B. G. Sartakov, J. P. Toennies, and A. F. Vilesov, *J. Chem. Phys.* **118** (19), 8656 (2003).

[29] S. Grebenev, B. Sartakov, J. P. Toennies, and A. Vilesov, *Phys. Rev. Lett.* **89** (22) 225301 (2002).

Chapter 6

Spectroscopic investigation of $(H_2)_N - HCCCN$ clusters

Previous studies of $He_N - HCCCN$ clusters ($N = 2\text{-}17, 26\text{-}31$)[1] and of the $H_2 -$ HCCCN dimer motivated the extension to larger $(H_2)_N - HCCCN$ clusters. The onset of superfluidity in the $He_N - HCCCN$ clusters occurred at $N = 10$,[1] a cluster size one helium atom larger than the $He_N - OCS$ clusters.[2,3] The doped hydrogen clusters studies are partly motivated by the possibility of observing superfluidity in *para*-hydrogen, the study of $(pH_2)_N - HCCCN$ clusters would provide another system for comparison with the $(pH_2)_N - OCS$ clusters.

This chapter describes the microwave rotational spectroscopic study of $(H_2)_N -$ HCCCN clusters ($N = 2\text{-}6$). The experimental setup and conditions used for the investigation of larger clusters will be discussed in Section 6.2. A discussion of the experimental results and spectroscopic analyses will follow in Section 6.3. The assignment of N, the number of solvating hydrogen molecules, will be detailed in Section 6.4.

6.1 Experimental details

In this thesis, the $(H_2)_N - HCCCN$ clusters were studied by high resolution microwave spectroscopy. The pulsed-jet Fourier transform microwave spectrometer described in Chapter 2 was used to observe the rotational spectra of $(H_2)_N - HCCCN$. The experimental details for the study of $(H_2)_N - HCCCN$ are quite similar to the previous studies of H_2 – HCCCN and $(H_2)_N$ – OCS. Briefly, the sample mixtures contained low concentrations (< 0.3 % HCCCN) with 1-3 % H_2 or enriched *para*H_2 gas in helium. The pressures used for the studies of larger clusters depend on the specific cluster size that is desired. The range of pressures used for the $(H_2)_N$ – HCCCN studies was between 10-90 atm. All studies using enriched *para*H_2 sample were performed with a diluted *para*H_2 (10%) in helium gas sample added to a cylinder containing the appropriate amount of HCCCN gas. The cyanoacetylene gas was synthesized as described in Chapter 4. The enriched *para*H_2 gas was obtained from a catalytic converter whose details have been presented in Chapter 2.

Microwave-microwave double resonance (DR) experiments were performed to determine the frequencies of transitions with higher J values. Details of the double resonance experiments are outlined in Chapter 2. The decoherence DR experiment scheme was successful with some $(H_2)_N$ – HCCCN clusters. The coherence DR experiment scheme was attempted, but did not lead to the same success as obtained in He_N – molecule studies.[1,3,4]

6.2 Results and analyses

Since no previous studies provided predictions for rotational constants of $(H_2)_N$ – HCCCN clusters, fractional changes were compared for He_N – OCS (Reference 4) and $(H_2)_N$ – OCS and I assumed that the HCCCN clusters would follow approximately the same trend. This is the same procedure as used for predictions of the $J_{KaKc} = 1_{01} - 0_{00}$ transition of the H_2 – HCCCN dimer. Transitions of minor isotopologues of cyanoacetylene ($HCCC^{15}N$ and DCCCN) were measured for some clusters. The clusters were measured as pure *para*H_2 molecule clusters, pure *ortho*H_2 molecule clusters, as well as mixed clusters containing a combination of *para*H_2 and *ortho*H_2 molecules. Spectra corresponding to clusters containing any number of *ortho*H_2 molecules show spin-spin hyperfine patterns. As with the study of $(H_2)_N$ – OCS clusters, the mixed clusters show evolving hyperfine patterns as the number of *ortho*H_2 molecules increase. Nuclear electric quadrupole hyperfine patterns were observed and analysed for ^{14}N [$I(^{14}\mathrm{N})$ = 1]and D [I(D) = 1] containing isotopologues. The coupling scheme used in the fitting procedure to account for the nuclear quadrupole coupling interaction for applicable nuclei was: $\mathbf{J} + \mathbf{I}_{14N} = \mathbf{F}_1$, $\mathbf{F}_1 + \mathbf{I}_D = \mathbf{F}$. For clusters with spin-spin interactions due to *ortho*H_2 molecules, a spin-spin coupling constant for each *ortho*H_2 molecule was included in the fit. As in the $(H_2)_N$ – OCS analysis, the spin-spin coupling constants were constrained to be equal.

6.2.1 $N = 2$

The gas mixture for the initial searches for $N = 2$ clusters contained < 0.3 % HCCCN with 1-3 % H_2 gas or enriched *para*H_2 gas in 10-12 atm of He. Three transitions, corresponding to the three possible H_2 spin modifications, with the appropriate hyperfine patterns and spacing for N=2 clusters were found and measured. The overall autoscan spectrum showing the three $J_{KaKc} = 1_{01}$ - 0_{00} transitions is shown in Figure 6.1. Decoherence DR experiments were successfully performed and the $J_{KaKc} = 2_{02} - 1_{01}$ transitions for the $N = 2$ clusters were measured. The transition frequencies and determined spectroscopic parameters for the $N = 2$ clusters are listed in Table 6.1. The signal intensities of the transitions were not strong enough to observe any possible *b*-type transitions of the $N = 2$ clusters. Transitions of $(pH_2)_2$ – HCCCN clusters are split by only the nuclear quadrupole coupling of ^{14}N nucleus, as expected since *para*H_2 molecules are spinless bosons. Transitions of $(o\mathrm{H}_2)_2 - \mathrm{HCCCN}$ clusters have additional hyperfine structure due to the spin-spin interaction of the two *ortho*H_2 molecules. The mixed cluster, $(p\mathrm{H}_2)(o\mathrm{H}_2) - \mathrm{HCCCN}$, contains one *ortho*$\mathrm{H}_2$ molecule and the splitting observed in the $J_{KaKc} = 1_{01} - 0_{00}$ transition is consistent with the spin-spin interaction of one *ortho*H_2 molecule.

Transition frequencies for minor isotopologues of $N = 2$ clusters were predicted from the changes in the moment of inertia with isotopic substitution. The search was guided by the predictions and transitions were successfully measured. Transitions of $(\mathrm{H}_2)_N - \mathrm{DCCCN}$ clusters were split by additional nuclear quadrupole coupling from the D nucleus. Transitions of $(\mathrm{H}_2)_N - \mathrm{HCCC^{15}N}$ clusters were helpful in analyzing the hyperfine pattern due to the *ortho*H_2 molecules in a particular cluster since no other hyperfine interaction is present. Figure 6.2 shows the evolving hyperfine pattern of the $J_{KaKc} = 1_{01} - 0_{00}$ transitions of $(\mathrm{H}_2)_2 - \mathrm{HCCC^{15}N}$ clusters with increasing number of *ortho*H_2 molecules. The transition frequencies, quantum number assignments, and determined spectroscopic parameters for $(\mathrm{H}_2)_2 - \mathrm{DCCCN}$ and $(\mathrm{H}_2)_2 - \mathrm{HCCC^{15}N}$ clusters are presented in Table 6.2.

6.2.2 $N = 3$

The optimized gas mixture for observing the $N = 3$ clusters contained < 0.3% HCCCN with 1-2% H_2 or enriched *para*H_2 gas in 14-16 atm of helium. The spectral searches for the $J = 1 - 0$ transition of $(\mathrm{H}_2)_3 - \mathrm{HCCCN}$ were performed by scanning at a lower frequency than the transitions of $(\mathrm{H}_2)_2 - \mathrm{HCCCN}$. From the $(\mathrm{H}_2)_N - \mathrm{OCS}$ studies, the rotational constant of larger clusters is expected to continue to decrease from the small-size regime. A set of transitions was observed with the appropriate spacing of mixed clusters, as well as with an evolving hyperfine pattern as the number of *ortho*H_2 molecules increases. Figure 6.3 shows an experimental scan of the frequency region with 8 averaging cycles. The transition frequencies and determined spectroscopic parameters are presented in Table 6.3. The predictions for minor isotopologues were obtained in the same manner as with $N = 2$ clusters. Due to the complicated splitting pattern when both ^{14}N and D quadrupole splittings and multiple *ortho*H_2 spin-spin interactions are present, it was difficult to resolve all components of the hyperfine pattern. For this reason, spectra of clusters containing more than two *ortho*H_2 molecules and DCCCN could not be analyzed for both nuclear quadrupole coupling of D and spin-spin interactions of the *ortho*H_2 molecules. For those clusters, the estimated centre frequencies of the unresolved transitions were fit to the nuclear quadrupole interaction of ^{14}N, which is large enough to be resolved. The transition frequencies and determined spectroscopic parameters of $(H_2)_3$ – DCCCN and $(H_2)_3$ – $HCCC^{15}N$ are shown in Table 6.4.

6.2.4 N > 3

This next section describes the experimental results for clusters larger than $N = 3$ where the assignments are less concrete due to some missing clusters that would help solidify the N number assignment. As more hydrogen molecules are added to the cyanoacetylene molecule, the complexity of the assignment of the spectra of the pure and mixed clusters increases. Additionally, the number of mixed clusters of a certain N size increases and the signal intensity is distributed over all the clusters.

The gas mixture used in the studies of $N > 3$ clusters contained <0.1 % HCCCN with 0.5-1 % H_2 or enriched *para*H_2 gas in high pressure helium up to pressures of 90 atm. Many transitions were measured at frequencies lower than the transitions of clusters with $N = 2$ and 3 hydrogen molecules. Additionally, the transitions were split by ^{14}N nuclear quadrupole interaction consistent with a $J = 1 - 0$ transition. Most transitions were split by spin-spin interactions due to the presence of at least one *ortho*-hydrogen molecule. Due to the small magnitude of the spin-spin coupling constant of the *ortho*-hydrogen molecule in the $(H_2)_N - HCCCN$ clusters, the splittings in clusters containing more than three *ortho*-hydrogen could not be fully resolved and analyzed. For the clusters containing more than three *ortho*-hydrogen molecules, the nuclear quadrupole coupling of ^{14}N was analyzed based on the centre frequency of the unresolved spin-spin hyperfine components. Due to this approximation, an additional error is introduced into the determined ^{14}N nuclear quadrupole coupling constants.

Despite many experimental attempts to assign a transition in the frequency region where the $(pH_2)_4 - HCCCN$ transition is predicted, no transitions showing only ^{14}N nuclear quadrupole coupling pattern were measured. All measured transitions in the frequency region, due to some additional splitting observed, contained at least one *ortho*H_2 molecule. In the $(H_2)_N - OCS$ study, the $J = 1 - 0$ transition of the $(pH_2)_4 - OCS$ cluster was very weak and difficult to measure. The predictions for the rotational constant obtained from the infrared study[5] were crucial in the measurement and assignment of $(pH_2)_4 - OCS$. Such predictions are not available for the rotational constant for $(pH_2)_4 - HCCCN$ and it is suspected that the $J = 1 - 0$ transition corresponding to the cluster has not been observed as of yet. The transition frequencies and determined spectroscopic parameters for the $N = 4$ clusters that have been assigned are in Table 6.5.

In the study of $(H_2)_N$ – OCS clusters, although the transition of the $(pH_2)_4$ – OCS cluster was not strong, the transitions of the $N = 5$-7 clusters were quite strong. It was expected that the same observation would be seen in the $(pH_2)_N$ – HCCCN clusters. In fact many transitions were measured in the frequency region consistent with $N = 5$ clusters and one of the transitions had no spin-spin fine structure and was assigned to the $(pH_2)_5$ – HCCCN transition. The transition frequencies and determined spectroscopic constants of all measured $N = 5$ clusters are given in Table 6.5.

The transition frequencies and determined spectroscopic constants for $N = 6$ clusters that were assigned are also shown in Table 6.5. Tables 6.6 and 6.7 provide the transition frequencies and determined spectroscopic constants for $(H_2)_N$ – $HCCC^{15}N$ and $(H_2)_N$ - DCCCN ($N = 4$-6) clusters, respectively. In the $(H_2)_N$ – DCCCN clusters, the complicated hyperfine splittings of the deuterium nuclear quadrupole and *ortho*-hydrogen spin-spin interactions could not be fully resolved and therefore no attempts were made to analyze the patterns. The ^{14}N nuclear quadrupole coupling constant was obtained from the experimental centre frequencies of the hyperfine components. Some measured transitions have not been assigned to a specific cluster size at this point, the transition frequencies of these unassigned lines are given in Table 6.8.

6.3 Discussion of experimental results

The nuclear quadrupole coupling constants along the *a*-inertial axis were determined for ^{14}N and some D containing complexes. For the $(H_2)_N$ – HCCCN clusters, the nuclear quadrupole coupling constants are all similar in magnitude ($\chi_{aa}(^{14}N) = -4.1628 - -4.2883$ MHz), although they vary by up to 3%. The deviation between the values can be partly attributed to the resolution of the hyperfine components as well as the observation of the $J = 2 - 1$ transition for some, but not all, clusters. The nuclear quadrupole coupling constants are in agreement with the values obtained from the He_N – HCCCN studies ($\chi_{aa}(^{14}N)$ = -4.117 - -4.231 MHz).[1] The ^{14}N nuclear quadrupole coupling constants are only slightly smaller than the monomer HCCCN value ($\chi_0(^{14}N)$ = -4.31924 MHz).[6] This is consistent with only modest large amplitude motions of the HCCCN unit within the principal inertial axis system and with the assumption that the field gradient at the ^{14}N nucleus is unchanged upon cluster formation. Using the equation [2.18], an average angle between the *a*-inertial axis and the HCCCN molecular axis can be obtained. As described in Chapter 2, the resulting angle is the average over the large amplitude motions of the individual cluster. The values obtained from the spectroscopically determined $\chi_{aa}(^{14}N)$ values are shown for each cluster in Tables 6.1 – 6.7. The values range from 4.0° to 8.9°, consistent with the HCCCN molecular axis being nearly coincident with the *a*-inertial axis. As the number of hydrogen molecules in the cluster increases up to five, the angle is consistently ~ 6°. When the sixth hydrogen molecule is added in the cluster, the angle increases to ~ 8°. The increase in the average angle obtained could be attributed to a ring of five molecules being formed, while the sixth molecule could be adding to the H-end of the HCCCN molecule. Unfortunately, it is not possible to determine the geometry of the clusters from the nuclear quadrupole coupling constants alone; additional information such as centrifugal distortion constants and isotopic data is required. In the He_N – HCCCN clusters, the sixth helium atom is added to the ring around the cyanoacetylene molecule and the seventh helium atom to the H-end of the molecule.[1]

Clusters containing at least one *ortho*H_2 molecule show spin-spin hyperfine patterns. For most clusters, the hyperfine pattern was resolved and analyzed using a spin-spin coupling constant for each *ortho*-hydrogen molecule in the cluster. Clusters which have one *ortho*H_2 molecule have a nuclear magnetic spin-spin coupling constant (S_{aa}) ranging from -58.4 kHz to -88.1 kHz. In fact, most of the coupling constants are between -82.9 - -88.1 kHz. The *ortho*H_2 spin-spin coupling constant of (pH_2)(oH_2) – HCCCN is slightly lower at S_{aa} = -58.4 kHz. The *ortho*H_2 spin-spin coupling constant of *ortho*H_2 – HCCCN is S_{aa} = -45.6 kHz, closer in magnitude to the spin-spin coupling constant of the (pH_2)(oH_2) – HCCCN cluster. For clusters containing two *ortho*H_2 molecules, the hyperfine patterns were fit with two equivalent spin-spin coupling constants, one for each *ortho*H_2 molecule in the cluster. For these clusters, the spin-spin coupling constants are in the range of S_{aa} = -39.7 - -65.7 kHz. Similarly, clusters containing three *ortho*H_2 molecules were analyzed with three equivalent spin-spin coupling constants. The spin-spin coupling constants for such clusters are S_{aa} = -31.0 - -130.9 kHz. The range of spin-spin coupling constants obtained for the clusters containing three *ortho*H_2 molecules is quite large. The discrepancy in the values is most likely due to the difficulty in resolving all spin-spin hyperfine components of the transitions. As the number of *ortho*H_2 molecules increases in the clusters, the spin-spin coupling constants increase very slightly compared to the spin-spin coupling constant obtained from the *ortho*H_2 – HCCCN studies. This trend is consistent with the results from the $(H_2)_N$ – OCS studies. Since the *ortho*H_2 spin-spin coupling constant in $(H_2)_N$ – HCCCN clusters are an order of magnitude smaller than in $(H_2)_N$ – OCS clusters, it is more difficult to resolve the hyperfine patterns and therefore it is more difficult to analyze the spectra of clusters with multiple *ortho*H_2 molecules. The analysis of mixed clusters or structural isomers within the mixed clusters is complicated by the difficulty in resolving the hyperfine structures.

For a few clusters, a centrifugal distortion constant Δ_J or D_J could be determined (see Tables 6.1 – 6.7). The values are difficult to interpret since they are only available for a select few clusters. In general, the magnitudes of the centrifugal distortion constants are consistent with weakly bound clusters. For $(oH_2)_2$ – HCCCN, centrifugal distortion constants were determined for both the main isotopologue and the $HCCC^{15}N$ cluster and both values agree well, with only 5.9% deviation. The $(H_2)_3$ – HCCCN and $(H_2)_5$ – HCCCN clusters each have two clusters for which centrifugal distortion constants could be determined. The agreement between the values is good with a deviation between each set of values of less than 7.4%. It is difficult to interpret the centrifugal distortion constants determined since the dimers with *ortho*H_2 molecules are more tightly bound than those with *para*H_2 molecules. The clusters containing either *ortho*H_2 or *para*H_2 molecules would be expected to behave differently as well. It is not possible to compare the centrifugal distortion constants to those of the $(H_2)_N$ – OCS clusters since no $J = 2 - 1$ transitions could be measured in the $(H_2)_N$ – OCS study. The centrifugal distortion constants of the He_N – HCCCN clusters decrease in value in going from $N = 3$ to 5, followed by an increase for $N = 6$.[1] The initial decrease was interpreted as an increase in rigidity of the cluster as the ring of atoms is formed. The sixth helium atom was also squeezed onto the ring, but caused a decrease in rigidity as seen by the increase in the centrifugal distortion constant. Unfortunately, the data available for the $(H_2)_N$ – HCCCN clusters are too limited to provide a similar analysis. Additional studies to measure the missing $J = 2 - 1$ transitions in $(H_2)_N - HCCCN$ clusters would aid in a detailed analysis of the centrifugal distortion constants.

In the helium cluster studies, the onset of superfluidity has been observed by examining the trend in the rotational constant as the cluster size increases. In $He_N - HCCCN$,[1] the rotational constants B_o decrease from $N = 1$ to 6, with a slight increase at $N = 7$ due to classical effects, similar to the $He_N - N_2O$ clusters.[7,8] The second turn-around which is due to quantum effects and deemed as the onset of superfluidity occurs at $N = 10$.[1] For the hydrogen clusters, it is also interesting to look at the trend in the rotational constant with increasing cluster size. For the clusters where the rotational constants cannot be determined since only $J = 1 - 0$ transitions were measured, the values plotted are half the rotational transition frequency. Figures 6.4 and 6.5 show the plots of rotational constants (B_o) from the current studies versus the size of the clusters (N) for $(pH_2)_N - HCCCN$ and $(oH_2)_N - HCCCN$, respectively. The rotational constants steadily decrease with the addition of hydrogen molecules, similar to the trend in the $He_N - HCCCN$ (Reference 1) and $(H_2)_N$ - OCS clusters up to $N = 6$. Since only clusters up to $N = 6$ were measured, it was expected that the rotational constant would decrease as the cluster size increased. A turn-around, if observed, is expected to occur at a larger cluster size than in the corresponding helium clusters due to the stronger intermolecular forces in hydrogen compared to helium.

6.4 Assignment of *N*, the number of solvating hydrogen molecules

Many experiments were performed to determine the dependence of the signal intensity on the sample pressure. When performing pressure dependence studies, the same high pressure sample was used to study the signal intensity behavior of all the transitions in question. Comparison can not be made between pressure dependence studies performed with different samples as the signal intensity also exhibits concentration dependence. Figure 6.6 shows a pressure study of $(oH_2)_N$ – HCCCN clusters. Clusters containing more hydrogen molecules require higher sample pressure to be produced in the molecular expansion. This can be seen in Figure 6.6 where the signal for $(oH_2)_2$ – HCCCN is visible at lower pressures than the signals for $(oH_2)_4$ – HCCCN and $(oH_2)_5$ – HCCCN clusters. The pressure dependence studies are a piece of the puzzle for the assignment of the number of hydrogen molecules in clusters.

Additionally, the observation and assignment of mixed clusters aids in the assignment of the number of solvating hydrogen molecules. In particular, the assignment is substantiated by the observation of a transition corresponding to a $(pH_2)_{N-1}(oH_2)$ – HCCCN cluster with the appropriate hyperfine pattern for one *ortho*H_2 molecule, as well as the observation of a $(pH_2)_N$ – HCCCN cluster without spin-spin hyperfine splittings. The evolving hyperfine structure of the clusters with increasing complexity in the hyperfine structure aids in the assignment of the *N* number. In the $(H_2)_N$ – HCCCN clusters, the smaller magnitude of the spin-spin coupling constants as compared to the constants obtained in the $(H_2)_N$ – OCS clusters can make the assignment of the evolving hyperfine pattern more difficult. Additional resolution of the *ortho*H_2 hyperfine components would be helpful for the assignment; unfortunately to date it has not been possible to achieve the necessary resolution.

6.5 Summary

Pure rotational transitions of $(pH_2)_N$–HCCCN and $(oH_2)_N$ - HCCCN clusters with N = 2 to 6 were investigated by microwave spectroscopy. Additionally, mixed clusters were investigated and showed the evolving hyperfine patterns consistent with an increasing number of *ortho*H_2 molecules. While the HCCCN and HCCC^{15}N isotopologues were primarily investigated, the $J = 1 - 0$ rotational transitions of some DCCCN isotopologues were also measured.

The clusters with $N = 2$ are asymmetric near prolate tops and were analysed for the $(B+C)/2$ rotational constants and a centrifugal distortion constant, Δ_J. The rotational transitions for clusters of $N > 2$ are effectively those of a prolate symmetric top. The B_o and D_J rotational parameters of a symmetric top molecule were fitted to the transition frequencies for the cyanoacetylene clusters with three hydrogen molecules or more. The rotational constant B_o decreases with increasing N for $(H_2)_N$ - HCCCN clusters. This is consistent with a classical picture for these smaller doped hydrogen clusters. Studies of larger clusters are necessary for the possible observation of manifestations of quantum effects in hydrogen molecule clusters. The rotational spectroscopic study of small doped hydrogen clusters shows the feasibility of such studies.

6.6 Figures

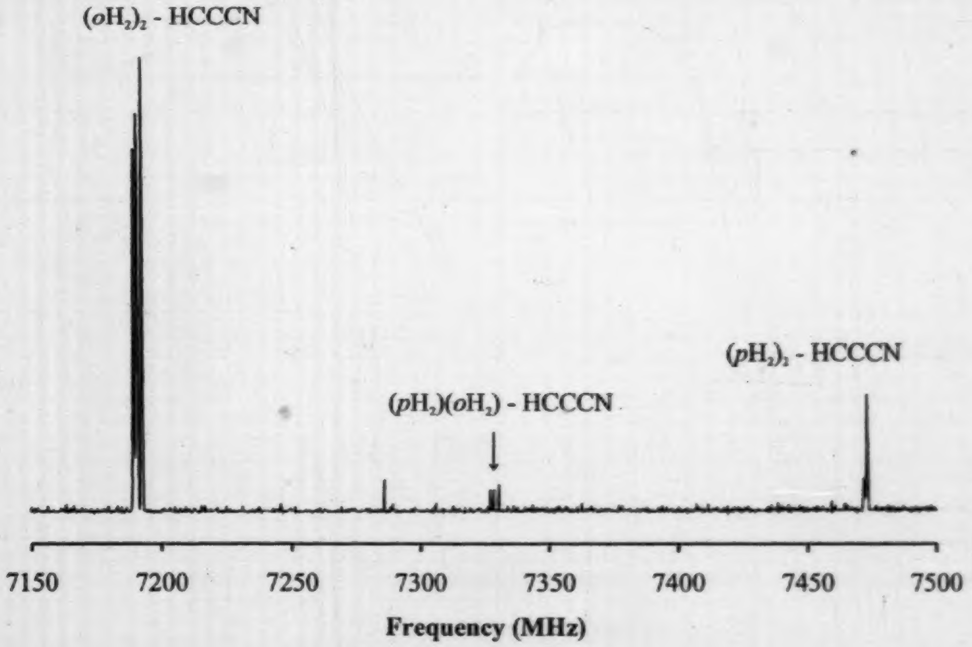

Figure 6.1: Composite experimental autoscan spectrum showing the $J_{KaKc} = 1_{01} - 0_{00}$ transitions of $(H_2)_2$ – HCCCN clusters obtained with 8 averaging cycles/step at 0.2 MHz/step. An enriched *para*H_2 sample was used for the measurements.

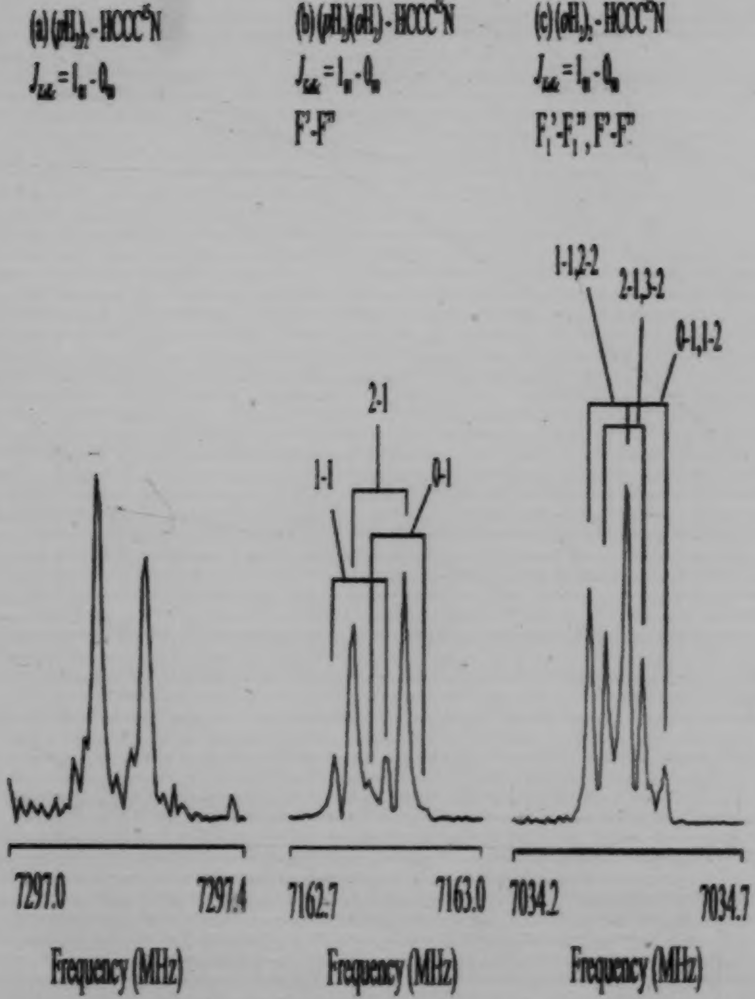

Figure 6.2: Experimental spectra of the $J_{KaKc} = 1_{01} - 0_{00}$ transition of (a) $(pH_2)_2$ – HCCC^{15}N, obtained with 1000 averaging cycles, of (b) $(pH_2)(oH_2)$ – HCCC^{15}N, obtained with 1000 averaging cycles, and (c) of $(oH_2)_2$ – HCCC^{15}N, obtained with 100 averaging cycles. The time domain signals were recorded at 10 ns second sampling interval to obtain 8k data points. The data set was supplemented with 8k zeros before Fourier transformation. An enriched HCCC^{15}N (10%) sample was used in all these experiments. Spectra containing *para*H_2 molecules were obtained with an enriched *para*H_2 sample.

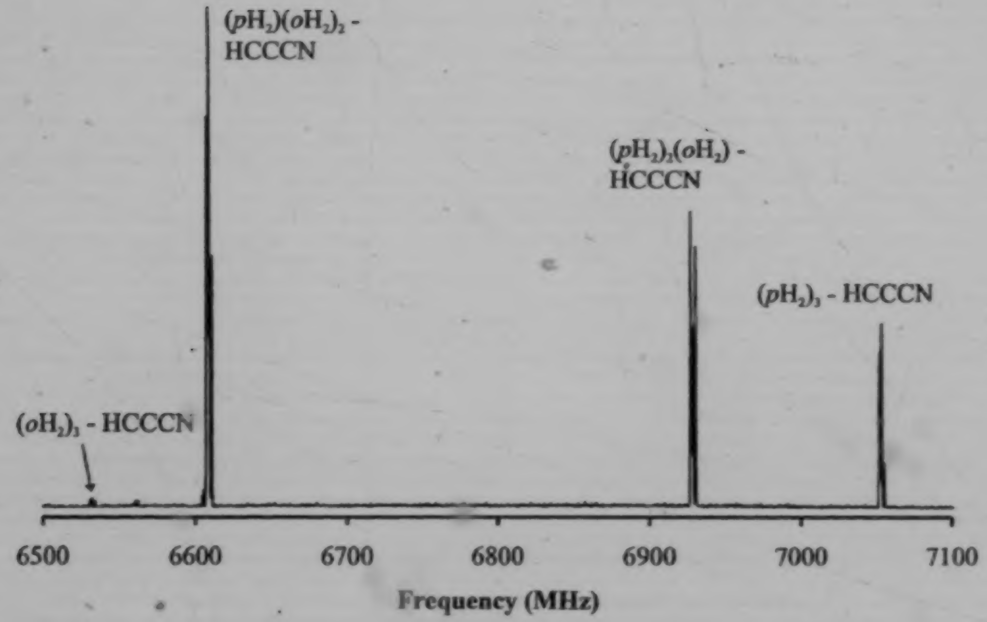

Figure 6.3: Composite experimental autoscan spectrum showing the $J = 1 - 0$ transitions of $(H_2)_3$ – HCCCN clusters obtained with 8 averaging cycles/step at 0.2 MHz/step. An enriched *para*H_2 sample was used for the measurements. The signal for $(oH_2)_3$ – HCCCN is visible, but quite weak.

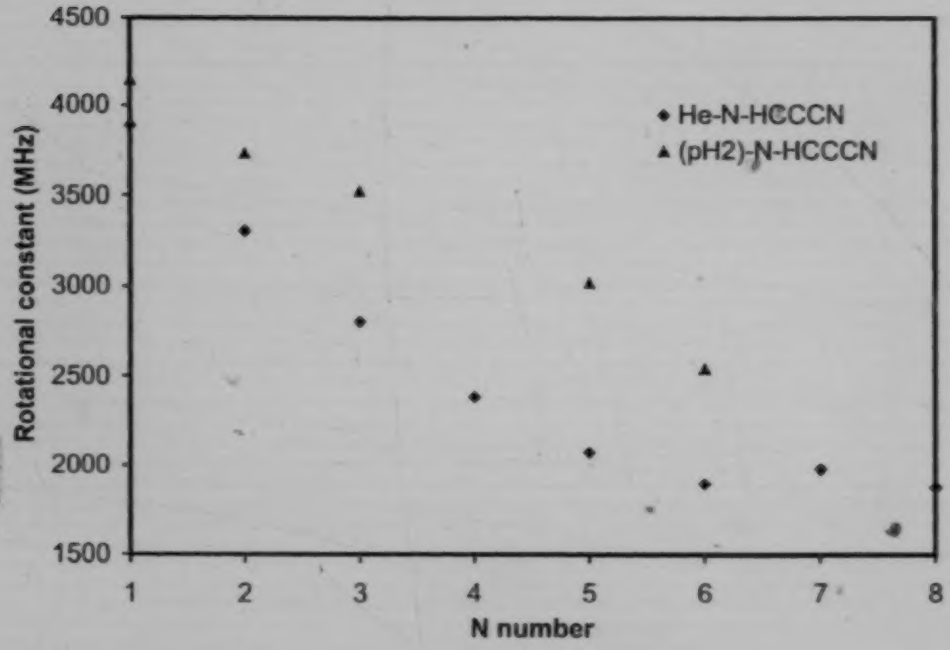

Figure 6.4: Plot of rotational constants, B_o, (in MHz) versus cluster size N for $(pH_2)_N$ – HCCCN clusters. The results are compared to the rotational constants for He_N – HCCCN clusters.[1]

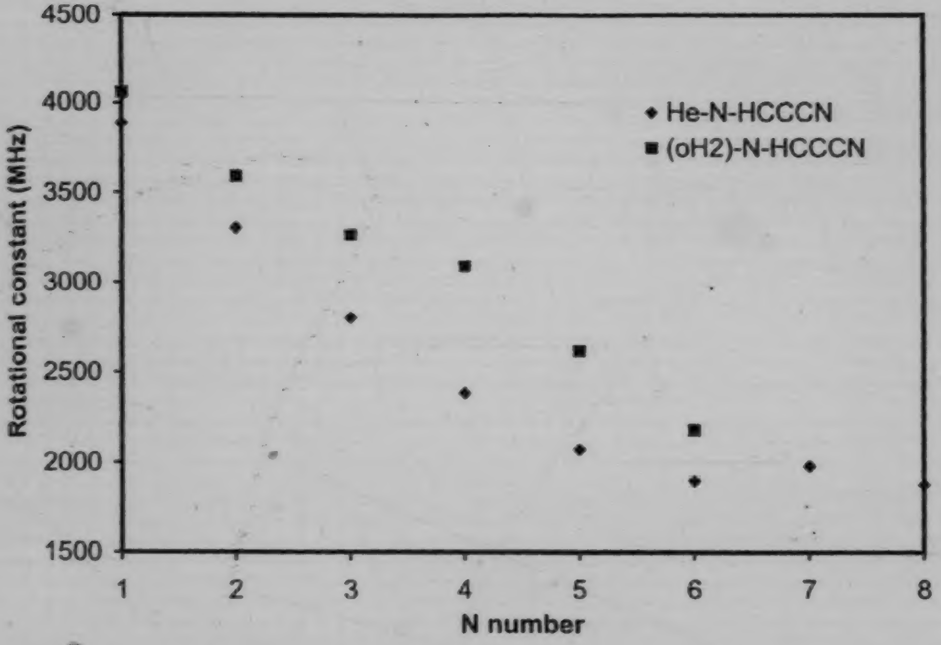

Figure 6.5: Plot of rotational constants, B_o, (in MHz) versus the cluster size N for $(o\mathrm{H}_2)_N$ – HCCCN clusters. The results are compared to the rotational constants for He_N – HCCCN clusters.[1]

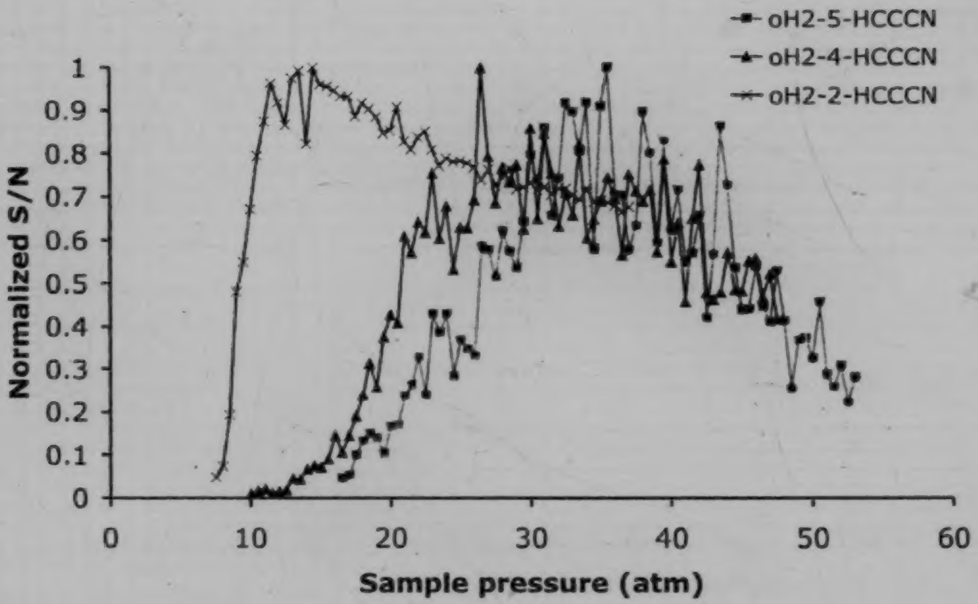

Figure 6.6: The dependence of the observed normalized signal-to-noise ratio of three $(oH_2)_N$ – HCCCN clusters on sample pressure. The J = 1-0 rotational transition F = 2-1 hyperfine component of each cluster was monitored.

6.7 Tables

Table 6.1

Measured rotational transition frequencies (in MHz), quantum number assignments, and determined spectroscopic constants (in MHz) for $(H_2)_2$ – HCCCN clusters.

Transition	F_2'-F_2''	F_1'-F_1''	F'-F''	$\nu_{obs.}$	$\Delta\nu^a$ (kHz)
$(pH_2)_2$ - HCCCN					
$1_{01} - 0_{00}$			1-1	7471.7440	0.04
			2-1	7473.0303	-0.07
			0-1	7474.9602	0.03
$\chi_{aa}(^{14}N)$	-4.28829(187)[b]				
$\theta_a(°)$[c]	4.0				
$(pH_2)(oH_2)$ - HCCCN					
$1_{01} - 0_{00}$		1-1	2-2	7327.0871	1.1
			1-2	7327.1101	7.3
		2-1	2-1	7328.3462	-1.5
			3-2	7328.3646	-9.3
			1-0	7328.3857	3.3
		0-1	1-2	7330.2926	5.6
$\chi_{aa}(^{14}N)$	-4.26339(163)				
$S_{aa}(oH_2)$	-0.0584(18)				
$\theta_a(°)$	5.3				
$(oH_2)_2$ - HCCCN					
$1_{01} - 0_{00}$	1-1	2-2	3-3	7189.2617	-5.1
		1-2	2-3	7189.2923	2.6
	2-1	2-1	2-1	7190.5259	4.3
		3-2	4-3	7190.5622	-1.9
		1-0	0-1	7190.5932	3.9
	0-1	1-2	2-3	7192.4724	-3.8
$2_{02} - 1_{01}$	1-0	1-1	2-2	14368.6514	-3.1
	2-1	2-1	3-2	14369.7016	-6.3
	2-1	3-2	4-3	14369.7537	0.1
	3-2	3-3	4-4	14369.8087	9.3
$(B+C)/2$	3596.081636(286)				
Δ_J	0.455808(44)				
$\chi_{aa}(^{14}N)$	-4.27086(153)				
$S_{aa}(oH_2)$[d]	-0.0526(84)				
$\theta_a(°)$	5.0				

[a] $\Delta\nu = \nu_{obs.} - \nu_{calc.}$ in kHz.

[b] Numbers in parenthesis are one standard deviation in units of the last significant figure.

[c] Average angle between the HCCCN molecular axis and the *a*-inertial axis determined from $\chi_{aa}(^{14}N)$; see text for details.

[d] Two equivalent spin-spin coupling constants were used to fit the hyperfine pattern.

Table 6.2

Measured rotational transition frequencies (in MHz), quantum number assignments, and determined spectroscopic constants (in MHz) for $(H_2)_2$ – DCCCN and $(H_2)_2$ – HCCC^{15}N clusters.

Transition	F_1'-F_1''	F'-F''	$\nu_{obs.}$	$\Delta\nu$[a] (kHz)
$(pH_2)_2$ – HCCC^{15}N				
$1_{01} - 0_{00}$			7297.1827	
$(pH_2)(oH_2)$ – HCCC^{15}N				
$1_{01} - 0_{00}$		1-1	7162.8028	-2.3
		2-1	7162.8319	3.8
		0-1	7162.8611	-1.5
$S_{aa}(oH_2)$	-0.03836(94)[b]			
$(oH_2)_2$ – HCCC^{15}N				
$1_{01} - 0_{00}$	1-1	2-2	7034.4001	0.2
	2-1	3-2	7034.4360	-0.6
	0-1	1-2	7034.4823	0.4
$2_{02} - 1_{01}$	2-2	3-3	14058.5318	0.4
	3-2	3-2	14058.5607	-0.4
$(B+C)/2$	3518.07206(41)			
Δ_J	0.428919(62)			
$S_{aa}(oH_2)$[c]	-0.04077(66)			
$(oH_2)_2$ - DCCCN				
$1_{01} - 0_{00}$		1-1	6754.3696	
		2-1	6755.5494	
			6755.6534	
		0-1	6757.5405	
$\chi_{aa}(^{14}N)$[d]	-4.23427(187)			
$\theta_a(°)$[e]	6.5			

[a] $\Delta\nu = \nu_{obs.} - \nu_{calc.}$ in kHz.

[b] Numbers in parenthesis are one standard deviation in units of the last significant figure.

[c] Two equivalent spin-spin coupling constants were used to fit the hyperfine pattern.

[d] The deuterium and *ortho*H_2 molecule hyperfine components were not resolved sufficiently for analysis, the centre of the unresolved components was fit to $\chi_{aa}(^{14}N)$.

[e] Average angle between the HCCCN molecular axis and the *a*-inertial axis determined from $\chi_{aa}(^{14}N)$; see text for details.

Table 6.3

Measured rotational transition frequencies (in MHz), quantum number assignments and determined spectroscopic constants (in MHz) for $(H_2)_3$ – HCCCN clusters.

Transition	F_3'-F_3''	F_2'-F_2''	F_1'-F_1''	F'-F''	$\nu_{obs.}$	$\Delta\nu^a$ (kHz)
$(pH_2)_3$ - HCCCN						
1 – 0				1-1	7051.9896	-20.1
				2-1	7053.2455	-2.9
				0-1	7055.1535	23.0
2 – 1				2-2	13826.0480	32.7
				1-0	13826.1860	-40.9
				2-1	13827.3353	50.8
				3-2	13827.3657	-9.4
				1-1	13829.3668	-33.2
$(B+C)/2$	3549.75466(40)[b]					
D_J	11.616697(53)					
$\chi_{aa}(^{14}N)$	-4.2026(121)					
$\theta_a(°)$[c]	6.7					
$(pH_2)_2(oH_2)$ - HCCCN						
1 – 0			1-1	2-2	6927.2624	-12.7
				1-2	6927.2900	-9.0
			2-1	2-1	6928.5248	8.5
				3-2	6928.5492	-4.9
				1-0	6928.5808	4.4
			0-1	1-2	6930.4592	13.8
2 – 1			2-2	2-2	13595.8674	21.8
			1-0	1-1	13596.0176	-10.3
			2-1	3-2	13597.1260	11.4
				1-0	13597.1658	-1.2
			3-2	4-3	13597.1936	-4.6
			1-1	2-2	13599.2061	-17.2
$(B+C)/2$	3485.797719(276)					
D_J	10.815212(38)					
$\chi_{aa}(^{14}N)$	-4.2195(114)					
$S_{aa}(oH_2)$	-0.0848(11)					
$\theta_a(°)$	7.1					
$(pH_2)(oH_2)_2$ - HCCCN						
1 – 0		1-1	2-2	3-3	6604.0921	-16.2
			1-2	2-3	6604.1253	-0.5
		2-1	2-1	2-1	6605.3792	8.9
			3-2	4-3	6605.4218	19.2
		0-1	1-2	2-3	6607.3074	-11.1
$\chi_{aa}(^{14}N)$	-4.2742(164)					

$S_{aa}(oH_2)^d$	-0.0397(14)					
θ_a(°)	4.8					
$(oH_2)_3$ – HCCCN						
1 – 0	1-1	0-1	1-1	2-2	6530.7260	4.3
		1-2	2-3	3-4	6530.7738	-62.6
	2-1	2-1	2-2	1-1	6531.9755	-1.5
		3-2	3-2	4-3	6532.0293	-27.6
		3-2	4-3	5-4	6532.0637	-32.4
		1-0	0-1	1-2	6532.2525	94.8
	0-1	1-2	2-3	3-4	6533.9553	-13.5
$\chi_{aa}(^{14}N)$	-4.23377(168)					
$S_{aa}(oH_2)^d$	-0.1309(80)					
θ_a(°)	6.6					

[a] $\Delta\nu = \nu_{obs.} - \nu_{calc.}$ in kHz.

[b] Numbers in parenthesis are one standard deviation in units of the last significant figure.

[c] Average angle between the HCCCN molecular axis and the *a*-inertial axis determined from $\chi_{aa}(^{14}N)$; see text for details.

[d] One spin-spin coupling constant is included in the fit for each *ortho*H_2 molecule and they are constrained to be equal.

Table 6.4

Measured rotational transition frequencies (in MHz), quantum number assignments, and determined spectroscopic constants (in MHz) for $(H_2)_3$ – DCCCN and $(H_2)_3$ – HCCC^{15}N clusters.

Transition		F_1'-F_1''	F'-F''	$\nu_{obs.}$	$\Delta\nu^a$
$(pH_2)_3$ – HCCC^{15}N					
1 – 0				6894.8918	
$(pH_2)_3$ – DCCCN					
1 – 0		1-1	1-2	6684.9737	-6.7
			2-2	6685.0376	25.5
		2-1	3-2	6686.2401	-17.3
			2-1	6686.2883	-14.0
		0-1	1-2	6688.1703	12.5
χ_{aa}(^{14}N)	-4.19878(171)^b				
χ_{aa}(D)	0.1972(43)				
θ_a(°)^c	7.7				
$(pH_2)_2(oH_2)$ – HCCC^{15}N					
1 – 0			1-1	6772.3616	-0.4
			2-1	6772.3822	0.6
			0-1	6772.4107	-0.2
$S_{aa}(oH_2)$	-0.03265(94)				
$(oH_2)_3$ - DCCCN					
1 – 0			1-1	6161.3698	
				6161.3970	
				6161.4457	
			2-1	6162.7076	
				6162.7376	
				6162.7695	
			0-1	6164.6202	
χ_{aa}(^{14}N)^d	-4.27963(187)				
θ_a(°)^c	4.3				

[a] $\Delta\nu = \nu_{obs.} - \nu_{calc.}$ in kHz.

[b] Numbers in parenthesis are one standard deviation in units of the last significant figure.

[c] Average angle between the HCCCN molecular axis and the *a*-inertial axis determined from χ_{aa}(^{14}N); see text for details.

[d] Hyperfine pattern too collapsed to analyse for all interactions present. Centre frequencies of ^{14}N nuclear quadrupole coupling components were fit to obtain χ_{aa}(^{14}N).

Table 6.5

Measured rotational transition frequencies (in MHz), quantum number assignments, and determined spectroscopic constants (in MHz) for $(H_2)_4$ – HCCCN clusters.

Transition	F_3'-F_3''	F_2'-F_2''	F_1'-F_1''	F'-F''	$\nu_{obs.}$	$\Delta\nu$[a]
$(pH_2)_3(oH_2)$ - HCCCN						
1 – 0			1-1	2-2	6559.4196	-7.0
				1-2	6559.4461	-4.6
			2-1	2-1	6560.6780	2.6
				3-2	6560.7296	16.5
			0-1	1-2	6562.6077	-7.7
$\chi_{aa}(^{14}N)$	-4.24451(165)[b]					
$S_{aa}(oH_2)$	-0.08527(24)					
θ_a(°)[c]	6.2					
$(pH_2)_2(oH_2)_2$ - HCCCN						
1 – 0		1-1	2-2	2-3	6393.9194	-4.3
		2-1	2-1	2-1	6395.1642	2.0
			3-2	4-3	6395.1974	-0.8
			1-0	2-1	6395.2161	6.0
		0-1	1-2	2-3	6397.1077	-2.9
$\chi_{aa}(^{14}N)$	-4.26827(191)					
$S_{aa}(oH_2)$[d]	-0.0446(12)					
θ_a(°)	5.1					
$(pH_2)(oH_2)_3$ - HCCCN						
1 – 0	1-1	0-1	1-1	2-2	6334.5936	7.4
		1-2	2-3	3-4	6334.6148	-9.4
	2-1	2-1	2-2	1-1	6335.8548	-8.8
		3-2	3-2	4-3	6335.8798	-2.7
			4-3	5-4	6335.9066	14.8
	0-1	1-2	2-3	3-4	6337.7894	-1.3
$\chi_{aa}(^{14}N)$	-4.23945(165)					
$S_{aa}(oH_2)$[d]	-0.0310(93)					
θ_a(°)	6.4					
$(oH_2)_4$ – HCCCN						
1 – 0				1-1	6183.7751	
					6183.7968	
				2-1	6185.0380	
					6185.0625	
				0-1	6186.9828	
$\chi_{aa}(^{14}N)$[e]	-4.26506(187)					
θ_a(°)	5.2					

[a] $\Delta\nu = \nu_{obs.} - \nu_{calc.}$ in kHz. [b] Numbers in parenthesis are one standard deviation in units of the last significant figure. [c] Average angle between the HCCCN molecular axis and the *a*-inertial; see text for details. [d] One spin-spin coupling constant is included in the fit for each *ortho*H_2 molecule. [e] Hyperfine pattern too collapsed to analyse for all interactions present. Centre frequencies of ^{14}N nuclear quadrupole coupling components were fit to obtain $\chi_{aa}(^{14}N)$.

Table 6.6

Measured rotational transition frequencies (in MHz), quantum number assignments, and determined spectroscopic constants (in MHz) for $(H_2)_5$– HCCCN clusters.

Transition	F_3'-F_3''	F_2'-F_2''	F_1'-F_1''	F'-F''	$\nu_{obs.}$	$\Delta\nu^a$
$(pH_2)_5$ - HCCCN						
1 – 0				1-1	5989.1038	-0.3
				2-1	5990.3754	0.6
				0-1	5992.2808	-0.2
2 – 1				3-2	11660.4175	0.0^b
$(B+C)/2$	$3021.74810(41)^c$					
D_J	13.333302(65)					
$\chi_{aa}(^{14}N)$	-4.23585(187)					
$\theta_a(°)^d$	6.5					
$(pH_2)_4(oH_2)$ – HCCCN						
1 – 0			1-1	2-2	5899.4365	-2.3
				1-2	5899.4615	-2.1
			2-1	2-1	5900.6912	5.0
				3-2	5900.7212	-4.2
				1-0	5900.7552	6.6
			0-1	1-2	5902.6240	-3.0
2 – 1			3-2	4-3	11502.7933	0.0^b
$(B+C)/2$	2975.111358(291)					
D_J	12.429589(54)					
$\chi_{aa}(^{14}N)$	-4.24332(163)					
$S_{aa}(oH_2)$	-0.0881(18)					
$\theta_a(°)$	6.2					
$(pH_2)_3(oH_2)_2$ – HCCCN						
1 – 0		1-1	2-2	3-3	5887.9167	-19.9
			1-2	2-3	5887.9848	20.7
		2-1	2-1	2-1	5889.1967	10.4
			3-2	4-3	5889.2249	-14.8
			1-0	0-1	5889.2722	1.4
		0-1	1-2	2-3	5891.1545	1.2
$\chi_{aa}(^{14}N)$	-4.27935(163)					
$S_{aa}(oH_2)^e$	-0.0657(11)					
$\theta_a(°)$	4.5					
$(pH_2)_2(oH_2)_3$ – HCCCN						
1 – 0	1-1	0-1	1-1	2-2	5530.9141	-1.8
		1-2	2-3	3-4	5530.9780	6.2
	2-1	2-1	2-2	1-1	5532.1873	2.0
		3-2	4-3	4-5	5532.2176	-9.4
	0-1	1-2	2-3	3-4	5534.1085	2.9
$\chi_{aa}(^{14}N)$	-4.20514(163)					

$S_{aa}(oH_2)^e$	-0.0459(94)		
$\theta_d(^\circ)$	7.6		
$(oH_2)_5$ - HCCCN			
1 – 0		1-1	5239.8055
			5239.8300
		2-1	5241.0821
			5241.0932
		0-1	5242.9935
$\chi_{aa}(^{14}N)^f$	-4.23445(187)		
$\theta_d(^\circ)$	6.6		

[a] $\Delta\nu = \nu_{obs.} - \nu_{calc.}$ in kHz.

[b] Small $\Delta\nu$ since the centrifugal distortion constant is calculated from the two transitions.

[c] Numbers in parenthesis are one standard deviation in units of the last significant figure.

[d] Average angle between the HCCCN molecular axis and the *a*-inertial axis determined from $\chi_{aa}(^{14}N)$; see text for details.

[e] One spin-spin coupling constant is included in the fit for each *ortho*H_2 molecule and they are constrained to be equal.

[f] Hyperfine pattern too collapsed to analyse for all interactions present. Centre frequencies of ^{14}N nuclear quadrupole coupling components were fit to obtain $\chi_{aa}(^{14}N)$.

Table 6.7

Measured rotational transition frequencies (in MHz), quantum number assignments, and determined spectroscopic constants (in MHz) for $(H_2)_6$ – HCCCN clusters.

Transition	F_1'-F_1''	F'-F''	$\nu_{obs.}$	$\Delta\nu^a$ (kHz)
$(pH_2)_6$ - HCCCN				
1 – 0		1-1	5084.5116	-0.1
		2-1	5085.7604	0.1
		0-1	5087.6337	-0.1
$\chi_{aa}(^{14}N)$	-4.16279(187)^b			
$\theta_a(°)^c$	8.9			
$(pH_2)_5(oH_2)$ - HCCCN				
1 – 0	1-1	2-2	5021.2880	-2.6
		1-2	5021.3151	1.1
	2-1	2-1	5022.5384	2.3
		3-2	5022.5717	-1.3
		1-0	5022.5963	1.5
	0-1	1-2	5024.4690	-1.0
$\chi_{aa}(^{14}N)$	-4.23223(163)			
$S_{aa}(oH_2)$	-0.0829(18)			
$\theta_a(°)$	6.7			
$(oH_2)_6$ - HCCCN				
1 – 0		1-1	4357.4962	
		2-1	4358.7508	
		0-1	4360.6228	
$\chi_{aa}(^{14}N)^d$	-4.16809(187)			
$\theta_a(°)$	8.8			

[a] $\Delta\nu = \nu_{obs.} - \nu_{calc.}$ in kHz.

[b] Numbers in parenthesis are one standard deviation in units of the last significant figure.

[c] Average angle between the HCCCN molecular axis and the *a*-inertial axis determined from $\chi_{aa}(^{14}N)$; see text for details.

[d] Hyperfine pattern too collapsed to analyse for all interactions present. Centre frequencies of ^{14}N nuclear quadrupole coupling components were fit to obtain $\chi_{aa}(^{14}N)$.

Table 6.8

Measured rotational transition frequencies (in MHz), quantum number assignments, and determined spectroscopic constants for $(H_2)_N - HCCC^{15}N$ clusters with $N = 4\text{-}6$.

Transition		$F'\text{-}F''$	$\nu_{obs.}$	$\Delta\nu^a$ (kHz)
$(pH_2)_5 - HCCC^{15}N$				
1 – 0			5877.7368	
$(pH_2)_6 - HCCC^{15}N$				
1 – 0			5007.6589	
$(pH_2)_5(oH_2) - HCCC^{15}N$				
1 – 0		1-1	4946.9246	0.2
		2-1	4946.9349	-0.4
		0-1	4946.9517	0.1
$S_{aa}(oH_2)$	-0.01811(94)[b]			

[a] $\Delta\nu = \nu_{obs.} - \nu_{calc.}$ in kHz.

[b] Numbers in parenthesis are one standard deviation in units of the last significant figure.

Table 6.9

Measured rotational transition frequencies (in MHz), quantum number assignments, and determined spectroscopic constants for $(H_2)_N$ – DCCCN clusters with $N = 4$-6.

Transition	F_2'-F_2''	F_1'-F_1''	F'-F''	$\nu_{obs.}$	$\Delta\nu^a$
$(pH_2)_5$ - DCCCN					
1 – 0		1-1	1-2	5676.6663	-21.0
			2-2	5676.7552	16.7
		2-1	3-2	5678.0165	21.7
			2-1	5678.0506	-14.5
		0-1	1-2	5679.9270	-3.9
$\chi_{aa}(^{14}N)$	-4.26057(173)^b				
$\chi_{aa}(D)$	0.3073(42)				
$\theta_a(°)^c$	5.3				
$(pH_2)_4(oH_2)$ - DCCCN					
1 – 0	1-1	2-2	3-3	5593.4414	-3.4
		0-1	1-2	5593.5062	1.2
	2-1	1-0	2-1	5594.6682	-12.9
		3-2	4-3	5594.7352	22.2
		2-1	3-2	5594.7620	-5.7
	0-1	1-2	2-3	5596.6402	-1.4
$\chi_{aa}(^{14}N)$	-4.2645(173)				
$\chi_{aa}(D)$	0.2475(33)				
$S_{aa}(oH_2)$	-0.0456^d				
$\theta_a(°)$	5.1				

[a] $\Delta\nu = \nu_{obs.} - \nu_{calc.}$ in kHz.

[b] Numbers in parenthesis are one standard deviation in units of the last significant figure.

[c] Average angle between the HCCCN molecular axis and the *a*-inertial axis determined from $\chi_{aa}(^{14}N)$; see text for details.

[d] Value fixed at spin-spin coupling constants obtained for *ortho*H_2 – HCCCN.

Table 6.10

Measured $J = 1$ -0 transition frequencies (in MHz) for unassigned $(H_2)_N$ – HCCCN clusters.

Transition frequencies of $(H_2)_N$ – HCCCN	$(H_2)_N$ – H CCC^{15}N analogues
6223.3533	
6223.3843	
6224.6354	
6224.6689	
6226.5565	
7107.4894	
7108.7594	6956.9242
7108.7932	6956.9583
7110.6781	

6.8 References

[1] W. Topic, W. Jäger, N. Blinov, P.-N. Roy, M. Botti, and S. Moroni, *J. Chem. Phys.* **125** (14), 144310 (2006).

[2] A. R. W. McKellar, Y. Xu, and W. Jäger, *Phys. Rev. Lett.* **97** (18), 183401 (2006).

[3] A. R. W. McKellar, Y. Xu, and W. Jäger, *J. Phys. Chem. A* **111** (31), 7329 (2007).

[4] Y. Xu and W. Jäger, *J. Chem. Phys.* **119** (11), 5457 (2003).

[5] J. Tang and A. R. W. McKellar, *J. Chem. Phys.* **121** (7), 3087 (2004).

[6] R. L. DeLeon and J. S. Muenter, *J. Chem. Phys.* **82**, 1702 (1985).

[7] Y. Xu, N. Blinov, W. Jäger, and P.-N. Roy, *J. Chem. Phys.* **124** (8), 081101 (2006).

[8] Y. Xu, W. Jäger, J. Tang, and A. R. W. McKellar, *Phys. Rev. Lett.* **91**, 163401 (2003).

Chapter 7

Conclusions

The rotational spectra of a number of doped hydrogen clusters have been measured using Fourier transform microwave spectroscopy. Many conclusions can be drawn from the results presented in Chapters 3-6. A number of them have been summarized in the corresponding chapters. This chapter will present some general conclusions about the study of doped hydrogen clusters.

The first conclusion is that Fourier transform microwave spectroscopy is a suitable technique for the study of weakly bound complexes and clusters. In particular, clusters with different spin isomers of hydrogen are separated spectrally by up to several GHz. The narrow linewidth achievable with our spectrometer allows for the measurement of a specific complex or clusters without spectral interference by other species in the molecular expansion. Another advantage of our spectrometer is the use of a pulsed-jet technique to the study doped hydrogen clusters, which makes it possible to tailor the experimental conditions to generate preferably clusters of a certain size range. The high sensitivity and resolution of the spectrometer allows for the detection of clusters containing minor isotopologues such as *ortho*$H_2 - OC^{33}S$ (0.75% naturally abundant) or *ortho*$H_2 - HCC^{13}CN$ (1.0% naturally abundant) in their natural abundances. The measurement of isotopologues with such low abundance is not possible with many other spectroscopic techniques. The rotational spectroscopic study of minor isotopologues allows for a better understanding of the complexes and clusters under investigation. In particular, structural information about the complexes can be derived from the corresponding rotational constants. Microwave spectroscopy is often used to determine molecular structures of stable molecules with higher precision than possible with other techniques.[1,2] For the cases of weakly bound complexes and clusters, only effective structures, averaged over the large amplitude zero-point vibrations can be obtained. The weak nature of the van der Waals forces holding the hydrogen – molecule complexes together is evident in the analysis of the rotational spectra by the number of centrifugal distortion constants necessary to fully describe the systems. Additionally, the inertial defects obtained from the analyses of H_2 – molecule dimers characterize the floppy nature of the complexes.

The high resolution capability of the Fourier transform microwave spectrometer allows one to resolve hyperfine patterns, which can arise from, for example, the spin-spin interaction in *ortho*H_2 molecules. Such narrow hyperfine patterns, often in the range of only a few kHz, are not resolvable by most other spectroscopic techniques. One illustration of the high resolution capability and the sensitivity of the Fourier transform microwave spectrometer is the observation and assignment of mixed clusters containing both *para*H_2 and *ortho*H_2 molecules. The assignments were aided by the evolving hyperfine patterns as the number of *ortho*H_2 molecules in the clusters increased. It is this sensitivity that allowed for the measurement of rotational transitions of structural isomers for some mixed clusters of $(H_2)_N$ – OCS.

The second general conclusion is that both chromophores, carbonyl sulfide and cyanoacetylene, are well suited for the study of doped hydrogen clusters. Both have their unique advantages and disadvantages, but they both provide an important microscopic probe of a relatively new environment: the hydrogen cluster. The rotational spectroscopic studies of the solvation of both chromophores with hydrogen molecules were made feasible by the relatively large permanent dipole moments of the molecules. The complementary studies of two chromophores, especially two with such a significant difference in rotor length, provide a starting point for comparison of the effect of rotor length on the solvation with hydrogen molecules.

Another component of this thesis was the calculation of a H_2 – HCCCN potential energy surface. Although the complexity of the hydrogen molecule compared to the helium atom increased the complexity of the calculations, the same method was used as with He – molecule systems. Several *para*H_2 – OCS potential energy surfaces have been calculated and used to predict properties of larger clusters, but few potential energy surfaces have been used to predict properties of *ortho*H_2 containing complexes.[3] One motivation for calculating the H_2 – HCCCN potential energy surface was to predict with reasonable accuracy the spectrum of *ortho*H_2 – HCCCN. This was achieved with simple scaling techniques for the main isotopologue as well as for $HCCC^{15}N$ and DCCCN containing complexes. Also, the potential energy surface was scaled to reproduce with reasonable accuracy the *para*H_2 – HCCCN spectrum. It is my hope that this potential energy surface study will spark additional work into understanding, theoretically, H_2 – molecule systems, for both *para*H_2 and *ortho*H_2 spin isomers.

The feasibility of studying larger doped-hydrogen clusters was demonstrated in this study. I was able to observe the rotational spectrum of clusters with up to seven hydrogen molecules solvating a chromophore molecule. The clusters were assigned based on several factors including the dependence of the signal on pressure and concentration of the sample. Also, the observation of the mixed clusters with evolving hyperfine patterns helped to substantiate the assignment of the pure (*para*$H_2)_N$ – molecule and pure (*ortho*$H_2)_N$ – molecule clusters.

This work demonstrates that Fourier transform microwave spectroscopy is a powerful technique for the study of doped hydrogen clusters. This study is a stepping stone hopefully leading to a better understanding of the solvation of linear rotors with hydrogen molecules. Although the onset of possible *para*-hydrogen superfluidity was not observed in this work, the study of doped hydrogen clusters has its own merits. It is my hope that this serves as a starting point for the investigation of larger doped hydrogen clusters with carbonyl sulfide or cyanoacetylene and perhaps other chromophores.

7.1 References

[1] W. Gordy and R. L. Cook, *Microwave Molecular Spectra No. XVIII in Techniques of Chemistry*, 3rd ed. (Wiley-Interscience Publishers, New York, 1970).

[2] C. H. Townes and A. L. Schawlow, *Microwave Spectroscopy*. (Dover Publications, New York, 1975).

[3] K. J. Higgins and W. Klemperer, *Private communication*.

Appendix A

Table A.1 *Ab initio* single point energies (E_h) in Hartree of the parallel orientation of H_2 – HCCCN potential energy surface, calculated at CCSD(T) level of theory with aug-cc-pVTZ basis sets supplemented with bond functions (α: *sp* 0.9, 0.3, 0.1; *d* 0.3, 0.2; *fg* 0.3).

R (Å)	θ = 2°	13°	24°	35°	46°	57°
2.50			2.3820E-01	1.1545E-01	5.0464E-02	2.0219E-02
2.75			1.4216E-01	6.3840E-02	2.5046E-02	8.8841E-03
3.00			8.5213E-02	3.3475E-02	1.1582E-02	3.3761E-03
3.25			4.5907E-02	1.6329E-02	4.8270E-03	9.0225E-04
3.50			2.2456E-02	7.2893E-03	1.6531E-03	-8.8862E-05
3.75			1.0097E-02	2.8666E-03	2.9054E-04	-4.0493E-04
4.00			4.1309E-03	8.7618E-04	-2.1234E-04	-4.4164E-04
4.25		4.0162E-03	1.4641E-03	7.4805E-05	-3.3949E-04	-3.8063E-04
4.50		1.5180E-03	3.7083E-04	-1.8991E-04	-3.2155E-04	-2.9863E-04
4.75	7.4262E-04	4.1394E-04	-2.3671E-05	-2.3545E-04	-2.6008E-04	-2.2394E-04
5.00	1.8023E-04	4.4616E-05	-1.3118E-04	-2.0472E-04	-1.9599E-04	-1.6421E-04
5.25	-5.9975E-06	-6.2679E-05	-1.3348E-04	-1.5665E-04	-1.4234E-04	-1.1918E-04
5.50	-4.9854E-05	-7.4898E-05	-1.0513E-04	-1.1231E-04	-1.0128E-04	-8.6174E-05
5.75	-4.6067E-05	-5.8765E-05	-7.3980E-05	-7.7530E-05	-7.1218E-05	-6.2303E-05
6.00	-3.1015E-05	-3.8671E-05	-4.8442E-05	-5.2096E-05	-4.9698E-05	-4.5086E-05
6.50	-5.7865E-06	-1.0104E-05	-1.6827E-05	-2.1729E-05	-2.3673E-05	-2.3689E-05
7.00	5.5539E-06	2.8911E-06	-2.4542E-06	-7.3928E-06	-1.0653E-05	-1.2355E-05
7.50	9.8608E-06	7.6976E-06	3.5619E-06	-7.1194E-07	-4.0110E-06	-6.1476E-06
8.00	1.0462E-05	8.8725E-06	5.7210E-06	2.2474E-06	-6.6794E-07	-2.7542E-06
8.50	9.7816E-06	8.6013E-06	6.2013E-06	3.4432E-06	9.9460E-07	-8.7229E-07
9.00	8.6919E-06	7.8010E-06	5.9676E-06	3.7881E-06	1.7744E-06	1.6287E-07
10.00	6.4740E-06	5.9584E-06	4.8558E-06	3.4848E-06	2.1407E-06	9.9030E-07
11.00	4.7320E-06	4.4139E-06	3.7274E-06	2.8415E-06	1.9371E-06	1.1241E-06
12.00	3.4863E-06	3.2751E-06	2.8317E-06	2.2417E-06	1.6195E-06	1.0381E-06
13.00	2.5952E-06	2.4637E-06	2.1642E-06	1.7603E-06	1.3212E-06	8.9802E-07

Table A.1, continued

R (Å)	θ = 68°	79°	90°	101°	112°	123°
2.50	7.8488E-03	3.3760E-03	2.7162E-03	5.0419E-03	1.1979E-02	2.8385E-02
2.75	2.6769E-03	5.5046E-04	3.1387E-04	1.5646E-03	5.2129E-03	1.4004E-02
3.00	4.6100E-04	-4.5927E-04	-5.0530E-04	1.4193E-04	1.9706E-03	6.4762E-03
3.25	-3.5672E-04	-7.0060E-04	-6.7322E-04	-3.4789E-04	5.2619E-04	2.7283E-03
3.50	-5.6572E-04	-6.5600E-04	-6.0858E-04	-4.4787E-04	-5.1195E-05	9.6565E-04
3.75	-5.3974E-04	-5.3130E-04	-4.8490E-04	-4.0564E-04	-2.3676E-04	1.9782E-04
4.00	-4.4297E-04	-4.0422E-04	-3.6583E-04	-3.2594E-04	-2.6052E-04	-9.7070E-05
4.25	-3.4046E-04	-2.9922E-04	-2.6953E-04	-2.4844E-04	-2.2730E-04	-1.8193E-04
4.50	-2.5372E-04	-2.1915E-04	-1.9706E-04	-1.8501E-04	-1.8139E-04	-1.8249E-04
4.75	-1.8653E-04	-1.6033E-04	-1.4426E-04	-1.3675E-04	-1.3889E-04	-1.5532E-04
5.00	-1.3665E-04	-1.1780E-04	-1.0628E-04	-1.0123E-04	-1.0477E-04	-1.2379E-04
5.25	-1.0020E-04	-8.7169E-05	-7.8976E-05	-7.5463E-05	-7.8887E-05	-9.6008E-05
5.50	-7.3970E-05	-6.5017E-05	-5.9298E-05	-5.6815E-05	-5.9793E-05	-7.4038E-05
5.75	-5.4623E-05	-4.8897E-05	-4.4965E-05	-4.3270E-05	-4.5740E-05	-5.7343E-05
6.00	-4.0662E-05	-3.7085E-05	-3.4455E-05	-3.3353E-05	-3.5472E-05	-4.4923E-05
6.50	-2.2872E-05	-2.1781E-05	-2.0808E-05	-2.0544E-05	-2.2301E-05	-2.8802E-05
7.00	-1.3025E-05	-1.3115E-05	-1.3004E-05	-1.3238E-05	-1.4812E-05	-1.9584E-05
7.50	-7.3548E-06	-7.9761E-06	-8.3111E-06	-8.8908E-06	-1.0265E-05	-1.3947E-05
8.00	-4.0995E-06	-4.9160E-06	-5.4641E-06	-6.1119E-06	-7.4369E-06	-1.0359E-05
8.50	-2.1694E-06	-3.0339E-06	-3.6655E-06	-4.3638E-06	-5.5656E-06	-7.9355E-06
9.00	-1.0170E-06	-1.8518E-06	-2.5044E-06	-3.1989E-06	-4.2761E-06	-6.2211E-06
10.00	8.0099E-08	-6.2413E-07	-1.2142E-06	-1.8331E-06	-2.6796E-06	-4.0234E-06
11.00	4.4354E-07	-1.1616E-07	-6.0877E-07	-1.1230E-06	-1.7808E-06	-2.7287E-06
12.00	5.3036E-07	9.3281E-08	-3.0298E-07	-7.2137E-07	-1.2292E-06	-1.9129E-06
13.00	5.1536E-07	1.7390E-07	-1.4582E-07	-4.7914E-07	-8.7279E-07	-1.3761E-06

Table A.1, continued

R (Å)	θ = 134°	146°	156°	167°
2.50	6.4315E-02	1.4089E-01	3.3977E-01	
2.75	3.4544E-02	8.5198E-02	2.2898E-01	
3.00	1.7780E-02	5.0326E-02	1.6234E-01	
3.25	8.6681E-03	2.8134E-02	1.0293E-01	4.5186E-01
3.50	3.9165E-03	1.4656E-02	5.7831E-02	2.0525E-01
3.75	1.5620E-03	7.0235E-03	2.9442E-02	9.3430E-02
4.00	4.7060E-04	3.0113E-03	1.3677E-02	4.1292E-02
4.25	1.1775E-05	1.0625E-03	5.6915E-03	1.7081E-02
4.50	-1.4977E-04	2.0077E-04	1.9704E-03	6.2614E-03
4.75	-1.8306E-04	-1.3077E-04	3.9309E-04	1.7339E-03
5.00	-1.6816E-04	-2.2513E-04	-1.8908E-04	2.8638E-05
5.25	-1.3985E-04	-2.2488E-04	-3.4756E-04	-4.9505E-04
5.50	-1.1187E-04	-1.9389E-04	-3.4501E-04	-5.6794E-04
5.75	-8.8423E-05	-1.5809E-04	-2.9341E-04	-4.9605E-04
6.00	-7.0037E-05	-1.2636E-04	-2.3564E-04	-3.9574E-04
6.50	-4.5287E-05	-8.0738E-05	-1.4577E-04	-2.3424E-04
7.00	-3.0828E-05	-5.3508E-05	-9.2073E-05	-1.4048E-04
7.50	-2.1942E-05	-3.7015E-05	-6.0810E-05	-8.8556E-05
8.00	-1.6242E-05	-2.6634E-05	-4.1992E-05	-5.8794E-05
8.50	-1.2371E-05	-1.9762E-05	-3.0079E-05	-4.0779E-05
9.00	-9.6341E-06	-1.5028E-05	-2.2193E-05	-2.9306E-05
10.00	-6.1396E-06	-9.1936E-06	-1.2937E-05	-1.6407E-05
11.00	-4.1028E-06	-5.9467E-06	-8.0656E-06	-9.9381E-06
12.00	-2.8399E-06	-4.0117E-06	-5.2920E-06	-6.3794E-06
13.00	-2.0229E-06	-2.8002E-06	-3.6150E-06	-4.2855E-06

Table A.2 *Ab initio* single point energies (E_h) in Hartree of the perpendicular orientation of H_2 – HCCCN potential energy surface, calculated at CCSD(T) level of theory with aug-cc-pVTZ basis sets supplemented with bond functions (α: *sp* 0.9, 0.3, 0.1; *d* 0.3, 0.2; *fg* 0.3).

R (Å)	θ = 2°	13°	24°	35°	46°	57°
2.50			2.7414E-01	1.2559E-01	5.7608E-02	2.5232E-02
2.75			1.6840E-01	7.2156E-02	2.9392E-02	1.1743E-02
3.00			9.6907E-02	3.8515E-02	1.4077E-02	4.9366E-03
3.25			5.1169E-02	1.8939E-02	6.1120E-03	1.7122E-03
3.50			2.4549E-02	8.3894E-03	2.2188E-03	3.0374E-04
3.75			1.0517E-02	3.1304E-03	4.6162E-04	-2.3637E-04
4.00		9.2501E-03	3.7584E-03	7.3061E-04	-2.3931E-04	-3.8955E-04
4.25		2.6093E-04	7.9813E-04	-2.3636E-04	-4.5435E-04	-3.8687E-04
4.50		-6.1597E-04	-3.3715E-04	-5.4093E-04	-4.6675E-04	-3.3333E-04
4.75	-5.2458E-04	-7.9982E-04	-6.6657E-04	-5.6923E-04	-4.0831E-04	-2.7103E-04
5.00	-8.4200E-04	-7.3634E-04	-6.7688E-04	-5.0056E-04	-3.3517E-04	-2.1556E-04
5.25	-8.0949E-04	-6.0804E-04	-5.8323E-04	-4.1072E-04	-2.6826E-04	-1.7067E-04
5.50	-6.7717E-04	-4.8171E-04	-4.7211E-04	-3.2799E-04	-2.1329E-04	-1.3574E-04
5.75	-5.3780E-04	-3.7673E-04	-3.7335E-04	-2.6000E-04	-1.7012E-04	-1.0894E-04
6.00	-4.1983E-04	-2.3306E-04	-2.9386E-04	-2.0671E-04	-1.3679E-04	-8.8427E-05
6.50	-2.5727E-04	-1.5011E-04	-1.8553E-04	-1.3412E-04	-9.1214E-05	-6.0229E-05
7.00	-1.6404E-04	-1.0118E-04	-1.2212E-04	-9.0724E-05	-6.3354E-05	-4.2696E-05
7.50	-1.0959E-04	-7.0913E-05	-8.3870E-05	-6.3796E-05	-4.5596E-05	-3.1294E-05
8.00	-7.6579E-05	-5.1414E-05	-5.9696E-05	-4.6300E-05	-3.3736E-05	-2.3505E-05
8.50	-5.5004E-05	-3.8327E-05	-4.3837E-05	-3.4563E-05	-2.5609E-05	-1.8090E-05
9.00	-4.0573E-05	-2.2742E-05	-3.3021E-05	-2.6400E-05	-1.9842E-05	-1.4171E-05
10.00	-2.4040E-05	-1.4428E-05	-1.9853E-05	-1.6268E-05	-1.2507E-05	-9.0953E-06
11.00	-1.5186E-05	-9.6347E-06	-1.2787E-05	-1.0615E-05	-8.2985E-06	-6.1169E-06
12.00	-1.0108E-05	-6.6922E-06	-8.6143E-06	-7.2386E-06	-5.7307E-06	-4.2671E-06
13.00	-6.9768E-06	9.2501E-03	-6.0240E-06	-5.1105E-06	-4.0855E-06	-3.0648E-06

Table A.2, continued

R (Å)	θ = 68°	79°	90°	101°	112°	123°
2.50	1.1825E-02	6.6685E-03	5.5552E-03	7.5535E-03	1.4068E-02	2.9284E-02
2.75	4.8523E-03	2.3122E-03	1.7710E-03	2.7378E-03	5.9936E-03	1.3972E-02
3.00	1.6378E-03	4.8859E-04	2.4067E-04	6.5068E-04	2.1354E-03	6.0629E-03
3.25	2.7738E-04	-1.8045E-04	-2.8646E-04	-1.5286E-04	4.3220E-04	2.2063E-03
3.50	-2.2384E-04	-3.6221E-04	-4.0289E-04	-3.9300E-04	-2.2930E-04	4.6416E-04
3.75	-3.5579E-04	-3.5981E-04	-3.7202E-04	-4.0795E-04	-4.2078E-04	-2.2974E-04
4.00	-3.4545E-04	-3.0176E-04	-3.0182E-04	-3.4804E-04	-4.2022E-04	-4.3714E-04
4.25	-2.9155E-04	-2.3717E-04	-2.3256E-04	-2.7442E-04	-3.5466E-04	-4.3986E-04
4.50	-2.3314E-04	-1.8180E-04	-1.7526E-04	-2.0876E-04	-2.7835E-04	-3.7128E-04
4.75	-1.8254E-04	-1.3871E-04	-1.3163E-04	-1.5577E-04	-2.1059E-04	-2.8943E-04
5.00	-1.4251E-04	-1.0645E-04	-9.9317E-05	-1.1665E-04	-1.5643E-04	-2.1626E-04
5.25	-1.1196E-04	-8.2567E-05	-7.5605E-05	-8.7169E-05	-1.1521E-04	-1.5769E-04
5.50	-8.8956E-05	-6.4898E-05	-5.8197E-05	-6.5463E-05	-8.4611E-05	-1.1328E-04
5.75	-7.1484E-05	-5.1715E-05	-4.5315E-05	-4.9473E-05	-6.2029E-05	-8.0516E-05
6.00	-5.8212E-05	-4.1754E-05	-3.5682E-05	-3.7631E-05	-4.5473E-05	-5.6682E-05
6.50	-3.9969E-05	-2.8167E-05	-2.2802E-05	-2.2151E-05	-2.4397E-05	-2.7096E-05
7.00	-2.8556E-05	-1.9782E-05	-1.5112E-05	-1.3292E-05	-1.2856E-05	-1.1777E-05
7.50	-2.1078E-05	-1.4366E-05	-1.0344E-05	-8.0889E-06	-6.4522E-06	-3.8665E-06
8.00	-1.5907E-05	-1.0654E-05	-7.2106E-06	-4.8871E-06	-2.7969E-06	2.3981E-07
8.50	-1.2295E-05	-8.1078E-06	-5.1634E-06	-2.9457E-06	-7.7291E-07	2.2359E-06
9.00	-9.6704E-06	-6.2855E-06	-3.7669E-06	-1.7278E-06	3.5171E-07	3.1308E-06
10.00	-6.2404E-06	-3.9700E-06	-2.0700E-06	-5.4000E-07	1.1800E-06	3.4300E-06
11.00	-4.2106E-06	-2.9445E-06	-1.2249E-06	5.2394E-08	1.4082E-06	3.0464E-06
12.00	-2.9418E-06	-1.7778E-06	-7.3975E-07	2.5166E-07	1.3033E-06	2.1274E-05
13.00	-2.1134E-06	-1.2503E-06	-4.5634E-07	3.1595E-07	1.1321E-06	2.5313E-06

Table A.2, continued

R (Å)	θ = 134°	146°	156°	167°
2.50	6.0742E-02	1.2118E-01	3.0792E-01	1.3051E+00
2.75	3.2240E-02	7.6320E-02	2.1825E-01	7.4308E-01
3.00	1.6179E-02	4.5496E-02	1.4672E-01	4.5363E-01
3.25	7.4839E-03	2.5385E-02	9.1988E-02	2.9730E-01
3.50	3.0121E-03	1.3068E-02	5.3231E-02	1.8848E-01
3.75	8.6899E-04	6.0744E-03	2.8417E-02	1.0562E-01
4.00	-5.1147E-05	2.4204E-03	1.3973E-02	5.3269E-02
4.25	-3.6936E-04	6.8827E-04	6.2738E-03	2.4978E-02
4.50	-4.1803E-04	-2.8427E-05	2.5064E-03	1.1032E-02
4.75	-3.6381E-04	-2.5688E-04	8.2872E-04	4.5897E-03
5.00	-2.8336E-04	-2.7772E-04	1.6753E-04	1.7930E-03
5.25	-2.0769E-04	-2.2683E-04	-4.4305E-05	6.6251E-04
5.50	-1.4642E-04	-1.6297E-04	-7.9998E-05	2.4342E-04
5.75	-1.0024E-04	-1.0753E-04	-5.9197E-05	1.0585E-04
6.00	-6.6737E-05	-6.5513E-05	-2.8550E-05	6.9541E-05
6.50	-2.6400E-05	-1.5786E-05	1.4271E-05	6.5168E-05
7.00	-7.0637E-06	5.5335E-06	3.0139E-05	6.3192E-05
7.50	1.8497E-06	1.3370E-05	3.2349E-05	5.4898E-05
8.00	5.7540E-06	1.5385E-05	2.9626E-05	4.5200E-05
8.50	7.1386E-06	1.4917E-05	2.5544E-05	3.6446E-05
9.00	7.3379E-06	1.3547E-05	2.1513E-05	2.9283E-05
10.00	6.4500E-06	1.0350E-05	1.4960E-05	1.9170E-05
11.00	5.1373E-06	7.7211E-06	1.0539E-05	1.2948E-05
12.00	4.0195E-06	5.7549E-06	7.5540E-06	9.0321E-06
13.00	3.1359E-06	4.3382E-06	5.5350E-06	6.4877E-06

Table A.3 *Ab initio* single point energies (E_h) in Hartree of the out-of-plane orientation of H_2 – HCCCN potential energy surface, calculated at CCSD(T) level of theory with aug-cc-pVTZ basis sets supplemented with bond functions (α: *sp* 0.9, 0.3, 0.1; *d* 0.3, 0.2; *fg* 0.3).

R (Å)	θ = 2°	13°	24°	35°	46°	57°
2.50			2.0821E-01	1.0946E-01	4.7871E-02	1.9786E-02
2.75			1.4411E-01	6.2787E-02	2.4557E-02	9.1329E-03
3.00			8.7241E-02	3.3704E-02	1.1865E-02	3.8167E-03
3.25			4.6936E-02	1.6890E-02	5.3100E-03	1.3348E-03
3.50			2.3126E-02	7.8615E-03	2.1180E-03	2.7157E-04
3.75			1.0578E-02	3.3411E-03	6.7051E-04	-1.2454E-04
4.00			4.4753E-03	1.2360E-03	7.7310E-05	-2.3011E-04
4.25		4.1321E-03	1.7055E-03	3.3575E-04	-1.2523E-04	-2.2294E-04
4.50		1.5180E-03	5.3655E-04	-4.4367E-06	-1.6497E-04	-1.8114E-04
4.75	7.4401E-04	4.6542E-04	8.9695E-05	-1.0431E-04	-1.4574E-04	-1.3593E-04
5.00	1.8110E-04	7.9155E-05	-5.3403E-05	-1.1162E-04	-1.1196E-04	-9.7743E-05
5.25	-5.4014E-06	-3.9274E-05	-7.9580E-05	-8.9856E-05	-7.9912E-05	-6.8491E-05
5.50	-4.9404E-05	-5.8838E-05	-6.7235E-05	-6.3715E-05	-5.4341E-05	-4.7142E-05
5.75	-4.5788E-05	-4.7552E-05	-4.6817E-05	-4.1618E-05	-3.5497E-05	-3.1947E-05
6.00	-3.0787E-05	-3.0691E-05	-2.8642E-05	-2.5156E-05	-2.2200E-05	-2.1270E-05
6.50	-5.6764E-06	-5.8204E-06	-5.7385E-06	-5.9364E-06	-6.8547E-06	-8.6494E-06
7.00	5.9593E-06	5.3613E-06	4.1168E-06	2.2934E-06	1.3525E-08	-2.5713E-06
7.50	9.8997E-06	9.1999E-06	7.6292E-06	5.4503E-06	2.9638E-06	3.8257E-07
8.00	1.0487E-05	9.8211E-06	7.1698E-06	6.2944E-06	4.0164E-06	1.7065E-06
8.50	9.7977E-06	9.2215E-06	7.9338E-06	6.1768E-06	4.2177E-06	2.2383E-06
9.00	8.7027E-06	8.2174E-06	6.9712E-06	5.6810E-06	4.0066E-06	2.3731E-06
10.00	6.4793E-06	6.1627E-06	5.4444E-06	4.4441E-06	3.3251E-06	2.1628E-06
11.00	4.7348E-06	4.5224E-06	4.0448E-06	3.3713E-06	2.4293E-06	1.7812E-06
12.00	3.4879E-06	3.3405E-06	3.0135E-06	2.5484E-06	2.0044E-06	1.3499E-06
13.00	2.5961E-06	1.3460E-05	2.2755E-06	1.9460E-06	1.5562E-06	1.1304E-06

Table A.3, continued

R (Å)	θ = 68°	79°	90°	101°	112°	123°
2.50	8.2769E-03	3.9848E-03	3.2279E-03	5.2241E-03	1.1276E-02	2.5249E-02
2.75	3.1785E-03	1.0438E-03	6.9646E-04	1.7279E-03	4.8543E-03	1.2268E-02
3.00	9.0499E-04	-8.8781E-05	-2.3647E-04	2.5828E-04	1.7684E-03	5.4854E-03
3.25	-2.5983E-06	-4.3126E-04	-4.8947E-04	-2.7503E-04	3.9323E-04	2.1280E-03
3.50	-2.9602E-04	-4.6226E-04	-4.8407E-04	-4.0711E-04	-1.5166E-04	5.7352E-04
3.75	-3.3826E-04	-3.9149E-04	-3.8224E-04	-3.8605E-04	-3.1933E-04	-7.7123E-05
4.00	-2.9316E-04	-3.0270E-04	-3.0806E-04	-3.1945E-04	-3.3070E-04	-3.0085E-04
4.25	-2.2877E-04	-2.2459E-04	-2.2965E-04	-2.4944E-04	-2.8728E-04	-3.3858E-04
4.50	-1.6988E-04	-1.6372E-04	-1.6925E-04	-1.8998E-04	-2.3241E-04	-3.0549E-04
4.75	-1.2300E-04	-1.1868E-04	-1.2466E-04	-1.4355E-04	-1.8214E-04	-2.5315E-04
5.00	-8.8047E-05	-8.6174E-05	-9.2349E-05	-1.0865E-04	-1.4115E-04	-2.0186E-04
5.25	-6.2682E-05	-6.2909E-05	-6.9003E-05	-8.2809E-05	-1.0934E-04	-1.5868E-04
5.50	-4.4546E-05	-4.6240E-05	-5.2113E-05	-6.3735E-05	-8.5229E-05	-1.2447E-04
5.75	-3.1664E-05	-3.4247E-05	-3.9772E-05	-4.9600E-05	-6.6979E-05	-9.8069E-05
6.00	-2.2482E-05	-2.5549E-05	-3.0682E-05	-3.9043E-05	-5.3211E-05	-7.7944E-05
6.50	-1.1217E-05	-1.4543E-05	-1.8817E-05	-2.5008E-05	-3.4726E-05	-5.0762E-05
7.00	-5.3617E-06	-8.3987E-06	-1.1965E-05	-1.6674E-05	-2.3611E-05	-3.4445E-05
7.50	-2.2053E-06	-4.8580E-06	-7.7840E-06	-1.1447E-05	-1.6566E-05	-2.4177E-05
8.00	-5.5482E-07	-2.7575E-06	-5.2220E-06	-8.1181E-06	-1.1992E-05	-1.7525E-05
8.50	3.0880E-07	-1.5859E-06	-3.5796E-06	-5.9044E-06	-8.9090E-06	-1.3037E-05
9.00	7.4673E-07	-8.4393E-07	-2.5009E-06	-4.3909E-06	-6.7618E-06	-9.9196E-06
10.00	1.0134E-06	-1.1211E-07	-1.2749E-06	-2.5640E-06	-4.1079E-06	-6.0526E-06
11.00	9.6693E-07	1.5570E-07	-6.7824E-07	-1.5882E-06	-2.6373E-06	-3.9010E-06
12.00	8.3554E-07	1.7587E-07	-3.6731E-07	-1.0238E-06	-1.7643E-06	-2.6233E-06
13.00	7.3146E-07	2.5857E-07	-1.9666E-07	-6.8213E-07	-1.0331E-06	-1.8237E-06

Table A.3, continued

R (Å)	θ = 134°	146°	156°	167°
2.50	5.4535E-02	1.0986E-01	2.1715E-01	5.2253E-01
2.75	2.9041E-02	6.8893E-02	1.7788E-01	4.7235E-01
3.00	1.4656E-02	4.0766E-02	1.2920E-01	4.0341E-01
3.25	6.8482E-03	2.2415E-02	8.1532E-02	2.6816E-01
3.50	2.8111E-03	1.1271E-02	4.5673E-02	1.5114E-01
3.75	8.5505E-04	5.0205E-03	2.3021E-02	7.6334E-02
4.00	-5.8601E-06	1.8032E-03	1.0350E-02	3.5190E-02
4.25	-3.2438E-04	3.0846E-04	3.9417E-03	1.4648E-02
4.50	-3.9540E-04	-2.8941E-04	1.0154E-03	5.1907E-03
4.75	-3.6695E-04	-4.6223E-04	-1.5581E-04	1.2204E-03
5.00	-3.0807E-04	-4.5674E-04	-5.2261E-04	-2.3843E-04
5.25	-2.4736E-04	-3.9091E-04	-5.6048E-04	-6.4475E-04
5.50	-1.9524E-04	-3.1527E-04	-4.8671E-04	-6.5735E-04
5.75	-1.5346E-04	-2.4816E-04	-3.9089E-04	-5.5235E-04
6.00	-1.2113E-04	-1.9402E-04	-3.0449E-04	-4.3288E-04
6.50	-7.7408E-05	-1.2020E-04	-1.8223E-04	-2.5212E-04
7.00	-5.1538E-05	-7.7436E-05	-1.1263E-04	-1.4991E-04
7.50	-3.5618E-05	-5.1970E-05	-7.2994E-05	-9.3868E-05
8.00	-2.5479E-05	-3.6354E-05	-4.9520E-05	-6.1950E-05
8.50	-1.8745E-05	-2.6230E-05	-3.4900E-05	-4.2735E-05
9.00	-1.4122E-05	-1.9443E-05	-2.5378E-05	-3.0564E-05
10.00	-8.4865E-06	-1.1391E-05	-1.4442E-05	-1.6978E-05
11.00	-5.4135E-06	-7.1260E-06	-8.8464E-06	-1.0226E-05
12.00	-3.6109E-06	-4.6850E-06	-5.7253E-06	-6.5357E-06
13.00	-2.5001E-06	-3.2045E-06	-3.8696E-06	-4.3759E-06

Table A.4 *Ab initio* single point energies (E_h) in Hartree of the averaged H_2 – HCCCN potential energy surface (equal weighting of the three orientations), calculated at CCSD(T) level of theory with aug-cc-pVTZ basis sets supplemented with bond functions (α: *sp* 0.9, 0.3, 0.1; *d* 0.3, 0.2; *fg* 0.3).

R (Å)	θ = 2°	13°	24°	35°	46°	57°
2.50			2.4018E-01	1.1683E-01	5.1981E-02	2.1746E-02
2.75			1.5156E-01	6.6261E-02	2.6332E-02	9.9200E-03
3.00			8.9787E-02	3.5231E-02	1.2508E-02	4.0431E-03
3.25			4.8004E-02	1.7386E-02	5.4163E-03	1.3164E-03
3.50			2.3377E-02	7.8467E-03	1.9966E-03	1.6215E-04
3.75			1.0397E-02	3.1127E-03	4.7422E-04	-2.5528E-04
4.00			4.1215E-03	9.4759E-04	-1.2478E-04	-3.5377E-04
4.25		6.2880E-03	1.3226E-03	5.8066E-05	-3.0636E-04	-3.3015E-04
4.50		1.0990E-03	1.9008E-04	-2.4509E-04	-3.1776E-04	-2.7103E-04
4.75	3.2068E-04	8.7798E-05	-2.0018E-04	-3.0300E-04	-2.7138E-04	-2.1030E-04
5.00	-1.6022E-04	-2.2535E-04	-2.8715E-04	-2.7230E-04	-2.1437E-04	-1.5917E-04
5.25	-2.7363E-04	-2.7943E-04	-2.6543E-04	-2.1908E-04	-1.6350E-04	-1.1945E-04
5.50	-2.5881E-04	-2.4726E-04	-2.1482E-04	-1.6800E-04	-1.2297E-04	-8.9685E-05
5.75	-2.0988E-04	-1.9601E-04	-1.6472E-04	-1.2638E-04	-9.2278E-05	-6.7730E-05
6.00	-1.6054E-04	-1.4870E-04	-1.2365E-04	-9.4654E-05	-6.9563E-05	-5.1594E-05
6.50	-8.9578E-05	-8.2995E-05	-6.9365E-05	-5.3928E-05	-4.0581E-05	-3.0856E-05
7.00	-5.0842E-05	-4.7286E-05	-4.0152E-05	-3.1941E-05	-2.4664E-05	-1.9207E-05
7.50	-2.9943E-05	-2.8094E-05	-2.4226E-05	-1.9686E-05	-1.5548E-05	-1.2353E-05
8.00	-1.8543E-05	-1.7406E-05	-1.5602E-05	-1.2586E-05	-1.0129E-05	-8.1842E-06
8.50	-1.1808E-05	-1.1197E-05	-9.9006E-06	-8.3143E-06	-6.7989E-06	-5.5747E-06
9.00	-7.7261E-06	-7.4362E-06	-6.6941E-06	-5.6436E-06	-4.6870E-06	-3.8784E-06
10.00	-3.6956E-06	-3.5403E-06	-3.1843E-06	-2.7797E-06	-2.3471E-06	-1.9807E-06
11.00	-1.9064E-06	-1.8306E-06	-1.6716E-06	-1.4674E-06	-1.3107E-06	-1.0705E-06
12.00	-1.0446E-06	-1.0064E-06	-9.2305E-07	-8.1616E-07	-7.0228E-07	-6.2637E-07
13.00	-5.9517E-07	3.0770E-06	-5.2811E-07	-4.6806E-07	-4.0270E-07	-3.4545E-07

Table A.4, continued

R (Å)	θ = 68°	79°	90°	101°	112°	123°
2.50	9.3169E-03	4.6764E-03	3.8331E-03	5.9398E-03	1.2441E-02	2.7640E-02
2.75	3.5692E-03	1.3022E-03	9.2711E-04	2.0101E-03	5.3536E-03	1.3415E-02
3.00	1.0013E-03	-1.9820E-05	-1.6703E-04	3.5030E-04	1.9581E-03	6.0082E-03
3.25	-2.7313E-05	-4.3744E-04	-4.8305E-04	-2.5859E-04	4.5054E-04	2.3542E-03
3.50	-3.6186E-04	-4.9349E-04	-4.9851E-04	-4.1599E-04	-1.4405E-04	6.6778E-04
3.75	-4.1126E-04	-4.2753E-04	-4.1305E-04	-3.9988E-04	-3.2562E-04	-3.6348E-05
4.00	-3.6053E-04	-3.3623E-04	-3.2524E-04	-3.3114E-04	-3.3715E-04	-2.7835E-04
4.25	-2.8693E-04	-2.5366E-04	-2.4391E-04	-2.5743E-04	-2.8975E-04	-3.2012E-04
4.50	-2.1891E-04	-1.8822E-04	-1.8052E-04	-1.9458E-04	-2.3072E-04	-2.8642E-04
4.75	-1.6402E-04	-1.3924E-04	-1.3352E-04	-1.4536E-04	-1.7721E-04	-2.3263E-04
5.00	-1.2240E-04	-1.0347E-04	-9.9315E-05	-1.0884E-04	-1.3412E-04	-1.8064E-04
5.25	-9.1614E-05	-7.7548E-05	-7.4528E-05	-8.1814E-05	-1.0115E-04	-1.3746E-04
5.50	-6.9157E-05	-5.8718E-05	-5.6536E-05	-6.2004E-05	-7.6544E-05	-1.0393E-04
5.75	-5.2590E-05	-4.4953E-05	-4.3351E-05	-4.7448E-05	-5.8249E-05	-7.8643E-05
6.00	-4.0452E-05	-3.4796E-05	-3.3606E-05	-3.6676E-05	-4.4719E-05	-5.9850E-05
6.50	-2.4686E-05	-2.1497E-05	-2.0809E-05	-2.2568E-05	-2.7141E-05	-3.5553E-05
7.00	-1.5648E-05	-1.3765E-05	-1.3360E-05	-1.4401E-05	-1.7093E-05	-2.1935E-05
7.50	-1.0213E-05	-9.0667E-06	-8.8130E-06	-9.4757E-06	-1.1094E-05	-1.3997E-05
8.00	-6.8538E-06	-6.1092E-06	-5.9656E-06	-6.3724E-06	-7.4087E-06	-9.2148E-06
8.50	-4.7185E-06	-4.2425E-06	-4.1362E-06	-4.4046E-06	-5.0825E-06	-6.2455E-06
9.00	-3.3136E-06	-2.9937E-06	-2.9241E-06	-3.1059E-06	-3.5621E-06	-4.3366E-06
10.00	-1.7156E-06	-1.5687E-06	-1.5197E-06	-1.6457E-06	-1.8692E-06	-2.2153E-06
11.00	-9.3338E-07	-9.6832E-07	-8.3730E-07	-8.8627E-07	-1.0033E-06	-1.1944E-06
12.00	-5.2530E-07	-5.0288E-07	-4.7001E-07	-4.9784E-07	-5.6342E-07	5.5791E-06
13.00	-2.8886E-07	-2.7261E-07	-2.6627E-07	-2.8177E-07	-2.5792E-07	-2.2284E-07

Table A.4, continued

R (Å)	θ = 134°	146°	156°	167°
2.50	5.9864E-02	1.2398E-01	2.8828E-01	
2.75	3.1942E-02	7.6804E-02	2.0837E-01	
3.00	1.6205E-02	4.5529E-02	1.4609E-01	
3.25	7.6667E-03	2.5311E-02	9.2150E-02	3.3911E-01
3.50	3.2466E-03	1.2999E-02	5.2245E-02	1.8162E-01
3.75	1.0953E-03	6.0395E-03	2.6960E-02	9.1795E-02
4.00	1.3786E-04	2.4116E-03	1.2667E-02	4.3250E-02
4.25	-2.2732E-04	6.8641E-04	5.3023E-03	1.8902E-02
4.50	-3.2107E-04	-3.9022E-05	1.8307E-03	7.4947E-03
4.75	-3.0461E-04	-2.8329E-04	3.5534E-04	2.5147E-03
5.00	-2.5320E-04	-3.1986E-04	-1.8139E-04	5.2774E-04
5.25	-1.9830E-04	-2.8087E-04	-3.1745E-04	-1.5910E-04
5.50	-1.5118E-04	-2.2404E-04	-3.0391E-04	-3.2729E-04
5.75	-1.1404E-04	-1.7126E-04	-2.4783E-04	-3.1418E-04
6.00	-8.5967E-05	-1.2863E-04	-1.8956E-04	-2.5302E-04
6.50	-4.9698E-05	-7.2240E-05	-1.0457E-04	-1.4040E-04
7.00	-2.9810E-05	-4.1803E-05	-5.8188E-05	-7.5733E-05
7.50	-1.8570E-05	-2.5205E-05	-3.3818E-05	-4.2510E-05
8.00	-1.1989E-05	-1.5867E-05	-2.0628E-05	-2.5181E-05
8.50	-7.9925E-06	-1.0358E-05	-1.3145E-05	-1.5689E-05
9.00	-5.4727E-06	-6.9745E-06	-8.6863E-06	-1.0196E-05
10.00	-2.7254E-06	-3.4114E-06	-4.1397E-06	-4.7383E-06
11.00	-1.4597E-06	-1.7839E-06	-2.1244E-06	-2.4053E-06
12.00	-8.1043E-07	-9.8059E-07	-1.1544E-06	-1.2943E-06
13.00	-4.6238E-07	-5.5551E-07	-6.4986E-07	-7.2456E-07

Appendix B

Table B.1 Rotational energy levels of *ortho*H_2–HCCCN in the ground vibrational state (cm^{-1}), for the potential energy surfaces corresponding to the parallel, perpendicular, and out-of-plane orientations, and the rotational energy levels determined for the parallel orientation surface when it is scaled by lengthening the van der Waals bond by 0.1 Å and 0.15 Å. Radial basis sets of 150 tri-diagonal Morse functions and angular basis sets of 150 Legendre polynomials were sufficient for convergence to within 0.0002 cm^{-1} for all calculated rotational energy transitions. The eigenvalues and eigenvectors of the Hamiltonian matrix were obtained using 3000 Lanczos iterations.

	orthoH_2 - HCCCN				
J_{KaKc}	Parallel	Parallel R + 0.10 Å	Parallel R + 0.15 Å	Perpendicular	Out-of-plane
0_{00}	-85.70769	-86.21954	-86.44925	-116.3158	-94.40422
1_{01}	-85.43226	-85.94534	-86.17568	-116.1093	-94.20757
1_{11}	-84.84688	-85.39907	-85.64794	-98.64136	-75.42432
1_{10}	-84.81888	-85.36991	-85.61820	-98.63822	-75.42122
2_{02}	-84.88236	-85.39807	-85.62975	-115.6962	-93.81427
2_{12}	-84.32440	-84.88022	-85.13093	-98.22624	-75.02696
2_{11}	-84.24042	-84.79275	-85.04170	-98.21682	-75.01767
3_{03}	-84.05995	-84.58000	-84.81390		
3_{13}	-83.54129	-84.10263	-84.35615		
3_{12}	-83.37335	-83.92772	-84.17718		

Table B.2 Rotational energy levels of *ortho*H_2–HCCC^{15}N and *ortho*H_2 - DCCCN in the ground vibrational state (cm^{-1}), for the potential energy surfaces corresponding to the parallel orientation when it is scaled by lengthening the van der Waals bond by 0.15 Å. Radial basis sets of 150 tri-diagonal Morse functions and angular basis sets of 150 Legendre polynomials were sufficient for convergence to within 0.0002 cm^{-1} for all calculated rotational energy transitions. The eigenvalues and eigenvectors of the Hamiltonian matrix were obtained using 3000 Lanczos iterations.

	orthoH_2 – HCCC^{15}N	*ortho*H_2 - DCCCN
J_{KaKc}	Parallel	Parallel
	R + 0.15 Å	R + 0.15 Å
0_{00}	-86.72724	-86.81372
1_{01}	-86.46002	-86.55899
1_{11}	-85.94723	-86.03892
1_{10}	-85.91811	-86.01241
2_{02}	-85.92677	-86.05051
2_{12}	-85.44227	-85.55630
2_{11}	-85.35491	-85.47677
3_{03}	-85.12991	-85.29025
3_{13}	-84.68556	-84.83297
3_{12}	-84.51087	-84.67393

Table B.3 Rotational energy levels of *para*H_2–HCCCN in the ground vibrational state (cm^{-1}), for the averaged potential energy surface (equal weighting all three orientations), and the rotational energy levels determined for the parallel orientation surface when it is scaled by shortening the van der Waals bond by 0.1 Å and 0.15 Å. Radial basis sets of 150 tri-diagonal Morse functions and angular basis sets of 150 Legendre polynomials were sufficient for convergence to within 0.0002 cm^{-1} for all calculated rotational energy transitions. The eigenvalues and eigenvectors of the Hamiltonian matrix were obtained using 3000 Lanczos iterations.

	paraH_2 - HCCCN		
J_{KaKc}	Averaged	Averaged R - 0.10 Å	Averaged R - 0.15 Å
0_{00}	-57.84563	-57.54157	-57.33015
1_{01}	-57.57077	-57.26554	-57.05349
1_{11}	-57.06112	-56.71927	-56.48842
1_{10}	-57.02879	-56.68811	-56.45782
2_{02}	-57.02251	-56.71463	-56.50134
2_{12}	-56.54478	-56.19934	-55.96681
2_{11}	-56.44778	-56.10588	-55.87502
3_{03}	-56.20377	-55.89148	-55.67608
3_{13}	-55.77107		-55.18503
3_{12}	-55.57716		-55.00154

Table B.4 Rotational energy levels of *para*H_2–HCCC^{15}N and *para*H_2 - DCCCN in the ground vibrational state (cm^{-1}), for the averaged potential energy surface (equal weighting all three orientations) when it is scaled by shortening the van der Waals bond by 0.15 Å. Radial basis sets of 150 tri-diagonal Morse functions and angular basis sets of 150 Legendre polynomials were sufficient for convergence to within 0.0002 cm^{-1} for all calculated rotational energy transitions. The eigenvalues and eigenvectors of the Hamiltonian matrix were obtained using 3000 Lanczos iterations.

	paraH_2 – HCCC^{15}N	*para*H_2 - DCCCN
J_{KaKc}	Averaged R - 0.15 Å	Averaged R - 0.15 Å
0_{00}	-57.36837	-57.41860
1_{01}	-57.09758	-57.16062
1_{11}	-56.52947	-56.58488
1_{10}	-56.50011	-56.55820
2_{02}	-56.55706	-56.64554
2_{12}	-56.01829	-56.09659
2_{11}	-55.93024	-56.01654
3_{03}	-55.74901	-55.87515
3_{13}	-55.25213	-55.36462
3_{12}	-55.07610	-55.20458